

Syracuse University

**SURFACE**

---

Dissertations - ALL

SURFACE

---

12-1-2016

## Kinetics of ketone hydrogenation over supported Ru catalysts

Omar Abdelrahman Ali Abdelrahman  
*Syracuse University*

Follow this and additional works at: <https://surface.syr.edu/etd>



Part of the [Engineering Commons](#)

---

### Recommended Citation

Abdelrahman, Omar Abdelrahman Ali, "Kinetics of ketone hydrogenation over supported Ru catalysts" (2016). *Dissertations - ALL*. 554.  
<https://surface.syr.edu/etd/554>

This Dissertation is brought to you for free and open access by the SURFACE at SURFACE. It has been accepted for inclusion in Dissertations - ALL by an authorized administrator of SURFACE. For more information, please contact [surface@syr.edu](mailto:surface@syr.edu).

## Abstract

A kinetic investigation of the production of  $\gamma$ -valerolactone (GVL) via the aqueous phase hydrogenation of levulinic acid (LA) over supported Ru catalysts was carried out, in order to understand how to better design a hydrogenation catalyst for such biomass catalytic strategies. At temperatures representative of biomass processing, the reaction proceeds first through the reduction of the LA ketone group to its corresponding alcohol, 4-hydroxypentanoic acid (HPA), which subsequently produces GVL via intramolecular esterification in solution. The governing kinetics of LA hydrogenation were found to be insensitive to the identity of the support material on which Ru catalysts were prepared. Conversely the stability of supported Ru catalysts in the aqueous phase were strongly dependent on the choice of support, exhibiting severe sintering of Ru nanoparticles, the extent of which appears to be dictated by the bulk electronegative properties of the support material.

The presence of a secondary functional group in LA (i.e., a carboxyl group) does not appear to perturb the activity of Ru sites in water, where LA and its mono-functional ketone analog (2-pentanone) hydrogenate at identical rates. LA hydrogenation thus appears kinetically equivalent to that of 2-pentanone. Given the similarity, C<sub>3</sub>-C<sub>5</sub> ketone hydrogenation over Ru/SiO<sub>2</sub> in the vapor-phase was examined, alleviating the need to consider solution phase complexities. A single universal microkinetic model for the hydrogenation of ketones over supported Ru catalysts was developed, based on a modified Horiuti-Polanyi-type mechanism involving two distinct surface sites. Through the application of surface lateral interactions to the developed ketone microkinetic model, solvent effects commonly reported for hydrogenations over Ru catalysts are rationalized on the basis of the stabilization of a kinetically relevant transition state.

# Kinetics of ketone hydrogenation over supported Ru catalysts

by

Omar Abdelrahman Ali Abdelrahman

B.Sc., American University of Sharjah, 2011

Dissertation

Submitted in partial fulfillment of the requirements for the degree of  
Doctor of Philosophy in Chemical Engineering.

Syracuse University  
December 2016

Copyright © Omar Abdelrahman Ali Abdelrahman 2016

All rights reserved

## **Acknowledgments**

I would like to thank my family for their constant support throughout this program. My wife, Alexis, who put up with all the late hours in the lab and gas chromatographs sitting on our living room floor. Syracuse is a special place to us both, we met here as freshman in graduate school, were married in Syracuse, built a home together and sadly now have to leave. I hope we can return to visit soon and relive some of the memories. I am extremely grateful to my parents, Maha and Abdelrahman, who constantly encouraged my education even if it meant moving halfway across the world. I am thankful for all the sacrifices you've made, and continue to make, so that I can have the education and life you've blessed me with. To my brothers, Ahmed, Mustafa and Medhat, thank you for being there to share in my joy and pain throughout these years that we've all been away from home. Thank you also for the drive you've all instilled in me, being the youngest child, through healthy sibling rivalry as we each pursued our own careers. I cannot wait for the day we all live in the same city again. I would also like to thank my Aunt and Uncle, Hannelore and Abdelmoneim, you've made DC my home away from home here in the US.

To all my friends here in Syracuse, thank you for making my time here as great as it has been. Thank you for all the barbeques, bike rides, snowball fights, late night food binges, road trips and just simply hanging out every weekend. I would like to especially acknowledge Elie, Maria, Mireille, Tariq, Can, Duygu, Sozen, Hakan, Manar, Rafic and Ogan for being the friends you have been. I would also like to thank all of the current and past Bond lab members for making my experience what it has been, never a dull day in the lab. I would especially like to thank Aimee and Argy, I will never forget the first day we all set foot in the lab together and finding it eerily empty. Argy, we've been at this for five years now and you've been my best friend in and out of the lab. I hope we get to be in the same area again sometime in the future.

I would also like to thank the facilities staff at Syracuse University, whom without the road to making the Bond lab what it is today would have been impossible. I want to thank Lou Buda and his team of phenomenal machinists that never said no to any design we brought them, and also put up with me going through their scrap room without really knowing what it is I was looking for. Sally Prash without whom all of our custom glass needs would've gone unanswered, thank

you for also fixing our quartz TPD cells no matter how many times we ended up breaking them. To Bill Dossert and Dick Chave, words will never do justice how you have shaped my experience at SU. I cannot point to a single instrument in our lab which one of you has not improved, designed or repaired in some way or the other. I have truly enjoyed our friendship, spending many hours chatting in the machine shop about so many different topics throughout the years.

To the faculty at my Alma matter, American University of Sharjah, I am forever in your debt for the wonderful education you have given me. To Dr. Taleb Ibrahim, I thank you for pushing me to get involved in research within the Chemical Engineering department early on in my undergraduate career and leading by example for what “good science” can be. Dr. Raafat Al-Naizy, your constant support as a research advisor and unique sense of humor kept me motivated through some really tough times. To Dr. Ahmad Aidan, you taught me how to be an experimental researcher and always gave me plenty of space to try my own ideas over the years. Despite my plans for becoming an Economics/ Chemical Engineering double major failing, I cannot express enough gratitude to Dr. George Naufal for introducing me to the world of research through the perspective of macroeconomics. I always enjoyed hanging out in your office and talking about economics, besides it being interesting, it gave me needed breaks from engineering at times!

I would also like to thank Syracuse University and the Biomedical and chemical engineering department, for the wealth of opportunity they have provided me with. I would like to thank the faculty members of the department, whom through coursework and just friendly interactions in school functions and the hallways, have truly made my experience here at SU a positive one. I would also like to thank my dissertation committee members, Professors Sureshkumar, Ren, Maye, Tavlarides and Sangani, for their patience and help throughout the process. I would also like to thank the National Science Foundation for their financial support of this research.

Finally, I would like to extend my sincere gratitude to my advisor, Professor Jesse Q. Bond, a person who believes in all his students and dedicates himself to their advancement. You’ve taught me how to be a kineticist, to truly appreciate catalysis in all its glory. You have been a friend and great source of support and motivation, as well as a boss that takes care of his own.

You truly have set the bar high for what I would one day hope to become as an academic researcher. I can honestly say that you change every person that passes through your lab for the better, by simply providing an environment where students are mentored and allowed to grow. You also definitely seem to pass on other qualities to your students that go beyond academia; our reputation at conferences has become that you only graduate from the Bond lab once you grow a beard and own a bike. It truly brings me pleasure and a great sense of pride to call myself your student, presenting the culmination of years of hard work mentored by you in this thesis.

*To my family*

# Table of Contents

<b>Abstract</b>	i
<b>Acknowledgments</b>	iv
<b>List of Figures</b>	xii
<b>List of Tables</b>	xix
<b>Chapter 1 Introduction</b>	1
1.1 The future of oil and its socioeconomic consequences	1
1.2 Biomass as a sustainable carbon source	3
1.3 The production of $\gamma$ -valerolactone from lignocellulosic biomass	7
1.4 Research overview	9
1.5 References	10
<b>Chapter 2 Experimental methods</b>	14
2.1 Catalyst preparation	14
2.2 Catalyst characterization	16
2.2.1 N <sub>2</sub> physical adsorption	16
2.2.2 Metal site titration with CO chemisorption	16
2.2.3 Transmission electron microscopy	19
2.2.4 X-ray Diffraction	19
2.3 Catalytic reactor setups	20
2.3.1 Flow reactor	20
2.3.2 Aqueous phase batch reactor	23
2.4 References	25
<b>Chapter 3 Analysis of kinetics and reaction pathways in the aqueous-phase hydrogenation of levulinic acid to form <math>\gamma</math>-valerolactone over Ru/C</b>	26
3.1 Introduction	26
3.2 Materials & Methods	28
3.2.1 Analytical Methodology	29
3.2.2 Bulk concentrations of dissolved LA and H <sub>2</sub>	30
3.2.3 Kinetic Studies	31
3.2.1.1 Levulinic Acid Hydrogenation	31

3.2.1.2	LA Dehydration	34
3.2.1.3	Intramolecular esterification of HPA	35
3.2.1.4	Stacked bed experiments	36
<b>3.3</b>	<b>Results and Discussion</b>	36
3.3.1	Primary analysis of LA hydrogenation products formed over Ru/C	36
3.3.2	Assessing transport control in liquid phase hydrogenation of LA	38
3.3.3	Kinetics of LA Hydrogenation	42
3.3.2.1	Reaction Orders: Levulinic Acid	45
3.3.2.2	Reaction Orders: Hydrogen	47
3.3.2.3	Temperature Effects	48
3.3.4	Analysis of Kinetic Data	50
3.3.5	Kinetics of the Intramolecular Esterification of HPA	52
3.3.4.1	Reaction Orders	53
3.3.4.2	Temperature Effects	54
3.3.6	Kinetic model for GVL production via LA hydrogenation	55
3.3.7	Stacked Bed Reactors	58
<b>3.4</b>	<b>Conclusion</b>	60
<b>3.5</b>	<b>References</b>	61
<b>Chapter 4 Towards rational design of stable, supported metal catalysts for aqueous phase processing: insights from the hydrogenation of levulinic acid</b>		64
<b>4.1</b>	<b>Introduction</b>	64
<b>4.2</b>	<b>Experimental</b>	66
4.2.1	Materials and methods	66
4.2.2	Catalyst preparation	67
4.2.3	Catalyst Characterization	67
4.2.4	TEM	68
4.2.5	Catalytic Activity Testing	69
<b>4.3</b>	<b>Results</b>	71
4.3.1	Catalyst Activity	71
4.3.2	Catalyst Stability	75
4.3.3	Irreversible deactivation	80

4.3.4	Reversible deactivation	87
<b>4.4</b>	<b>Discussion</b>	91
<b>4.5</b>	<b>Conclusion</b>	97
<b>4.6</b>	<b>References</b>	100
<b>Chapter 5 Microkinetic analysis of C<sub>3</sub> – C<sub>5</sub> ketone hydrogenation over supported Ru catalysts</b>		105
<b>5.1</b>	<b>Introduction</b>	105
<b>5.2</b>	<b>Experimental</b>	106
4.2.1	Materials and methods	106
4.2.2	Catalyst preparation	107
4.2.3	Catalyst Characterization	107
4.2.4	Catalytic Activity Testing	107
<b>5.3</b>	<b>Results</b>	110
5.3.1	Catalyst synthesis & characterization	110
5.3.2	Estimating Initial rates	110
5.3.3	Assessing kinetic control	113
5.3.4	Apparent Kinetics of ketone hydrogenation: low temperatures	115
5.3.5	Apparent Kinetics of ketone hydrogenation: high temperatures	117
5.3.6	Apparent Kinetics of ketone hydrogenation: co-feeding conditions	119
<b>5.4</b>	<b>Discussion</b>	120
5.4.1	Elementary surface steps	120
5.4.2	Single site model	121
5.4.3	Two site model	124
5.4.4	Identifying potential adsorption sites on Ru surfaces	129
5.4.4.1	Identifying potential adsorption sites on Ru surfaces: Hydrogen	130
5.4.4.2	Identifying potential adsorption sites on Ru surfaces: Ketone	131
5.4.4.3	Identifying potential adsorption sites on Ru surfaces: Half-hydrogenated intermediate	132
5.4.4.4	Identifying potential adsorption sites on Ru surfaces: Alcohol	134
5.4.5	Microkinetic analysis	135
5.4.5.1	Microkinetic analysis: gas phase thermochemistry	136

5.4.5.2	Microkinetic analysis: adsorption energetics	138
5.4.5.3	Microkinetic analysis: kinetics of the rate controlling step	144
5.4.5.4	Microkinetic analysis: regression results	146
5.4.5.5	Microkinetic analysis: simulation results and comparison to experimental data	151
<b>5.5</b>	<b>Conclusion</b>	<b>154</b>
<b>5.6</b>	<b>References</b>	<b>156</b>
<b>Chapter 6</b>	<b>Future work</b>	<b>161</b>
<b>6.1</b>	<b>References</b>	<b>172</b>
<b>VITA</b>		<b>173</b>

## List of Figures

<b>Figure 1.1</b> Average WTI monthly price in \$/bbl over the past 20 years	2
<b>Figure 1.2</b> – Average breakdown of lignocellulosic biomass	4
<b>Figure 1.3</b> Levulinic acid as a platform chemical	5
<b>Figure 1.4</b> Landscape of chemical pathways possible from GVL	6
<b>Figure 1.5</b> - Proposed aqueous phase processing strategy of lignocellulosic biomass	8
<b>Figure 2.1</b> Schematic of catalyst reduction cell	15
<b>Figure 2.2</b> Cross-sectional view of supported Ru nanoparticle on support surface adopting a spherical geometry. Shaded Ru atoms indicate exposed Ru surface atoms which may provide a catalytic surface.	17
<b>Figure 2.3</b> Schematic representation of the X-ray diffractometer with a $\theta:2\theta$ goniometer	20
<b>Figure 2.4</b> A differential catalyst element $dW$ across which the molar flow rate of A changes by a differential amount $dF_A$ as a result of a reaction on the catalyst surface.	21
<b>Figure 2.5</b> Schematic of catalytic reactor setup employed for aqueous phase hydrogenations	22
<b>Figure 2.6</b> Schematic of catalytic reactor setup employed for vapor phase hydrogenation	23
<b>Figure 2.7</b> Batch reactor setup used for measuring the kinetics of the acid catalyzed intramolecular fisher trans-esterification of HPA to GVL in solution	24
<b>Figure 3.1</b> Pathways leading to $\gamma$ -valerolactone during hydrogenation of levulinic acid.	26
<b>Figure 3.2</b> a) Rates of LA hydrogenation over Ru/C at 323K ( $\diamond$ ), 343K ( $\circ$ ), and 363K ( $\square$ ) as a function of time on stream. b) Linearized rate data illustrating second order deactivation and method employed for estimation of rates at zero time on stream. For all experiments summarized here, the aqueous phase concentrations of LA and $H_2$ were 0.50M and 0.016M.	43

**Figure 3.3** Observed LA hydrogenation rates as a function of time on stream at  $T = 323\text{K}$ ,  $C_{\text{H}_2} = 0.016\text{M}$ ,  $C_{\text{LA}} = 0.1\text{M}$ . ( $\circ$ ) Fresh catalyst, ( $\Delta$ ) first regeneration, ( $\square$ ) second regeneration, ( $\diamond$ ) third regeneration. Regeneration was performed in situ by interrupting aqueous feeds and reducing the catalyst under flowing  $\text{H}_2$  (100 sccm, 4h, 673K,  $1\text{K min}^{-1}$ ) 44

**Figure 3.4** Correlation between levulinic acid concentration and hydrogenation rate.

Experiments illustrated here were carried out at 323K, 0.016M  $\text{H}_2$  concentration, and varying WHSV to maintain LA conversions below 3%. Turnover frequencies are reported in  $\text{s}^{-1}$  and LA concentrations are reported in  $\text{mol L}^{-1}$ . 47

**Figure 3.5** Correlation between dissolved aqueous phase hydrogen concentration and hydrogenation rate. Experiments illustrated here were carried out at 323K, 0.5M LA, and varying WHSV to maintain LA conversions below 3%. Turnover frequencies are reported in  $\text{s}^{-1}$  and  $\text{H}_2$  concentrations are reported in  $\text{mol L}^{-1}$ . 48

**Figure 3.6** Correlation between reaction temperature and levulinic acid hydrogenation rate. Experiments illustrated here were carried out at 0.5M LA, 0.016M  $\text{H}_2$ , and varying WHSV to maintain LA conversions below 3%. Apparent rate constants here are reported in  $\text{L}^{0.5} \text{mol}^{0.5} \text{g}^{-1} \text{s}^{-1}$ . 50

**Figure 3.7** a) Batch kinetic data for intramolecular esterification of HPA at ( $\Delta$ ) 300 K,  $C_{\text{H}^+} = 1.65 \text{mM}$ ,  $C_{\text{HPA}0} = 47.7\text{mM}$ , ( $\nabla$ ) 318K,  $C_{\text{H}^+} = 1.65 \text{mM}$ ,  $C_{\text{HPA}0} = 47.7\text{mM}$ , ( $\circ$ ) 339K,  $C_{\text{H}^+} = 1.65 \text{mM}$ ,  $C_{\text{HPA}0} = 47.7\text{mM}$ , ( $\square$ ) 339K,  $C_{\text{H}^+} = 2.69 \text{mM}$ ,  $C_{\text{HPA}0} = 41.2 \text{mM}$ . b) Apparent rate constants for intramolecular esterification of HPA determined at ( $\Delta$ ) 339K and ( $\circ$ ) 318K at various values of pH.  $k'$  is reported here in units of  $\text{min}^{-1}$ . 54

**Figure 3.8** Arrhenius plot illustrating the temperature dependence of rate constants for intramolecular esterification of HPA. Apparent rate constants are reported here in units of  $\text{L mol}^{-1} \text{min}^{-1}$ . 55

**Figure 3.9** Summary of the empirical kinetic model employed here to predict LA hydrogenation rates and GVL selectivities in a differential Packed Bed Reactor operating between  $T = 303$  to  $343\text{K}$ ,  $C_{\text{LA}} = 0.025 - 1.5\text{M}$ , and  $C_{\text{H}_2} = 0.0028 - 0.028\text{ M}$ . 56

**Figure 3.10** Comparison between model predicted trends and experimental observations at various LA and  $\text{H}_2$  concentrations below  $363\text{K}$ . (a) Describes the trends observed in GVL production rates, which captures selectivity during LA hydrogenation. (b) Describes the trends in TOF of LA hydrogenation. 58

**Figure 4.1** Functional relationship between mass-normalized ketone hydrogenation rates and Ru surface site densities as determined by CO chemisorption. Hydrogenation rates were measured at  $0.5\text{M}$  ketone concentration at  $323\text{K}$  and  $24\text{ bar H}_2$ . ( $\diamond$ ) Ru/ $\text{TiO}_2$ , ( $\circ$ ) Ru/C, ( $\Delta$ ) Ru/ $\text{SiO}_2$ , ( $\square$ ) Ru/ $\gamma\text{-Al}_2\text{O}_3$ . Open symbols represent LA hydrogenation rates. Filled symbols represent 2-pentanone hydrogenation rates. The slope of the regression line indicated in the figure is  $1.0 \pm 0.14$ , which is consistent with criteria given by Koros and Nowak for demonstration of kinetically controlled hydrogenation rates at a given temperature. 75

**Figure 4.2** LA hydrogenation activity as a function of time on stream for Ru supported on (a)  $2.7\text{ wt\%}$  on  $\text{SiO}_2$ , (b)  $1.3\text{ wt\%}$  on  $\gamma\text{-Al}_2\text{O}_3$ , (c)  $0.4\text{ wt\%}$  on  $\text{TiO}_2$  and (d)  $0.5\text{ wt\%}$  on C. Observed deactivation profiles for samples prepared at different Ru loadings were qualitatively similar to the above trends such that this selection of samples is appropriate for the following discussion. 77

- Figure 4.3** Comparison of hydrogenation activity of Ru supported on (a) SiO<sub>2</sub> and (b)  $\gamma$ -Al<sub>2</sub>O<sub>3</sub>. Open symbols represent LA hydrogenation rates. Filled symbols represent 2-pentanone hydrogenation rates. 79
- Figure 4.4** PXRD of a) 0.4% Ru/P25, b) 1.3% Ru/ $\gamma$ -Al<sub>2</sub>O<sub>3</sub>, c) 0.5% Ru/C, d) 5% Ru/C. Solid line indicates fresh catalyst and dashed indicates spent catalyst 81
- Figure 4.5** PXRD of 2.7% Ru/SiO<sub>2</sub>. Solid line indicates fresh catalyst and dashed indicates spent catalyst 82
- Figure 4.6** Loss in irreversible CO uptake in comparison to inverse of particle growth. Line of parity indicated by dashed line. ( $\diamond$ ) Ru/TiO<sub>2</sub>, ( $\circ$ ) Ru/C-B, ( $\Delta$ ) Ru/SiO<sub>2</sub>-A, ( $\square$ ) Ru/ $\gamma$ -Al<sub>2</sub>O<sub>3</sub>. Initial particle diameters for Ru/TiO<sub>2</sub>, Ru/SiO<sub>2</sub>, and Ru/ $\gamma$ -Al<sub>2</sub>O<sub>3</sub> were determined by TEM, and the initial particle diameter of Ru/C-B was calculated from irreversible CO uptake. All final particle diameters were determined by TEM. 84
- Figure 4.7** Illustration of first order (irreversible) decay in activity with time on stream for Ru supported on ( $\Delta$ ) Ru/SiO<sub>2</sub>-A, ( $\circ$ ) Ru/C-B, ( $\diamond$ ) Ru/TiO<sub>2</sub>, and ( $\square$ ) Ru/ $\gamma$ -Al<sub>2</sub>O<sub>3</sub>. Here, irreversible losses are attributed to particle sintering. 85
- Figure 4.8** Profiles of reversible activity loss with time on stream observed for (a) Ru/SiO<sub>2</sub>-A, (b) Ru/ $\gamma$ -Al<sub>2</sub>O<sub>3</sub>, (c) Ru/TiO<sub>2</sub> and (d) Ru/C-B. Open symbols represent rates of LA hydrogenation. Filled symbols represent rates of 2-pentanone hydrogenation. Reversible deactivation profiles were obtained by correcting activity profiles shown in Figures 2 and 3 for irreversible deactivation due to particle sintering. 88
- Figure 4.9** Activity profile of Ru/ $\gamma$ -Al<sub>2</sub>O<sub>3</sub> during the hydrogenation of 2-pentanone in the presence of propanoic acid. 91

**Figure 4.10** Correlation between sintering constants and electronegativity of a bulk oxide. ( $\diamond$ ) Ru/TiO<sub>2</sub>, ( $\Delta$ ) Ru/SiO<sub>2</sub>-A and ( $\square$ ) Ru/ $\gamma$ -Al<sub>2</sub>O<sub>3</sub>. Open symbols represent sintering rates during LA hydrogenation. Filled symbols represent sintering rates during 2-pentanone hydrogenation 93

**Figure 4.11** Correlation between PZC (and surface charge) with the extent of reversible deactivation on each Ru-support combination considered during the hydrogenation of levulinic acid and 2-pentanone. ( $\diamond$ ) Ru/TiO<sub>2</sub>, ( $\circ$ ) Ru/C-B, ( $\Delta$ ) Ru/SiO<sub>2</sub>-A, ( $\square$ ) Ru/ $\gamma$ -Al<sub>2</sub>O<sub>3</sub>. Open symbols represent reversible losses during LA hydrogenation. Filled symbols represent reversible losses during 2-pentanone hydrogenation. 96

**Figure 5.1** Observed 2-pentanone hydrogenation activity as a function of time on stream at T = 322 K, P<sub>H<sub>2</sub></sub> = 910 Torr, P<sub>2-pentanone</sub> = 4.8 Torr. ( $\diamond$ ) 0.3% Ru/SiO<sub>2</sub>, ( $\circ$ ) 0.6% Ru/SiO<sub>2</sub>, ( $\Delta$ ) 0.84% Ru/SiO<sub>2</sub>, ( $\square$ ) 1.5% Ru/SiO<sub>2</sub>. 111

**Figure 5.2** Comparison of deactivation models for a 0.6wt% Ru/SiO<sub>2</sub> catalyst during 2-pentanone hydrogenation at 322K, 4.8 Torr 2-pentanone and 910 Torr H<sub>2</sub>. Dashed line represents single 1<sup>st</sup> order deactivation model. Solid line represents two 1<sup>st</sup> order deactivation models with a non-zero asymptote. 113

**Figure 5.3** Functional relationship between mass-normalized ketone hydrogenation rates and Ru surface site densities as determined by CO chemisorption. Hydrogenation rates were measured at 4.8 Torr ketone and 910 Torr H<sub>2</sub>, open and closed symbols indicate rates at 322 K and 341 K respectively. For (a) acetone hydrogenation, the slope of the regression lines indicated in the figure are  $1.04 \pm 0.11$  (322K) and  $1.1 \pm 0.9$  (341K). For (b) 2-pentanone hydrogenation, the slope of the regression lines indicated in the figure are  $0.96 \pm 0.30$  (322K) and  $1.1$  (341K). This is consistent with criteria given by Koros and Nowak for demonstration of kinetically controlled

hydrogenation rates at the given temperatures. Confidence intervals were calculated at a 95% confidence level. 114

**Figure 5.4** Effect of (a) ketone and (b) hydrogen partial pressure on the site time yield of hydrogenation at 322 K for (○) 2-pentanone, (□) 2-butanone and (Δ) acetone. Ketone partial pressures varied from approximately 0.3 – 30 Torr. Hydrogen partial pressures varied from 90-910 Torr. 116

**Figure 5.5** Arrhenius plot for ketone hydrogenation from 303 - 359 K at a ketone and hydrogen partial pressure of 4.8 and 910 Torr respectively for (○) 2-pentanone, (□) 2-butanone and (Δ) acetone. 116

**Figure 5.6** Arrhenius plot for acetone hydrogenation from 303 - 456 K at ketone and hydrogen partial pressures of 4.8 and 910 Torr. 118

**Figure 5.7** Effect of (a) ketone and (b) hydrogen partial pressure on the site time yield of acetone hydrogenation at 442 K. Ketone partial pressures varied from 0.5 – 4.8 Torr. Hydrogen partial pressures varied from 250-910 Torr. 119

**Figure 5.8** Effect of ketone conversion on the rate of acetone hydrogenation at 442 K, 4.8 Torr acetone and 910 Torr H<sub>2</sub>. 128

**Figure 5.9** Ru (0001) facet with a lattice constant of 2.71 Å with the distinct adsorption sites: 1) top, 2) bridge, 3) three-fold fcc and 4) three-fold hcp. Dashed lines indicate atoms in the second layer. 130

**Figure 5.10** Spectroscopically observed adsorption modes of acetone on a clean Ru (0001) surface [37] 132

**Figure 5.11** Expected adsorption modes of alkoxide and hydroxyalkyl intermediates on the surface 133

**Figure 5.12** Comparison of predicted to experimentally measured STY of ketone hydrogenation for (○) 2-pentanone, (□) 2-butanone and (Δ) acetone. Reaction conditions were varied across temperatures of 303-456 K, 0.3 - 30 Torr of ketone and 75 - 910 Torr of H<sub>2</sub>. 148

**Figure 5.13** Predicted coverages of ketone (Δ), alkoxide (○), hydrogen (◇) and vacant ‘\*’ sites (\*) from 303-456 K at fixed partial pressures of 4.8 Torr ketone and 910 Torr H<sub>2</sub> for a) acetone, b) 2-butanone, and c) 2-pentanone hydrogenation. Note that hydrocarbon species are assumed to bind at ‘\*’ sites and hydrogen atoms bind at ‘s’ sites. 152

**Figure 6.1** H<sup>1</sup>-NMR spectra of condensed reactor effluents under co-feeding conditions of 40 Torr of a) D<sub>2</sub>O and b) CD<sub>3</sub>OD at 322 K. 166

**Figure 6.2** Mass spectrum fragmentations of a 2-pentanol standard (blue) and reactor effluent (orange) at 322 K with 40 Torr of D<sub>2</sub>O co-fed with 4 Torr of 2-pentanone and 910 Torr H<sub>2</sub>. 167

## List of Tables

<b>Table 3.1</b> Experimentally observed LA conversions and product selectivities during hydrogenation of LA over Ru/C under inert and reducing environments and at temperatures ranging from 323 - 423K.	36
<b>Table 3.2</b> Experimentally observed LA conversions and product selectivities during hydrogenation of LA over Ru/C and A15. $T = 323\text{K}$ , $C_{\text{LA}} = 0.5\text{ M}$ , $C_{\text{H}_2} = 0.016\text{ M}$ .	60
<b>Table 4.1</b> Physical and chemical properties of supported Ru catalysts employed in this study.	72
<b>Table 4.2.</b> Summary of initial rates of hydrogenation for both levulinic acid and 2-pentanone in bulk water at 323K, 24 bar $\text{H}_2$ , and 0.5M dissolved organic. Conversions and rates are both reported at zero time on stream.	73
<b>Table 4.3</b> Comparison of physical and chemical characterization of catalyst samples in fresh and spent states. The table also summarizes the percentage of initial activity that was lost irreversibly during the indicated period on stream.	80
<b>Table 4.4</b> Estimated sintering constants for various supported Ru catalysts at 90% confidence level.	86
<b>Table 4.5</b> Summary of estimated reversible deactivation parameters during the hydrogenation of LA and 2-pentanone over Ru on various supports.	90
<b>Table 4.6</b> Summary of PZC values of the various supports employed	95
<b>Table 5.1</b> Physical properties and irreversible CO uptake measurements of various supported Ru/SiO <sub>2</sub> catalysts.	110
<b>Table 5.2</b> Initial STY of hydrogenation of various ketones measured at 322 K, 4.8 Torr of ketone and 910 Torr of $\text{H}_2$ . Confidence intervals are calculated at 95%.	115

<b>Table 5.3</b> Summary of apparent activation barriers and reaction orders based for the various ketones studied over supported Ru/SiO <sub>2</sub> catalysts. Activation barriers were determined at 4.8 and 910 Torr of ketone and H <sub>2</sub> respectively. Reaction orders were determined at 322 K. Confidence intervals calculated at 95%.	117
<b>Table 5.4</b> Summary of relative 2-pentanone hydrogenation rates at 322 K in the presence of different ketones over supported Ru/SiO <sub>2</sub> catalysts.	120
<b>Table 5.5</b> Proposed set of elementary steps to describe ketone hydrogenation over Ru surfaces. Proposed set of elementary steps to describe ketone hydrogenation over Ru surfaces.	121
<b>Table 5.6</b> Proposed set of elementary steps to describe ketone hydrogenation over Ru surfaces, with the non-competitive adsorption of hydrogen.	125
<b>Table 5.7</b> Summary of energetics of stable gas phase species.	137
<b>Table 5.8</b> Summary of potentially adjustable parameters and their initial estimates.	146
<b>Table 5.9</b> Summary of optimized parameters found from the regression of experimental data. Uncertainty in optimized values was estimated at a 95% confidence level.	147
<b>Table 5.10</b> Comparison of experimentally measured and predicted apparent reaction kinetics for all ketones	153
<b>Table 6.1</b> Measured relative rate of 2-pentanone hydrogenation in the presence of various solvents. 2-pentanone and hydrogen partial pressure were maintained at 4 and 910 Torr respectively.	162
<b>Table 6.2</b> Regression results of Eq. (6) and hydrogen bond donor and acceptor capability. Hydrogen bonding properties of water and deuterium oxide are taken to be the same.	171

## **Chapter 1 Introduction**

### **1.1 The future of oil and its socioeconomic consequences**

The dwindling prospect of economically feasible petroleum feedstocks has been a matter of public concern since the early 1970s, when gasoline prices reached record highs due to geopolitical factors impacting the supply of crude oil. Since that time, the occurrence of similar events coupled with an increased global demand for petroleum based products have resulted in a realistic concern for the reliability of such feedstocks. This can be best embodied by the concept of peak oil, more famously expressed as “Hubbert’s peak”, which attempts to predict the inevitable peak in global oil production. While predictions made by various peak oil hypotheses such as Hubbert’s peak have not been always accurate as to when peak global oil production would be reached, it stands to reason that peak oil is inevitable. The demand for the end use products from crude oil, however, are unlikely to dwindle; rather, demand will continue to grow with increased global populations and average human life spans. This places a strain on societies given the significant reliance on petroleum derived products. This concern is especially exacerbated in countries that are net importers of petroleum such as the United States [1].

Shown in Figure 1.1 is the average monthly price for a barrel of WTI oil over the past 20 years, where from the mid-1980s to the early-2000s, the price did not exhibit much variability. Within the last decade, however, the price of oil has seen dramatic shifts from a high of \$145 per barrel in early 2008 to \$29 per barrel in February of 2016. Volatility in the price of oil negatively impacts chemical and energy sectors, which rely on petroleum as their primary feedstock.

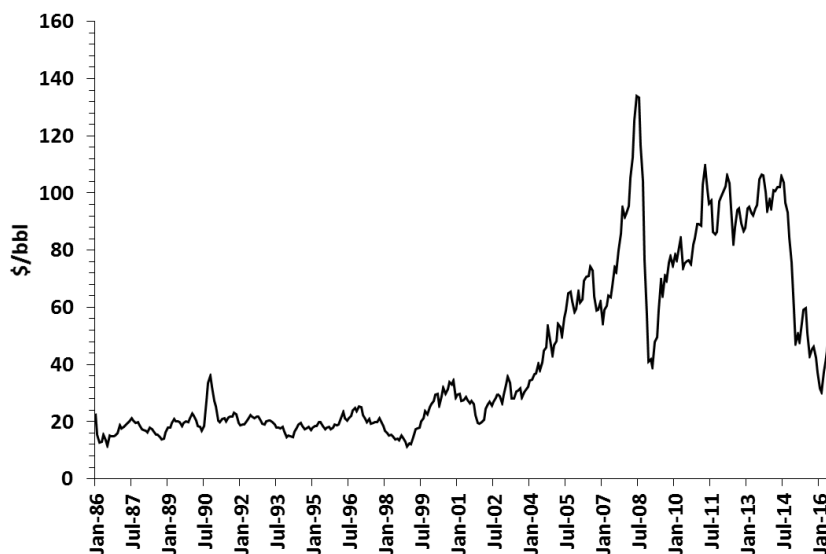


**Figure 1.1** Average WTI monthly price in \$/bbl over the past 20 years

In addition to economic considerations, there is growing concern as to the environmental impact of the current level of petroleum based product consumption. Specifically fossil fuel use in transportation and energy sectors where combustion technologies are ubiquitous. Despite improvements in combustion technologies over the years, the net release of carbon dioxide amongst other pollutants is inevitable due to fossil fuel consumption, which diminishes the sustainability of such practices.

Driven by a desire for economic and environmental sustainability, interest in alternative energy and hydrocarbon sources has surged in recent years. While entities such as transportation and power sectors could one day switch to non-carbon based technologies, a carbon source will remain imperative for chemical industries. In addition, finding an alternative carbon source would allow for the continued utilization of the extensive hydrocarbon based infrastructure in place. So while there has been much effort focused on moving away from a hydrocarbon based economy, finding an alternative feedstock that can sustain the current demand for hydrocarbons

remains more attractive. It is therefore necessary to identify a potential feedstock that can act as a source of hydrocarbons that is sustainable and chemically resembles the hydrocarbons currently consumed.

## **1.2 Biomass as a sustainable carbon source**

A variety of potentially sustainable carbon sources have been proposed, of which biomass has emerged as a promising option. An appealing aspect of utilizing biomass as a carbon source is its relative abundance. The United States possesses the capacity to produce 1.3 billion dry tons of biomass annually, sufficient to replace one third of the current domestic petroleum consumption [2]. A substantial research effort over the last decade has therefore been devoted to converting biomass into chemicals. For ethical reasons, the use of food crops as a carbon source is undesirable, the current focus is therefore on biomass sources that do not compete with food resources. Of the various categories of biomass, lignocellulosic biomass is one such example which is not a food crop, and does not compete for arable land better suited for food production. Typically, lignocellulosic biomass is obtained from inedible portions of plants, agricultural by-products and forest residues [3]. The precise chemical composition of lignocellulosic biomass is highly complex, it can however be grouped into three fractions of lignin, cellulose and hemicellulose. Shown in Figure 1.2 is the average composition of the three fractions by mass for varying sources of lignocellulosic biomass [4].

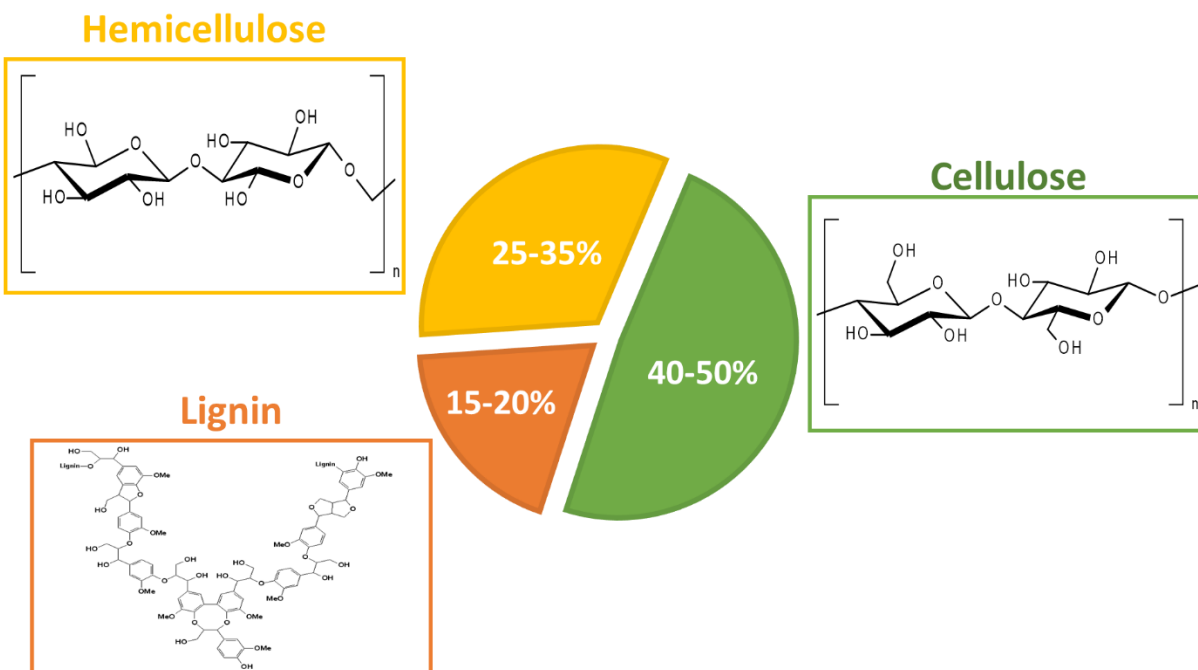


**Figure 1.2** – Average breakdown of lignocellulosic biomass

For the purpose of biomass serving as a carbon source, the cellulose and hemicellulose fractions (65-85% by mass) are of interest. From the cellulose and hemicellulose fractions a myriad of industrially relevant products can be attained, the routes to which have been reviewed elsewhere [5]. One particular route of interest is the production levulinic acid (LA). LA is a five-carbon  $\gamma$ -ketoacid that has been identified as a “top ten” bio-based chemical from biomass in a 2004 report by the United States Department of Energy [6]; LA serves as a precursor to various chemical compounds with existing large volume commodity markets (Figure 1.3) [7-15]. Unlike many lignocellulosic biomass upgrading technologies which have only been demonstrated at the bench scale, the production of LA however has been optimized through the Biofine process and has surpassed proof of concept with extensive pilot plant testing [16, 17].

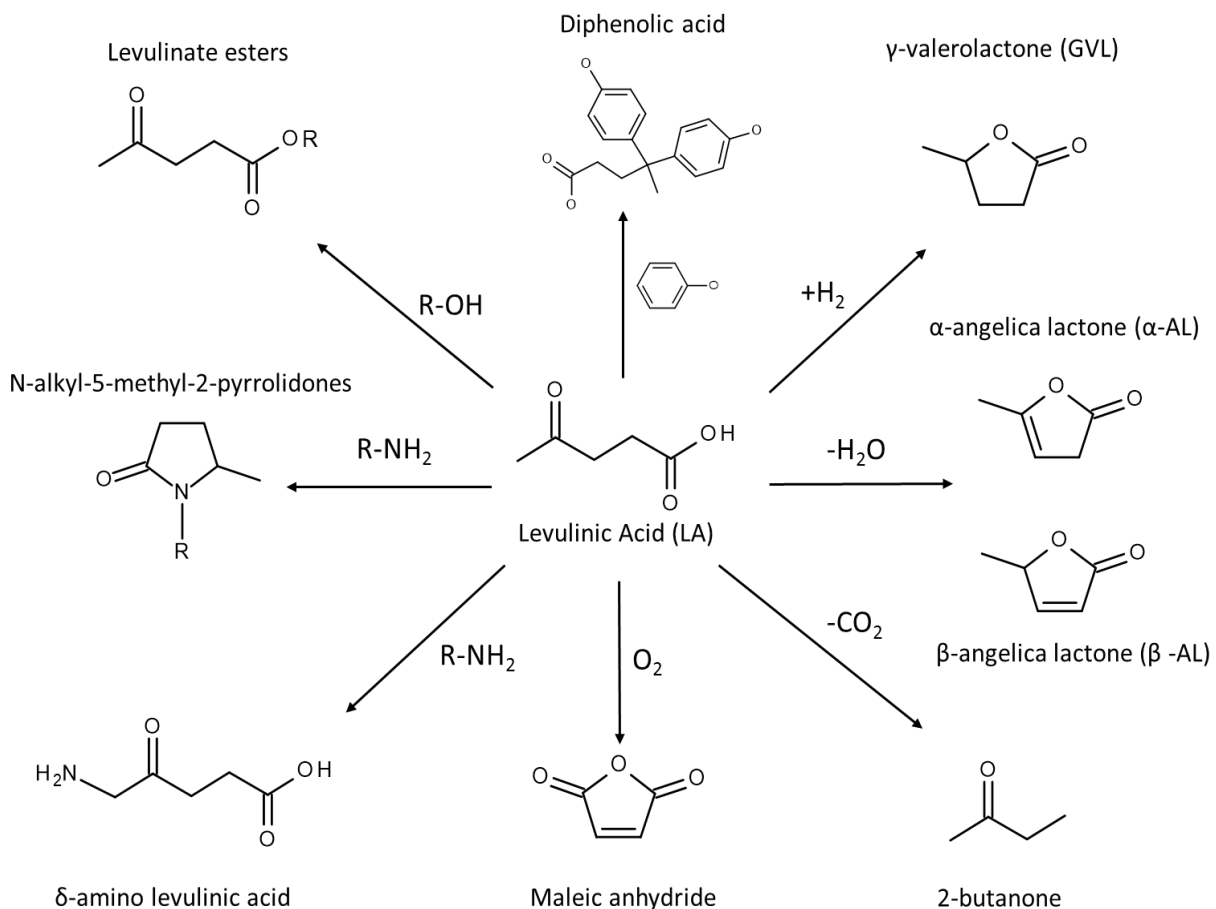


**Figure 1.3** Levulinic acid as a platform chemical

Of the various chemical pathways illustrated in Figure 1.3, the production of  $\gamma$ -valerolactone (GVL) from LA is especially attractive. GVL is of interest as a lignocellulosic platform chemical given the flexibility in downstream applications it offers, providing a pathway to a variety of chemicals with reduced oxygen functionality. For example, GVL can serve directly as a gasoline blender[18] or be subsequently processed to yield relatively energy dense fuel additives, such as methyltetrahydrofuran [19], valeric biodiesel [20], or liquid alkanes [21-27]. GVL is also remarkably versatile as a biorefining solvent [28], particularly for expediting the production of sugars, furans, levulinic acid, and their numerous derivatives from lignocellulose [29-34].

Recently GVL has also been shown to provide a promotive solvent environment for various acid catalyzed reactions related to biomass upgrading technologies [35, 36]. Finally, GVL can be converted to chemical intermediates such as 1,4 pentanediol [19], alkyl pentenoates [37], and  $\alpha$ -methylene- $\gamma$ -valerolactone [38], any of which may find application in the production of bio-based polymers.

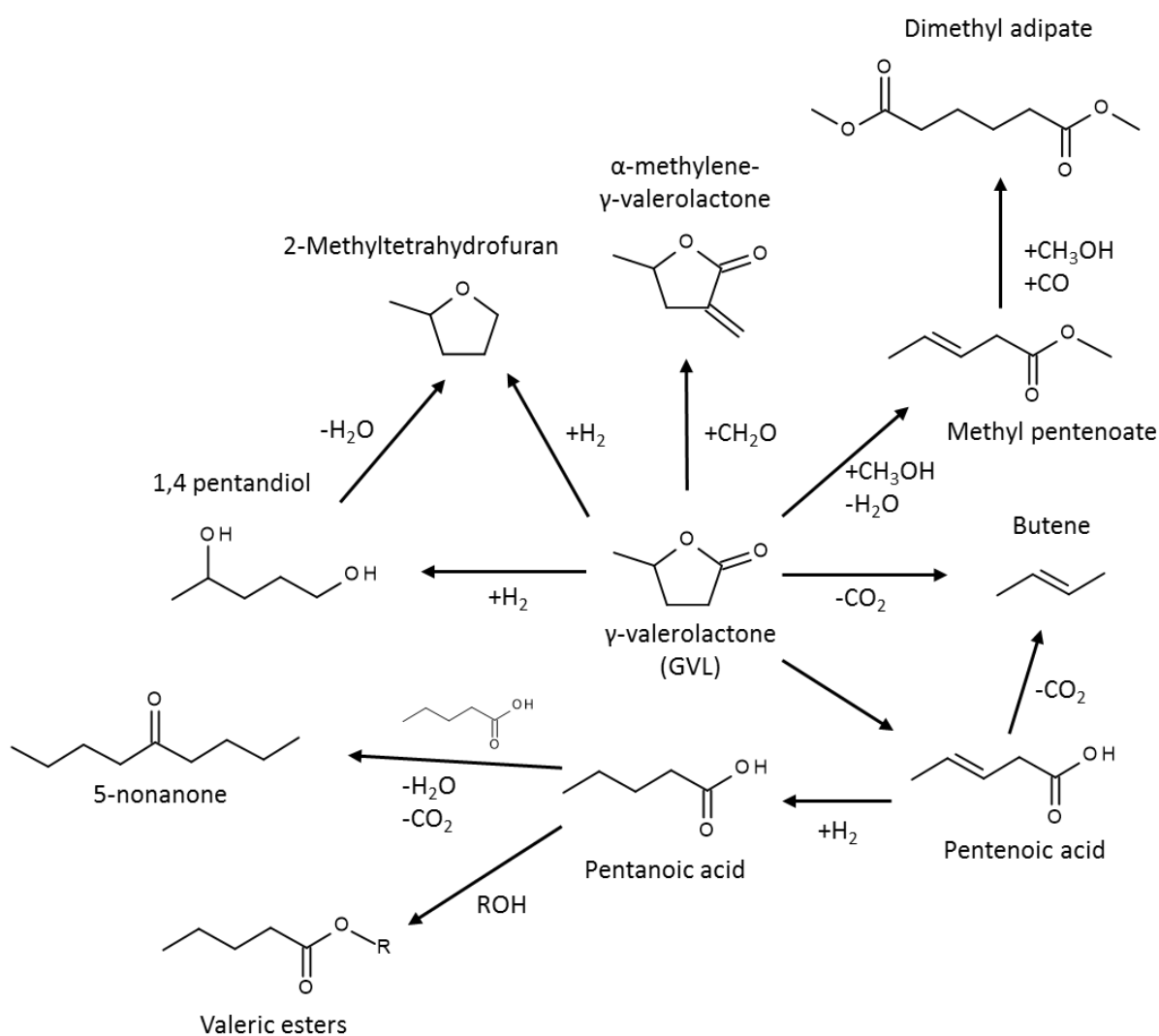


**Figure 1.4** Landscape of chemical pathways possible from GVL

### 1.3 The production of $\gamma$ -valerolactone from lignocellulosic biomass

The primary route envisioned for the production of lignocellulosic GVL is the hydrogenation of LA [39], which may be prepared from both 5- and 6-carbon sugars present in cellulose and hemicellulose through hydrolysis of either 5-hydroxymethylfurfural (HMF) or furfuryl alcohol (Figure 1.5) [11, 17, 40-47]. First, through a variety of pre-treatment strategies, the lignin fraction can be removed leaving behind the cellulose and hemicellulose fractions [48]. Considering the cellulose fraction, the polymer be broken down to its glucose monomer units through acid catalyzed hydrolysis of the  $\beta$ -1,4 glycosidic linkages. Glucose can then further undergo dehydration to yield HMF, a valuable chemical commodity in itself. However quantitative yields to HMF are difficult to achieve due to undesired polymerization reactions, in addition to hydration reactions leading to the formation of LA and formic acid. In the case of the hemicellulose fraction, it can also be broken down into its respective C<sub>5</sub> sugar monomer unit xylose via acid hydrolysis of its  $\beta$ -1,4 glycosidic linkages. Xylose can then undergo acid catalyzed dehydration to form furfural. Furfural can then be hydrogenated to yield furfural alcohol, which similar to HMF can be hydrated to form LA.

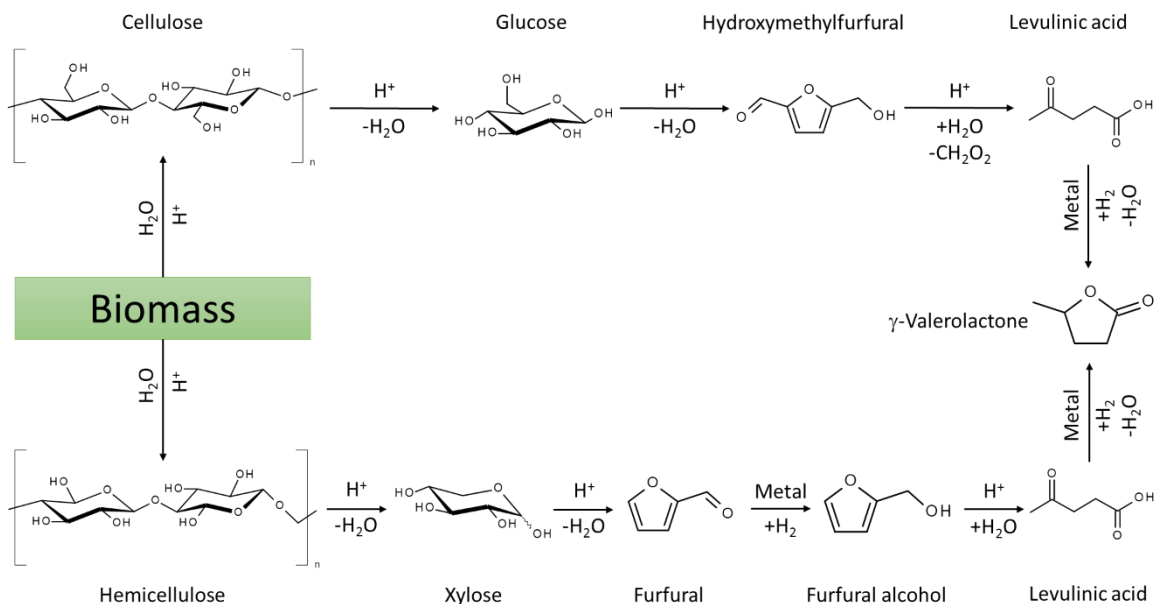


**Figure 1.5** - Proposed aqueous phase processing strategy of lignocellulosic biomass

Once LA is formed from either cellulose or hemicellulose a common processing point is reached, from which LA can be converted to GVL through hydrogenation strategies typically over supported metal catalysts. There are multiple options for the selective hydrogenation of LA, and both homogeneous [19] and heterogeneous systems [39] have been employed. Despite burgeoning interest in transfer hydrogenation for GVL production [49-51], the majority of LA hydrogenation processes have used molecular  $H_2$  as a reducing agent and supported metals, such as Cu [52, 53], Ru [38, 54-57], Ir [58], Au [51], or bimetallics, such as RuRe [59, 60] or RuSn [61, 62] as catalysts. Further, recent studies focusing on the scale up and economic feasibility of a GVL-centered biorefinery have favored Ru or Ru-bimetallics, which offer good hydrogenation rates, high GVL selectivity, and (particularly in the case of bimetallics) good stability [24, 59, 60, 63].

The fundamentals of LA hydrogenation in the aqueous phase however are relatively unclear, both in terms of the mechanistic route by which the hydrogenation proceeds as well as the governing kinetics. This hampers the biomass community's capability to rationally propose and design hydrogenation catalysts that could improve the efficiency of GVL production from biomass. This deficiency is further exacerbated by the scarcity of studies that consider the stability of catalysts tested for LA hydrogenation; a catalyst must be able to retain its activity for it to be industrially viable. Thus, detailed consideration of the kinetics and stability of LA hydrogenation, specifically over Ru catalysts which display exceptional activity is warranted and is the central focus of this thesis.

#### **1.4 Research overview**

The experimental methods employed in the preparation, characterization and kinetic evaluation of catalysts employed in this work are described in Chapter 2. The mechanistic aspects of the target reaction, LA to GVL, are explored in an attempt to identify and extract apparent kinetic parameters for the reaction pathways involved in Chapter 3. Given the supported nature of the Ru catalysts, Chapter 4 explores the effect of support material identity on the activity and stability of the overall Ru catalyst. A comparison is also drawn between LA and its mono-functional analog, 2-pentanone, from which LA and 2-pentanone hydrogenation are found to proceed at identical rates. Expanding on this observation of kinetic similarity, a detailed kinetic study of ketone hydrogenation in the vapor phase is conducted in Chapter 5. The absence of secondary functionalities and the condensed phase, allow for a less complicated kinetic analysis from which fundamental kinetic parameters are estimated. Finally in Chapter 6, concluding remarks are made along with future recommendations based on preliminary kinetic results which directly probe the possible origins of solvent effects observed for ketone hydrogenation.

## 1.5 References

- [1] E.I. Administration, Annual Energy Outlook 2016, in, 2016.
- [2] R.D.W. Perlack, L. L.; Turhollow, A.; Graham, R. L; Stokes, B.; Erbach, D. C, Biomass as Feedstock for a Bioenergy and Bioproducts Industry: The Technical Feasibility of a Billion-Ton Annual Supply, in, Oak Ridge National Laboratory, Oak Ridge, TN, 2005.
- [3] A. Limayem, S.C. Ricke, Lignocellulosic biomass for bioethanol production: Current perspectives, potential issues and future prospects, *Prog. Energy Combust. Sci.*, 38 (2012) 449-467.
- [4] C.E. Wyman, B.E. Dale, R.T. Elander, M. Holtzapple, M.R. Ladisch, Y.Y. Lee, Coordinated development of leading biomass pretreatment technologies, *Bioresour. Technol.*, 96 (2005) 1959-1966.
- [5] G.W. Huber, J.N. Chheda, C.J. Barrett, J.A. Dumesic, Production of Liquid Alkanes by Aqueous-Phase Processing of Biomass-Derived Carbohydrates, *Science*, 308 (2005) 1446-1450.
- [6] T. Werpy, G. Petersen, A. Aden, J. Bozell, J. Holladay, J. White, A. Manheim, D. Eliot, L. Lasure, S. Jones, Top value added chemicals from biomass. Volume 1-Results of screening for potential candidates from sugars and synthesis gas, in, DTIC Document, 2004.
- [7] K. Min, S. Kim, T. Yum, Y. Kim, B.-I. Sang, Y. Um, Conversion of levulinic acid to 2-butanone by acetoacetate decarboxylase from *Clostridium acetobutylicum*, *Appl. Microbiol. Biotechnol.*, 97 (2013) 5627-5634.
- [8] Y. Gong, L. Lin, J. Shi, S. Liu, Oxidative Decarboxylation of Levulinic Acid by Cupric Oxides, *Molecules*, 15 (2010) 7946.
- [9] G. Pasquale, P. Vázquez, G. Romanelli, G. Baronetti, Catalytic upgrading of levulinic acid to ethyl levulinate using reusable silica-included Wells-Dawson heteropolyacid as catalyst, *Catal. Commun.*, 18 (2012) 115-120.
- [10] S. Dharme, V.V. Bokade, Esterification of levulinic acid to n-butyl levulinate over heteropolyacid supported on acid-treated clay, *J. Nat. Gas Chem.*, 20 (2011) 18-24.
- [11] J.J. Bozell, L. Moens, D.C. Elliott, Y. Wang, G.G. Neuenschwander, S.W. Fitzpatrick, R.J. Bilski, J.L. Jarnefeld, Production of levulinic acid and use as a platform chemical for derived products, *Resources, Conservation and Recycling*, 28 (2000) 227-239.
- [12] R.H. Leonard, Method of converting levulinic acid into alpha angelica lactone, in, Heyden Newport Chemical Corp, United States 1957.
- [13] A.S. Touchy, S.M.A. Hakim Siddiki, K. Kon, K.-i. Shimizu, Heterogeneous Pt Catalysts for Reductive Amination of Levulinic Acid to Pyrrolidones, *ACS Catal.*, 4 (2014) 3045-3050.
- [14] A. Chatzidimitriou, J.Q. Bond, Oxidation of levulinic acid for the production of maleic anhydride: breathing new life into biochemicals, *Green Chem.*, 17 (2015) 4367-4376.
- [15] X. Yu, Y. Guo, K. Li, X. Yang, L. Xu, Y. Guo, J. Hu, Catalytic synthesis of diphenolic acid from levulinic acid over cesium partly substituted Wells–Dawson type heteropolyacid, *J. Mol. Catal. A: Chem.*, 290 (2008) 44-53.
- [16] S.W. Fitzpatrick, The Biofine Technology: A "Bio-Refinery" Concept Based on Thermochemical Conversion of Cellulosic Biomass, in: *Feedstocks for the Future*, American Chemical Society, 2006, pp. 271-287.
- [17] S.W. Fitzpatrick, Production of levulinic acid from carbohydrate-containing materials, in: USPTO (Ed.), US, 1997.

- [18] I.T. Horvath, H. Mehdi, V. Fabos, L. Boda, L.T. Mika, gamma-Valerolactone - a sustainable liquid for energy and carbon-based chemicals, *Green Chemistry*, 10 (2008) 238-242.
- [19] H. Mehdi, V. Fabos, R. Tuba, A. Bodor, L.T. Mika, I.T. Horvath, Integration of homogeneous and heterogeneous catalytic processes for a multi-step conversion of biomass: From sucrose to levulinic acid, gamma-valerolactone, 1,4-pentanediol, 2-methyl-tetrahydrofuran, and alkanes, *Topics in Catalysis*, 48 (2008) 49-54.
- [20] J.P. Lange, R. Price, P. Ayoub, J. Louis, L. Petrus, L. Clarke, H. Gosselink, Valeric Biofuels: A Platform of Cellulosic Transportation Fuels, *Angewandte Chemie International Edition*, 49 (2010) 4479-4483.
- [21] J.Q. Bond, D.M. Alonso, D. Wang, R.M. West, J.A. Dumesic, Integrated Catalytic Conversion of gamma-Valerolactone to Liquid Alkenes for Transportation Fuels, *Science*, 327 (2010) 1110-1114.
- [22] J.Q. Bond, D. Martin Alonso, R.M. West, J.A. Dumesic, gamma-Valerolactone Ring-Opening and Decarboxylation over SiO<sub>2</sub>/Al<sub>2</sub>O<sub>3</sub> in the Presence of Water, *Langmuir*, 26 (2010) 16291-16298.
- [23] J.Q. Bond, D. Wang, D. Martin Alonso, J.A. Dumesic, Interconversion between [gamma]-valerolactone and pentenoic acid combined with decarboxylation to form butene over silica/alumina, *Journal of Catalysis*, 281 (2011) 290-299.
- [24] J.C. Serrano-Ruiz, D.J. Braden, R.M. West, J.A. Dumesic, Conversion of cellulose to hydrocarbon fuels by progressive removal of oxygen, *Applied Catalysis B: Environmental*, 100 (2010) 184 -189.
- [25] D. Martin Alonso, J.Q. Bond, J.A. Dumesic, Catalytic Conversion of Biomass to Biofuels, *Green Chemistry*, 12 (2010) 1493-1513.
- [26] D. Martin Alonso, J.Q. Bond, J.C. Serrano-Ruiz, J.A. Dumesic, Production of liquid hydrocarbon transportation fuels by oligomerization of biomass-derived C<sub>9</sub> alkenes, *Green Chemistry*, 12 (2010) 992-999.
- [27] D. Alonso, J. Bond, D. Wang, J. Dumesic, Activation of Amberlyst-70 for Alkene Oligomerization in Hydrophobic Media, *Topics in Catalysis*, 54 (2011) 447-457.
- [28] I.T. Horvath, Solvents from nature, *Green Chemistry*, 10 (2008) 1024-1028.
- [29] S.G. Wettstein, D.M. Alonso, Y.X. Chong, J.A. Dumesic, Production of levulinic acid and gamma-valerolactone (GVL) from cellulose using GVL as a solvent in biphasic systems, *Energy and Environmental Science*, 5 (2012) 8199-8203.
- [30] D.M. Alonso, J.M.R. Gallo, M.A. Mellmer, S.G. Wettstein, J.A. Dumesic, Direct conversion of cellulose to levulinic acid and gamma-valerolactone using solid acid catalysts, *Catal. Sci. Technol.*, 3 (2013) 927-931.
- [31] E.I. Gurbuz, J.M.R. Gallo, D.M. Alonso, S.G. Wettstein, W.Y. Lim, J.A. Dumesic, Conversion of Hemicellulose into Furfural Using Solid Acid Catalysts in gamma-Valerolactone, *Angew. Chem.-Int. Edit.*, 52 (2013) 1270-1274.
- [32] D.M. Alonso, S.G. Wettstein, J.A. Dumesic, Gamma-valerolactone, a sustainable platform molecule derived from lignocellulosic biomass, *Green Chemistry*, 15 (2013) 584-595.
- [33] D.M. Alonso, S.G. Wettstein, M.A. Mellmer, E.I. Gurbuz, J.A. Dumesic, Integrated conversion of hemicellulose and cellulose from lignocellulosic biomass, *Energy and Environmental Science*, 6 (2013) 76-80.
- [34] J.S. Luterbacher, J.M. Rand, D.M. Alonso, J. Han, J.T. Youngquist, C.T. Maravelias, B.F. Pfleger, J.A. Dumesic, Nonenzymatic Sugar Production from Biomass Using Biomass-Derived  $\gamma$ -Valerolactone, *Science*, 343 (2014) 277-280.

- [35] M.A. Mellmer, J.M.R. Gallo, D. Martin Alonso, J.A. Dumesic, Selective Production of Levulinic Acid from Furfuryl Alcohol in THF Solvent Systems over H-ZSM-5, *ACS Catal.*, 5 (2015) 3354-3359.
- [36] M.A. Mellmer, C. Sener, J.M.R. Gallo, J.S. Luterbacher, D.M. Alonso, J.A. Dumesic, Solvent Effects in Acid-Catalyzed Biomass Conversion Reactions, *Angewandte Chemie International Edition*, 53 (2014) 11872-11875.
- [37] J.P. Lange, J.Z. Vestering, R.J. Haan, Towards 'bio-based' Nylon: conversion of gamma-valerolactone to methyl pentenoate under catalytic distillation conditions, *Chemical Communications*, (2007) 3488-3490.
- [38] L.E. Manzer, Catalytic synthesis of alpha-methylene-gamma-valerolactone: a biomass-derived acrylic monomer, *Applied Catalysis A: General*, 272 (2004) 249-256.
- [39] W.R.H. Wright, R. Palkovits, Development of Heterogeneous Catalysts for the Conversion of Levulinic Acid to gamma-Valerolactone, *ChemSusChem*, 5 (2012) 1657-1667.
- [40] J.P. Lange, W.D. van de Graaf, R.J. Haan, Conversion of Furfuryl Alcohol into Ethyl Levulinate using Solid Acid Catalysts, *ChemSusChem*, 2 (2009) 437-441.
- [41] E.I. Gurbuz, S.G. Wettstein, J.A. Dumesic, Conversion of Hemicellulose to Furfural and Levulinic Acid using Biphasic Reactors with Alkylphenol Solvents, *ChemSusChem*, 5 (2012) 383-387.
- [42] G.M.G. Maldonado, R.S. Assary, J.A. Dumesic, L.A. Curtiss, Acid-catalyzed conversion of furfuryl alcohol to ethyl levulinate in liquid ethanol, *Energy and Environmental Science*, 5 (2012) 8990-8997.
- [43] P. Gallezot, Conversion of biomass to selected chemical products, *Chemical Society Reviews*, 41 (2012) 1538-1558.
- [44] S. Van de Vyver, J. Thomas, J. Geboers, S. Keyzer, M. Smet, W. Dehaen, P.A. Jacobs, B.F. Sels, Catalytic production of levulinic acid from cellulose and other biomass-derived carbohydrates with sulfonated hyperbranched poly(arylene oxindole)s, *Energy and Environmental Science*, 4 (2011) 3601-3610.
- [45] S.W. Fitzpatrick, Production of Levulinic Acid from Carbohydrate-Containing Materials, in: WIPO (Ed.), 1996.
- [46] B. Girisuta, L.P.B.M. Janssen, H.J. Heeres, Kinetic Study on the Acid-Catalyzed Hydrolysis of Cellulose to Levulinic Acid, *Industrial & Engineering Chemistry Research*, 46 (2007) 1696-1708.
- [47] M. Mascal, E.B. Nikitin, High yield conversion of plant biomass into the key value-added feedstocks 5-(hydroxymethyl)furfural, levulinic acid, and levulinic esters via 5-(chloromethyl)furfural, *Green Chemistry*, 12 (2009) 370-373.
- [48] G.W. Huber, S. Iborra, A. Corma, Synthesis of Transportation Fuels from Biomass: Chemistry, Catalysts, and Engineering, *Chem. Rev.*, 106 (2006) 4044-4098.
- [49] H. Heeres, R. Handana, D. Chunai, C.B. Rasrendra, B. Girisuta, H.J. Heeres, Combined dehydration/(transfer)-hydrogenation of C6-sugars (D-glucose and D-fructose) to gamma-valerolactone using ruthenium catalysts, *Green Chemistry*, 11 (2009) 1247-1255.
- [50] L. Deng, J. Li, D.M. Lai, Y. Fu, Q.X. Guo, Catalytic Conversion of Biomass-Derived Carbohydrates into gamma-Valerolactone without Using an External H<sub>2</sub> Supply, *Angew. Chem.-Int. Edit.*, 48 (2009) 6529-6532.
- [51] M. Chia, J.A. Dumesic, Liquid-phase catalytic transfer hydrogenation and cyclization of levulinic acid and its esters to gamma-valerolactone over metal oxide catalysts, *Chemical Communications*, 47 (2011) 12233-12235.

- [52] K. Yan, J.Y. Liao, X. Wu, X.M. Xie, A noble-metal free Cu-catalyst derived from hydrotalcite for highly efficient hydrogenation of biomass-derived furfural and levulinic acid, *RSC Adv.*, 3 (2013) 3853-3856.
- [53] A.M. Hengne, C.V. Rode, Cu-ZrO<sub>2</sub> nanocomposite catalyst for selective hydrogenation of levulinic acid and its ester to gamma-valerolactone, *Green Chemistry*, 14 (2012) 1064-1072.
- [54] W.H. Luo, U. Deka, A.M. Beale, E.R.H. van Eck, P.C.A. Bruijninx, B.M. Weckhuysen, Ruthenium-catalyzed hydrogenation of levulinic acid: Influence of the support and solvent on catalyst selectivity and stability, *Journal of Catalysis*, 301 (2013) 175-186.
- [55] Z.J. Wu, S.H. Ge, C.X. Ren, M.H. Zhang, A. Yip, C.M. Xu, Selective conversion of cellulose into bulk chemicals over Bronsted acid-promoted ruthenium catalyst: one-pot vs. sequential process, *Green Chemistry*, 14 (2012) 3336-3343.
- [56] L. Deng, Y. Zhao, J.A. Li, Y. Fu, B. Liao, Q.X. Guo, Conversion of Levulinic Acid and Formic Acid into gamma-Valerolactone over Heterogeneous Catalysts, *ChemSusChem*, 3 (2010) 1172-1175.
- [57] R. Luque, J.H. Clark, Water-tolerant Ru-Starbon (R) materials for the hydrogenation of organic acids in aqueous ethanol, *Catal. Commun.*, 11 (2010) 928-931.
- [58] X.L. Du, Y.M. Liu, J.Q. Wang, Y. Cao, K.N. Fan, Catalytic conversion of biomass-derived levulinic acid into gamma-valerolactone using iridium nanoparticles supported on carbon nanotubes, *Chin. J. Catal.*, 34 (2013) 993-1001.
- [59] S. Murat Sen, C.A. Henao, D.J. Braden, J.A. Dumesic, C.T. Maravelias, Catalytic conversion of lignocellulosic biomass to fuels: Process development and techno-economic evaluation, *Chemical Engineering Science*, 67 (2012) 57-67.
- [60] D.J. Braden, C.A. Henao, J. Heltzel, C.C. Maravelias, J.A. Dumesic, Production of liquid hydrocarbon fuels by catalytic conversion of biomass-derived levulinic acid, *Green Chemistry*, 13 (2011) 1755-1765.
- [61] D. Martin Alonso, S.G. Wettstein, J.Q. Bond, T.W. Root, J.A. Dumesic, Production of Biofuels from Cellulose and Corn Stover Using Alkylphenol Solvents, *ChemSusChem*, 4 (2011) 1078-1081.
- [62] S.G. Wettstein, J.Q. Bond, D.M. Alonso, H.N. Pham, A.K. Datye, J.A. Dumesic, RuSn bimetallic catalysts for selective hydrogenation of levulinic acid to  $\gamma$ -valerolactone, *Applied Catalysis B: Environmental*, 117-118 (2012) 321-329.
- [63] S.M. Sen, E.I. Gurbuz, S.G. Wettstein, D.M. Alonso, J.A. Dumesic, C.T. Maravelias, Production of butene oligomers as transportation fuels using butene for esterification of levulinic acid from lignocellulosic biomass: process synthesis and techno-economic evaluation, *Green Chemistry*, 14 (2012) 3289-3294.

## Chapter 2 Experimental methods

The ultimate goal of this thesis is to develop a fundamental understanding of ketone hydrogenation over supported Ru catalysts, which can facilitate the rational design of hydrogenation catalysts specifically for catalytic biomass routes. The effect of various catalytic properties on both the activity and stability of the Ru catalysts will therefore need to be understood. To accomplish this, a variety of characterization techniques are required to understand the nature of the catalysts tested. Coupled with reliable information on catalyst properties, rigorous methodologies for assessing the kinetics and deactivation of ketone hydrogenation over supported Ru catalyst need to be developed.

### 2.1 Catalyst preparation

Supported Ru catalysts of various metal loadings were employed throughout this work, where carbon, alumina, silica and titania served as support materials. The support material's function is to provide a high surface area material on which Ru nanoparticles can be grafted, typically in the range of 1- 10 nm, increasing the exposed Ru surface area per unit mass. Supported Ru catalysts utilized throughout this thesis have been prepared using the method of incipient wetness impregnation or dry impregnation as it may commonly be referred to. The preparation method relies on bringing a Ru salt solution ( $\text{RuCl}_3$  in water) in intimate contact with the desired catalyst support, where the metal salt then preferentially adsorbs onto the support surface. Here the volume of solution added per unit mass of catalyst is fixed at the incipient volume, the volume necessary to fill the porous catalyst structure and reach a point where the solid is "just wet". To achieve this the Ru salt solution is added drop wise to the support material until reaching the point of incipient wetness. To promote the dispersion of the solution evenly throughout the solid

material, the support is placed in a sonicator while the solution is added. Once the incipiently wet slurry of support material and Ru salt is prepared, it is left to stand at room temperature for at least an hour after which point it is dried overnight in a furnace at 403 K. The unfinished catalyst is then reduced in a flow cell under a stream of  $\text{H}_2$  at elevated temperatures, to remove the anionic portion ( $\text{Cl}^-$ ) from the support surface leaving behind only zerovalent Ru nanoparticles. Catalyst reduction was performed in a  $100 \text{ ml min}^{-1}$  stream of  $\text{H}_2$  in a downflow quartz U-cell under atmospheric pressure. The temperature was linearly ramped to 673 K at a rate of  $3 \text{ K min}^{-1}$  and held for 6 hours, after which point the catalyst was allowed to cool down. The temperature was measured using an in-situ thermocouple placed directly above the catalyst bed. Once at room temperature the cell was flushed with He, followed by a passivation of the Ru catalyst in a 1%  $\text{O}_2$  in He stream for 10 mins.

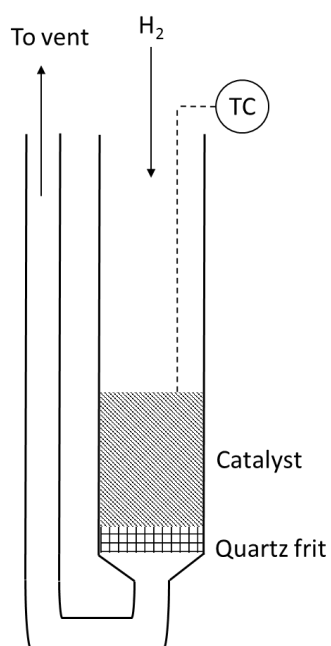


**Figure 2.1** Schematic of catalyst reduction cell

## 2.2 Catalyst characterization

In order to better understand the nature of the supported Ru catalysts on which catalytic studies were performed, multiple characterization techniques were employed to aid in a more fundamental view of the catalysis at play. Specifically, it was of importance to understand the physical and structural properties of both the Ru nanoparticles grafted and the support material itself.

### 2.2.1 N<sub>2</sub> physical adsorption

Utilizing the adsorption of gases on solid surfaces, the total surface area of porous solid materials such as the support materials used in this work can be determined. One such method commonly employed is the Brunauer-Emmett-Teller (BET) method, where N<sub>2</sub> physisorption isotherms are used to determine the surface area of a material. In the case of pore size and its distribution, the Barrett-Joyner-Halenda (BJH) method is utilized which also relies on the N<sub>2</sub> physisorption isotherms.

### 2.2.2 Metal site titration with CO chemisorption

To correctly assess the activity of a Ru supported metal catalyst, or any supported metal catalyst, the rate of reaction on mass of catalyst basis must be normalized by the number of exposed metal surface sites available for catalysis. The number of surface sites is a function of the shape and size of the supported Ru nanoparticles; typically the shape of the supported Ru nanoparticles is taken to be a hemisphere. Shown below in Figure 2.2 is an illustration of a Ru nanoparticle cross-section grafted onto a support surface; only the shaded surface may provide a catalytic surface for reactive adsorbates.

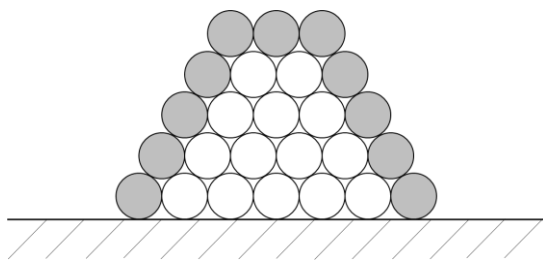


**Figure 2.2** Cross-sectional view of supported Ru nanoparticle on support surface adopting a spherical geometry. Shaded Ru atoms indicate exposed Ru surface atoms which may provide a catalytic surface.

The number of surface sites can be expressed as a density quantifying the moles of Ru per unit mass of catalyst ( $N_{Ru}$ ), where the smaller the Ru nanoparticle the larger this surface site density will be. Taking the ratio of this value to the theoretical maximum number of moles of exposed Ru is known as the dispersion.

$$D = \frac{N_{Ru} \cdot M}{W} \quad (1)$$

Here  $M$  is the molar mass of Ru and  $W$  the weight percent loading of Ru defined as mass of Ru per unit of total catalyst mass. The dispersion is a function of the catalyst preparation method, precursor salt, support material and reduction treatment employed [1]. Therefore while the mass loading of Ru per unit mass of catalyst is a known and controlled variable, the Ru dispersion and hence surface site density site is not known a priori.

One method commonly employed for measuring the dispersion of supported metal catalyst is selective gas adsorption, where a gas probe preferentially adsorbs on exposed Ru atoms on the catalyst surface. Carbon monoxide is known to act as a poison for metal catalysts such as Ru,  $\Delta H_{ads} = -160 \text{ kJ mol}^{-1}$  on Ru (0001) [2]. The adsorption of carbon monoxide on the support materials used in this work however tends to be physical (physisorption) in nature. Carbon

monoxide can therefore irreversibly adsorb on Ru while sparsely interacting with the support material, serving as a selective titrant for Ru.

Ru surface sites were therefore quantified by CO adsorption at 308K using a Micromeritics ASAP 2020 instrument, which utilizes a static volume adsorption design. A known mass of catalyst, ~ 100 mg, is placed in a quartz U-cell where the catalyst is first degassed under vacuum at 673 K to remove weakly adsorbed molecules. Samples are then reduced in flowing H<sub>2</sub> (3h, 673K, 3 K min<sup>-1</sup>), evacuated at 673K for 1h to remove physisorbed hydrogen, and cooled to 308K under vacuum. In the first part of the analysis a CO adsorption isotherm is collected at 308 K; this represents the total adsorption on both Ru and support surfaces. The sample is then evacuated for 1 hour to remove physisorbed CO, followed by collecting a second adsorption isotherm. Irreversible CO adsorption can then be determined from the difference in CO adsorption between the first and second isotherms. Here, irreversible CO uptake is taken as equivalent to the Ru surface site density, which assumes a CO adsorption stoichiometry of 1. From the irreversible CO uptake measured and known mass of catalyst analyzed, the moles of exposed Ru per mass of catalyst is calculated.

Finally from the measured surface site density, the average particle size of Ru nanoparticles on the surface can be estimated. Surface averaged Ru particle diameters based on irreversible CO uptake were calculated according to Eq. (2-3), which assumes a spherical morphology:

$$d_{p,CO} = \frac{6}{S \cdot \rho_{Ru}} \quad (2)$$

$$S = N_{Ru} A_m N_a \quad (3)$$

Where  $S$  is the surface area of Ru per gram of catalyst calculated from irreversible CO uptake,  $\rho_{Ru}$  is the density of metallic Ru and  $N_a$  is Avagadro's constant. The cross sectional area of a single Ru atom was assumed to be  $6.14 \text{ \AA}^2$ , and  $12.30 \text{ g cm}^{-3}$  was used as the density of Ru [3].

### 2.2.3 Transmission electron microscopy

A mode of deactivation which commonly plagues supported catalysts, is the aggregation or sintering of the nanoparticles on the support surface. As the size of the supported Ru nanoparticles increases the exposed surface area decreases, leading to decreased catalytic activity on a total mass of supported catalyst basis. Therefore to evaluate the extent to which sintering is responsible for deactivation in the various hydrogenation reactions considered, it was necessary to determine the Ru nanoparticle size before and after reaction.

Average Ru cluster sizes and particle size distributions were determined using transmission electron microscopy (TEM). Catalyst samples were suspended in excess acetone via sonication, and suspension aliquots were deposited on 300 mesh carbon film Cu grids (EMS) and dried overnight under ambient conditions. Images were taken using a JEOL 2010F equipped with a Schottky field emission gun operating at 200 KV and captured with a CCD camera. Particle size distributions were extracted from TEM images using image processing software (ImageJ). X-ray diffraction

### 2.2.4 X-ray Diffraction

X-ray diffraction (XRD) was used to determine whether any structural changes occurred in the support materials, this was especially significant for the metal oxide supports used in the aqueous phase reactor setup. Powder x-ray diffractions (PXRD) were collected using a Bruker D8

diffractometer using Cu K $\alpha$  radiation (40 kV, 40 mA). Scans were performed from  $2\theta = 10$  to  $80^\circ$  with a step size of  $0.1^\circ$  at a rate of 5 min per degree.

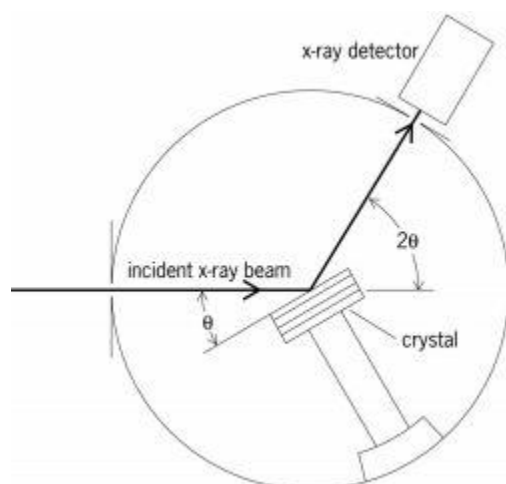


**Figure 2.3** Schematic representation of the X-ray diffractometer with a  $\theta:2\theta$  goniometer

## 2.3 Catalytic reactor setups

### 2.3.1 Flow reactor

In the evaluation of the catalytic activity of Ru catalysts towards hydrogenation chemistry, the use of various reaction environments and need to isolate individual chemistries necessitated the use of multiple reactor designs. The use of a flow reactor setup was suited for measuring hydrogenation kinetics of the various ketones explored in this work, both in the aqueous and vapor phase, as it allows for facile estimation of instantaneous rates of hydrogenation.

Specifically a packed bed reactor design was used, where a known amount of catalyst mass is fixed between two plugs of quartz wool to hold it in place.

Shown below in Figure 2.4 is an illustration of the operation of a packed bed reactor. At the entrance of the differential catalyst element (dW), the molar flow rate of the reactant is known

( $F_a,0$ ). As a result of the reaction across the differential element, the molar flow rate of “a” changes by the amount  $dF_a$ .

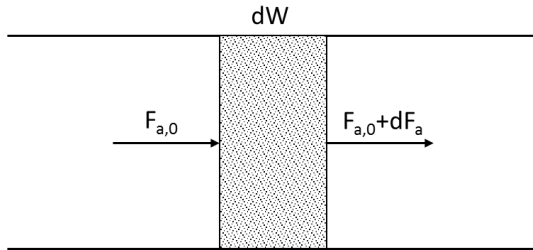


**Figure 2.4** A differential catalyst element  $dW$  across which the molar flow rate of A changes by a differential amount  $dF_a$  as a result of a reaction on the catalyst surface.

Performing a mass balance across the differential element one can obtain:

$$0 = F_{a,0} - (F_{a,0} + dF_a) - r_a dW \quad (4)$$

Where  $r_a$  is the rate of reaction on a molar basis normalized by the mass of catalyst ( $\text{mol mass}^{-1} \text{time}^{-1}$ ). We can then rearrange Eq. (4):

$$\frac{dF_a}{dW} = -r_a \quad (5)$$

To simplify the analysis and estimation of reaction kinetics, the packed bed reactor can be operated differentially by maintain reactant conversion below  $\sim 5\%$ . With this constraint, the differential term in Eq. (5) can be approximated to be an exact one.

$$\frac{\Delta F_a}{\Delta W} = -r_a \quad (6)$$

Therefore if the change across the catalyst bed and mass of catalyst bed are known, under differential conditions they provide a direct measurement of the rate of reaction.

Flow reactors also allow for rigorous estimation of the extent of deactivation, which tends to be severe with Ru catalysts, enabling an estimation of the initial rate on fresh catalysts prior to the onset of deactivation. Given the objective of also rationally designing catalysts from the perspective of stability, the ability to track the extent of deactivation with time on stream essential.

Schematics of the flow reactors applied for vapor and liquid phase experiments conducted throughout the thesis are presented in Figure 2.5 and Figure 2.6. The precise method of operation for the flow reactors depends upon the reaction chemistry investigated, details are therefore given in each relevant chapter.

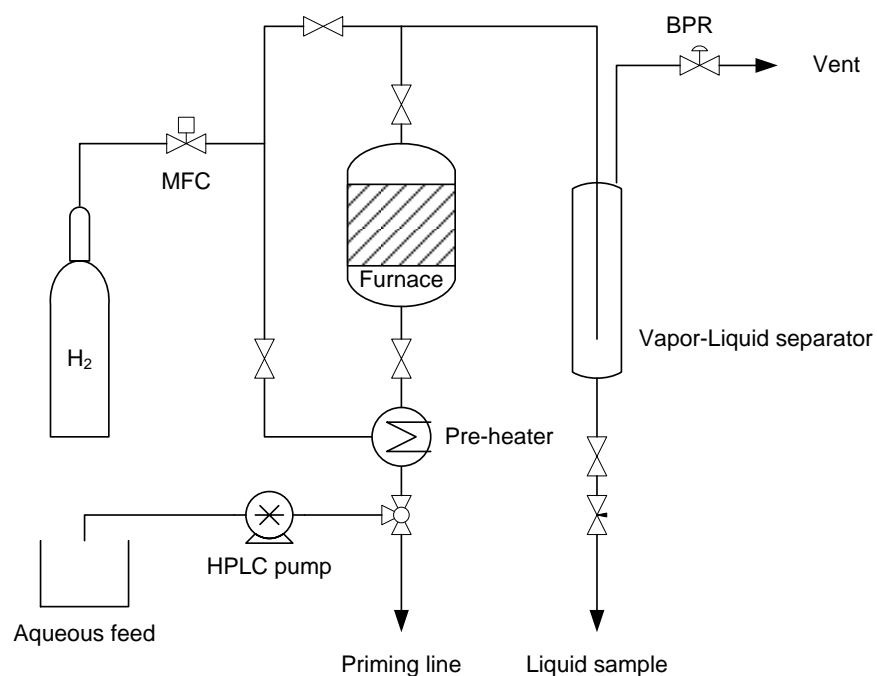


**Figure 2.5** Schematic of catalytic reactor setup employed for aqueous phase hydrogenations

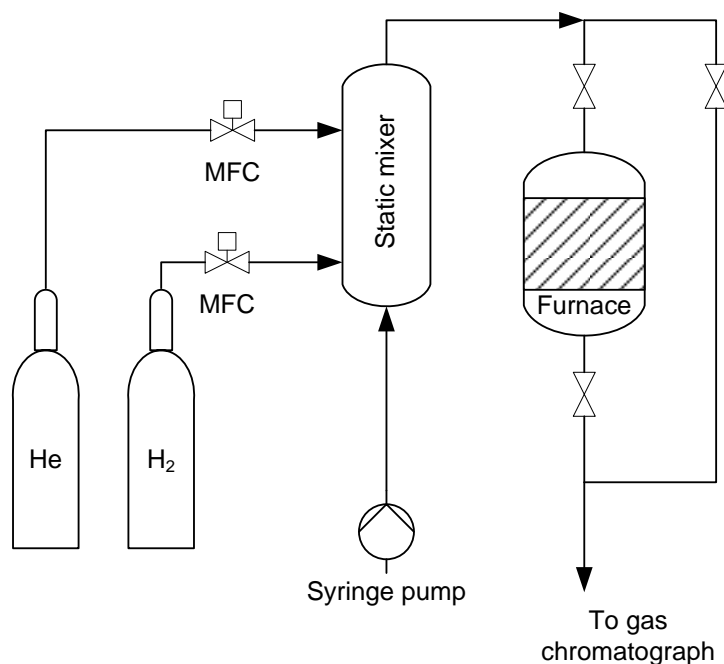


**Figure 2.6** Schematic of catalytic reactor setup employed for vapor phase hydrogenation

### 2.3.2 Aqueous phase batch reactor

Homogeneous chemistries which did not exhibit deactivating behavior were conducted in a batch reactor, given its operational simplicity relative to flow reactors. Briefly reactants were placed within a glass reactor along with a magnetic stir bar, equipped with a septum that allowed for sampling using a syringe. The whole reactor apparatus was placed within a second glass vessel filled with silicone oil that acted as a thermal bath, at the bottom of which was a magnetic stir bar which aided in maintaining a constant temperature across the bath. A thermocouple was placed within the oil bath to monitor the temperature at which the reaction was conducted. The entire apparatus was placed upon a heated stir plate which both heated the oil bath and magnetically drove both stir bars.

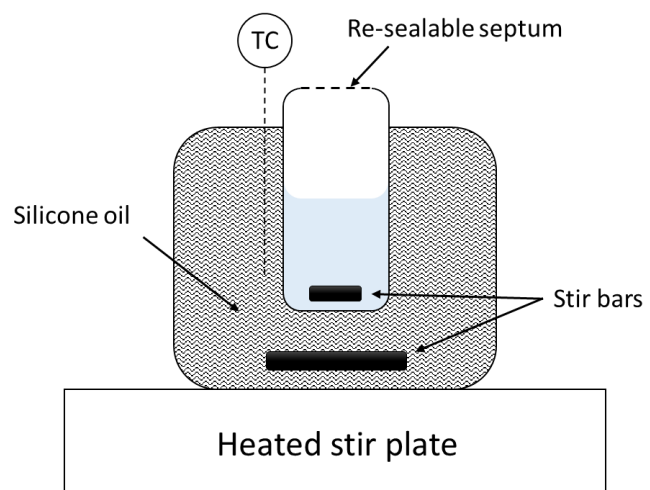


**Figure 2.7** Batch reactor setup used for measuring the kinetics of the acid catalyzed intramolecular fisher trans-esterification of HPA to GVI in solution

## 2.4 References

- [1] J. Regalbuto, Catalyst preparation: science and engineering, CRC Press, 2016.
- [2] H. Pfnür, D. Menzel, Lateral interactions for CO/Ru(001): Order-disorder transitions of the 3 structure, Surf. Sci., 148 (1984) 411-438.
- [3] S. Lowell, Characterization of Porous Solids and Powders: Surface Area, Pore Size and Density, Springer, 2004.

### Chapter 3 Analysis of kinetics and reaction pathways in the aqueous-phase hydrogenation of levulinic acid to form $\gamma$ -valerolactone over Ru/C

#### 3.1 Introduction

Between temperatures of 298 and 473K and over supported Ru catalysts, LA is converted selectively to GVL via reduction with molecular  $H_2$  (10 – 35 bar) [1, 2]. Producing GVL requires both hydrogenation and dehydration of LA, and we may envision two different pathways for the transformation, depending on the order in which dehydration and hydrogenation occur (Figure 3.1).

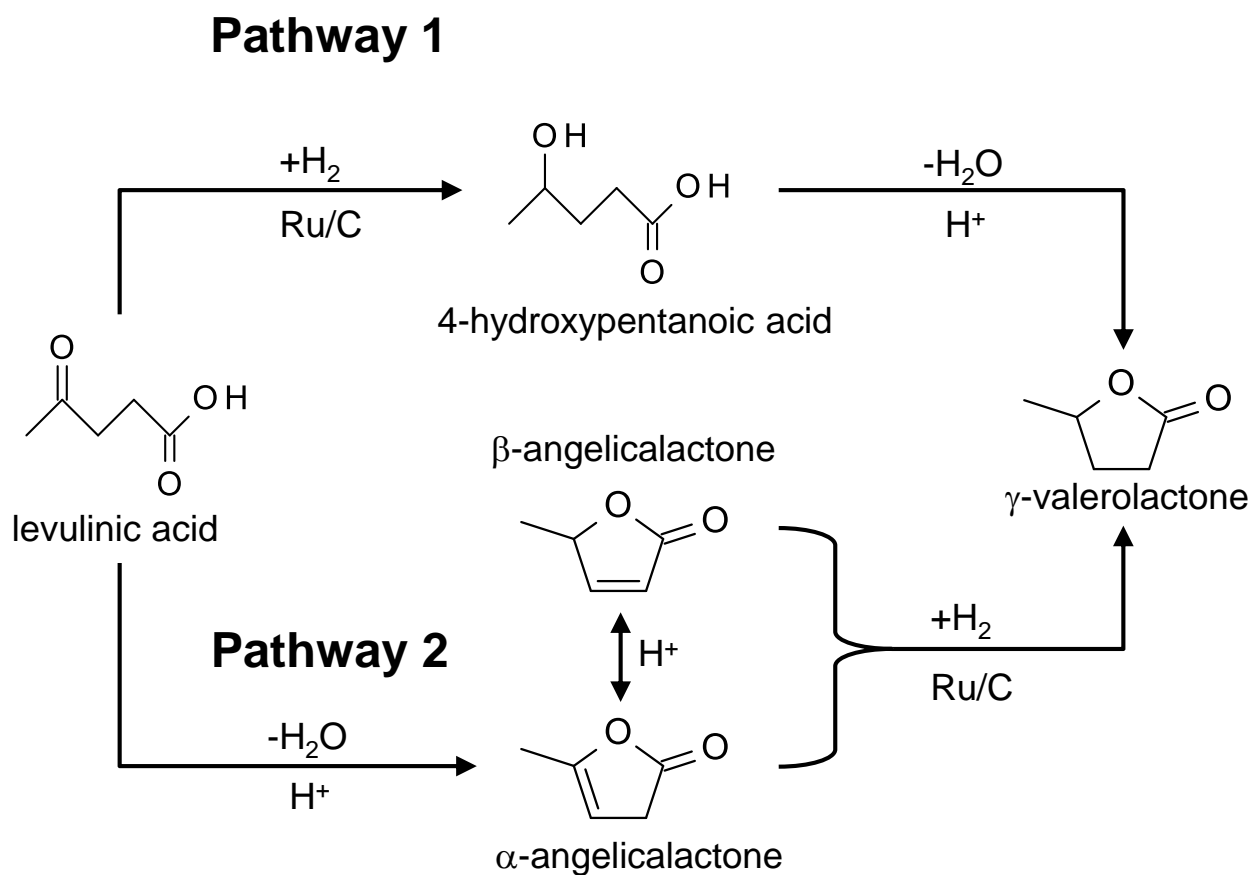


**Figure 3.1** Pathways leading to  $\gamma$ -valerolactone during hydrogenation of levulinic acid.

Pathway 1 illustrates the sequence initiated by hydrogenation of the ketone group in LA to form 4-hydroxypentanoic acid (HPA). Subsequently, HPA undergoes acid-catalyzed, intramolecular esterification (ring closure) to form the thermodynamically preferred lactone, GVL. Alternatively, angelicalactones (AL) can form via endothermic dehydration of LA, and they become increasingly prevalent in acidic media and at elevated temperatures (Pathway 2). In the presence of Ru/C and under H<sub>2</sub> atmospheres, angelicalactones are anticipated to rapidly hydrogenate, forming GVL. To date, the relative contributions of each pathway have not been delineated, and it is unclear which reactions in the above network are kinetically significant. Further, depending on operating conditions [3, 4], choice of solvent [1, 5-7], presence of metal promoters (e.g., Re or Sn) [8, 9], and presence of residual impurities in levulinic acid feeds (e.g., H<sub>2</sub>SO<sub>4</sub> or acid-soluble lignin) [9], Ru-based catalysts can display pronounced differences in both hydrogenation activity [3, 10] and on-stream stability [9].

Here, we present an investigation of the reaction pathways and kinetics of aqueous-phase LA hydrogenation over supported Ru, which is representative of LA feedstocks obtained via acid hydrolysis of lignocellulose. Kinetic studies have been carried out only for monometallic Ru/C having a single metal loading (5 wt%). Our motivation in doing so is to establish governing phenomena on a practically employed catalyst in the absence of confounding effects, thus providing a foundation for subsequent studies examining the influence of Ru-promoters and feed impurities in greater detail. In consideration of this model system, we have decoupled HPA- and angelicalactone-mediated hydrogenation pathways to illustrate that GVL formation occurs primarily through ketone hydrogenation followed by intramolecular esterification (Pathway 1, Figure 3.1). Upon identifying acid catalyzed intramolecular esterification of HPA as the kinetic

bottleneck in GVL formation at low temperatures, we demonstrate that high yields of GVL can be achieved at 323 K using stacked beds of Ru/C followed by Amberlyst 15 (A15).

### 3.2 Materials & Methods

5 wt% Ru/C was purchased from Strem chemicals, and its surface area and average pore diameter were determined to be 756 m<sup>2</sup>/g and 5.04 nm via N<sub>2</sub> adsorption at 77K. Ru dispersion was calculated to be 40.4% from irreversible CO uptake at 308K assuming 1:1 adsorption stoichiometry. For 5 wt% Ru/C, this corresponds to a Ru site density of 200 μmol g<sup>-1</sup>.

Levulinic Acid (LA, 98%, Sigma Aldrich), γ-valerolactone (GVL, 98%, Sigma Aldrich), Sulfuric Acid (95-98wt%, Sigma Aldrich), and acetonitrile (HPLC grade 99.9 % purity, Fisher Scientific) were employed as supplied by the manufacturer. A 4-hydroxypentanoic acid (HPA) calibration standard was synthesized by alkaline hydrolysis of GVL in sodium hydroxide (1 M) to produce 4-hydroxypentanoate, which forms HPA upon protonation. HPA used in esterification kinetic studies was synthesized via partial hydrogenation of aqueous LA (0.5 M) over Ru/C in a packed bed reactor (298K, 23 bar H<sub>2</sub>). After synthesis, esterification feeds were refrigerated (274K) to minimize ring closure during storage (<24 h), but some amount of GVL formation was inevitable. Zero-time concentrations of HPA, LA, and GVL were thus rigorously determined by HPLC analysis prior to starting each experiment. Concentrations of HPA (0.04 – 0.06 M), LA (0.15 – 0.45 M), and GVL (5 x 10<sup>-4</sup> – 1.5 x 10<sup>-3</sup> M) varied depending upon the intended experiment. Water used in preparing reactor feeds, calibration standards, and HPLC mobile phases was purified in house by sequential reverse osmosis, UV oxidation, and double ion exchange. H<sub>2</sub> (99.999%, Airgas), N<sub>2</sub> (99.999%, Airgas), CO (99.99% Praxair) employed in flow systems and chemisorption experiments were used without further purification.

### 3.2.1 Analytical Methodology

High performance liquid chromatography (HPLC) was used for quantification of LA, HPA, and GVL, which are the three products observed during LA hydrogenation and HPA ring closure experiments. Resolution of reaction products was achieved by elution through a reverse phase column (Agilent, C<sub>18</sub> Zorbax) using a mobile phase comprised of 0.5 mM H<sub>2</sub>SO<sub>4</sub> in 90%/10% (v/v) H<sub>2</sub>O/Acetonitrile (1.0 ml min<sup>-1</sup>). LA, GVL, and HPA were quantified using a variable wavelength detector (195 nm). Retention times and UV response factors for LA and GVL were determined using commercial standards. Since HPA is not commercially available, we employed a two-step approach for calibrating its HPLC response. The HPA retention time was confirmed based on comparisons with 4-hydroxypentanoate, which protonates to form HPA in the acidic mobile phase (pH 3). Since some quantity of ring closure is inevitable in HPA samples, it is difficult to prepare HPA quantitatively. As such, HPA responses were calibrated indirectly based on established GVL response factors. Briefly, HPA standards prepared by ambient temperature LA hydrogenation were analyzed at regular intervals during extended storage (48 hours) at ambient conditions. During this time period, HPA peak areas were observed to decrease while GVL peak areas increase, and the two quantities displayed a linear correlation coefficient of -1. This result indicates that increases in GVL concentration are attributed exclusively to consumption of HPA, permitting changes in HPA concentration—and thus a response factor—to be determined by mole balance according to Eq. (1).



Accounting for HPA, LA, and GVL allowed over 95% closure of carbon balances in all kinetic studies. Though not observed during hydrogenation,  $\alpha$ - and  $\beta$ -angelicalactones formed during

LA dehydration studies were quantified by Gas Chromatography (GC, Agilent) using an INNOWAX column and an FID detector. Both were referenced to commercial standards. The GC injector and FID detector were both held at 523K, Helium was used as a carrier gas (1.5 sccm), and the column temperature was ramped from 383K to 493K at 10 K min<sup>-1</sup>.

### 3.2.2 Bulk concentrations of dissolved LA and H<sub>2</sub>

The aqueous phase concentration of LA in the reactor is assumed to be equal to that of the feed solution, and the concentration of dissolved H<sub>2</sub> is, at phase equilibrium, governed by system temperature and H<sub>2</sub> partial pressure. Because H<sub>2</sub> has limited solubility in this system, we can approximate the equilibrium concentration of dissolved hydrogen at a given temperature and H<sub>2</sub> partial pressure using Henry's Law (Eq. 2-3).

$$C_{H_2} = K_{H_2}(T) \cdot P_{H_2} \quad (2)$$

$$K_{H_2}(T) = K_{H_2}(T_0) \cdot e^{[C(\frac{1}{T} - \frac{1}{T_0})]} \quad (3)$$

C and K<sub>H2</sub> are empirical constants describing the solubility of H<sub>2</sub> in water. K<sub>H2</sub>, in molar units, has a value of 11.5 mol L<sup>-1</sup> bar<sup>-1</sup> at 298 K, and C is 500 K [11]. Strictly speaking, the above model applies to binary H<sub>2</sub>/water systems, and H<sub>2</sub> solubility is expected to vary with LA concentration; however, this model provides a reasonable approximation for dissolved H<sub>2</sub> concentrations here because our study is limited to relatively dilute LA concentrations (0.025 – 1.5M, >97 mol % H<sub>2</sub>O). In this limit, H<sub>2</sub> solubility in water is expected to dominate solution properties. The use of Henry's law is predicated on the assumption of gas-liquid equilibrium, which is only true for this reacting system if gas-to-liquid transport occurs rapidly relative to the

rate of hydrogenation. To probe the validity of this assumption, we measured hydrogenation rates as a function of bed position and gas flow rate at the highest temperature considered in this study (423 K) since transport limitations are anticipated to be the most demanding at this condition. Here, we observed that hydrogenation rates are independent of both bed position and gas flow rate, suggesting that gas-to-liquid mass transfer occurs rapidly relative to hydrogenation rates, and that vapor and liquid phases are equilibrated throughout the packed bed such that bulk  $H_2$  concentrations are appropriately modeled using Henry's Law.

### 3.2.3 Kinetic Studies

Kinetic data were collected for three separate reactions illustrated in Figure 3.1. First, the rate of LA hydrogenation over Ru/C was determined in a packed bed reactor under a  $H_2$  atmosphere. Second, LA dehydration rates were quantified under typical LA hydrogenation conditions over Ru/C in a packed bed reactor under a non-reducing atmosphere. Finally, HPA esterification to form GVL was carried out in a batch reactor. Details for each experiment are provided in the following subsections.

#### 3.2.1.1 Levulinic Acid Hydrogenation

Prior to use in kinetic studies, 5 wt% Ru/C was graded through a series of standard mesh sieves. Unless otherwise noted, particles in the range of 45 – 90  $\mu\text{m}$  were used. Before loading into reactors, the stock catalyst was diluted to 1 gram 5 wt% Ru/C to 99 grams 45 – 90  $\mu\text{m}$  quartz particles, which were obtained by milling and grading fused quartz granules (4 – 20 mesh  $\text{SiO}_2$ , Sigma Aldrich). 1 – 5 mg of undiluted 5 wt% Ru/C were generally required for typical reactor operation; as such, we employed a high dilution ratio to improve precision in catalyst mass

loading. Reference experiments confirmed that hydrogenation rates were independent of the dilution scheme, suggesting that this protocol does not induce bypassing of the catalyst particles.

Hydrogenation of LA was carried out using the above described Ru/C dilution in a concurrently fed, stainless steel packed bed reactor (1/4" x 12"). The reactor was operated in an upflow configuration over a range of temperatures (323K to 423K) and H<sub>2</sub> pressures (4.1 bar to 41.5 bar). Relatively small amounts of catalyst were required for all of the studies reported here, and bed lengths were on the order of 0.5" – 1.0". Catalyst beds were positioned at the center of the heated section of the reactor and held in place by two quartz wool plugs. The tube upstream of the catalyst bed was packed with coarse (850-1200 μm) quartz granules to minimize dead volume, while the section immediately downstream of the catalyst bed was packed with smaller quartz granules (<45 μm) to minimize entrainment of carbon fines. Quartz packing was fixed in place with two quartz wool end plugs, and the reactor was placed in line using compression fittings. Aqueous LA feeds (0.025 – 1.5M) were introduced to the system using an HPLC pump (Lab Alliance Series 1). H<sub>2</sub> feeds were regulated by mass flow controller (Brooks 5850S) and mixed with the aqueous feed prior to introduction into the reactor. To ensure thermal equilibration of the reactor feed, both the H<sub>2</sub> and the aqueous LA feeds were circulated through a pre-heater section that was maintained at reactor temperature. Feed temperature was monitored by an in-line Type K thermocouple and controlled using a PID controller (Love 16A-3010). The combined feed was then introduced to the packed bed, which was positioned in the center of a 2" aluminum rod held within a ceramic furnace (Applied Test Systems). Reactor temperature was monitored at the external wall of the catalyst bed using a Type K thermocouple and controlled with a PID controller. System pressure was controlled using a back pressure regulator (Tescom Model 26-1766-24) and monitored both upstream and downstream of the packed bed using

analog pressure gauges. The effluent of the system flowed directly into a vapor-liquid separator. Since no volatile products are formed during this reaction, the gas phase was vented continuously without analysis. The aqueous product was collected at regular intervals (15 – 30 minutes) and analyzed immediately using HPLC (Agilent 1100 Series). Prior to use, catalyst beds were reduced in-situ (673K, 4 hour hold, 1 K min<sup>-1</sup>) under flowing H<sub>2</sub> (100 SCCM, 1 bar).

Since LA hydrogenation occurs in a three-phase system, we anticipate that interphase, interparticle, and intraparticle transport limitations may govern concentrations of LA, dissolved H<sub>2</sub>, and temperature at catalytic centers and thus control the rate of hydrogenation. A thorough consideration of transport and kinetically controlled operating regimes is presented in Section 3.3.2. For the experiments described here, we observed that interphase H<sub>2</sub> transport is rapid such that dissolved H<sub>2</sub> concentrations are well-approximated by their equilibrium value as determined by gas-phase H<sub>2</sub> pressures and Henry's law. Further, linear fluid velocities at or beyond volumetric aqueous feed rates of 0.4 ml min<sup>-1</sup> are sufficiently high to eliminate any external concentration or temperature gradients. Finally, for 5 wt% Ru/C, intraparticle transport limitations were negligible at and below 343K for catalyst particles smaller than 125 μm.

Where higher conversions are not otherwise indicated, reactors operated differentially (< 3% LA conversion), and the only reaction products observed were HPA and GVL. Since conversion ranges for differential operation are within the precision expected of mass balance closure and HPLC analysis, LA conversion and product selectivity were determined based on product formation as defined in Eq. (4) and (5), where  $n_{\text{HPA}}$  and  $n_{\text{GVL}}$  are the total molar quantities of HPA and GVL recovered in a given reactor sample, and  $n_{\text{LA}0}$  is the total molar quantity of LA fed into the system. Yield is calculated as the product of LA conversion,  $X_{\text{LA}}$ , and selectivity,  $S_i$ .

$$X_{LA} = \frac{n_{4-HPA} + n_{GVL}}{n_{LA_0}} \quad (4)$$

$$S_i = \frac{n_i}{n_{4-HPA} + n_{GVL}} \quad (5)$$

Site Time Yields (STY) are reported for both HPA and GVL over a range of conversions. They were calculated according to Eq. (6).

$$STY_i = \frac{F_i}{m_{cat} \cdot N_{Ru}} \quad (6)$$

Where  $F_i$  is the effluent molar flow rate of either HPA or GVL,  $m_{cat}$  is the mass of catalyst in the bed, and  $N_{Ru}$  is the loading of Ru surface sites per gram of catalyst as determined by CO chemisorption. In all data summarized here, site time yields have units of moles product per mole of Ru surface sites per second, which is reported as  $s^{-1}$  for convenience.

### 3.2.1.2 LA Dehydration

To probe the extent to which angelicalactones contribute to GVL formation, the baseline rate of LA dehydration was determined in an inert atmosphere over Ru/C. This experiment was motivated by the fact that C=C bond hydrogenation is anticipated to be rapid over Ru/C relative to LA dehydration, making it difficult to distinguish between GVL formed via LA dehydration and LA hydrogenation in a reducing environment. To provide an accurate accounting of GVL fractions formed by pathways 1 and 2 (Figure 3.1), it is thus necessary to quantify the rate of dehydration independent of hydrogenation. To this end, a reference experiment was carried out identically to the protocol described in section 3.2.1.1 (LA Hydrogenation), with the exception that the  $H_2$  feed was replaced with  $N_2$  to suppress both LA and angelicalactone hydrogenation.

### 3.2.1.3 Intramolecular esterification of HPA

The intramolecular esterification (ring closure) of 4-hydroxypentanoic acid (HPA) to form GVL was studied in batch reactors in dilute aqueous solutions of LA. A feed HPA solution was prepared by partial hydrogenation of LA, stored at 275K to inhibit ring closure, divided into aliquots, and loaded into magnetically stirred autoclave reactors (10 mL) that were subsequently placed in a temperature-controlled oil-bath. Batch experiments were conducted at ambient pressure and temperatures ranging from 300 – 339K. To determine whether ring closure is heterogeneously catalyzed in this system, identical experiments were carried out with the addition of both Ru/C and quartz granules (0.05 g/g feed). Batch vessels were stirred at 700 RPM to eliminate extraparticle gradients, and solid particles of 45 – 90  $\mu\text{m}$  were employed to minimize internal diffusion limitations where relevant. LA, HPA, and GVL concentrations were monitored as a function of time by withdrawing 200  $\mu\text{L}$  aliquots from the reactor using a syringe. Each sample was analyzed by HPLC as described in Section 3.2.1. Intramolecular esterification of HPA was the only reaction observed in these experiments, and LA concentrations remained constant throughout. Solution pH was measured at ambient temperature at the beginning and end of every experiment, and we observed a maximum change of 2.3% in dissolved  $\text{H}^+$  concentration over the course of a single experiment, indicating that HPA consumption did not have a significant effect on  $\text{H}^+$  concentration. Based on previously compiled data regarding the effect of temperature on the dissociation of LA[12] and related carboxylic acids,[12-14] dissolved  $\text{H}^+$  concentrations were determined to vary minimally (<5%) over the experimental temperature range (300 – 339K). This observation is consistent with prior results,[15] and we therefore consider the measured starting pH to be constant throughout each experiment.

### 3.2.1.4 Stacked bed experiments

Ru/C and Amberlyst-15 were coupled in stacked beds to facilitate both LA hydrogenation and HPA ring closure in a single reactor at low temperatures. To accommodate the relatively low thermal stability of A15, Ru/C used in stacked beds was reduced *ex situ* in H<sub>2</sub> at 673K and subsequently passivated at 298K in 1% O<sub>2</sub>/N<sub>2</sub>. Passivated Ru/C and unmodified A15 were sequentially loaded into a single ¼” stainless steel tube to create two stacked beds separated by a quartz wool plug. The entire bed was then reduced at 373K (3 K min<sup>-1</sup>) in 100 sccm of H<sub>2</sub> for 2 hours to remove the oxygen monolayer from Ru surface sites. Blank experiments confirmed that Ru/C reduced and passivated *ex situ* (used in stacked beds) performed identically to Ru/C reduced *in situ* (used in LA hydrogenation kinetic studies). As such, this experiment reveals only the effect of adding secondary acid functionality downstream of the hydrogenation system.

## 3.3 Results and Discussion

### 3.3.1 Primary analysis of LA hydrogenation products formed over Ru/C

Table 3.1 summarizes experimental observations during the aqueous-phase hydrogenation of LA over Ru/C.

**Table 3.1** Experimentally observed LA conversions and product selectivities during hydrogenation of LA over Ru/C under inert and reducing environments and at temperatures ranging from 323 - 423K.

Run	Gas	T (K)	WHSV (hr <sup>-1</sup> )	X <sub>LA</sub> (%)	STY (s <sup>-1</sup> )			Selectivity (%)		
					HPA	GVL	AL	HPA	GVL	AL
1	H <sub>2</sub>	323	550	1	0.09	0.004	--	96	4	0
2	H <sub>2</sub>	323	37	20	0.09	0.002	--	98	2	0

3	H <sub>2</sub>	323	5.0	99	0.06	0.003	--	95	5	0
4	N <sub>2</sub>	323	550	Trace	--	--	5 x 10 <sup>-7</sup>	0	0	100
5	N <sub>2</sub>	423	550	Trace	--	--	1 x 10 <sup>-6</sup>	0	0	100
6	H <sub>2</sub>	343	730	2	0.17	0.02	--	89	11	0
7	H <sub>2</sub>	363	720	3	0.18	0.04	--	81	19	0
8	H <sub>2</sub>	383	920	3	0.23	0.13	--	63	36	0
9	H <sub>2</sub>	403	790	5	0.25	0.17	--	59	40	0
10	H <sub>2</sub>	423	1500	3	0.12	0.48	--	19	81	0

From data in entries 1-3, we observe that hydrogenation of LA over Ru/C at near ambient temperatures (323K) yields only two products, HPA and GVL, over LA conversions ranging from 1 – 100%. Over the entire conversion range, we note that GVL selectivity is poor (<5%) at 323K, and the major LA hydrogenation product is HPA (>95% selectivity). This suggests that the HPA-mediated pathway illustrated in Figure 3.1 **Figure 3.** likely dominates GVL production and may indicate that intramolecular esterification of HPA, rather than hydrogenation of LA, controls the rate of GVL formation over Ru/C. To further probe the extent to which angelicalactone formation contributes to GVL production, we consider entry 4, which is identical to entry 1 except that the reducing gas (H<sub>2</sub>) has been replaced with an inert (N<sub>2</sub>). Under these conditions, we observe trace LA conversion with complete selectivity to angelicalactones, indicating that in the absence of H<sub>2</sub>, LA is only consumed by dehydration. However, the site time yield to angelicalactones over Ru/C (5 x 10<sup>-7</sup> s<sup>-1</sup>) is several orders of magnitude lower than site time yields observed for HPA (0.085 s<sup>-1</sup>) and GVL (0.005 s<sup>-1</sup>) in the presence of Hydrogen (Entry 1). Even upon increasing the system temperature to 423K (Entry 5), site time yields for dehydration (10<sup>-6</sup> s<sup>-1</sup>) remain well below hydrogenation rates summarized in entries 1 - 3. Since LA dehydration is essentially not observed over Ru/C relative to the scale of HPA and GVL

production over the range of temperatures considered here (303 – 423K), we conclude that GVL formation over Ru/C occurs exclusively through the HPA-mediated pathway (Pathway 1, Figure 3.) in this temperature range. Entries 6 to 10 compare HPA and GVL selectivity and site time yields at reaction temperatures from 343K to 423K. As the reaction temperature increases, LA hydrogenation rates increase, and GVL selectivity improves relative to HPA. This is attributed to an increase in the rate of ring closure relative to the rate of hydrogenation. Intramolecular esterification of HPA is reversible such that HPA/GVL distributions in hydrogenation products will ultimately be determined by chemical equilibrium. A concentration based equilibrium constant for esterification of HPA in aqueous solution at 298K was experimentally determined here to be 14.5, which is in good agreement with the mean value of those previously reported for this reaction (13.8).[16] HPA ring closure is estimated to be only slightly exothermic (-3 kJ/mol) based on prior accounts of  $\gamma$ -hydroxybutyric acid esterification;[17] thus, equilibrium GVL selectivities are not expected to change drastically with increasing temperature and should exceed 90% at each experimental condition described here. This was confirmed by experimental observation, where nearly complete GVL selectivity was observed at chemical equilibrium over a range of temperatures from 298 – 423K. We therefore conclude that HPA ring closure is not equilibrated in any of the experiments described in Table 3.1 and attribute the improved GVL selectivity to an increased rate of HPA esterification relative to the rate of LA hydrogenation. This suggests that HPA ring closure proceeds with a higher activation barrier than LA hydrogenation and may also reflect increasing mass transfer limitations in LA hydrogenation at high temperatures.

### 3.3.2 Assessing transport control in liquid phase hydrogenation of LA

Mears' criteria (Eq. 7 - 8) establish a theoretical framework for determining whether external heat ( $C_{EHT}$ ) and mass transport ( $C_{EMT}$ ) limitations are significant in controlling reaction kinetics [18].

$$C_{EHT} = \frac{|\Delta H| \cdot r''' \cdot r_p}{h \cdot T_b} \cdot \frac{\Delta E_a}{RT_b} < 0.15 \quad (7)$$

$$C_{EMT} = \frac{r''' \cdot r_p}{C_b \cdot k_c} < \frac{0.15}{n} \quad (8)$$

Here,  $r'''$  is the rate of reaction per bed volume,  $r_p$  is the diameter of bed particles,  $C_b$  is the bulk concentration of reactants in the aqueous phase,  $k_c$  is a mass transfer coefficient,  $n$  is a reaction order in a particular reactant,  $\Delta H$  is the enthalpy change of reaction,  $h$  is a heat transfer coefficient,  $T_b$  is the bulk fluid temperature,  $R$  is the universal gas constant, and  $\Delta E_a$  is the apparent activation energy for the reaction. The majority of parameters in the above equations were obtained from experimental data; however, heat and mass transfer coefficients were estimated using standard correlations for liquid phase flow through packed beds [19, 20]. For the purpose of this analysis,  $n$  was considered to be one for both LA and H<sub>2</sub>, since both will maximally exhibit first order dependencies if ketone hydrogenation occurs through sequential addition of atomic hydrogen to a surface bound ketone [21]. Due to the small particle sizes employed in this study (<100  $\mu\text{m}$ ) and the extensive dilution of the catalyst (1 wt% in quartz), external heat transfer criteria ( $C_{EHT}$ ) are satisfied by at least one order of magnitude under even the most demanding conditions ( $T = 303\text{K}$ ) for any reasonable combination of enthalpy of reaction (-20 to -250 kJ/mol), activation barrier (20 to 250 kJ/mol), and heat transfer coefficient ( $10^2$  to  $10^6$  W m<sup>-2</sup> K).

A similar analysis of external mass transport using a conservative mass transfer coefficient ( $1.4 \times 10^{-4} \text{ m sec}^{-1}$ ) for representative liquid feed rates ( $0.4 \text{ mL min}^{-1}$ ) reveals that external mass transfer of LA is sufficiently rapid such that it does not control the rate of hydrogenation; however, because of the dilute  $\text{H}_2$  concentrations in this system, external  $\text{H}_2$  transport can become rate controlling at high temperatures. Given the uncertainty in estimating mass transfer coefficients, experimental quantification of external mass transport limitations was warranted. LA hydrogenation was thus carried out over a range of volumetric liquid feed rates ( $0.1 - 0.6 \text{ ml min}^{-1}$ ) while maintaining a constant  $\text{H}_2$  pressure (33 bar),  $\text{H}_2$  flow rate (35 sccm), and Weight Hourly Space Velocity (WHSV,  $315 \text{ g LA (g Ru/C hr)}^{-1}$ ) at 423K. This maintained our residence time constant in terms of the catalyst while increasing the linear velocity of the aqueous phase. Between flow rates of  $0.1$  and  $0.2 \text{ ml min}^{-1}$ , we observed slight fluctuations in hydrogenation rate, suggesting external mass transfer may influence kinetics at low feed rates; however, at feed rates from  $0.4 - 0.6 \text{ mL min}^{-1}$ , we observed an invariant rate of hydrogenation. Since this observation was made under the most demanding conditions for mass transfer (i.e., the highest rate of reaction), we concluded that a feed rate of  $0.4 \text{ ml min}^{-1}$  was sufficient in this system to eliminate external transport effects such that temperature and concentration at the particle surface approach those in the bulk.

We can similarly examine the influence of internal heat and mass transfer using theoretical analysis of diffusion and conduction relative to reaction rates as given by the criteria in Eq. (9) – (10) [22, 23].

$$C_{HT} = \frac{|\Delta H| \cdot r''' \cdot r_p^2}{\lambda \cdot T_s} \cdot \frac{\Delta E_A}{R \cdot T_s} < 0.75 \quad (9)$$

$$C_{WP} = \frac{r^m \cdot r_p^2}{C_s \cdot D_e} < 1.0 \quad (10)$$

The majority of symbols are defined in the preceding section. In addition,  $\lambda$  is the thermal conductivity of the catalyst support,  $T_s$  is the temperature at the external particle surface,  $C_s$  is concentration of a reactant at the external particle surface, and  $D_e$  is the effective diffusivity of the same reactant in the catalyst pores. Rates, activation barriers, heats of reaction, particle radii, thermal conductivity, and reactant concentrations were obtained either from established databases [11] or experimental data. Since experimental protocols were established to minimize external transport limitations, surface temperature and concentrations of LA and H<sub>2</sub> are taken as equal to those in the bulk. Effective diffusivities were estimated based on bulk diffusivities and the average pore diameter of the carbon support. As observed in our analysis of external heat transfer limitations, small catalyst particle sizes ensure that internal temperature gradients do not exist in this system, and  $C_{IHT}$  was observed to be at least 2 orders of magnitude below the indicated threshold (0.75) for all reasonable ranges of enthalpy change and activation barriers. Intraparticle mass transfer limitations are much more severe in this system, particularly in the case of hydrogen. For first order reactions, which we take to be the limiting case for both LA and H<sub>2</sub> in the case of a ketone hydrogenation, the Weisz Prater criteria ( $C_{WP}$ ) established by Eq. (10) should be less than 1. Mindful of this limit, we estimate that intraparticle mass transport should be significant at temperatures of 363K and above. Specifically, at an LA concentration of 0.5 M and a dissolved H<sub>2</sub> concentration of 0.0157 M, we measured turnover frequencies for LA hydrogenation to be sufficiently high ( $>0.2 \text{ s}^{-1}$ ) at 363K that intraparticle transport is likely to control the rate of hydrogenation. At this temperature and concentration, we calculate  $C_{WP}$

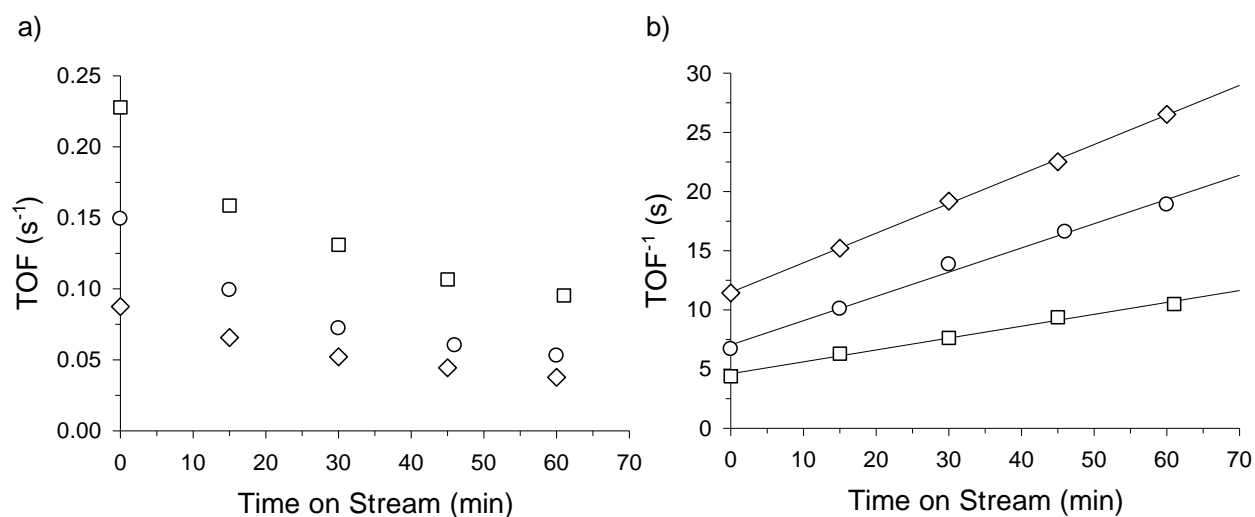
values of roughly 0.2 and >1 for LA and H<sub>2</sub>, respectively. At temperatures of 343K, we observe that  $C_{WP}$  is below 1 for both LA (<0.1) and H<sub>2</sub> (<0.7), suggesting kinetic control; however, given the uncertainty in estimating diffusivities, this result cannot be taken as a conclusive indication that intraparticle mass transfer constraints are absent. To ensure the kinetic relevance of rate data reported here, internal diffusion limitations were probed experimentally by examining the effect of catalyst particle size on observed hydrogenation rates. At a temperature of 343K with aqueous phase concentrations of 0.5 and 0.0157M in LA and H<sub>2</sub> respectively, LA hydrogenation TOFs were measured over Ru/C particles of mesh sizes 45-90  $\mu\text{m}$  and 90-125  $\mu\text{m}$  at a constant WHSV of 710  $\text{g}_{\text{LA}} \text{g}_{\text{cat}}^{-1} \text{hr}^{-1}$ . For these two sieve fractions, initial hydrogenation TOFs were 0.145 and 0.146  $\text{s}^{-1}$ , respectively, suggesting that intraparticle transport effects in this catalyst system do not control the observed rate of reaction at temperatures of 343K and below. At temperatures of 363 K and above, we did observe the hydrogenation rate to exhibit characteristics of transport control.

### 3.3.3 Kinetics of LA Hydrogenation

Since LA dehydration is demonstrated to have a negligible contribution to GVL production below 423K (Section 3.3.1), the sum of production rates for GVL and HPA can be taken as the total rate at which the ketone group in LA is hydrogenated. Because differential conditions were maintained in kinetic studies reported hereafter, turnover frequencies for LA (ketone) hydrogenation are well-approximated as the sum of site time yields for HPA and GVL.

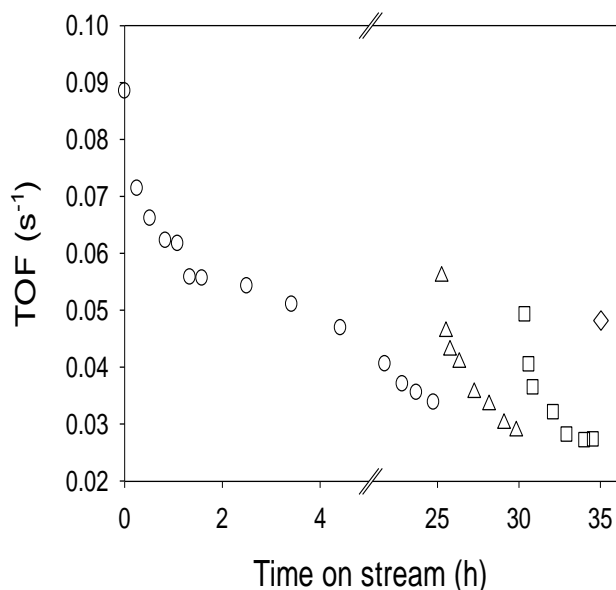
$$TOF_{LA} = STY_{HPA} + STY_{GVL} \quad (11)$$

Figure 3.2 plots turnover frequencies of LA hydrogenation over Ru/C as a function of time on stream at several representative reaction conditions. It is evident that LA hydrogenation rates decay rapidly in this aqueous-phase system, even at mild temperatures (323 K). Ultimately, we were unable to identify an operating regime where deactivation does not occur; as such, initial turnover frequencies at a given experimental condition were estimated by extrapolation of rate data to zero time on stream. Independent of the reaction conditions, the time decay of hydrogenation rates at short times on stream (below 8 hours) was well-described by a second order model such that declining reaction rates can be linearized by plotting inverse turnover frequencies against time on stream as described by Bartholomew [24]. Regression of linearized data sets permits quantification of initial hydrogenation turnover frequencies via estimation of a y-intercept, and all initial turnover frequencies reported here for LA hydrogenation were approximated using this method.



**Figure 3.2** a) Rates of LA hydrogenation over Ru/C at 323K ( $\diamond$ ), 343K ( $\circ$ ), and 363K ( $\square$ ) as a function of time on stream. b) Linearized rate data illustrating second order deactivation and method employed for estimation of rates at zero time on stream. For all experiments summarized here, the aqueous phase concentrations of LA and  $H_2$  were 0.50M and 0.016M.

Detailed consideration of Ru/C deactivation is outside the focus of this article; however, some discussion is warranted because of the ubiquity of noble metal-on-carbon catalysts in emerging aqueous phase hydrogenation processes targeting biorenewables. Figure 3.3 summarizes on stream performance of Ru/C during LA hydrogenation at 323 K. Here, we observe that TOFs for LA hydrogenation ultimately stabilize at 20 – 30% of their original values after 48 – 72 hours on stream. Regeneration attempts via in situ reduction reveal that this loss of activity occurs through a combination of reversible and irreversible phenomena. After reaching steady state, catalysts can be restored to only 50 – 60% of their initial activity, and their renewed activity decays quickly (within 5 hours) to the steady state value after being placed on stream again. To date, the mode of reversible deactivation has not been conclusively identified, but it may be attributed to either strongly bound hydrocarbon intermediates or surface oxidation of Ru nanoparticles.



**Figure 3.3** Observed LA hydrogenation rates as a function of time on stream at  $T = 323\text{K}$ ,  $C_{\text{H}_2} = 0.016\text{M}$ ,  $C_{\text{LA}} = 0.1\text{M}$ . ( $\circ$ ) Fresh catalyst, ( $\Delta$ ) first regeneration, ( $\square$ ) second regeneration, ( $\diamond$ ) third regeneration. Regeneration was performed in situ by interrupting aqueous feeds and reducing the catalyst under flowing  $\text{H}_2$  (100 sccm, 4h, 673K, 1K min<sup>-1</sup>)

With respect to irreversible deactivation, we have not observed Ru leaching or attrition of the carbon support in this system, nor does the carbon support undergo significant physical changes as determined by N<sub>2</sub> adsorption. As such, irreversible deactivation observed here is most likely attributed to particle sintering. Ru dispersion, determined by CO chemisorption, decreases from 40% to 21% in pre- and post-reaction samples. Since leaching, attrition, and structural degradation have not been observed, this loss of dispersion suggests an increase in Ru cluster size from roughly 3.6 nm in fresh samples to 6.8 nm in samples recovered after 65 hours on stream. Sintering is typically considered a high temperature phenomenon; however, water can facilitate particle agglomeration close to room temperature [25]. These observations are supported by the works of Davis, who reported metal cluster growth during aqueous phase hydrogenation of glucose over Ru/SiO<sub>2</sub> at 373 K [26] and Marin, who observed particle growth from 2.2 to 3.2 nm during the aqueous phase oxidation methyl- $\alpha$ -D-glucoside over Pt/C [27]. Sintering is thus a realistic consideration in this system, and future efforts geared toward rational design of stable hydrogenation catalysts for biomass processing should consider strategies for maintaining high Ru dispersions in the aqueous phase. In the interest of brevity and maintaining a focus on the kinetics of LA hydrogenation, we will defer a more comprehensive characterization of spent catalyst samples to subsequent communications. In the remainder of this section, we discuss observed trends in initial LA hydrogenation turnover frequency as a function of LA concentration, dissolved H<sub>2</sub> concentration, and reaction temperature.

### 3.3.2.1 Reaction Orders: Levulinic Acid

The concentration of LA in the aqueous phase was found to have a minimal and slightly inhibitory effect on the initial rate of hydrogenation. This trend is illustrated in Figure 3.4, and

regression of the data there reveals an apparent reaction order of  $-0.04 \pm 0.04$  over a range of LA concentrations (0.025 – 1.5M), indicating that the rate of LA hydrogenation is nearly independent of bulk LA concentrations over practical values. This observation is consistent with prior studies of both gas and liquid phase reactions where apparent zero order kinetics with respect to the hydrocarbon are generally observed for both C=O and C=C hydrogenations over group VIII metals. For example, hydrogenation of d-glucose [28] and arabionic acid [29] are both zero order in the oxygenate over Ru/C above concentrations of 0.3 M and 1 M respectively. Other supported, noble metals exhibit similar behavior. For example, Vannice has reported that benzene [30] and citral [31] hydrogenation over supported Pt and Pd catalysts, respectively, are zero-order in organic concentration. Similarly, for the gas phase hydrogenation of ethylene over Pt, Dumesic observed zero order dependence on ethylene at low temperatures and high partial pressures of ethylene [32]. Apparent zero order dependencies on organic species during hydrogenation is typically attributed to the presence of strongly bound hydrocarbon intermediates that saturate available metal surface sites during hydrogenation [33], and a more detailed interpretation will be provided in section 3.3.4.

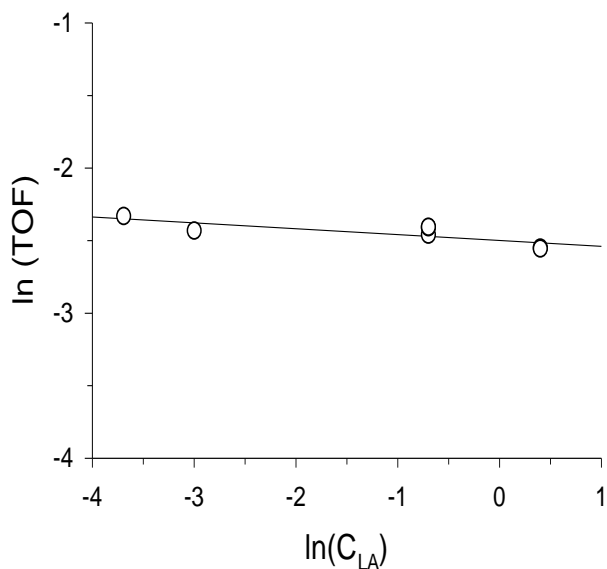


**Figure 3.4** Correlation between levulinic acid concentration and hydrogenation rate. Experiments illustrated here were carried out at 323K, 0.016M  $\text{H}_2$  concentration, and varying WHSV to maintain LA conversions below 3%. Turnover frequencies are reported in  $\text{s}^{-1}$  and LA concentrations are reported in  $\text{mol L}^{-1}$ .

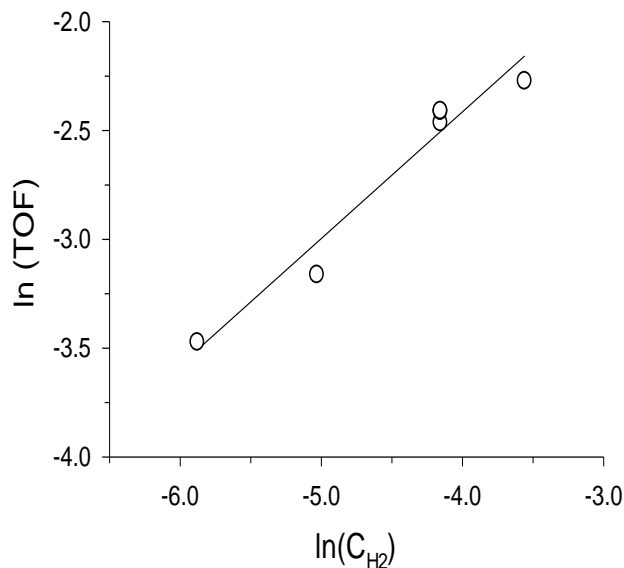
### 3.3.2.2 Reaction Orders: Hydrogen

Figure 3.5 illustrates the dependence of hydrogenation turnover frequency on the concentration of dissolved hydrogen in the aqueous phase. Here, a pronounced effect is observed, and regression of the rate data reveals a fractional order of  $0.6 \pm 0.2$ . This outcome suggests that  $\text{H}_2$  adsorption is rapid, such that surface reactions involving the addition of atomic hydrogen to adsorbed organic species control the rate of LA hydrogenation. Similar half-order hydrogen dependencies were observed by Vannice during benzene and acetic acid hydrogenation over supported Pt [30, 34], Dumesic during ethylene hydrogenation over Pt [32], and Mahajani in the hydrogenation of n-valeraldehyde[35] and iso-valeraldehyde[36] over supported Ru.

Reconciliation between this observation and a proposed reaction pathway will be discussed in subsequent analysis (section 3.3.4). At this stage, our consideration of apparent reaction orders

suggests that LA hydrogenation is well-represented under the conditions reported here by the empirical rate law given in Eq. (12).

$$r_{LA} = k' \cdot c_{H_2}^{\frac{1}{2}} \quad (12)$$



**Figure 3.5** Correlation between dissolved aqueous phase hydrogen concentration and hydrogenation rate. Experiments illustrated here were carried out at 323K, 0.5M LA, and varying WHSV to maintain LA conversions below 3%. Turnover frequencies are reported in s<sup>-1</sup> and H<sub>2</sub> concentrations are reported in mol L<sup>-1</sup>.

### 3.3.2.3 Temperature Effects

Assuming the empirical rate law derived in the preceding section (Eq. 12) is valid over the range of experimental conditions tested, we can estimate apparent rate constants for the hydrogenation of LA by normalizing measured turnover frequencies by the square root of the concentration of dissolved hydrogen. Subsequently, we may examine their temperature dependence to extract apparent activation energies and pre-exponential factors for this reaction. Apparent rate constants are plotted on a logarithmic scale against inverse temperature in Figure 3.6, which reveals two distinct regimes. At relatively high temperatures (363 – 423K), the data suggest an

apparent activation barrier of  $20 \pm 6 \text{ kJ mol}^{-1}$ , which is lower than that anticipated of kinetic rate control and likely indicates that internal pore diffusion dominates at higher temperatures. This observation is consistent with our preliminary analysis of the Weisz-Prater criteria (Section 3.3.2), which suggests that pore diffusion becomes significant at temperatures around 363K. At lower temperatures (303 – 343K), regression of linearized rate data indicate an apparent activation energy of  $48 \pm 5 \text{ kJ mol}^{-1}$  and an apparent pre-exponential factor of roughly  $3.1 \times 10^7 \text{ L}^{0.5} \text{ mol}^{-0.5} \text{ s}^{-1}$  on a Ru site basis or  $6.2 \times 10^3 \text{ (L}\cdot\text{mol)}^{0.5} \text{ (g}\cdot\text{sec)}^{-1}$  on a catalyst mass basis. Importantly, data in the low temperature region were demonstrated to be free of internal diffusion limitations through the observation of invariant hydrogenation turnover frequencies as a function of mean particle size at 343K. In line with our observations, prior studies have reported activation barriers ranging from 34 to 64  $\text{kJ mol}^{-1}$  over supported Ru for cinnamaldehyde [37], d-lactose [38], d-glucose [28] and arabinonic acid [29]. Similar activation energies of hydrogenation were also reported over supported Pt for benzene [30] and ethylene [32]. We therefore consider that an apparent barrier on the order of  $48 \text{ kJ mol}^{-1}$  is reasonable for levulinic acid hydrogenation over Ru/C.

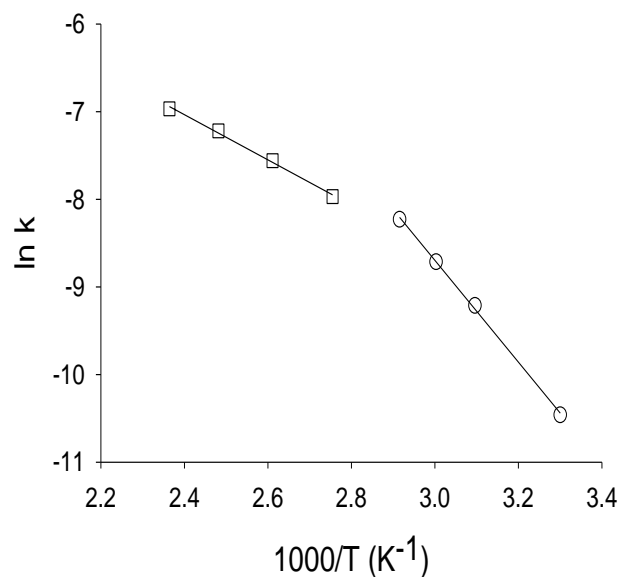


**Figure 3.6** Correlation between reaction temperature and levulinic acid hydrogenation rate. Experiments illustrated here were carried out at 0.5M LA, 0.016M H<sub>2</sub>, and varying WHSV to maintain LA conversions below 3%. Apparent rate constants here are reported in L<sup>0.5</sup> mol<sup>0.5</sup> g<sup>-1</sup> s<sup>-1</sup>.

### 3.3.4 Analysis of Kinetic Data

The observed reaction orders and apparent activation energy align well with previously documented studies considering both C=O and C=C hydrogenation. All observations can be reconciled with a conventional Horiuti-Polanyi interpretation [21], which is illustrated in a simplified scheme of LA hydrogenation in Eq. (13) – (16). Briefly, according to this mechanism, LA adsorbs molecularly and H<sub>2</sub> adsorbs dissociatively at Ru surface sites. Surface bound LA is subsequently reduced in two steps by sequential addition of hydrogen atoms, ultimately forming the hydroxyacid (HPA), which we assume desorbs irreversibly from the surface.





Based on prior computational studies [39], the half-hydrogenated intermediate (LAH, formed in step 3) is expected to be the dominant hydrocarbon species bound to Ru surface sites, and the second addition of atomic hydrogen (step 4) is generally considered to be rate determining. This assumption will yield the overall rate expression for LA hydrogenation given by Eq. (17).

$$r = k_4 \theta_{LAH} \theta_H \quad (17)$$

Half-hydrogenated species are expected to adsorb favorably on Ru surface sites under most conditions [33]. If we make the assumption that H<sub>2</sub> adsorption and hydrocarbon adsorption are fully competitive and that the two species occupy identical surface sites, then we would expect—in the limit of a surface dominated by bound hydrocarbon intermediates—that the rate of hydrogenation would exhibit apparent reaction orders of -1 in LA and 0 in H<sub>2</sub>, which are significantly different from our observed apparent orders of -0.04 and 0.6 for LA and H<sub>2</sub>, respectively. Alternatively, our preliminary Density Functional Theory results suggest that on flat terrace sites of Ru, adsorbed H-atoms are the dominant surface species. In this case, competitive adsorption of H<sub>2</sub> and hydrocarbon species would predict apparent reaction orders of +1 in LA and 0 in H<sub>2</sub>, which is again significantly different from our observations. Data collected in the regimes summarized here are thus more easily reconciled with the assumption that surface bound hydrocarbons and hydrogen atoms adsorb noncompetitively and can be considered in separate site balances. In the case of non-competitive adsorption, we predict via

Langmuir-Hinshelwood analysis that the overall hydrogenation rate should take the form given by Eq. (18).

$$r = \frac{k_4 K_1 K_2 K_3 C_{LA} C_{H_2}}{\left(1 + K_1 C_{LA} + K_1 K_2^{\frac{1}{2}} K_3 C_{LA} C_{H_2}^{\frac{1}{2}}\right) \left(1 + K_2^{\frac{1}{2}} C_{H_2}^{\frac{1}{2}}\right)} \quad (18)$$

Considering that the half-hydrogenated LAH intermediate is likely bound strongly and difficult to hydrogenate, we may apply the simplifying assumptions that the coverage of the hydrocarbon intermediate approaches saturation on sites available for hydrocarbon adsorption, and the coverage of levulinic acid approaches zero. The assumption of a small LA coverage is reasonable since close structural analogs, such as 2-butanone, are reported to bind weakly relative to hydrogenation intermediates at Ru sites [39]. Since we observe a distinct, positive reaction order with respect to hydrogen, we additionally assume that sites accessible to atomic hydrogen are far from saturation. Applying these limiting assumptions, the overall hydrogenation rate manifests as in Eq. (19), which reconciles well with our observed reaction orders of -0.04 and 0.6 in LA and H<sub>2</sub>.

$$r = k_4 \cdot K_2^{\frac{1}{2}} C_{H_2}^{\frac{1}{2}} \quad (19)$$

### 3.3.5 Kinetics of the Intramolecular Esterification of HPA

As demonstrated in Section 3.3.1, intramolecular esterification of HPA is the final step in the low-temperature production of GVL. Examination of selectivity trends suggests that HPA esterification is kinetically significant in the production of GVL over Ru/C, and we expect that this step is acid catalyzed. In the system considered here, the primary source of acidity is likely

solvated protons dissociated from LA and HPA, both of which are weak organic acids having pKa values of 4.59 and 5.69 [16], respectively. However, because oxidized carbon and Ru may also exhibit some acidity, we cannot conclude a priori that ring closure is exclusively a homogeneous reaction in this system. Prior to investigating reaction kinetics, control experiments were carried out to determine whether Ru/C and quartz influence the rate of HPA ring closure. At 303 K, we observed no difference in esterification rates observed with and without the addition of Ru/C and quartz, indicating that heterogeneous reactions do not contribute to HPA ring closure during hydrogenation. Subsequent sections describe experiments designed to capture reaction orders and temperature dependencies in the intramolecular esterification of HPA.

#### 3.3.4.1 Reaction Orders

Based on the intramolecular esterification mechanism, we expect that the rate of ring closure will exhibit some dependence on the concentrations of HPA and dissolved protons as summarized in Eq. (20) and (21).

$$r = k' \cdot C_{HPA}^{\alpha} \quad (20)$$

$$k' = k \cdot C_{H^+}^{\beta} \quad (21)$$

For a set of batch kinetic studies having varied HPA concentrations, LA concentrations, and reaction temperatures, Figure 3.7a illustrates HPA concentration normalized by its initial value as a function of time on a logarithmic scale. The demonstration of linearity in each data set indicates that HPA ring closure is first order in HPA concentration, and regression of each data set yields an apparent rate constant into which the concentration of dissociated protons has been

lumped (Eq. 21). Figure 3.7b plots these apparent rate constants calculated against the measured concentration of solvated protons on a logarithmic scale, and examination of the correlation between  $k'$  and  $C_{H^+}$  again reveals a first order dependence. First order dependencies on HPA and proton concentrations are consistent with prior descriptions of the intramolecular esterification of HPA in homogeneous systems.[40, 41]

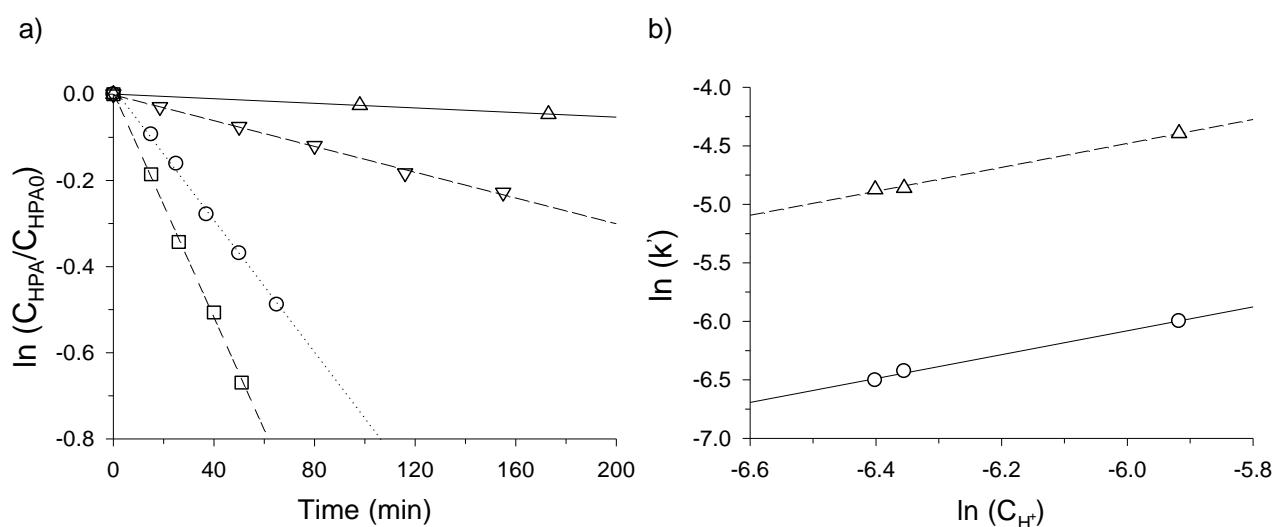


**Figure 3.7** a) Batch kinetic data for intramolecular esterification of HPA at ( $\Delta$ ) 300 K,  $C_{H^+} = 1.65$  mM,  $C_{HPA0} = 47.7$  mM, ( $\nabla$ ) 318 K,  $C_{H^+} = 1.65$  mM,  $C_{HPA0} = 47.7$  mM, ( $\circ$ ) 339 K,  $C_{H^+} = 1.65$  mM,  $C_{HPA0} = 47.7$  mM, ( $\square$ ) 339 K,  $C_{H^+} = 2.69$  mM,  $C_{HPA0} = 41.2$  mM. b) Apparent rate constants for intramolecular esterification of HPA determined at ( $\Delta$ ) 339 K and ( $\circ$ ) 318 K at various values of pH.  $k'$  is reported here in units of  $\text{min}^{-1}$ .

### 3.3.4.2 Temperature Effects

Having established reaction orders for both HPA and  $H^+$ , the rate constant,  $k$ , can be explicitly determined, and batch kinetic studies were carried out at various temperatures to quantify Arrhenius parameters. Rate constants determined at each temperature are plotted on a logarithmic scale against inverse temperature in Figure 3.8. Regression of this data indicates that the pre-exponential factor and activation barrier for the intramolecular esterification of HPA are, respectively,  $2.0 \times 10^{10} \text{ L mol}^{-1} \text{ s}^{-1}$  and  $70 \pm 0.4 \text{ kJ mol}^{-1}$ . We note that this barrier is slightly

higher than that observed for LA hydrogenation ( $48 \text{ kJ mol}^{-1}$ , Section 3.3.2.3). This result is consistent with our observations that ring closure appears to control GVL production rates at low temperatures and that GVL selectivities improve relative to HPA with increasing reaction temperature.

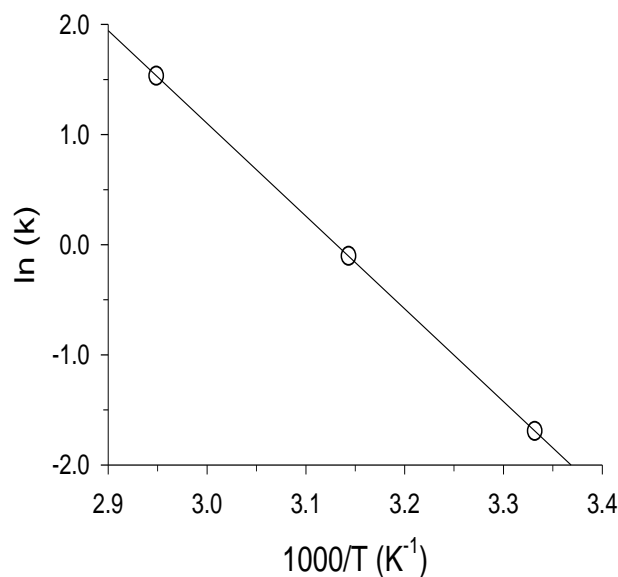


**Figure 3.8** Arrhenius plot illustrating the temperature dependence of rate constants for intramolecular esterification of HPA. Apparent rate constants are reported here in units of  $\text{L mol}^{-1} \text{ min}^{-1}$ .

### 3.3.6 Kinetic model for GVL production via LA hydrogenation

With reaction orders and temperature dependencies for both heterogeneously catalyzed LA hydrogenation and homogeneously catalyzed HPA ring closure established, the two reactions can be modeled independently to predict both LA hydrogenation rates and GVL selectivities over Ru/C. The reaction pathway and empirical kinetic parameters derived from experimental observations summarized to this point are compiled in Figure 3.9.



The catalyst mass in the system is calculated as a product of the system volume and  $\rho_b$ , the bulk density of the catalyst bed, and the concentration of solvated protons are calculated based on acid dissociation constants and concentrations of LA and HPA. As detailed in the materials and methods section, carboxylic acid dissociation is expected to vary minimally over the range of temperatures considered here, and its effect was neglected in our calculations. Modeling this system is complicated slightly by the fact that LA hydrogenation is heterogeneously catalyzed on Ru sites, while HPA ring closure is homogeneous. Thus, LA hydrogenation only occurs in the relatively small Ru/C bed, while HPA ring closure occurs homogeneously throughout both the Ru/C bed and in reactor sections filled with inert packing. To address this issue, reactors were simulated as being comprised of separate hydrogenation and inert sections, and the effluent from the hydrogenation section was used as the input to the inert section. As illustrated in Figure 3.10, we were able to reconcile, without further adjustment of parameters, predicted LA hydrogenation turnover frequencies and GVL production rates in each of the differential kinetic studies, indicating that the empirical model developed here is sufficient for predicting both LA conversion and GVL selectivity in kinetically controlled regimes. Since the catalysts employed here are deactivating, the steady state balances given by Eq. (22) – (24) apply only for prediction of initial LA hydrogenation and GVL production rates, and the data summarized in Figure 3.10 indicate values estimated at zero time on stream. Based on replicates of rate data collected at a well-defined reference condition ( $C_{LA} = 0.5$  M,  $C_{H_2} = 0.016$  M,  $T = 323$ K), rates of LA hydrogenation and GVL production measured in this system deviate by roughly 5% from the mean, and the error bars in Figure 3.10 reflect this uncertainty.

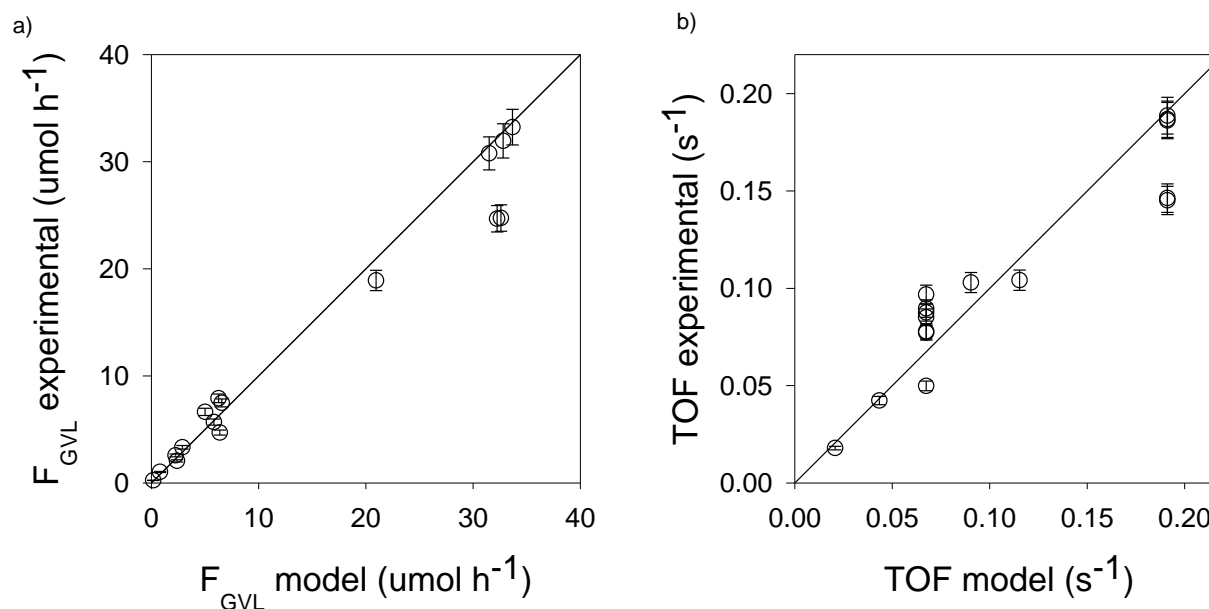


**Figure 3.10** Comparison between model predicted trends and experimental observations at various LA and  $\text{H}_2$  concentrations below 363K. (a) Describes the trends observed in GVL production rates, which captures selectivity during LA hydrogenation. (b) Describes the trends in TOF of LA hydrogenation.

### 3.3.7 Stacked Bed Reactors

Results from the preceding sections indicate that LA hydrogenation turnover frequencies are reasonable at near ambient temperatures (e.g., approximately  $0.08 \text{ s}^{-1}$  at 323K, 0.5M LA, 0.016 M  $\text{H}_2$ ), and that transport limitations become significant as temperatures increase substantially beyond this point. At low temperatures, we additionally observe that HPA ring closure appears to control the rate of GVL production such that GVL selectivity is less than 5%, independent of LA conversion. Increasing reaction temperature improves GVL selectivity since ring closure has a slightly larger activation barrier ( $70 \text{ kJ mol}^{-1}$ ) than LA hydrogenation ( $48 \text{ kJ mol}^{-1}$ ), and we observe nearly 80% selectivity to GVL during differential LA hydrogenation at 423K. However, high temperature operation is perhaps an inefficient choice for increasing productivity over a 5 wt% Ru/C catalyst. Pore diffusion quickly becomes rate controlling such that dramatic increases in reaction temperature yield only marginal enhancement in hydrogenation rates (e.g.,  $0.08 \text{ s}^{-1}$  at 323K compared to  $0.6 \text{ s}^{-1}$  at 423K); thus, the additional investment in energy input is not fully

recovered as substantially decreased residence times for LA hydrogenation. Results summarized thus far demonstrate that the rate of HPA esterification scales with proton concentration.

Therefore, an alternate approach to improving GVL selectivity is to introduce a second, acidic catalyst to expedite ring closure. Although many homogeneous and heterogeneous combinations of Ru and acidity are likely possible, we have employed a simple, stacked bed of Ru/C followed by A15 to facilitate sequential hydrogenation of LA and intramolecular esterification of HPA. Though the same outcome could be more elegantly accomplished using a bifunctional catalyst, introducing acidity in parallel to hydrogenation may encourage angelicalactone formation and thus alter the kinetics of GVL formation according to Figure 3.1. By separating metal- and acid-functionalities, we were able to directly probe the hypothesis that expediting HPA ring closure improves GVL production rates without altering LA hydrogenation rates. Observed stacked-bed hydrogenation rates and product selectivities are summarized in Table 3.2.

Control experiments carried out under differential conditions (Entries 1 and 2) illustrate that, despite employing different Ru/C pretreatment protocols (i.e., *in situ* vs. *ex situ* reduction), hydrogenation rates over Ru/C are not altered in the stacked bed reactor. Entry 2 shows that even a small quantity of A15 resin drastically shifts product selectivity toward GVL; however, conversions (<2%) and selectivities (<20%) remain below what would be desirable in a practical implementation. Entry 3 demonstrates that complete conversion of LA via hydrogenation over Ru/C at 323K is achieved at a weight hourly space velocity of 5 h<sup>-1</sup>; however, GVL selectivity remains poor over the metal catalyst. By adding a second bed of A15 (Entry 4), product selectivity can be shifted almost entirely to GVL at 323K, facilitating nearly 80% yield of GVL at practical residence times in a single reactor.

**Table 3.2** Experimentally observed LA conversions and product selectivities during hydrogenation of LA over Ru/C and A15.  $T = 323\text{K}$ ,  $C_{\text{LA}} = 0.5\text{ M}$ ,  $C_{\text{H}_2} = 0.016\text{ M}$ .

Run	WHSV <sup>†</sup> (h <sup>-1</sup> )	WHSV <sup>‡</sup> (h <sup>-1</sup> )	$X_{\text{LA}}$ (%)	TOF (s <sup>-1</sup> )	STY (s <sup>-1</sup> )			
					HPA	GVL	HPA	GVL
1	550	0	2	0.107	0.104	0.003	97	3
2	560	16.8	2	0.093	0.074	0.019	80	20
3	5	0	99	--	0.056	0.003	95	5
4	5	0.15	92	--	0.007	0.048	12	88

<sup>†</sup>LA Weight hourly space velocity based on Ru/C loadings.

<sup>‡</sup>LA Weight hourly space velocity based on Amberlyst-15 loadings.

### 3.4 Conclusion

We have shown that LA can be hydrogenated at near ambient temperatures, proceeding primarily through an HPA-mediated pathway in which hydrogenation occurs first and is followed by acid-catalyzed dehydration. At low temperatures, intramolecular esterification of HPA appears to control the rate of GVL formation, while at high temperatures, mass transfer limits the rate of hydrogenation. By recognizing this and developing an understanding of the kinetics of the sequential hydrogenation and dehydration steps, we have demonstrated that it is possible to leverage a strongly acidic catalyst in conjunction with a hydrogenation metal to significantly improve GVL production rates at low temperatures. With respect to rational design, it appears that that LA hydrogenation is best-suited to bifunctional catalysts exhibiting hydrogenation functionality alongside acidity. We have additionally observed pronounced deactivation of monometallic Ru/C in this model system, even under mild conditions. Although underlying causes have not been conclusively established, sintering appears to cause an irreversible loss of activity, suggesting that it is critical to identify strategies for retaining metal dispersion during aqueous phase hydrogenation.

### 3.5 References

- [1] M.G. Al-Shaal, W.R.H. Wright, R. Palkovits, Exploring the ruthenium catalysed synthesis of gamma-valerolactone in alcohols and utilisation of mild solvent-free reaction conditions, *Green Chemistry*, 14 (2012) 1260-1263.
- [2] J.C. Serrano-Ruiz, D.J. Braden, R.M. West, J.A. Dumesic, Conversion of cellulose to hydrocarbon fuels by progressive removal of oxygen, *Applied Catalysis B: Environmental*, 100 (2010) 184 -189.
- [3] W.R.H. Wright, R. Palkovits, Development of Heterogeneous Catalysts for the Conversion of Levulinic Acid to gamma-Valerolactone, *ChemSusChem*, 5 (2012) 1657-1667.
- [4] P.P. Upare, J.-M. Lee, D.W. Hwang, S.B. Halligudi, Y.K. Hwang, J.-S. Chang, Selective hydrogenation of levulinic acid to  $\gamma$ -valerolactone over carbon-supported noble metal catalysts, *Journal of Industrial and Engineering Chemistry*, 17 (2011) 287-292.
- [5] B.S. Akpa, C. D'Agostino, L.F. Gladden, K. Hindle, H. Manyar, J. McGregor, R. Li, M. Neurock, N. Sinha, E.H. Stitt, D. Weber, J.A. Zeitler, D.W. Rooney, Solvent effects in the hydrogenation of 2-butanone, *Journal of Catalysis*, 289 (2012) 30-41.
- [6] H.W.A.V.R.V.C.B. Subramaniam, Kinetic investigations of unusual solvent effects during Ru/C catalyzed hydrogenation of model oxygenates, *Journal of Catalysis*, 309 (2014) 174 - 184.
- [7] W. Luo, U. Deka, A.M. Beale, E.R.H. van Eck, P.C.A. Bruijninx, B.M. Weckhuysen, Ruthenium-catalyzed hydrogenation of levulinic acid: Influence of the support and solvent on catalyst selectivity and stability, *Journal of Catalysis*, 301 (2013) 175-186.
- [8] S.G. Wettstein, J.Q. Bond, D.M. Alonso, H.N. Pham, A.K. Datye, J.A. Dumesic, RuSn bimetallic catalysts for selective hydrogenation of levulinic acid to  $\gamma$ -valerolactone, *Applied Catalysis B: Environmental*, 117-118 (2012) 321-329.
- [9] D.J. Braden, C.A. Henao, J. Heltzel, C.C. Maravelias, J.A. Dumesic, Production of liquid hydrocarbon fuels by catalytic conversion of biomass-derived levulinic acid, *Green Chemistry*, 13 (2011) 1755-1765.
- [10] W.H. Luo, U. Deka, A.M. Beale, E.R.H. van Eck, P.C.A. Bruijninx, B.M. Weckhuysen, Ruthenium-catalyzed hydrogenation of levulinic acid: Influence of the support and solvent on catalyst selectivity and stability, *Journal of Catalysis*, 301 (2013) 175-186.
- [11] D.R. Lide, H.P.R. Frederikse, *CRC Handbook of Chemistry and Physics*, 76th ed., CRC Press, Inc., Boca Raton, FL, 1995.
- [12] A.W. Walde, Calculation of Heat of Reaction from Equilibrium Constants at Two Temperatures; Some New Heats of Ionization of Organic Acids., *The Journal of Physical Chemistry*, 43 (1939) 431-438.
- [13] A.W.a.T.H.V. Martin, The Ionization Constant of Lactic Acid, 0-50°, from Conductance Measurements, *Journal of the American Chemical Society*, 59 (1937) 2672-2675.
- [14] H.S.a.E.R.W. Harned, The Dissociation Constant of Propionic Acid from 0 to 60°, *Journal of the American Chemical Society*, 55 (1933) 2379-2383.
- [15] R. Jetse C. , G. Leonardo G., K. Ernst, Temperature dependence of acidity constants, a tool to affect separation selectivity in capillary electrophoresis, *Journal of Chromatography A*, 1155 (2007) 142 - 145.
- [16] E.W. Washburn, Core Historical Literature of Agriculture, in: *International critical tables of numerical data, physics, chemistry and technology*, 1930, pp. 140.

- [17] M.T. Pérez-Prior, J.A. Manso, M. del Pilar García-Santos, E. Calle, J. Casado, Reactivity of Lactones and GHB Formation, *The Journal of Organic Chemistry*, 70 (2004) 420-426.
- [18] H.S. Fogler, *Elements of Chemical Reaction Engineering*, Pearson Education, Inc., Upper Saddle River, NJ, 2006.
- [19] P.N. Dwivedi, S. Upadhyay, Particle-fluid mass transfer in fixed and fluidized beds, *Industrial & Engineering Chemistry Process Design and Development*, 16 (1977) 157-165.
- [20] C.J.x. Geankoplis, *Transport processes and unit operations*, Allyn and Bacon, Boston, 1978&#x9;
- [21] I. Horiuti, M. Polanyi, Exchange reactions of hydrogen on metallic catalysts, *Transactions of the Faraday Society*, 30 (1934) 1164-1172.
- [22] J.A. Dumesic, D.F. Rudd, L.M. Aparicio, J.E. Rekoske, A.A. Trevino, *The Microkinetics of Heterogeneous Catalysis*, American Chemical Society, Washington, D.C., 1993.
- [23] M.A. Vannice, *Kinetics of Catalytic Reactions*, Springer, New York, 2005.
- [24] C.H. Bartholomew, Mechanisms of catalyst deactivation, *Applied Catalysis A: General*, 212 (2001) 17-60.
- [25] M. Besson, P. Gallezot, Deactivation of metal catalysts in liquid phase organic reactions, *Catalysis Today*, 81 (2003) 547-559.
- [26] E.P. Maris, W.C. Ketchie, V. Oleshko, R.J. Davis, Metal Particle Growth during Glucose Hydrogenation over Ru/SiO<sub>2</sub> Evaluated by X-ray Absorption Spectroscopy and Electron Microscopy, *The Journal of Physical Chemistry B*, 110 (2006) 7869-7876.
- [27] Y. Schuurman, B.F.M. Kuster, K. van der Wiele, G.B. Marin, Selective oxidation of methyl  $\alpha$ -d-glucoside on carbon supported platinum: III. Catalyst deactivation, *Applied Catalysis A: General*, 89 (1992) 47-68.
- [28] E. Crezee, B.W. Hoffer, R.J. Berger, M. Makkee, F. Kapteijn, J.A. Moulijn, Three-phase hydrogenation of d-glucose over a carbon supported ruthenium catalyst—mass transfer and kinetics, *Applied Catalysis A: General*, 251 (2003) 1-17.
- [29] L. Fabre, P. Gallezot, A. Perrard, Catalytic Hydrogenation of Arabinonic Acid and Lactones to Arabitol, *Journal of Catalysis*, 208 (2002) 247-254.
- [30] U.K. Singh, M.A. Vannice, Kinetic and thermodynamic analysis of liquid-phase benzene hydrogenation, *AIChE Journal*, 45 (1999) 1059--1071.
- [31] U.K. Singh, M.A. Vannice, Liquid-Phase Hydrogenation of Citral over Pt/SiO<sub>2</sub> Catalysts: I. Temperature Effects on Activity and Selectivity, *Journal of Catalysis*, 191 (2000) 165-180.
- [32] R.D. Cortright, S.A. Goddard, J.E. Rekoske, J.A. Dumesic, Kinetic study of ethylene hydrogenation, *Journal of Catalysis*, 127 (1991) 342-353.
- [33] M. Boudart, G. Djéga-Mariadassou, *Kinetics of heterogeneous catalytic reactions*, Princeton University Press, Princeton, NJ, 1984.
- [34] W. Rachmady, M.A. Vannice, Acetic acid hydrogenation over supported platinum catalysts, *J. Catal.*, 192 (2000) 322-334.
- [35] P.D. Vaidya, V.V. Mahajani, Kinetics of liquid-phase hydrogenation of n-valeraldehyde to n-amyl alcohol over a catalyst, *Chemical Engineering Science*, 60 (2005) 1881-1887.
- [36] M.A. Tike, V.V. Mahajani, Kinetics of Liquid-Phase Hydrogenation of Iso-valeraldehyde to Iso-amyl Alcohol Over A Ru/Al<sub>2</sub>O<sub>3</sub> Catalyst, *The Canadian Journal of Chemical Engineering*, 84 452-458.
- [37] G. Neri, L. Bonaccorsi, S. Galvagno, Kinetic Analysis of Cinnamaldehyde Hydrogenation over Alumina-Supported Ruthenium Catalysts, *Industrial & Engineering Chemistry Research*, 36 (1997) 3554-3562.

- [38] J.-P.M. Jyrki Kuusisto, Mona Sparv, Johan Warna, Hannu Karhu, Tapio Salmi, Kinetics of the catalytic hydrogenation of D-Lactose on carbon supported ruthenium catalyst, *Chemical Engineering Journal*, 139 (2008) 69-77.
- [39] N.K. Sinha, M. Neurock, A first principles analysis of the hydrogenation of C1-C4 aldehydes and ketones over Ru(0 0 0 1), *Journal of Catalysis*, 295 (2012) 31-44.
- [40] H.S. Taylor, H.W. Close, Catalysis in Lactone Formation, *The Journal of Physical Chemistry*, 29 (1924) 1085-1098.
- [41] W.N. Fishbein, S.P. Bessman, Purification and Properties of an Enzyme in Human Blood and Rat Liver Microsomes Catalyzing the Formation and Hydrolysis of  $\gamma$ -Lactones, *Journal of Biological Chemistry*, 241 (1966) 4842 - 4847.

## **Chapter 4    Towards rational design of stable, supported metal catalysts for aqueous phase processing: insights from the hydrogenation of levulinic acid**

### **4.1 Introduction**

A number of catalytic technologies have been explored for converting biomass and its derivative platforms into energy-dense fuels and value-added chemicals. Aqueous phase reforming allows the production of H<sub>2</sub> and/or syngas directly from carbohydrates [1, 2]; decarbonylation and decarboxylation of carboxylic acids delivers alkenes and alkanes [3-7]; and hydrodeoxygenation facilitates selective cleavage of C-O bonds to form fully reduced alkanes that retain the entire carbon content of the parent feedstock (i.e., they occur without C-C cleavage) [8-11]. A common characteristic of the above is that each requires metal catalysts in some capacity. Aqueous-phase reforming employs metal sites to facilitate dehydrogenation, C-C cleavage, and water-gas shift [1, 2, 12-15]; and metal surfaces similarly activate carboxylic acids for decarboxylation and decarbonylation [3, 7]. Although HDO strategies leverage acid sites to cleave C-O bonds through dehydration, extensive reduction in oxygen content—as required for biofuel production—inevitably requires H<sub>2</sub> addition and suggests complementary use of metal catalysts [8-10]. Similarly, processes such as transfer hydrogenation for carbonyl reduction, which can be catalyzed by Lewis acidic solid oxides [16-19], require reduced metal sites in ancillary roles [20].

In light of the above points, it is no surprise that the biomass processing literature is rich with examples of processes that employ supported metal catalysts in aqueous media [1, 12-15, 21-31]. Unfortunately, metal catalysts are relatively expensive, and their price contributes significantly to the (present) high cost of bio-based commodities [32]. To minimize catalyst expenses where metals are employed, they must provide intrinsically high activity and offer stable on-stream

performance. While the former is frequently demonstrated, the latter remains elusive. Aqueous media and high temperatures alone can expedite catalyst deactivation; furthermore, mineral and organic acids are commonly encountered in biomass processing, and many applications additionally demand that metal catalysts perform stably at low pH [3, 33-37]. The severity of the aqueous phase—and its effect on catalyst stability—has been frequently considered, and prior discussion has largely centered on support hydrothermal stability [38-42]. Given that carbon is relatively impervious to hydrolysis, it has emerged as a favored support for aqueous-phase applications. However, while support stability is necessary for catalyst stability, it is not sufficient to guarantee catalyst stability. For example, Ru/C is a popular catalyst choice for carbonyl hydrogenation; however, we recently observed that, despite retention of support integrity, undergoes pronounced deactivation during aqueous phase hydrogenation of the ketone group in bifunctional levulinic acid (LA, 4-oxopentanoic acid), even under relatively mild conditions (323K, 0.5M LA, pH = 2.45) [21]. A portion of the observed deactivation was irreversible and attributed to particle sintering, while a secondary deactivation mechanism appeared largely reversible. These observations are qualitatively consistent with prior accounts of Ru deactivation in related systems, and it is broadly acknowledged that improving the stability of Ru-based catalysts could improve the economic viability of  $\gamma$ -valerolactone production from biomass resources. From an applied standpoint, bimetallic formulations appear to offer enhanced stability during LA hydrogenation[31, 43, 44]; however, the mechanism by which promoter metals prevent Ru deactivation is unclear. Much of this uncertainty—and hence our ability to rationally design hydrogenation catalysts that offer stable performance in aquo—stems from a poor understanding of the phenomena that govern Ru deactivation in this system. Accordingly, the present study further considers the reversible and irreversible modes of deactivation that

affect supported Ru catalysts during aqueous phase ketone hydrogenation and correlates their severity with fundamental properties of the catalyst and the media in which it is employed.

Through consideration of both LA and 2-pentanone hydrogenation over Ru supported on SiO<sub>2</sub>,  $\gamma$ -Al<sub>2</sub>O<sub>3</sub>, TiO<sub>2</sub>, and C, we highlight the influence of support identity and solution pH on the intrinsic activity and stability of Ru surface sites during aqueous phase ketone hydrogenation.

Although the hydrothermal stability of solid oxides is generally poor compared to carbon, they provide us with relatively well-defined model surfaces, and their consideration alongside carbon should aid in mapping design criteria that allow stabilization of supported metals in aqueous, acidic media.

## 4.2 Experimental

### 4.2.1 Materials and methods

Levulinic acid (LA, 98%, Sigma Aldrich),  $\gamma$ -valerolactone (GVL, 98%, Sigma Aldrich), 2-pentanone (99%, Acros Organics), 2-pentanol (DL, 98%, Acros Organics), propanoic acid (99%, Acros Organics), sulfuric acid (95-98wt%, Sigma Aldrich), and acetonitrile (HPLC grade 99.9%, Fisher Scientific) were used in kinetic studies, standard preparation, and liquid chromatography. Catalyst syntheses employed ruthenium (III) chloride hexahydrate (35-40% Ru, Acros Organics), amorphous SiO<sub>2</sub> (481 m<sup>2</sup>/g, Sigma Aldrich),  $\gamma$ -Al<sub>2</sub>O<sub>3</sub> (231 m<sup>2</sup>/g, Strem Chemicals) and TiO<sub>2</sub> (Aeroxide<sup>®</sup> P25, 55 m<sup>2</sup>/g, Acros Organics). Commercial 0.5 wt% Ru/C and 5 wt% Ru/C samples were purchased from Strem Chemicals. H<sub>2</sub> (99.999%, Airgas), N<sub>2</sub> (99.999%, Airgas), and CO (99.99% Praxair) were employed in kinetic studies, catalyst pretreatment, and catalyst characterization. All above reagents were used as supplied by the manufacturer. Water used in

preparation of catalysts, reactor feeds, calibration standards, and HPLC mobile phases was purified in house by sequential reverse osmosis, UV oxidation, and double ion exchange.

#### 4.2.2 Catalyst preparation

Catalysts comprised of Ru supported on  $\gamma$ -Al<sub>2</sub>O<sub>3</sub>, SiO<sub>2</sub>, and TiO<sub>2</sub> were prepared via incipient wetness impregnation of the desired support with aqueous ruthenium (III) chloride hexahydrate. Impregnated catalysts were dried in air at 393K and subsequently reduced in flowing H<sub>2</sub> (100 ml min<sup>-1</sup>, 673K, 3K min<sup>-1</sup>). Prior to removal from reduction vessels, samples were passivated at 298K in a stream of 1% O<sub>2</sub> in He.

#### 4.2.3 Catalyst Characterization

Catalyst surface area and porosity were probed by N<sub>2</sub> physisorption at 77K (Micromeritics ASAP 2020). Before N<sub>2</sub> dosing, samples were outgassed under vacuum (6h, 623K). Total surface areas and pore size distributions were obtained through BET and BJH analyses of the N<sub>2</sub> adsorption/desorption isotherm. Pore volumes were estimated from the total N<sub>2</sub> uptake at a relative pressure of 0.995.

Ru surface sites were quantified by adsorption of CO at 308K (Micromeritics ASAP 2020). Prior to dosing, samples were reduced in flowing H<sub>2</sub> (3h, 673K, 3 K min<sup>-1</sup>), evacuated at 673K for 1h to remove chemisorbed hydrogen, and cooled to 308K under vacuum. Analysis was then performed at 308K by collecting an adsorption isotherm, evacuating the sample for 1 h to remove physisorbed CO, and collecting a second isotherm. Irreversible CO adsorption was determined from the difference in CO adsorption between the first and second isotherms. Here, irreversible CO uptake was taken as equivalent to the Ru surface site density, which assumes a

CO adsorption stoichiometry of 1. Surface averaged Ru particle diameters based on irreversible CO uptake were calculated according to Eq. (1), which assumes a spherical morphology:

$$d_{p,CO} = \frac{6}{S \cdot \rho_{Ru}} \quad (1)$$

Where  $S$  is the surface area of Ru per gram of catalyst calculated from irreversible CO uptake, and  $\rho_{Ru}$  is the density of metallic Ru. The cross sectional area of a single Ru atom was assumed to be  $6.14 \text{ \AA}^2$ , and  $12.30 \text{ g cm}^{-3}$  was used as the density of Ru [45].

#### 4.2.4 TEM

Average Ru cluster sizes and particle size distributions were determined using transmission electron microscopy (TEM). Catalyst samples were suspended in excess acetone via sonication, and suspension aliquots were deposited on 300 mesh carbon film Cu grids (EMS) and dried overnight under ambient conditions. Images were taken using a JEOL 2010F equipped with a Schottky field emission gun operating at 200 KV and captured with a CCD camera. Particle size distributions were extracted from TEM images using image processing software (ImageJ).

Average particle sizes reported here represent the surface averaged diameter, which is calculated according to Eq. (2) [46]:

$$d_{p,TEM} = \frac{\sum_i n_i \cdot d_i^3}{\sum_i n_i \cdot d_i^2} \quad (2)$$

In Eq.(2)  $d_i$  represents the mean of a specified range of particle diameters,  $n_i$  represents the number of particles within that range, and  $d_{p,TEM}$  is the average particle size. Standard deviations for the surface averaged diameter were calculated according to Eq. (3) [46]:

$$\sigma = \sqrt{\frac{\sum_i n_i d_i^2 (d_i - d_{p,TEM})^2}{\sum_i n_i d_i^2}} \quad (3)$$

#### 4.2.5 Catalytic Activity Testing

Aqueous-phase hydrogenations were carried out in an upflow, packed bed reactor that has been described elsewhere [21]. Reactor feeds were prepared by dissolving levulinic acid (0.5M) or 2-pentanone (0.5M) in double deionized water, and catalysts were reduced in situ under flowing H<sub>2</sub> (673K, 4h, 3K min<sup>-1</sup>) prior to feed introduction. The liquid effluent was collected in a vapor-liquid separator and analyzed offline. LA and its hydrogenation products, 4-hydroxypentanoic acid (HPA) and GVL, were quantified using high performance liquid chromatography (HPLC, Agilent 1100) by eluting reactor samples through an Agilent Hi-Plex H column with a 5mM aqueous H<sub>2</sub>SO<sub>4</sub> mobile phase. Analyte concentrations were determined using a variable wavelength detector operating at 195 nm. Cyclization of HPA to form GVL is both thermodynamically favorable and relatively facile. A portion of the HPA present in reaction products always forms GVL under our analysis conditions, which complicates an explicit determination of HPA/GVL selectivity. We have previously reported upon HPA and GVL selectivity[21]; however, our discussion here only requires estimating the total rate of LA (ketone) hydrogenation. This can be reliably obtained from the sum of HPA and GVL production rates, which are independent of the precise HPA/GVL distribution. 2-pentanone and its hydrogenation product, 2-pentanol, were quantified by GC-FID (Agilent 7890) using an HP-Innowax column (Agilent). This analytical approach led to >95% closure of carbon balances. For all reported experiments, reactors were operated under conditions that have been previously

demonstrated to be free of mass transfer limitations during levulinic acid hydrogenation over 5 wt% Ru/C [21]. Though we have not exhaustively investigated diffusion limitations in this study, all catalysts tested have porosities, areal Ru site densities, and volumetric ketone hydrogenation rates that are—with respect to transport limitations—comparable to or more favorable than 5 wt% Ru/C. We thus assume that data reported here represent kinetically controlled hydrogenation rates.

This study focuses on the activity and on-stream stability of supported Ru during the aqueous phase hydrogenation of LA and 2-pentanone. The chemistry of interest in each case is hydrogenation of a ketone functional group; accordingly, our discussion emphasizes rates of ketone hydrogenation. To allow meaningful comparisons among catalysts having varied supports and metal loadings, hydrogenation rates are reported on a per-site basis as the total site time yield (STY) of hydrogenation products:

$$STY_i = \frac{\sum_j F_j}{S_{R_i}} \quad (4)$$

In Eq. (4),  $F_j$  is the molar flowrate of an individual hydrogenation product, and  $S_R$  is the total molar quantity of Ru surface sites in a given catalyst bed. For LA, the hydrogenation STY reflects the sum of HPA and GVL production per Ru surface site [21]. For 2-pentanone, it is based only on the rate of 2-pentanol production. Catalysts in all experiments deactivate with time on stream. To allow meaningful correlation with ex-situ methods of site titration, hydrogenation rates are reported as initial rates, which were estimated by extrapolation of deactivation profiles to zero time on stream [21].

To probe the reversibility of deactivation, aqueous feeds were periodically interrupted, and catalysts were reduced in situ under flowing  $\text{H}_2$  ( $100 \text{ ml min}^{-1}$ , 1 bar). For most samples, reduction was carried out at 673K as discussed in the catalyst preparation section; however, regeneration at this temperature induced anomalous, irreversible deactivation in Ru/TiO<sub>2</sub>. As such, Ru/TiO<sub>2</sub> was regenerated at 323K. Spent catalysts were recovered for characterization after drying in situ under  $\text{N}_2$  ( $90 \text{ ml min}^{-1}$ , 3h, 573 K,  $1 \text{ K min}^{-1}$ ).

## 4.3 Results

### 4.3.1 Catalyst Activity

Table 4.1 summarizes physical and chemical characteristics of the supported Ru catalysts considered in this study. Our intent was to compare, as closely as possible, catalysts having similar Ru dispersions and particle sizes, and most considered here were prepared at comparable areal Ru loadings to a previously studied catalyst, Ru/C-A (Entry 1) [21]. 0.5 wt% Ru/C and 0.3 wt% Ru/SiO<sub>2</sub> samples were additionally included in an attempt to extend the range of particle sizes considered on these supports. Where possible, particle sizes were determined by both CO chemisorption and TEM. Results of the two methods generally agree, revealing that that initial Ru particle sizes are within the range of 1 – 4 nm for all samples. Based on its CO adsorption capacity, the particle diameter for Ru/C-B appears overestimated by TEM, and we consider CO uptake to provide the more reliable estimate of initial cluster size for this sample (1.2 nm). Particle sizes vary with support and metal loading, which is anticipated according to prior reports employing impregnation methods for the preparation of supported Ru catalysts [47-49], and we

account for this variation to the extent possible in subsequent analyses. CO uptakes from Table 4.1 provide the basis for calculation of site time yields, and other properties are highlighted where relevant.

**Table 4.1** Physical and chemical properties of supported Ru catalysts employed in this study.

Sample	SA (m <sup>2</sup> /g)	V <sub>p</sub> (cm <sup>3</sup> /g)	D <sub>p</sub> (nm) <sup>a</sup>	Ru (wt %) <sup>b</sup>	Ru (μmol/m <sup>2</sup> )	CO uptake (μmol/g)	d <sub>p,TEM</sub> (nm) <sup>c</sup>	d <sub>p,CO</sub> (nm) <sup>d</sup>
Ru/C-A	756	0.70	5.1	5.0	0.65	220	4.0 ± 0.3	3.2
Ru/C-B	780	0.66	5.1	0.5	0.07	61	4.0 ± 0.3	1.2
Ru/SiO <sub>2</sub> -A	468	0.82	5.5	2.7	0.57	116	2.7 ± 0.1	3.3
Ru/SiO <sub>2</sub> -B	468	0.82	5.5	0.3	0.06	18	-	2.2
Ru/γ-Al <sub>2</sub> O <sub>3</sub>	230	0.44	5.7	1.3	0.56	105	1.7 ± 0.1	1.6
Ru/TiO <sub>2</sub>	55	0.42	24.1	0.4	0.69	15	3.1 ± 0.3	3.3

a – Average pore diameter determined by BJH analysis of N<sub>2</sub> adsorption/desorption data.

b – Based upon concentrations of impregnating solutions, incipient volume and support mass

c – Confidence intervals calculated at 95%

d – Estimated from CO chemisorption

Table 4.2 summarizes site time yields of ketone hydrogenation products observed during hydrogenation of LA (0.5M, aq.) and 2-pentanone (0.5M, aq.) over Ru supported on C, SiO<sub>2</sub>, Al<sub>2</sub>O<sub>3</sub>, and TiO<sub>2</sub> at 323K. Importantly, this presentation relies on site-normalized hydrogenation rates, which correct for variations in metal dispersion and allow us to rigorously discuss the influence of particle size on rates of ketone hydrogenation in the aqueous phase. Excepting Ru-SiO<sub>2</sub>-B, each catalyst was tested at both relatively high and relatively low space velocities. The former allowed estimation of site time yields under conditions of low ketone conversion, and the latter ensured sufficient mass loadings to facilitate recovery and characterization of spent catalysts. For any given sample, one observes that hydrogenation STYs over Ru sites are, within the precision of our estimates, invariant with space velocity and ketone conversion. This result is consistent with prior observations that both gas- and liquid-phase ketone hydrogenations appear zero order in the ketone over the range of concentrations considered [50-52]. Moreover, no

significant variation in (initial) site-time yield is observed between any two supports, suggesting that intrinsic rates of LA hydrogenation over Ru in water are not strongly affected by metal-support interactions. This result agrees with data reported by both Subramaniam and Rooney, which indicate comparable turnover frequencies during aqueous-phase hydrogenation of 2-butanone over Ru supported on C [53] and SiO<sub>2</sub> [54]. Finally, entries 12 - 15 indicate that rates of 2-pentanone hydrogenation are comparable to those of LA hydrogenation, allowing the conclusion that the secondary carboxylic acid functionality in LA and the resultant increase in aqueous proton concentrations do not strongly perturb the intrinsic ketone hydrogenation activity of Ru sites in water.

**Table 4.2.** Summary of initial rates of hydrogenation for both levulinic acid and 2-pentanone in bulk water at 323K, 24 bar H<sub>2</sub>, and 0.5M dissolved organic. Conversions and rates are both reported at zero time on stream.

Entry	Sample	Feed	WHSV (g ketone g catalyst <sup>-1</sup> hr <sup>-1</sup> )	Conversion (%)	STY (s <sup>-1</sup> ) <sup>a</sup>
1	Ru/C-A	LA	520	2	0.09 ± 0.028
2	Ru/C-A	LA	37	20	0.08 ± 0.011
3	Ru/C-B	LA	34	8	0.11 ± 0.009
4	Ru/C-B	LA	12	33	0.15 ± 0.011
5	Ru/SiO <sub>2</sub> -A	LA	32	16	0.11 ± 0.019
6	Ru/SiO <sub>2</sub> -A	LA	18	42	0.16 ± 0.007
7	Ru/SiO <sub>2</sub> -B	LA	22	4	0.10 ± 0.012
8	Ru/Al <sub>2</sub> O <sub>3</sub>	LA	27	14	0.09 ± 0.007
9	Ru/Al <sub>2</sub> O <sub>3</sub>	LA	11	35	0.10 ± 0.005
10	Ru/TiO <sub>2</sub>	LA	25	3	0.11 ± 0.015
11	Ru/TiO <sub>2</sub>	LA	11	7	0.12 ± 0.014
12	Ru/SiO <sub>2</sub> -A	2-pentanone	27	18	0.11 ± 0.021
13	Ru/SiO <sub>2</sub> -A	2-pentanone	13	36	0.13 ± 0.004
14	Ru/Al <sub>2</sub> O <sub>3</sub>	2-pentanone	20	29	0.14 ± 0.010
15	Ru/Al <sub>2</sub> O <sub>3</sub>	2-pentanone	12	44	0.14 ± 0.010

<sup>a</sup> –Confidence intervals calculated at 95%.

The initial rates summarized in Table 4.2 were obtained by extrapolation of decaying

hydrogenation rates to zero-time-on-stream, and some scatter in the data is inevitable. Despite

this, Figure 4. illustrates that, for all catalysts summarized in Table 4.1, mass-normalized

hydrogenation rates during reduction of both 2-pentanone and LA are first order in Ru surface site density. Furthermore, both sets of data are captured by a single, linear correlation. This allows determination of an average STY for ketone hydrogenation via regression of hydrogenation rates as a function of site densities, and we estimate it to be  $0.11 \pm 0.016 \text{ s}^{-1}$  under the reported conditions. It must be acknowledged that many of the hydrogenation rates illustrated in Figure 4.1. **Figure 4.** were not obtained under conditions of differential ketone conversion; however, since hydrogenation rates appear zero order with respect to the ketone, site time yields of hydrogenation products should be invariant with ketone conversion. Therefore, the average site time yield measured here provides a reasonable estimate for the turnover frequency of both 2-pentanone and LA hydrogenation over Ru sites at 323K and 24 bar  $\text{H}_2$ . A final consequence of the data shown in Figure 4. is that, since one clearly observes a linear correlation between catalyst productivity and Ru site density, data are consistent with kinetically controlled hydrogenation rates for all samples considered [55, 56]. Since initial metal dispersions varied in this study, Figure 4. also suggests that Ru cluster sizes do not substantially affect turnover frequencies for ketone hydrogenation in the size range considered here (1 – 4 nm). Glucose hydrogenation on Ru [26] and acetone hydrogenation on Pt [51, 52] are both reported to be structure independent; as such, our observation of structure insensitivity in this system is consistent with prior accounts of carbonyl hydrogenation over Group VIII metals.

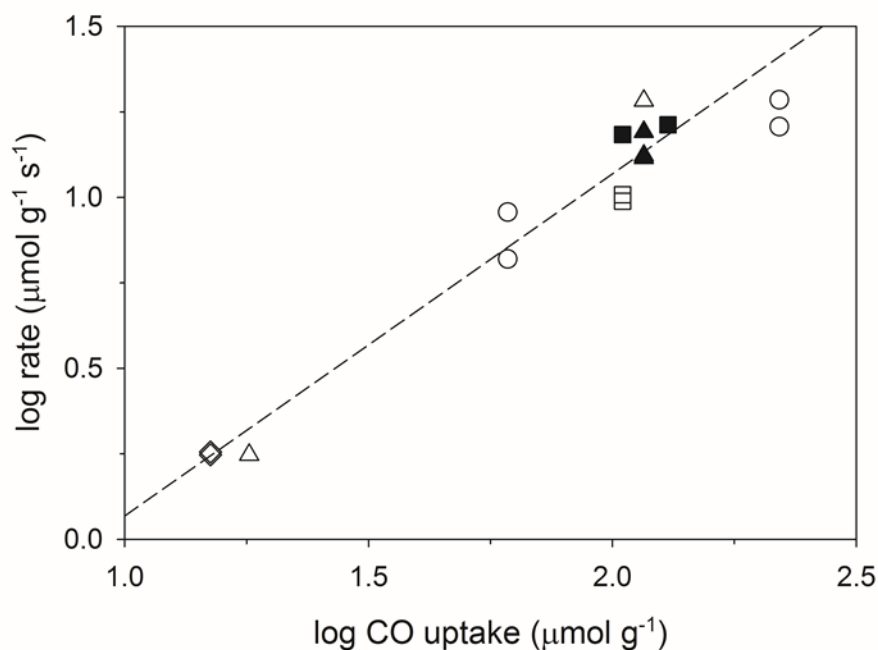


**Figure 4.1** Functional relationship between mass-normalized ketone hydrogenation rates and Ru surface site densities as determined by CO chemisorption. Hydrogenation rates were measured at 0.5M ketone concentration at 323K and 24 bar H<sub>2</sub>. (◇) Ru/TiO<sub>2</sub>, (○) Ru/C, (Δ) Ru/SiO<sub>2</sub>, (□) Ru/γ-Al<sub>2</sub>O<sub>3</sub>. Open symbols represent LA hydrogenation rates. Filled symbols represent 2-pentanone hydrogenation rates. The slope of the regression line indicated in the figure is 1.0 ± 0.14, which is consistent with criteria given by Koros and Nowak for demonstration of kinetically controlled hydrogenation rates at a given temperature.

#### 4.3.2 Catalyst Stability

We first consider the stability of Ru supported on SiO<sub>2</sub>, γ-Al<sub>2</sub>O<sub>3</sub>, TiO<sub>2</sub>, and C by examining their activity (*a*) with time-on-stream during LA hydrogenation (Figure 4.2). Activity for each catalyst is defined as its measured rate of ketone hydrogenation at a given time on stream normalized by its estimated rate of hydrogenation at zero time on stream. Samples were subjected to periodic regeneration to determine the extent to which activity losses were reversible, and regeneration attempts are indicated by dashed vertical lines. Our standard regeneration procedure was to reduce catalyst samples in flowing H<sub>2</sub> at 673K; however, this treatment was observed to substantially and irreversibly diminish hydrogenation rates of

Ru/TiO<sub>2</sub>. This could be possibly due to an induced state of strong metal support interaction, where the Ru sorption capacity is decreased[57, 58]. We have observed that reduction at 323K is sufficient to restore reversible deactivation of supported Ru catalysts in this system without inducing irreversible deactivation in Ru/TiO<sub>2</sub>. Accordingly, we have employed this alternative protocol for regeneration of Ru/TiO<sub>2</sub>.

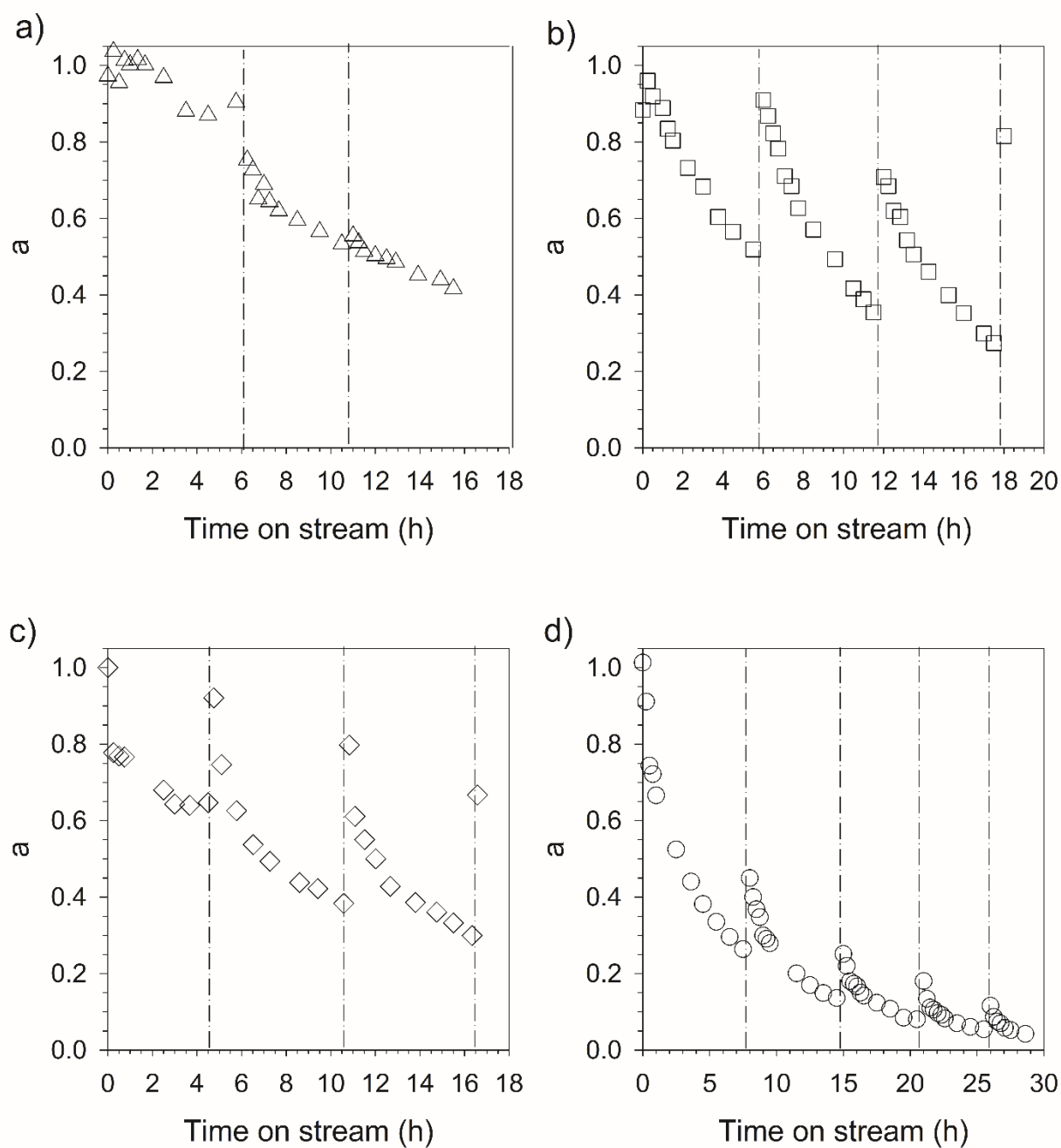


**Figure 4.2** LA hydrogenation activity as a function of time on stream for Ru supported on (a) 2.7 wt% on  $\text{SiO}_2$ , (b) 1.3 wt% on  $\gamma\text{-Al}_2\text{O}_3$ , (c) 0.4 wt% on  $\text{TiO}_2$  and (d) 0.5 wt% on C. Observed deactivation profiles for samples prepared at different Ru loadings were qualitatively similar to the above trends such that this selection of samples is appropriate for the following discussion.

Measured hydrogenation site time yields in this system are relatively high ( $\approx 0.01 - 0.1 \text{ sec}^{-1}$ ), and the volumetric residence time in each experiment is relatively small ( $\approx 10 \text{ min}$ ), suggesting that the system should approach steady state within an hour. Reference experiments carried out under steady state conditions confirmed that normally anticipated transient phenomena (e.g., those associated with system volume and/or transients in surface coverage) are complete within 15 – 20 minutes, whereas Figure 4.2 illustrates that catalyst activity decays on the scale of hours. This indicates that catalyst deactivation underlies the observed transient phenomena.

Deactivation profiles in Figure 4.2 reveal that supported Ru catalysts are susceptible to both reversible and irreversible activity losses during aqueous phase hydrogenation of LA at 323K; however, the extent of each deactivation pathway varies considerably in the catalysts tested. For example, activity lost by Ru/SiO<sub>2</sub> is entirely non-recoverable upon in situ reduction (Figure 4.2a), whereas activity losses observed for Ru/ $\gamma$ -Al<sub>2</sub>O<sub>3</sub> appear to be primarily reversible in nature (Figure 4.2b). Ru nanoparticles supported on TiO<sub>2</sub> and C undergo both types of deactivation to varying extents. Based on control experiments performed with Ru/ $\gamma$ -Al<sub>2</sub>O<sub>3</sub>, activity is only restored through treatment in H<sub>2</sub>; catalyst regeneration was not possible in analogous treatments in He.

Before proceeding with further analysis of the two modes of instability, we highlight differences observed during aqueous phase hydrogenation of LA and 2-pentanone (Figure 4.3). For this comparison, Ru/SiO<sub>2</sub> and Ru/ $\gamma$ -Al<sub>2</sub>O<sub>3</sub> were selected since these two catalysts displayed extreme differences in extents of reversible and irreversible activity losses during LA hydrogenation. Over Ru/SiO<sub>2</sub> there is no quantifiable difference in catalyst stability during aqueous phase hydrogenation of 2-pentanone and LA (Figure 4.3a). In both cases, deactivation is irreversible,

and it occurs to comparable extents over 16 hours on stream. In contrast, Ru/ $\gamma$ -Al<sub>2</sub>O<sub>3</sub> is considerably more stable during 2-pentanone hydrogenation than it is during LA hydrogenation (Figure 4.3b). Based on initial rates measured after each regeneration attempt, Ru/ $\gamma$ -Al<sub>2</sub>O<sub>3</sub> appears to exhibit comparable irreversible deactivation in both cases, while the extent of reversible deactivation is greater during LA hydrogenation.

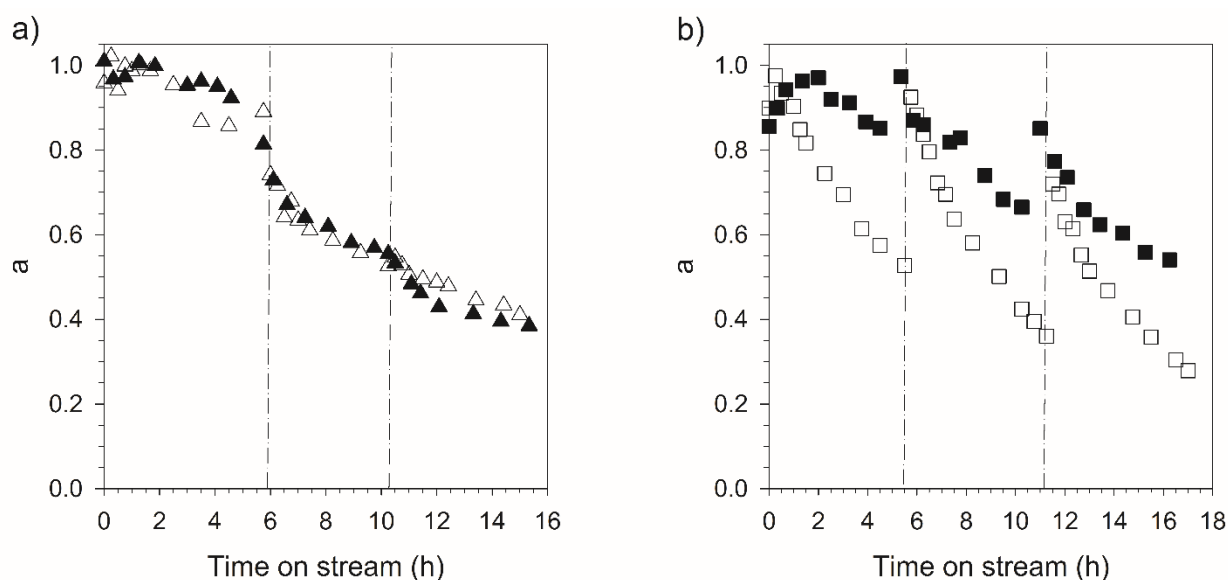


**Figure 4.3** Comparison of hydrogenation activity of Ru supported on (a) SiO<sub>2</sub> and (b)  $\gamma$ -Al<sub>2</sub>O<sub>3</sub>. Open symbols represent LA hydrogenation rates. Filled symbols represent 2-pentanone hydrogenation rates.

A number of phenomena can cause deactivation of supported metals, and the severity of any can be influenced by several factors including the nature of the metal, its interaction with the support, the size of metal clusters, operational parameters, and the environment in which the catalyst is employed. Considering the complexity of catalyst deactivation, direct comparison of the results summarized in Figure 4.2 and Figure 4.3 is difficult. In subsequent sections, we attempt to decouple the observed deactivation pathways and arrive at a set of principles that govern the stability of supported Ru catalysts during aqueous-phase ketone hydrogenation.

### 4.3.3 Irreversible deactivation

Table 4.3 summarizes physicochemical properties of spent catalysts, which were recovered from LA hydrogenation reactors after the period on stream indicated in Figure 4.2. To facilitate comparison and correlation, analogous data are presented for each catalyst in a pristine state. The table further summarizes the percentage of activity irreversibly lost during the on stream period.

**Table 4.3** Comparison of physical and chemical characterization of catalyst samples in fresh and spent states. The table also summarizes the percentage of initial activity that was lost irreversibly during the indicated period on stream.

Sample	TOS (h)	Irr. loss (%)	BET (m <sup>2</sup> /g)		BJH (nm)		CO uptake (μmol/g)		d <sub>p,TEM</sub> (nm) <sup>a</sup>	
			Pre	Post	Pre	Post	Pre	Post	Pre	Post
Ru/γ-Al <sub>2</sub> O <sub>3</sub>	17	17	230	295	5.7	6.9	105	85	1.7 ± 0.1	2.1 ± 0.2
Ru/TiO <sub>2</sub>	16	33	55	48	24.1	27.4	15	9	3.1 ± 0.3	5.1 ± 1.2
Ru/SiO <sub>2</sub> -A	15	47	468	456	5.5	5.5	116	40	2.7 ± 0.1	5.1 ± 0.4
Ru/C-B	25	87	780	770	5.1	5.0	61	11	4.0 ± 0.3	7.3 ± 0.6

a –Confidence intervals calculated at 95%.

From the data in Table 4.3, it is evident that physical properties associated with support structure do not change significantly between fresh and spent catalysts, and no substantial perturbations in surface area and porosity are observed in any system. Although support hydrothermal stability is critical in aqueous-phase catalysis [39, 41], support degradation does not appear to underlie irreversible deactivation in this study.

The absence of any phase change to the support material as a result of the hydrothermal conditions employed in the study was confirmed using powder X-ray diffraction (XRD). XRD patterns do not show a significant change in support structure between pre-and post-reaction samples. Though not particularly meaningful for amorphous C and SiO<sub>2</sub>, retention of initial diffraction patterns for γ-Al<sub>2</sub>O<sub>3</sub> and TiO<sub>2</sub> indicates that phase changes, which are realistic for

these materials in water [59, 60], are sufficiently slow at 323K that they are not observed over the reported times on stream.

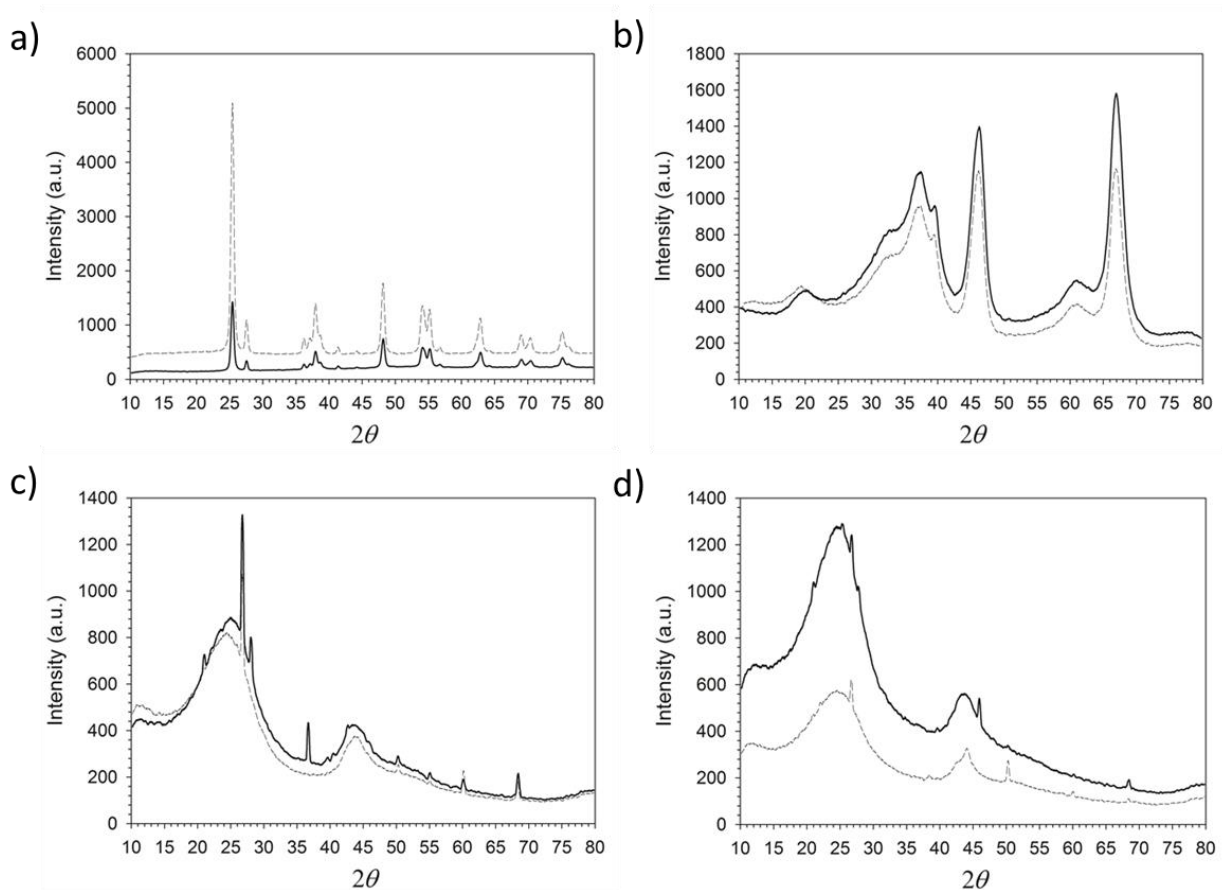


**Figure 4.4** PXRD of a) 0.4% Ru/P25, b) 1.3% Ru/ $\gamma$ - $\text{Al}_2\text{O}_3$ , c) 0.5% Ru/C, d) 5% Ru/C. Solid line indicates fresh catalyst and dashed indicates spent catalyst

Given the locality of measuring particle size using a microscopy technique, the diffraction patterns were also used to detect the presence of any larger particles that could have been missed. With the exception of Ru supported on  $\text{SiO}_2$ , no peaks that could be assigned to Ru were detected. In the case of the spent of Ru/ $\text{SiO}_2$ , diffraction peaks that can be assigned to metallic Ru ( $2\theta = 38.4^\circ, 42.2^\circ, 44.0^\circ, 58.3^\circ, 69.4^\circ$ ) [61] were found. Similarly larger particles were observed using transmission electron microscopy (TEM) in excess of 10nm, compared to a

starting average diameter of 2.7 nm in the fresh catalyst. This is in line with the Ru particles supported on SiO<sub>2</sub> experienced the greatest degree of sintering allowing larger particles to be detected by XRD.

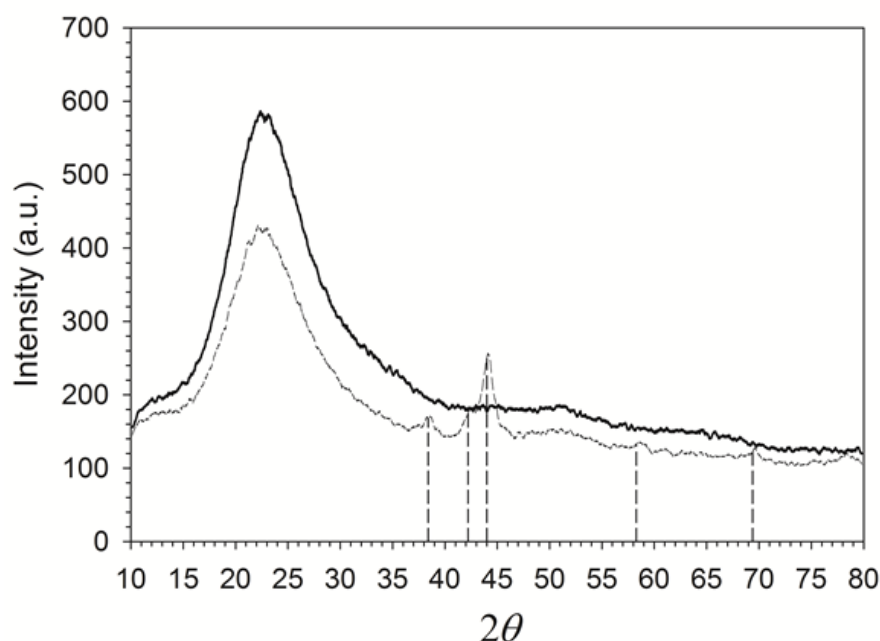


**Figure 4.5** PXRD of 2.7% Ru/SiO<sub>2</sub>. Solid line indicates fresh catalyst and dashed indicates spent catalyst

Examining CO uptake in fresh and spent catalysts (Table 4.3), it is apparent that irreversible decreases in hydrogenation activity correlate with a decrease in CO uptake, which we take to indicate a loss of accessible Ru surface sites with time on stream. Previously, we analyzed reactor effluents from LA hydrogenation over 5 wt% Ru/C via ICP-MS, and we found no evidence of metal leaching [21]. This is consistent with multiple prior accounts describing the insolubility of zerovalent Ru in water [26, 27, 54, 62]. We thus conclude that Ru leaching does not occur in the systems described here—at least not on scales commensurate with the observed activity losses. As such, irreversible activity losses are most likely attributed either to particle sintering or to irreversible site poisoning through binding of species that block CO uptake and

cannot be removed by a reductive treatment (e.g., hard coke, metal ions). Irreversible poisoning is certainly realistic in this system. Data were obtained in stainless steel reactors under acidic conditions where dissolution of metal ions from reactor walls is possible and could contribute to catalyst deactivation. Further, carbon deposition can occur on metal surfaces [63]. Poisoning and irreversible coking may occur under our reaction conditions. Although we are not able to definitively exclude either as a potential cause of irreversible deactivation, we believe that neither contributes significantly to irreversible deactivation in the present study. Specifically, data in Table 4.3 clearly indicate particle growth as the source of reduced CO uptake with time on stream. For all samples exhibiting irreversible deactivation, average Ru particle diameters are observed to increase via TEM. Moreover, Figure 4.6 illustrates that normalized decreases in CO uptake between fresh and spent samples agree well with dispersion losses calculated based on average particle diameters. We therefore conclude that metal particle growth, as opposed to poison or coke deposition, is the primary source of irreversible deactivation in this system. Although sintering of noble metal particles under reducing environments is typically considered to be a high temperature phenomenon [63], this is generally true only for gas-phase treatments. In a bulk condensed phase—especially in water—metal nanoparticles have been demonstrated to sinter under mild conditions [26, 30, 40, 46, 64-66]. Thus, despite the low temperature employed

in this study, Ru particle growth is a realistic concern. It occurs rapidly, and it contributes substantially to irrecoverable activity losses during aqueous-phase ketone hydrogenation.

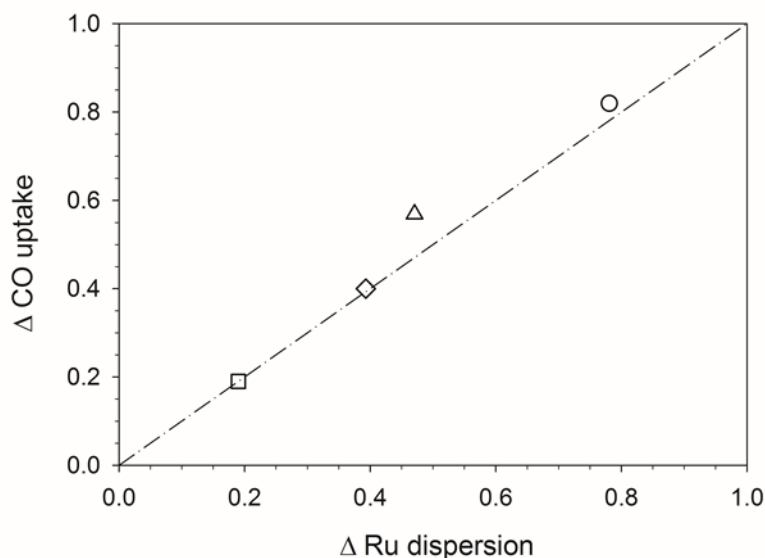


**Figure 4.6** Loss in irreversible CO uptake in comparison to inverse of particle growth. Line of parity indicated by dashed line. (◇) Ru/TiO<sub>2</sub>, (○) Ru/C-B, (Δ) Ru/SiO<sub>2</sub>-A, (□) Ru/γ-Al<sub>2</sub>O<sub>3</sub>. Initial particle diameters for Ru/TiO<sub>2</sub>, Ru/SiO<sub>2</sub>, and Ru/γ-Al<sub>2</sub>O<sub>3</sub> were determined by TEM, and the initial particle diameter of Ru/C-B was calculated from irreversible CO uptake. All final particle diameters were determined by TEM.

The extent of sintering in the period on stream varies considerably between supports, and our results suggest that particle growth is least severe on γ-Al<sub>2</sub>O<sub>3</sub> and occurs to larger extents on SiO<sub>2</sub>, TiO<sub>2</sub>, and C (Table 4.3). Since initial catalyst preparations differ in particle size, on-stream periods vary between samples, and we did not determine equilibrium particle size distributions, it is difficult to make a rigorous determination of whether the supports tested offer varying degrees of “sinter resistance” in aqueous media. Nevertheless, over relatively short times on stream, rates of irreversible deactivation appear first order for all samples (Figure 4.7), and we can make an empirical comparison of sintering kinetics on each support. Assuming that the rate of

sintering scales directly with metal dispersion, irreversible deactivation can be modeled using Eq. (5).

$$\left(\frac{da}{dt}\right)_{irr} = -k_s \cdot D \quad (5)$$

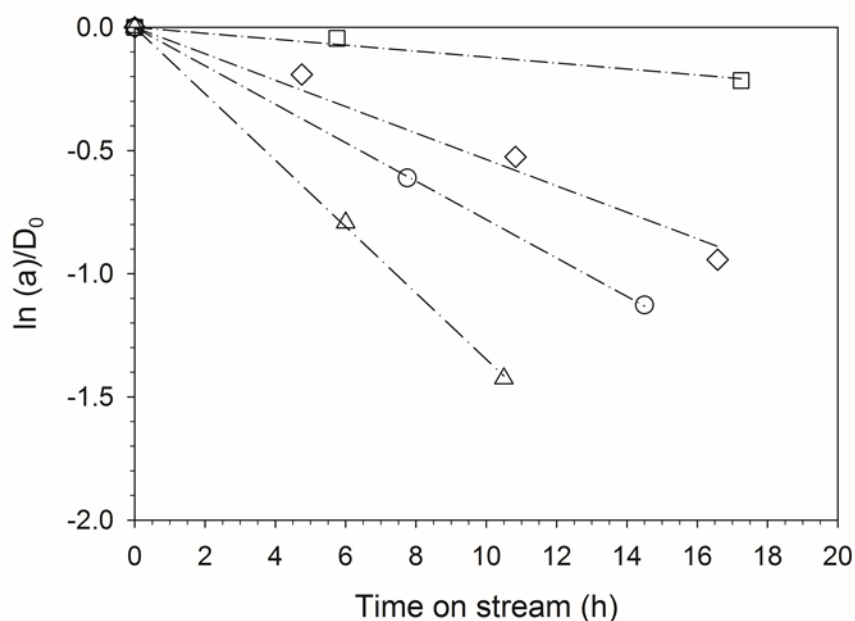


**Figure 4.7** Illustration of first order (irreversible) decay in activity with time on stream for Ru supported on (Δ) Ru/SiO<sub>2</sub>-A, (○) Ru/C-B, (◇) Ru/TiO<sub>2</sub>, and (□) Ru/γ-Al<sub>2</sub>O<sub>3</sub>. Here, irreversible losses are attributed to particle sintering.

Here,  $a$  is the catalyst activity defined as its rate of hydrogenation at a given time normalized by its rate of hydrogenation at zero time,  $k_s$  is a rate constant that captures sintering kinetics, and  $D$  is the metal dispersion at a given time on stream. Since this analysis considers only irreversible activity losses attributed to sintering, and hydrogenation rates should scale linearly with metal dispersion, one may assume that the current activity of a catalyst is given by the ratio of  $D/D_0$ , where  $D_0$  is the metal dispersion of the pristine catalyst calculated from irreversible CO uptake. Solution of the resulting differential equation yields Eq. (6), which captures the observed first

order decay in activity. Importantly, this treatment empirically corrects for differences in initial metal dispersion such that sintering kinetics can be quantitatively discussed for all samples despite variation in initial Ru particle size.

$$\ln(a)_{irr} = -k_s \cdot D_0 \cdot t \quad (6)$$

Irreversible activity losses during LA hydrogenation were determined from initial hydrogenation rates measured after each catalyst regeneration shown in Figure 4.2. From these data, sintering constants were estimated via least squares regression using the model given by Eq. (6). Model fits are illustrated as dashed lines in Figure 4.7, and parameter estimates are given in Table 4.4. For comparison, sintering constants estimated from irreversible activity losses during 2-pentanone hydrogenation over Ru/ $\gamma$ -Al<sub>2</sub>O<sub>3</sub> and Ru/SiO<sub>2</sub>-A are additionally included in Table 4.4.

**Table 4.4** Estimated sintering constants for various supported Ru catalysts at 90% confidence level.

Entry	Sample	Ketone	$k_s$ (min <sup>-1</sup> )
1	Ru/ $\gamma$ -Al <sub>2</sub> O <sub>3</sub>	LA	0.72 ± 0.18
2	Ru/ $\gamma$ -Al <sub>2</sub> O <sub>3</sub>	2-Pentanone	0.74 ± 0.67
3	Ru/SiO <sub>2</sub> -A	LA	8.09 ± 0.20
4	Ru/SiO <sub>2</sub> -A	2-Pentanone	8.47 ± 1.87
5	Ru/TiO <sub>2</sub>	LA	3.21 ± 0.40
6	Ru/C-B	LA	4.44 ± 0.15

Considering entries 1, 3, 5, and 6, it is evident that the rate of Ru particle sintering during aqueous phase ketone hydrogenation varies with the support, decreasing in the order SiO<sub>2</sub> > C ~ TiO<sub>2</sub> >  $\gamma$ -Al<sub>2</sub>O<sub>3</sub>. Comparison of sintering constants estimated during LA and 2-pentanone hydrogenation over Ru/ $\gamma$ -Al<sub>2</sub>O<sub>3</sub> (Entries 1 and 2) and Ru/SiO<sub>2</sub> (Entries 3 and 4) reveals that, for a

given support, sintering rates are nearly identical. This suggests that particle growth is not exacerbated by acidity or interactions with LA (at 0.5M); rather, it appears to be driven by the presence of liquid water and governed by the support. Consistent with observations from high-temperature treatments in H<sub>2</sub>,  $\gamma$ -Al<sub>2</sub>O<sub>3</sub> provides the best retention of initial metal dispersion while particles supported on SiO<sub>2</sub> appear most sinter-prone [63, 67].

#### 4.3.4 Reversible deactivation

Figure 4.8 illustrates the extent of reversible deactivation in each system as a function of time on stream. Reversible deactivation profiles were generated by correcting activity profiles shown in Figure 4.2 and Figure 4.3 for irreversible deactivation using Eq. (7), which is based upon a first order sintering model, and kinetic parameters summarized in Table 4.4.

$$\ln(a_{rev}) = \ln(a_{overall}) - k_s \cdot D_0 \cdot t \quad (7)$$

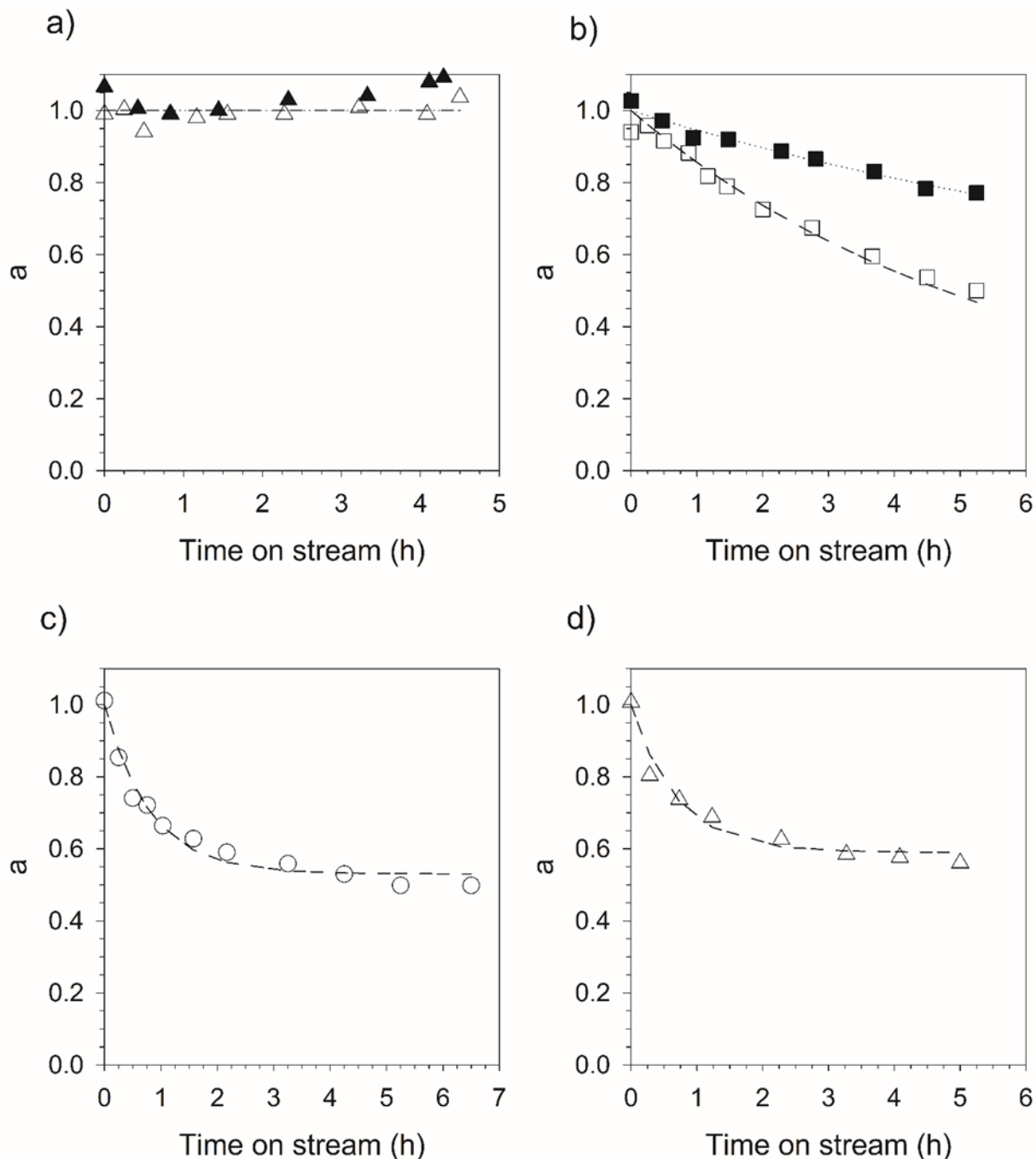


**Figure 4.8** Profiles of reversible activity loss with time on stream observed for (a) Ru/SiO<sub>2</sub>-A, (b) Ru/ $\gamma$ -Al<sub>2</sub>O<sub>3</sub>, (c) Ru/TiO<sub>2</sub> and (d) Ru/C-B. Open symbols represent rates of LA hydrogenation. Filled symbols represent rates of 2-pentanone hydrogenation. Reversible deactivation profiles were obtained by correcting activity profiles shown in Figures 2 and 3 for irreversible deactivation due to particle sintering.

As observed for sintering, the extent of reversible deactivation during LA hydrogenation over Ru varies with the identity of the support. At the extremes, Ru/SiO<sub>2</sub> displays no quantifiable

reversible deactivation (Figure 4.8a), whereas the activity of Ru/ $\gamma$ -Al<sub>2</sub>O<sub>3</sub> reversibly decays to 50% of its initial value within 5 hours on stream under identical conditions (Figure 4.8b). Interestingly, the extent of reversible deactivation further varies with the nature of the ketone. For example, reversible deactivation is not observed during either 2-pentanone hydrogenation or LA hydrogenation over Ru/SiO<sub>2</sub> (Figure 4.8a). In contrast, the difference in reversible activity loss for the analogous experiments over Ru/ $\gamma$ -Al<sub>2</sub>O<sub>3</sub> is considerable (Figure 4.8b). These observations suggest that reversible deactivation is tied both to the identity of the support and to the presence of the carboxylic acid functionality of LA.

Reversible deactivation profiles are captured by a first order model (Eq. 8) that allows for activity to approach a non-zero steady state value.

$$\frac{da_{rev}}{dt} = -k_{rev} \cdot (a_{rev} - a_{\infty}) \quad (8)$$

This model provides two variable parameters that capture the kinetic approach to steady state ( $k_{rev}$ ) and the activity remaining at steady state ( $a_{\infty}$ ). Optimal parameter estimates for Ru/ $\gamma$ -Al<sub>2</sub>O<sub>3</sub>, Ru/TiO<sub>2</sub>, and Ru/C are summarized in Table 4.5, and their values were used to generate model fits illustrated in Figure 4.8. Ru/SiO<sub>2</sub> displayed no quantifiable reversible deactivation during either LA or 2-pentanone hydrogenation, and parameter values were accordingly not estimated for these systems. Reversible deactivation occurs quickly relative to sintering, which is indicated by first order decay constants that are generally an order of magnitude larger than sintering constants given in Table 4.4. Further, the extent of reversible deactivation during LA hydrogenation, indicated by the value of  $a_{\infty}$ , decreases with support identity in the order Al<sub>2</sub>O<sub>3</sub> > TiO<sub>2</sub> ~ C > SiO<sub>2</sub>.

**Table 4.5** Summary of estimated reversible deactivation parameters during the hydrogenation of LA and 2-pentanone over Ru on various supports.

Sample	Ketone	$k_{rev}(\text{min}^{-1})$	$a_{\infty}^a$
Ru/SiO <sub>2</sub> -A	LA	0	1.0
Ru/ $\gamma$ -Al <sub>2</sub> O <sub>3</sub>	LA	11	0.13 $\pm$ 0.35
Ru/TiO <sub>2</sub>	LA	86	0.59 $\pm$ 0.05
Ru/C-B	LA	74	0.53 $\pm$ 0.03
Ru/SiO <sub>2</sub> -A	2-pentanone	0	1.0
Ru/ $\gamma$ -Al <sub>2</sub> O <sub>3</sub>	2-pentanone	6	0.43 $\pm$ 0.79

a- Calculated at 95% confidence level

Given that Ru/ $\gamma$ -Al<sub>2</sub>O<sub>3</sub> exhibits more pronounced (reversible) deactivation during LA hydrogenation than it does during 2-pentanone hydrogenation, it appears that carboxylic acids exacerbate this mode of instability. To further probe this, the on-stream stability of Ru/ $\gamma$ -Al<sub>2</sub>O<sub>3</sub> was monitored during 2-pentanone hydrogenation at 323K and 24 bar H<sub>2</sub> in the presence of propanoic acid (0.5M, pH=2.59). The results of this experiment are presented in Figure 4.9. Whereas Ru/ $\gamma$ -Al<sub>2</sub>O<sub>3</sub> is relatively stable during 2-pentanone hydrogenation (Figure 4.3), it deactivates rapidly in the presence of 0.5M propanoic acid (Figure 4.9). During this experiment, 2-pentanol was the only hydrogenation product observed; no propanoic acid hydrogenation products were detected by GC-MS. Upon removal of propanoic acid, the rate of 2-pentanone hydrogenation improves, returning to 54% of the original activity within 2 h. The aqueous flow was then stopped, and the catalyst was left under H<sub>2</sub> (100 ml min<sup>-1</sup>, 323K, 15h) to evaluate the extent of reversibility. Upon re-introducing an aqueous, acid-free 2-pentanone feed, the catalyst achieved 88% of its initial activity, with the 12% irrecoverable loss attributed to sintering. Using parameters summarized in Table 4.4, we estimate that, in water, our fresh Ru/ $\gamma$ -Al<sub>2</sub>O<sub>3</sub> sample should lose 5 - 10% of its metal surface area to sintering during its first 7 hours on stream, which agrees with the 12% irreversible loss in activity observed here.

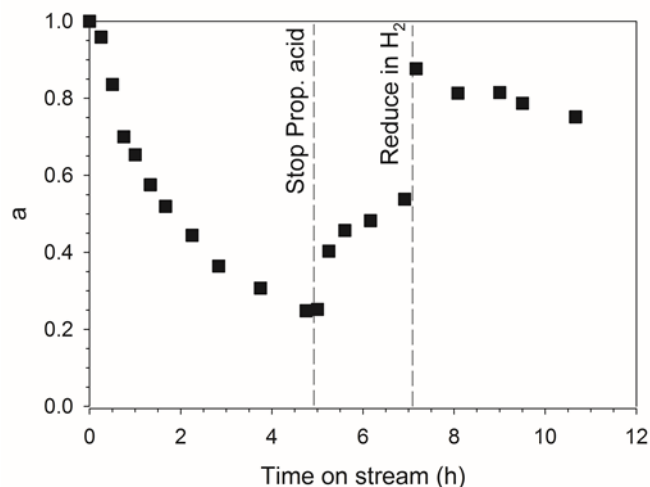


**Figure 4.9** Activity profile of Ru/ $\gamma$ -Al<sub>2</sub>O<sub>3</sub> during the hydrogenation of 2-pentanone in the presence of propanoic acid.

#### 4.4 Discussion

Results summarized in the preceding sections demonstrate that Ru nanoparticles supported on various carbons and solid oxides display comparable intrinsic activity toward aqueous-phase ketone hydrogenation but are susceptible to varying extents of irreversible and reversible deactivation. The former is support-dependent and attributed to particle sintering, which is accelerated in bulk water relative to bulk gas phases. The mechanism of the latter is unclear, but its severity depends both on the nature of the support and the presence of carboxylic acids.

With respect to sintering,  $\gamma$ -Al<sub>2</sub>O<sub>3</sub> appears to stabilize Ru dispersion in water relatively well compared to SiO<sub>2</sub>, TiO<sub>2</sub>, and C. Electronegativity has been previously employed to explain different sintering extents on various supports [67, 68], and we build on this argument here. M-O-Ru bonds, in which M is the support cation (Si<sup>4+</sup>, Ti<sup>4+</sup>, or Al<sup>3+</sup>), change character with the nature of M. Specifically, as support cations become increasingly electronegative (e.g., Si<sup>4+</sup>), the electron density on the oxygen is decreased, and one may expect less favorable M-O-Ru

interactions. In contrast, for support cations with relatively low electronegativities (e.g.,  $\text{Ti}^{4+}$ ,  $\text{Al}^{3+}$ ), the oxygen of the M-O-Ru bond should have a relatively high electron density, and one may expect more favorable Ru-support interactions. Our data generally agrees with this interpretation; however, instead of relating particle sintering to cation electronegativity, we observe a stronger correlation with the mean electronegativity of the bulk oxide, which can be calculated as the geometric mean of the electronegativity of the metal cation and oxygen in the oxide lattice according to Eq. (9) [69]:

$$\chi_{M_xO_y} = [\chi_M^x \cdot \chi_O^y]^{\frac{1}{x+y}} \quad (9)$$

In Eq. (9),  $\chi_j$  is the electronegativity of a given species. As illustrated in Figure 4.10 for  $\gamma\text{-Al}_2\text{O}_3$ ,  $\text{TiO}_2$ , and  $\text{SiO}_2$ , we observe that sintering constants increase as the mean electronegativity of the oxide increases. Based on this correlation, we interpret sinter resistance in the context of Hard-Soft Acid-Base theory. Specifically, solid oxides with low electronegativities (e.g.,  $\gamma\text{-Al}_2\text{O}_3$ ,  $\text{TiO}_2$ ) can be considered relatively soft bases whereas those with high electronegativity (e.g.,  $\text{SiO}_2$ ) may be classified as relatively hard bases. Low-valent Ru is considered a relatively soft acid [70], and it stands to reason that its interactions are more favorable with supports that are softer bases. According to this interpretation, the severity of sintering should decrease on oxide supports in the order  $\text{SiO}_2 > \text{TiO}_2 > \gamma\text{-Al}_2\text{O}_3$ , which is consistent with our observations. Because of its surface heterogeneity, it is difficult to include carbon in a discussion based on support electronegativity; however, the insight that Ru particle stability correlates with electron density of a support surface could aid in developing a sinter-resistant carbon support, provided that the surface functionality of carbon can be controlled during catalyst synthesis and retained under reaction conditions.

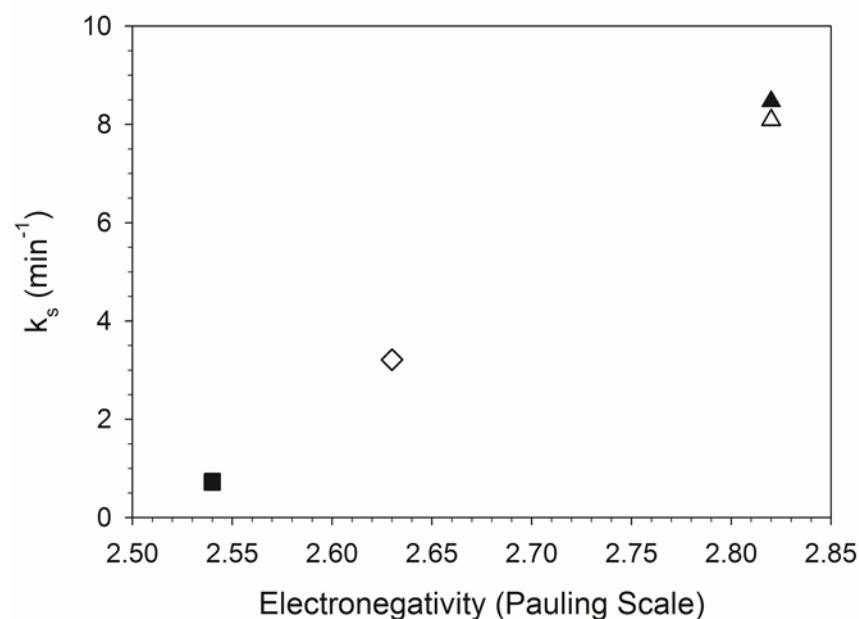


**Figure 4.10** Correlation between sintering constants and electronegativity of a bulk oxide. ( $\diamond$ ) Ru/TiO<sub>2</sub>, ( $\Delta$ ) Ru/SiO<sub>2</sub>-A and ( $\square$ ) Ru/ $\gamma$ -Al<sub>2</sub>O<sub>3</sub>. Open symbols represent sintering rates during LA hydrogenation. Filled symbols represent sintering rates during 2-pentanone hydrogenation

Based on the experimental evidence presented here, we cannot conclusively define a mechanism for reversible deactivation; nonetheless, it is worth examining potential causes. Because activity not lost through sintering can be restored by reductive treatment—although not through thermal treatment in an inert atmosphere—it stands to reason that this mode of deactivation is oxidative in nature. Further, as demonstrated in Figure 4.9, carboxylic acids exacerbate reversible deactivation, suggesting that system pH or carboxylate adsorption may underlie the phenomena. Based on measured turnover frequencies and residence times, we anticipate the reported systems should reach steady state on the scale of minutes, yet we observe that hydrogenation activity continues to decay (reversibly) on the scale of hours.

Considering oxidative phenomena in a bulk aqueous phase, it is possible that water dissociation could result in the formation of bound hydroxyls on Ru surfaces. Surface hydroxyls should be

removed by reduction in dry H<sub>2</sub>, restoring Ru sites to their metallic state. However, one would typically expect adsorption processes to equilibrate quickly such that competitive binding should manifest as a diminished steady state hydrogenation rate rather than a transient decay in hydrogenation rate. Surface science experiments have suggested that dissociative adsorption of water on Ru is an activated process [71, 72]. It is thus possible that water dissociation occurs slowly relative to the adsorption of reactive species such that hydroxyl coverages equilibrate on relatively long time scales, which might explain the gradual decrease in activity with time on stream.

Although surface oxidation via hydroxyl binding is potentially consistent with observed activity profiles, prior reports argue against Ru oxidation under our experimental conditions. Based on a redox potential of -0.5 to -0.7 V for H<sub>2</sub> saturated water [8], Pourbaix diagrams suggest that bulk Ru in aqueous solution is metallic at any pH [73]. Further, Davis has employed in-situ X-Ray absorption spectroscopy to conclude that Ru is zerovalent in H<sub>2</sub> saturated water at 373K, and that it remains fully reduced upon exposure to N<sub>2</sub> saturated water at the same temperature [26]. That said, the above results are most applicable to bulk Ru metal and perhaps less so to Ru surfaces. Without a surface sensitive in situ characterization method (e.g., XPS), it is not possible to either confirm or eliminate oxidation of Ru surface sites as a source of reversible deactivation in this system.

Reversible deactivation during LA hydrogenation is most severe on the least electronegative oxide ( $\gamma$ -Al<sub>2</sub>O<sub>3</sub>) and not detected on the most electronegative oxide (SiO<sub>2</sub>). Thus, in contrast to sintering, reversible deactivation appears to correlate inversely with mean oxide electronegativity. Another property of solid oxides that scales in this fashion is their point of

zero charge (PZC) in aqueous media, and our observations are interpreted further on this basis. Taken relative to solution pH, the PZC of a material is a predictor of its net surface charge [74]. If a material is suspended in a solution that has a pH above its PZC, that material's surface should be, on average, negatively charged. In contrast, if a material is employed in a solution that has a pH below its PZC, that material's surface should be positively charged [75]. Furthermore, as the magnitude of the gap between PZC and solution pH increases,  $|\text{PZC}-\text{pH}|$ , so does the deviation from a net zero surface charge. PZCs for the supports employed here are summarized in Table 4.6. Values for  $\text{SiO}_2$ ,  $\gamma\text{-Al}_2\text{O}_3$ , and  $\text{TiO}_2$  were taken from reference data[76], and the value for C was measured using an equilibrium-based mass titration method [38].

**Table 4.6** Summary of PZC values of the various supports employed

Sample	PZC
Ru/SiO <sub>2</sub> -A	1.8
Ru/ $\gamma$ -Al <sub>2</sub> O <sub>3</sub>	8.8
Ru/TiO <sub>2</sub>	6.3
Ru/C-B	6.6

Under the LA hydrogenation conditions in this study, the initial pH of the aqueous phase was measured at 2.45. At this pH,  $\text{SiO}_2$  should have a net negative surface charge, and all other supports should be positively charged. Interestingly, we observe only irreversible deactivation in Ru/SiO<sub>2</sub>, whereas some portion of the deactivation is always reversible in the remaining three catalysts. These observations suggest that, when supported on positively charged surfaces, Ru will exhibit reversible deactivation during ketone hydrogenation in the presence of carboxylic acids. Moreover,  $\gamma\text{-Al}_2\text{O}_3$  should have a high density of positive surface charges relative to, e.g., TiO<sub>2</sub>, indicating that the severity of reversible deactivation scales with increasing positive

surface charge. This correlation, along with its connection to solution pH and a material's PZC, is illustrated in Figure 4.11.

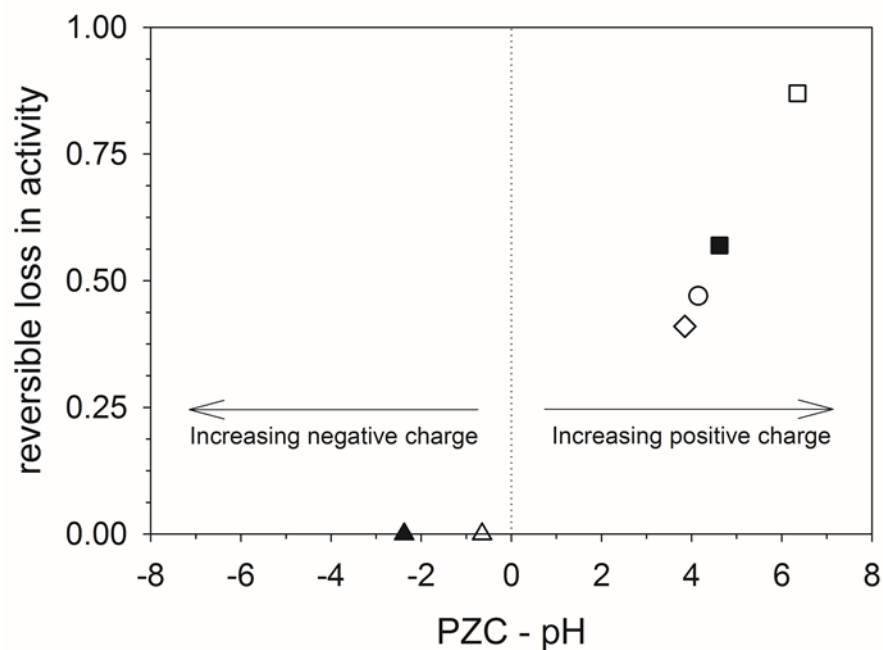


**Figure 4.11** Correlation between PZC (and surface charge) with the extent of reversible deactivation on each Ru-support combination considered during the hydrogenation of levulinic acid and 2-pentanone. ( $\diamond$ ) Ru/TiO<sub>2</sub>, ( $\circ$ ) Ru/C-B, ( $\Delta$ ) Ru/SiO<sub>2</sub>-A, ( $\square$ ) Ru/ $\gamma$ -Al<sub>2</sub>O<sub>3</sub>. Open symbols represent reversible losses during LA hydrogenation. Filled symbols represent reversible losses during 2-pentanone hydrogenation.

A potential explanation is that carboxylate anions present in solution bind favorably to positively charged supports and less so to negatively charged supports. This argument, applied to ionic metal complexes, underlies the strong electrostatic adsorption method of catalyst synthesis [77], and should extend to carboxylate anions under reaction conditions. Accordingly, one might expect high carboxylate coverage on  $\gamma$ -Al<sub>2</sub>O<sub>3</sub> while the surface of SiO<sub>2</sub> remains relatively carboxylate-free under identical conditions. However, it is unlikely that variation in carboxylate coverage on the support should impact the carboxylate coverage on Ru particles, which will ultimately reflect equilibrium with the bulk. That said, it may be possible that ketone and/or H<sub>2</sub>

coordination at Ru sites become increasingly hindered on carboxylate covered supports. If so, one might expect that interfacial sites—and thus smaller Ru particles, such as those as observed on  $\gamma$ -Al<sub>2</sub>O<sub>3</sub>—would be particularly susceptible to this mode of “site blocking.”

#### 4.5 Conclusion

The activity and stability of Ru nanoparticles during the aqueous phase hydrogenation of LA and 2-pentanone was studied across various supports. The intrinsic rate of hydrogenation was found to be invariant with support identity and particle size, indicating a structure insensitive reaction and no strong metal support interactions. Comparable rates of LA and 2-pentanone hydrogenation show that the secondary carboxylic functionality of LA does not perturb the intrinsic rate of ketone hydrogenation over Ru surfaces in water. Deactivation of Ru nanoparticles occurs through reversible and irreversible phenomena, both of which appear to be governed by the mean electronegativity of the support. The irreversible loss in activity is attributed to the sintering of Ru nanoparticles, and it increases in severity with the electronegativity of the support. The source of reversible deactivation could not be conclusively identified; however, it is both support- and carboxylic acid-dependent, and its extent appears to scale with the prevailing surface charge of the support. Hydrogenation of carboxylic acids in water is unique in that the reaction media comprises an electrolyte solution. It stands to reason that electrostatic interactions between dissociated ions and charged surfaces may influence catalyst stability; however, broader consideration of support systems and reaction media is necessary to substantiate any such connections.

The experiments summarized here were carried out under continuous flow conditions, and they reveal time- and media-dependent changes in the catalytic activity of Ru sites during aqueous

phase hydrogenations. Aqueous phase reactions in general and biomass upgrading reactions in particular are most commonly studied in batch vessels, and conclusions regarding catalytic activity are frequently drawn from time-dependent reactor balances and ex-situ characterization methods (e.g., chemisorption). In systems, such as this one, where the catalyst undergoes pronounced structure and/or activity changes on time scales that are comparable to the duration of a typical experiment, rigorous analysis of batch kinetic data is challenging, and it can be difficult to estimate meaningful turnover frequencies from such experiments. Here, we have addressed this issue through estimation of initial rates, but the approach is time consuming and imprecise relative to acquisition of steady state rate data. Reliable, experimental determination of site-specific rates in aqueous phase systems would benefit from the development of an accessible, operando method for active site titration and/or structural analysis under aqueous-phase reaction conditions.

With respect to catalyst design, our observations suggest that multiple aspects of aqueous phase stability are influenced by the electronegativity of the support. Unfortunately, these dependencies appear varied in nature, and tension may exist between, e.g., stabilizing against sintering and stabilizing against reversible deactivation. Although we are not presently able to envision a single Ru-support combination that might satisfy all stability criteria, insights into governing phenomena are useful. For example, composite materials that have distinct, well-defined domains of varying electronegativity may be a compelling choice of support for Ru when it is employed in aqueous media[78]. Further, we emphasize the significance of efforts to stabilize metal dispersion through *physical* encapsulation of nanoclusters using, for example, Atomic Layer Deposition [79-81]. Such approaches may allow one to decouple reversible and irreversible modes of deactivation and thus design a truly resilient catalyst for use in harsh

media. With respect to support selection, it is important to mention that, although we have used solid oxides here to probe fundamental aspects of activity and stability, they are unlikely to be suitable supports under all reaction conditions. For aqueous-phase processes, complexity is added by the fact that one must additionally ensure that support integrity is maintained at high temperatures and pressures.

## 4.6 References

- [1] J.W. Shabaker, G.W. Huber, J.A. Dumesic, Aqueous-phase reforming of oxygenated hydrocarbons over Sn-modified Ni catalysts, *J. Catal.*, 222 (2004) 180-191.
- [2] R.D. Cortright, R.R. Davda, J.A. Dumesic, Hydrogen from catalytic reforming of biomass-derived hydrocarbons in liquid water, *Nature*, 418 (2002) 964-967.
- [3] J.A. Lopez-Ruiz, R.J. Davis, Decarbonylation of heptanoic acid over carbon-supported platinum nanoparticles, *Green Chem.*, 16 (2014) 683-694.
- [4] J.Q. Bond, D. Wang, D.M. Alonso, J.A. Dumesic, Interconversion between  $\gamma$ -valerolactone and pentenoic acid combined with decarboxylation to form butene over silica/alumina, *J. Catal.*, 281 (2011) 290-299.
- [5] A.B. Kellicutt, R. Salary, O.A. Abdelrahman, J.Q. Bond, An examination of the intrinsic activity and stability of various solid acids during the catalytic decarboxylation of [ $\gamma$ ]-valerolactone, *Cat.Sci. Tech.*, 4 (2014) 2267-2279.
- [6] D. Wang, S.H. Hakim, D. Martin Alonso, J.A. Dumesic, A highly selective route to linear alpha olefins from biomass-derived lactones and unsaturated acids, *Chem. Commun.*, 49 (2013) 7040-7042.
- [7] M. Snåre, I. Kubičková, P. Mäki-Arvela, K. Eränen, D.Y. Murzin, Heterogeneous Catalytic Deoxygenation of Stearic Acid for Production of Biodiesel, *Ind. Eng. Chem. Res.*, 45 (2006) 5708-5715.
- [8] I.M. Piskarev, V.A. Ushkanov, N.A. Aristova, P.P. Likhachev, T.S. Myslivets, Establishment of the redox potential of water saturated with hydrogen, *BIOPHYSICS*, 55 (2010) 13-17.
- [9] R.M. West, Z.Y. Liu, M. Peter, J.A. Dumesic, Liquid Alkanes with Targeted Molecular Weights from Biomass-Derived Carbohydrates, *ChemSusChem*, 1 (2008) 417-424.
- [10] B.M. Moreno, N. Li, J. Lee, G.W. Huber, M.T. Klein, Modeling aqueous-phase hydrodeoxygenation of sorbitol over Pt/SiO<sub>2</sub>-Al<sub>2</sub>O<sub>3</sub>, *RSC Adv.*, 3 (2013) 23769-23784.
- [11] G.W. Huber, J.N. Chheda, C.J. Barrett, J.A. Dumesic, Production of Liquid Alkanes by Aqueous-Phase Processing of Biomass-Derived Carbohydrates, *Science*, 308 (2005) 1446-1450.
- [12] G.W. Huber, J.W. Shabaker, S.T. Evans, J.A. Dumesic, Aqueous-phase reforming of ethylene glycol over supported Pt and Pd bimetallic catalysts, *Appl. Catal., B*, 62 (2006) 226-235.
- [13] E.L. Kunkes, D.A. Simonetti, J.A. Dumesic, W.D. Pyrz, L.E. Murillo, J.G. Chen, D.J. Buttrely, The role of rhenium in the conversion of glycerol to synthesis gas over carbon supported platinum-rhenium catalysts, *J. Catal.*, 260 (2008) 164-177.
- [14] J.W. Shabaker, R.R. Davda, G.W. Huber, R.D. Cortright, J.A. Dumesic, Aqueous-phase reforming of methanol and ethylene glycol over alumina-supported platinum catalysts, *J. Catal.*, 215 (2003) 344-352.
- [15] T. van Haasterecht, C.C.I. Ludding, K.P. de Jong, J.H. Bitter, Toward stable nickel catalysts for aqueous phase reforming of biomass-derived feedstock under reducing and alkaline conditions, *J. Catal.*, 319 (2014) 27-35.
- [16] H.Y. Luo, D.F. Consoli, W.R. Gunther, Y. Román-Leshkov, Investigation of the reaction kinetics of isolated Lewis acid sites in Beta zeolites for the Meerwein-Ponndorf-Verley reduction of methyl levulinate to  $\gamma$ -valerolactone, *J. Catal.*, 320 (2014) 198-207.

- [17] M. Chia, J.A. Dumesic, Liquid-phase catalytic transfer hydrogenation and cyclization of levulinic acid and its esters to [gamma]-valerolactone over metal oxide catalysts, *Chem. Commun.*, 47 (2011) 12233-12235.
- [18] J. Jae, E. Mahmoud, R.F. Lobo, D.G. Vlachos, Cascade of Liquid-Phase Catalytic Transfer Hydrogenation and Etherification of 5-Hydroxymethylfurfural to Potential Biodiesel Components over Lewis Acid Zeolites, *ChemCatChem*, 6 (2014) 508-513.
- [19] J.D. Lewis, S. Van de Vyver, A.J. Crisci, W.R. Gunther, V.K. Michaelis, R.G. Griffin, Y. Román-Leshkov, A Continuous Flow Strategy for the Coupled Transfer Hydrogenation and Etherification of 5-(Hydroxymethyl)furfural using Lewis Acid Zeolites, *ChemSusChem*, 7 (2014) 2255-2265.
- [20] L. Bui, H. Luo, W.R. Gunther, Y. Román-Leshkov, Domino Reaction Catalyzed by Zeolites with Brønsted and Lewis Acid Sites for the Production of  $\gamma$ -Valerolactone from Furfural, *Angew. Chem. Int. Ed.*, 52 (2013) 8022-8025.
- [21] O.A. Abdelrahman, A. Heyden, J.Q. Bond, Analysis of Kinetics and Reaction Pathways in the Aqueous-Phase Hydrogenation of Levulinic Acid To Form  $\gamma$ -Valerolactone over Ru/C, *ACS Catal.*, 4 (2014) 1171-1181.
- [22] L.E. Manzer, Catalytic synthesis of alpha-methylene-gamma-valerolactone: a biomass-derived acrylic monomer, *Appl. Catal., A*, 272 (2004) 249-256.
- [23] Z.J. Wu, S.H. Ge, C.X. Ren, M.H. Zhang, A. Yip, C.M. Xu, Selective conversion of cellulose into bulk chemicals over Bronsted acid-promoted ruthenium catalyst: one-pot vs. sequential process, *Green Chemistry*, 14 (2012) 3336-3343.
- [24] L. Deng, Y. Zhao, J.A. Li, Y. Fu, B. Liao, Q.X. Guo, Conversion of Levulinic Acid and Formic Acid into gamma-Valerolactone over Heterogeneous Catalysts, *ChemSusChem*, 3 (2010) 1172-1175.
- [25] R. Luque, J.H. Clark, Water-tolerant Ru-Starbon (R) materials for the hydrogenation of organic acids in aqueous ethanol, *Catal. Commun.*, 11 (2010) 928-931.
- [26] E.P. Maris, K.W. C, O. Vladimir, D.R. J, Metal Particle Growth during Glucose Hydrogenation over Ru/SiO<sub>2</sub> Evaluated by X-ray Absorption Spectroscopy and Electron Microscopy, *J. Phys. Chem. B*, 110 (2006) 7869-7876.
- [27] B.J. Arena, Deactivation of ruthenium catalysts in continuous glucose hydrogenation, *Appl. Catal., A*, 87 (1992) 219-229.
- [28] K. Yan, J. Liao, X. Wu, X. Xie, A noble-metal free Cu-catalyst derived from hydrotalcite for highly efficient hydrogenation of biomass-derived furfural and levulinic acid, *RSC Adv.*, 3 (2013) 3853-3856.
- [29] A.M. Hengne, C.V. Rode, Cu-ZrO<sub>2</sub> nanocomposite catalyst for selective hydrogenation of levulinic acid and its ester to [gamma]-valerolactone, *Green Chem.*, 14 (2012) 1064-1072.
- [30] Y. Wang, S. Van de Vyver, K.K. Sharma, Y. Roman-Leshkov, Insights into the stability of gold nanoparticles supported on metal oxides for the base-free oxidation of glucose to gluconic acid, *Green Chem.*, 16 (2014) 719-726.
- [31] D.J. Braden, C.A. Henao, J. Heltzel, C.C. Maravelias, J.A. Dumesic, Production of liquid hydrocarbon fuels by catalytic conversion of biomass-derived levulinic acid, *Green Chemistry*, 13 (2011) 1755-1765.
- [32] J.Q. Bond, A.A. Upadhye, H. Olcay, G.A. Tompsett, J. Jae, R. Xing, D.M. Alonso, D. Wang, T. Zhang, R. Kumar, A. Foster, S.M. Sen, C.T. Maravelias, R. Malina, S.R.H. Barrett, R. Lobo, C.E. Wyman, J.A. Dumesic, G.W. Huber, Production of renewable jet fuel range alkanes

and commodity chemicals from integrated catalytic processing of biomass, *Energy Environ. Sci.*, 7 (2014) 1500-1523.

[33] M.S. Ide, D.D. Falcone, R.J. Davis, On the deactivation of supported platinum catalysts for selective oxidation of alcohols, *J. Catal.*, 311 (2014) 295-305.

[34] R.D. Cortright, M. Sanchez-Castillo, J.A. Dumesic, Conversion of biomass to 1,2-propanediol by selective catalytic hydrogenation of lactic acid over silica-supported copper, *Appl. Catal., B*, 39 (2002) 353-359.

[35] Z. Zhang, J.E. Jackson, D.J. Miller, Aqueous-phase hydrogenation of lactic acid to propylene glycol, *Appl. Catal., A*, 219 (2001) 89-98.

[36] M.A.N. Santiago, M.A. Sánchez-Castillo, R.D. Cortright, J.A. Dumesic, Catalytic Reduction of Acetic Acid, Methyl Acetate, and Ethyl Acetate over Silica-Supported Copper, *J. Catal.*, 193 (2000) 16-28.

[37] E.L. Kunkes, D.A. Simonetti, R.M. West, J.C. Serrano-Ruiz, C.A. Gärtner, J.A. Dumesic, Catalytic Conversion of Biomass to Monofunctional Hydrocarbons and Targeted Liquid-Fuel Classes, *Science*, 322 (2008) 417-421.

[38] A.H. Van Pelt, O.A. Simakova, S.M. Schimming, J.L. Ewbank, G.S. Foo, E.A. Pidko, E.J.M. Hensen, C. Sievers, Stability of functionalized activated carbon in hot liquid water, *Carbon*, 77 (2014) 143-154.

[39] H.N. Pham, A.E. Anderson, R.L. Johnson, K. Schmidt-Rohr, A.K. Datye, Improved Hydrothermal Stability of Mesoporous Oxides for Reactions in the Aqueous Phase, *Angew. Chem. Int. Ed.*, 51 (2012) 13163-13167.

[40] W.C. Ketchie, E.P. Maris, R.J. Davis, In-situ X-ray Absorption Spectroscopy of Supported Ru Catalysts in the Aqueous Phase, *Chem. Mater.*, 19 (2007) 3406-3411.

[41] H. Xiong, H.N. Pham, A.K. Datye, Hydrothermally stable heterogeneous catalysts for conversion of biorenewables, *Green Chem.*, 16 (2014) 4627-4643.

[42] H. Xiong, H.N. Pham, A.K. Datye, A facile approach for the synthesis of niobia/carbon composites having improved hydrothermal stability for aqueous-phase reactions, *J. Catal.*, 302 (2013) 93-100.

[43] W. Luo, M. Sankar, A.M. Beale, Q. He, C.J. Kiely, P.C.A. Bruijninx, B.M. Weckhuysen, High performing and stable supported nano-alloys for the catalytic hydrogenation of levulinic acid to  $\gamma$ -valerolactone, *Nat. Commun.*, 6 (2015).

[44] S.G. Wettstein, J.Q. Bond, D.M. Alonso, H.N. Pham, A.K. Datye, J.A. Dumesic, RuSn bimetallic catalysts for selective hydrogenation of levulinic acid to  $\gamma$ -valerolactone, *Appl. Catal., B*, 117-118 (2012) 321-329.

[45] S. Lowell, *Characterization of Porous Solids and Powders: Surface Area, Pore Size and Density*, Springer, 2004.

[46] J.H. Vleeming, B.F.M. Kuster, G.B. Marin, F. Oudet, P. Courtine, Graphite-Supported Platinum Catalysts: Effects of Gas and Aqueous Phase Treatments, *J. Catal.*, 166 (1997) 148-159.

[47] P. Reyes, M.E. König, G. Pecchi, I. Concha, M. López Granados, J.L.G. Fierro, o-xylene hydrogenation on supported ruthenium catalysts, *Catalysis Letters*, 46 (1997) 71-75.

[48] G. Neri, L. Mercadante, A. Donato, A.M. Visco, S. Galvagno, Influence of Ru precursor, support and solvent in the hydrogenation of citral over ruthenium catalysts, *Catalysis Letters*, 29 (1994) 379-386.

[49] A. Basińska, L. Kępiński, F. Domka, The effect of support on WGS activity of ruthenium catalysts, *Appl. Catal., A*, 183 (1999) 143-153.

- [50] N.V. Pavlenko, A.I. Tripol'skii, G.I. Golodets, Vapor-phase hydrogenation of acetone on applied metals of the platinum group, *Theor Exp Chem*, 22 (1987) 667-675.
- [51] B. Sen, M.A. Vannice, Metal-support effects on acetone hydrogenation over platinum catalysts, *J. Catal.*, 113 (1988) 52-71.
- [52] F. Rositani, S. Galvagno, Z. Poltarzewski, P. Staiti, P.L. Antonucci, Kinetics of acetone hydrogenation over Pt/Al<sub>2</sub>O<sub>3</sub> catalysts, *J. Chem. Technol. Biotechnol.*, 35 (1985) 234-240.
- [53] H. Wan, A. Vitter, R.V. Chaudhari, B. Subramaniam, Kinetic investigations of unusual solvent effects during Ru/C catalyzed hydrogenation of model oxygenates, *J. Catal.*, 309 (2014) 174-184.
- [54] H.G. Manyar, D. Weber, H. Daly, J.M. Thompson, D.W. Rooney, L.F. Gladden, E. Hugh Stitt, J. Jose Delgado, S. Bernal, C. Hardacre, Deactivation and regeneration of ruthenium on silica in the liquid-phase hydrogenation of butan-2-one, *J. Catal.*, 265 (2009) 80-88.
- [55] R.J. Madon, M. Boudart, Experimental criterion for the absence of artifacts in the measurement of rates of heterogeneous catalytic reactions, *Ind. Eng. Chem. Fundam.*, 21 (1982) 438-447.
- [56] R.M. Koros, E.J. Nowak, A diagnostic test of the kinetic regime in a packed bed reactor, *Chem. Eng. Sci.*, 22 (1967) 470.
- [57] S.J. Tauster, Strong metal-support interactions, *Acc. Chem. Res.*, 20 (1987) 389-394.
- [58] S.J. Tauster, S.C. Fung, R.L. Garten, Strong metal-support interactions. Group 8 noble metals supported on titanium dioxide, *JACS*, 100 (1978) 170-175.
- [59] G. Lefèvre, M. Duc, P. Lepeut, R. Caplain, M. Fédoroff, Hydration of  $\gamma$ -Alumina in Water and Its Effects on Surface Reactivity, *Langmuir*, 18 (2002) 7530-7537.
- [60] J. Duan, Y.T. Kim, H. Lou, G.W. Huber, Hydrothermally stable regenerable catalytic supports for aqueous-phase conversion of biomass, *Catalysis Today*, 234 (2014) 66-74.
- [61] X. Ni, B. Zhang, C. Li, M. Pang, D. Su, C.T. Williams, C. Liang, Microwave-assisted green synthesis of uniform Ru nanoparticles supported on non-functional carbon nanotubes for cinnamaldehyde hydrogenation, *Catal. Commun.*, 24 (2012) 65-69.
- [62] W. Luo, U. Deka, A.M. Beale, E.R.H. van Eck, P.C.A. Bruijninx, B.M. Weckhuysen, Ruthenium-catalyzed hydrogenation of levulinic acid: Influence of the support and solvent on catalyst selectivity and stability, *J. Catal.*, 301 (2013) 175-186.
- [63] C.H. Bartholomew, Mechanisms of catalyst deactivation, *Appl. Catal., A*, 212 (2001) 17-60.
- [64] A. Doudah, P. Marécot, S. Labruquère, J. Barbier, Stability of supported platinum catalysts in aqueous phase under hydrogen atmosphere, *Appl. Catal., A*, 210 (2001) 111-120.
- [65] A. Doudah, P. Marécot, J. Barbier, Toward a better understanding of the stability of supported platinum catalysts in aqueous phase under hydrogen atmosphere at room temperature, *Appl. Catal., A*, 225 (2002) 11-19.
- [66] M. Besson, P. Gallezot, Deactivation of metal catalysts in liquid phase organic reactions, *Catal. Today*, 81 (2003) 547-559.
- [67] Y. Nagai, T. Hirabayashi, K. Dohmae, N. Takagi, T. Minami, H. Shinjoh, S.i. Matsumoto, Sintering inhibition mechanism of platinum supported on ceria-based oxide and Pt-oxide-support interaction, *J. Catal.*, 242 (2006) 103-109.
- [68] K. Asakura, Y. Iwasawa, Surface structure and catalysis for CO hydrogenation of the supported Ru species derived from the Ru<sub>3</sub>(CO)<sub>12</sub> inorganic oxides, *J. Chem. Soc., Faraday Trans.*, 86 (1990) 2657-2662.
- [69] M.A. Butler, D.S. Ginley, Prediction of Flatband Potentials at Semiconductor-Electrolyte Interfaces from Atomic Electronegativities, *J. Electrochem. Soc.*, 125 (1978) 228-232.

- [70] R.G. Pearson, Hard and soft acids and bases, HSAB, part 1: Fundamental principles, *J. Chem. Educ.*, 45 (1968) 581.
- [71] K. Andersson, A. Gómez, C. Glover, D. Nordlund, H. Öström, T. Schiros, O. Takahashi, H. Ogasawara, L.G.M. Pettersson, A. Nilsson, Molecularly intact and dissociative adsorption of water on clean Cu(1 1 0): A comparison with the water/Ru(0 0 1) system, *Surf. Sci.*, 585 (2005) L183-L189.
- [72] K. Andersson, A. Nikitin, L.G.M. Pettersson, A. Nilsson, H. Ogasawara, Water Dissociation on Ru(001): An Activated Process, *Phys. Rev. Lett.*, 93 (2004) 196101.
- [73] H. Cui, J.-H. Park, J.-G. Park, Effect of Oxidizers on Chemical Mechanical Planarization of Ruthenium with Colloidal Silica Based Slurry, *J. Solid State Sci. Technol.*, 2 (2013) P26-P30.
- [74] M. Kosmulski, The pH-Dependent Surface Charging and the Points of Zero Charge, *J. Colloid Interface Sci.*, 253 (2002) 77-87.
- [75] J.S. Noh, J.A. Schwarz, Estimation of the point of zero charge of simple oxides by mass titration, *J. Colloid Interface Sci.*, 130 (1989) 157-164.
- [76] I.E. Wachs, Molecular structures of surface metal oxide species: Nature of catalytic active sites in mixed metal oxides, in: J.L.G. Fierro (Ed.) *Metal oxides: chemistry and applications*, Taylor & Francis, 2006, pp. 4.
- [77] X. Hao, L. Quach, J. Korah, W.A. Spieker, J.R. Regalbuto, The control of platinum impregnation by PZC alteration of oxides and carbon, *J. Mol. Catal. A: Chem.*, 219 (2004) 97-107.
- [78] J.E. Samad, S. Hashim, S. Ma, J.R. Regalbuto, Determining surface composition of mixed oxides with pH, *J. Colloid Interface Sci.*, 436 (2014) 204-210.
- [79] B.J. O'Neill, D.H.K. Jackson, A.J. Crisci, C.A. Farberow, F. Shi, A.C. Alba-Rubio, J. Lu, P.J. Dietrich, X. Gu, C.L. Marshall, P.C. Stair, J.W. Elam, J.T. Miller, F.H. Ribeiro, P.M. Voyles, J. Greeley, M. Mavrikakis, S.L. Scott, T.F. Kuech, J.A. Dumesic, Stabilization of Copper Catalysts for Liquid-Phase Reactions by Atomic Layer Deposition, *Angew. Chem.*, 125 (2013) 14053-14057.
- [80] A.C. Alba-Rubio, B.J. O'Neill, F. Shi, C. Akatay, C. Canlas, T. Li, R. Winans, J.W. Elam, E.A. Stach, P.M. Voyles, J.A. Dumesic, Pore Structure and Bifunctional Catalyst Activity of Overlayers Applied by Atomic Layer Deposition on Copper Nanoparticles, *ACS Catal.*, 4 (2014) 1554-1557.
- [81] J. Lu, J.W. Elam, P.C. Stair, Synthesis and Stabilization of Supported Metal Catalysts by Atomic Layer Deposition, *Acc. Chem. Res.*, 46 (2013) 1806-1815.

## **Chapter 5    Microkinetic analysis of C<sub>3</sub> – C<sub>5</sub> ketone hydrogenation over supported Ru catalysts**

### **5.1 Introduction**

Despite the recent popularity of LA hydrogenation, the community is lacking a quantitative, elementary description of reaction kinetics and catalyst performance in this system, which limits our ability to rationally design active and stable materials tailored for the reduction of levulinic acid.

Because of its reactivity and low vapor pressure, LA hydrogenation is generally performed in condensed media using Ru-based catalysts [1], which consistently delivers good GVL selectivity at high LA conversions [2-6]. Unfortunately, kinetic analysis of this system is challenging. Liquid-phase reactions present a number of practical and fundamental difficulties, each of which obscure the elementary phenomena that are, as kineticists, our primary interests. For example, the presence of a condensed phase may induce various modes of deactivation [7-12], cause active site restructuring [8-11], severely constrain rates of mass diffusion [13, 14], and force one to consider the implications of thermodynamic non-idealities [15, 16]. Accordingly, it can be challenging to extract high quality kinetics from heterogeneously catalyzed reactions occurring in the liquid phase.

Relative to condensed media, the confounding effects of deactivation, restructuring, mass transfer, and solvation can be substantially mitigated in the vapor-phase; therefore, vapor-phase reactions are generally a more appropriate choice for framing a fundamental kinetic analysis of a given system. Unfortunately, generating sufficient partial pressures of levulinic acid over the full range of temperatures appropriate for consideration of hydrogenation kinetics (298 – 456 K) is nontrivial,

if not occasionally impossible, which makes this particular system a poor choice for vapor phase analysis. As was demonstrated in chapter 4 however, the rate of levulinic acid hydrogenation in water is identical to that of 2-pentanone in water. This suggests that LA hydrogenation can be viewed as a specific example of a generic ketone hydrogenation [8], which is a generally feasible system for vapor-phase analysis. Accordingly, a reasonable first step in understanding the kinetics of LA hydrogenation is to define expectations for ketone hydrogenation in the vapor phase. Once established, one may then view the subtleties of solution-phase ketone hydrogenations as perturbations to this idealized framework. Our effort here is therefore focused on establishing and reconciling a universal, microkinetic description of vapor phase C<sub>3</sub> – C<sub>5</sub> ketone hydrogenation on supported Ru catalysts. Ultimately, the hope is that this will both aid in the rational design of supported metal hydrogenation catalysts and provide a foundation for subsequent analysis of solvent effects in metal-catalyzed hydrogenations.

## 5.2 Experimental

### 4.2.1 Materials and methods

Acetone (99+%, Acros Organics), 2-butanone (99+%, Acros Organics), 2-pentanone (99%, Acros Organics), isopropyl alcohol (reagent grade, Acros Organics), 2-butanol (99%, Alfa Aesar), and 2-pentanol (98%, Acros Organics) were used as reactor feeds and/or for instrument calibration. Catalysts were synthesized using ruthenium (III) chloride hexahydrate (35-40% Ru, Acros Organics) and amorphous SiO<sub>2</sub> (481 m<sup>2</sup>/g, Sigma Aldrich). H<sub>2</sub> (99.999%, Airgas), He (99.999%, Airgas), N<sub>2</sub> (99.999%, Airgas) and CO (99.99% Praxair) were employed in kinetic studies, catalyst pretreatment, and catalyst characterization. 5% H<sub>2</sub> and 5% D<sub>2</sub> blends in 1% Ar with a He balance (Airgas) were used in isotope switching experiments. Each reagent was used as supplied by the

manufacturer. Water used in preparation of catalysts was purified in house by reverse osmosis, UV oxidation, and ion exchange to achieve a resistivity equal to at least  $18.2 \text{ M}\Omega \text{ cm}^{-1}$ .

#### 4.2.2 Catalyst preparation

Ru/SiO<sub>2</sub> catalysts were prepared by incipient wetness impregnation of amorphous SiO<sub>2</sub> with aqueous ruthenium (III) chloride hexahydrate. SiO<sub>2</sub> was selected because it is devoid of strong acid/base functionality, and reference experiments confirmed it to be inert to both feed molecules (2-ketones) and products (2-alcohols) under reaction conditions. An incipient volume of 1.6 ml of solution per gram of support was used. Impregnated catalysts were dried in air at 393 K overnight and subsequently reduced in flowing H<sub>2</sub> (100 ml min<sup>-1</sup>, 673 K, 3 K min<sup>-1</sup>). Prior to removal from reduction vessels, samples were passivated at 298 K in a stream of 1% O<sub>2</sub> in He.

#### 4.2.3 Catalyst Characterization

Catalyst surface area and porosity were probed by N<sub>2</sub> physisorption at 77 K (Micromeritics ASAP 2020). Ru surface site densities were quantified by CO adsorption at 308 K (Micromeritics ASAP 2020).

#### 4.2.4 Catalytic Activity Testing

Hydrogenations of acetone, 2-butanone, and 2-pentanone were carried out in a downflow, packed bed reactor. Catalyst particle sizes were restricted to the 45-90  $\mu\text{m}$  range to minimize length scales for intraparticle diffusion. Carbonyl hydrogenation is exothermic ( $\approx -55 \text{ kJ mol}^{-1}$ ). As a precaution against localized heating, active catalysts (Ru/SiO<sub>2</sub>) were diluted 10-20:1 (diluent:catalyst) in amorphous SiO<sub>2</sub> (45 – 90  $\mu\text{m}$ ). This admixture was loaded into a 6.35 mm OD 316 stainless steel tube, and the bed was held in place by quartz wool plugs. The void volume below the catalyst bed was packed with 850-2000  $\mu\text{m}$  quartz chips. Prior to kinetic analysis, the catalyst bed was reduced

in situ under H<sub>2</sub> (100 sccm) at 673 K for 4 h with a ramp rate of 5 K min<sup>-1</sup>. The bed was then cooled to the desired reaction temperature under a continuous H<sub>2</sub> purge. Reactor temperature was monitored and controlled at the outer wall of the packed bed using a Type K thermocouple and a PID temperature controller (LOVE 16A 3010). Kinetic data are reported at the bed temperature, which was measured by an auxiliary, in-line K-type thermocouple positioned in the void space just above the catalyst bed.

During kinetic experiments, gaseous reactor feeds (He and H<sub>2</sub>) were regulated using mass flow controllers (Brooks 5850S). Liquid ketones were introduced using a syringe pump (Cole-Parmer series 100) and fed through a 130 μm PEEK capillary into a heated vaporization chamber where they were contacted with pre-heated gas feeds. Ketone partial pressures were maintained below 15% of their saturation pressure to ensure complete vaporization of the liquid feed. The combined feed was then passed through a temperature-controlled static mixer, where it was pre-heated to reaction temperature. During reactor startup, the feed stream was diverted through a bypass and monitored using online GC analysis. Upon reaching steady state, the feed stream was introduced into the reactor, and the point of valve switching was taken as zero time on stream. Ketone co-feeding experiments were performed by adding a second vaporization unit.

Quantitative product analysis was achieved using an on-line Agilent 7890 GC equipped with a 6-port gas sampling valve, an HP-INNOWAX column, and an FID detector. This configuration permitted resolution and quantification of all ketones and alcohols considered in this study. The identities of products and reactants were confirmed using an Agilent 7890 GC-MS equipped with an Agilent 5975C MS detector and an HP-INNOWAX column. Carbon balances closed to within 5%, and residence times were adjusted to maintain ketone conversions below 11%. The

anticipated equilibrium ketone conversion exceeds 96% under all reaction conditions reported here. Accordingly, all production rate data were obtained at or below roughly 12% of the equilibrium limit, which allows the conclusion that kinetic data reflect differential operation and that measured production rates represent the forward rate of ketone hydrogenation under all experimental conditions.

To allow for meaningful comparisons among catalysts having varied metal loadings, hydrogenation rates are reported on a per-site basis as the total site time yield (STY) of hydrogenation products:

$$STY_i = \frac{\sum_j F_j}{S_{R_i}} \quad (1)$$

In Eq. (1),  $F_j$  is the effluent molar flowrate of an individual hydrogenation product—a C<sub>3</sub> to C<sub>5</sub> alcohol—and  $S_R$  is the total molar quantity of Ru surface sites in a given catalyst bed as estimated by CO chemisorption. Baseline activity was measured over amorphous SiO<sub>2</sub>; no extent of ketone hydrogenation or alcohol dehydrogenation were observed in the absence of Ru. Across all catalysts, reaction conditions, and extents of deactivation, 2-ketone hydrogenation was 100% selective to the secondary alcohol.

During vapor-phase ketone hydrogenation, the activity of Ru/SiO<sub>2</sub> decays with time-on-stream. Importantly, the time scale over which this decay is observed (hours) is substantially longer than system transients, which were experimentally determined to last, at most, 10 min at any condition reported here. This suggests that the decay in activity does not reflect an approach to steady state; rather, it is attributed to catalyst deactivation. Since ex-situ characterization methods were used to

titrate surface sites, meaningful STYs and structure-activity relations are generated only by estimating the rate of reaction at zero time-on-stream, which can be correlated with CO uptake on pristine catalysts. Accordingly, *all* absolute hydrogenation rates reported in this manuscript were corrected to zero time on stream using the approach described in the section 5.3.2.

## 5.3 Results

### 5.3.1 Catalyst synthesis & characterization

Ru clusters were supported on amorphous SiO<sub>2</sub> at a range of loadings. Physicochemical properties of these catalysts are summarized in Table 5.1. Although CO uptakes change substantially, Ru dispersions are uniform, suggesting similar cluster sizes and structures despite variation in metal surface area.

**Table 5.1** Physical properties and irreversible CO uptake measurements of various supported Ru/SiO<sub>2</sub> catalysts.

Ru wt% <sup>a</sup>	SA (m <sup>2</sup> g <sup>-1</sup> )	Pore Diameter (Å) <sup>b</sup>	Irreversible CO uptake (μmol g <sup>-1</sup> )	CO <sub>irr</sub> /Ru
0	481	56.5	-	-
0.3	471	49.9	11	0.36
0.6	514	48.6	15	0.25
0.84	494	50.1	35	0.42
1.5	520	49.9	62	0.41

a- Based upon concentrations of impregnating solutions, incipient volume, and support mass.

b- Average pore diameter determined by BJH analysis of N<sub>2</sub> adsorption/desorption data.

### 5.3.2 Estimating Initial rates

As illustrated in Figure 5.1 *Figure 5.1*, all catalysts employed here deactivate substantially with time on stream during ketone hydrogenation.

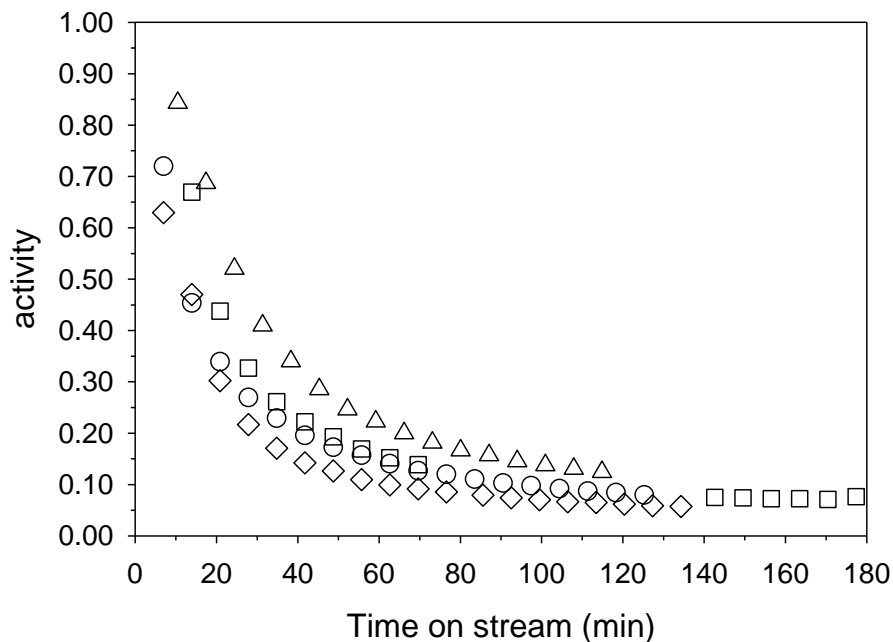


**Figure 5.1** Observed 2-pentanone hydrogenation activity as a function of time on stream at  $T = 322\text{ K}$ ,  $P_{\text{H}_2} = 910\text{ Torr}$ ,  $P_{2\text{-pentanone}} = 4.8\text{ Torr}$ . ( $\diamond$ ) 0.3% Ru/SiO<sub>2</sub>, ( $\circ$ ) 0.6% Ru/SiO<sub>2</sub>, ( $\Delta$ ) 0.84% Ru/SiO<sub>2</sub>, ( $\square$ ) 1.5% Ru/SiO<sub>2</sub>.

Often, deactivation profiles can be fit to first order deactivation model:

$$\frac{da}{dt} = -k_d a t \quad (2)$$

In Eq. (2),  $k_d$  is a first order deactivation rate constant and  $a$  is the activity of the catalyst, which we define as the rate of reaction observed as a function of time normalized by the rate of reaction at zero time on stream, i.e.,  $a = r/r_0$ . Unfortunately, as illustrated in **Figure 5.2**, a simple first order model fails to capture the deactivation profile for supported Ru catalysts during ketone hydrogenation, suggesting more complex behavior. We observe that there is an initial period of rapid deactivation, which quickly subsides giving way to a period of more gradual deactivation at longer times on stream. This type of profile can be captured empirically by two first order deactivation models, one for each regime of deactivation.

At short times on stream, deactivation is rapid, but short-lived. This phenomenon can be described by Eq. (3), which allows deactivation rates to approach zero at long times on stream and thus predicts a non-zero steady state hydrogenation rate.

$$\frac{da}{dt} = -k_d (a - a_\infty) t \quad (3)$$

At longer times on stream, deactivation is slow, but unabating such that catalyst activity, on the time scales of our experiments, never reaches a true steady state. This phenomenon is captured by a standard first order deactivation model, Eq. (4).

$$\frac{da}{dt} = -k_d' a t \quad (4)$$

To estimate activity at zero time, Eq. (4) is first applied to the second regime of milder deactivation, allowing regression of a first order deactivation rate constant ( $k_d'$ ). Once obtained, the decay profile can be corrected for the incessant slow deactivation. The corrected profile therefore reaches a steady state, and it is thus well-described by Eq. (3). Applying this model to the corrected activity profile permits regression of  $k_d$  and  $a_\infty$ , which allows estimation of  $r_0$ —the rate of reaction at zero time on stream. While this model is not likely to explain the deactivation process on a fundamental level, it accurately captures the deactivation profile as shown in **Figure 5.2**.

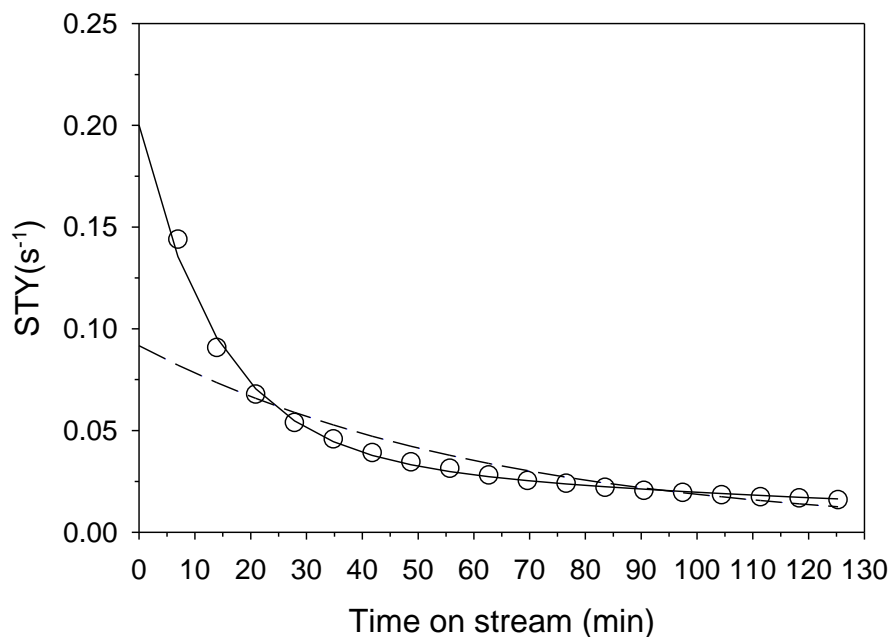


**Figure 5.2** Comparison of deactivation models for a 0.6wt% Ru/SiO<sub>2</sub> catalyst during 2-pentanone hydrogenation at 322K, 4.8 Torr 2-pentanone and 910 Torr H<sub>2</sub>. Dashed line represents single 1<sup>st</sup> order deactivation model. Solid line represents two 1<sup>st</sup> order deactivation models with a non-zero asymptote.

### 5.3.3 Assessing kinetic control

The extent of kinetic control was examined by applying the Koros-Nowak criterion to hydrogenation rates estimated at zero time on stream for acetone and 2-pentanone [17, 18], which represent the two systems most likely constrained by mass diffusion. Specifically, acetone exhibited the highest rate of hydrogenation per unit mass of catalyst, and 2-pentanone, the largest molecule considered, had the smallest diffusivity. Results are summarized in Figure 5., which plots initial (zero-time), mass-normalized hydrogenation rates for acetone and 2-pentanone against irreversible CO uptake on logarithmic axes at 322 and 341 K. The slope of the regression lines for acetone and 2-pentanone are near unity at both temperatures, indicating a system free of both mass and heat transfer limitations per Madon and Boudart [18]. Because rates of 2-butanone hydrogenation never exceed those of acetone hydrogenation and because 2-butanone diffusion should be at least as fast as that of 2-pentanone, we assume that 2-butanone hydrogenation rates

are also kinetically controlled. Furthermore, because of the pronounced catalyst deactivation in this system, the initial rates illustrated in Figure 5.3 represent the highest *measured* absolute hydrogenation rates per unit mass of catalyst under any experimental condition. *Reported* rates in this manuscript always reflect the initial rate of reaction prior to the onset of deactivation and, in many cases, these exceed reaction rates where it would be feasible to maintain kinetic control. However, *measured* rates were collected over substantially deactivated catalyst beds, where volumetric reaction rates were always lower than those reported in Figure 5.3, and subsequently *corrected* to zero time on stream. Thus, initial rates reported here represent hypothetical, kinetically-controlled rates at zero time on stream.

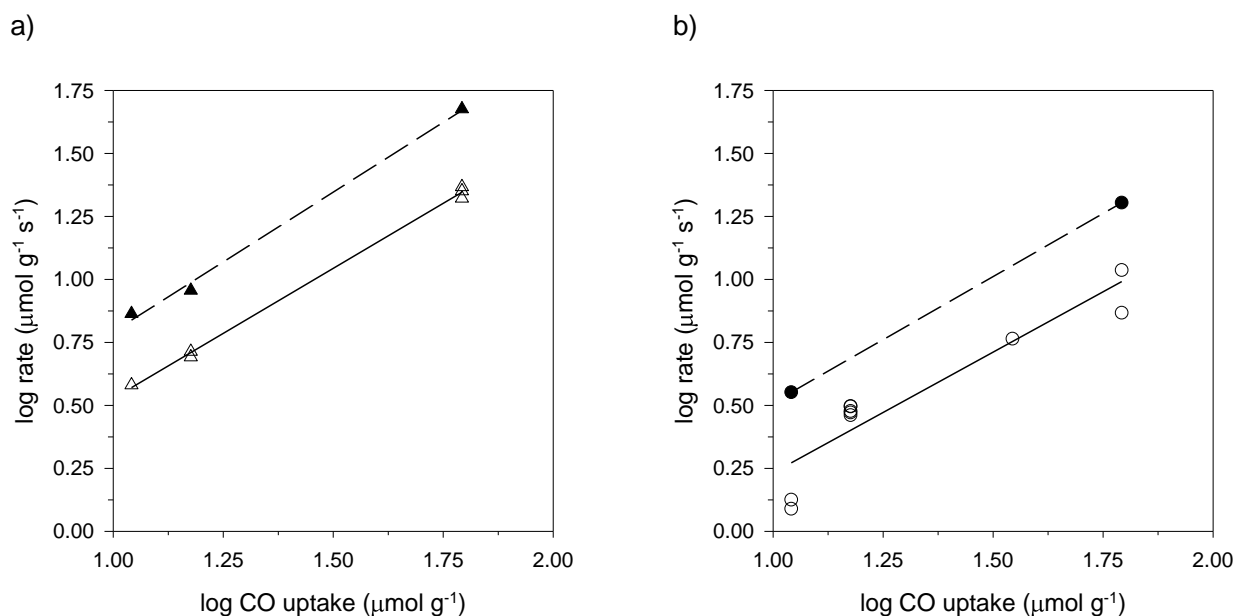


**Figure 5.3** Functional relationship between mass-normalized ketone hydrogenation rates and Ru surface site densities as determined by CO chemisorption. Hydrogenation rates were measured at 4.8 Torr ketone and 910 Torr  $\text{H}_2$ , open and closed symbols indicate rates at 322 K and 341 K respectively. For (a) acetone hydrogenation, the slope of the regression lines indicated in the figure are  $1.04 \pm 0.11$  (322K) and  $1.1 \pm 0.9$  (341K). For (b) 2-pentanone hydrogenation, the slope of the regression lines indicated in the figure are  $0.96 \pm 0.30$  (322K) and  $1.1$  (341K). This is consistent with criteria given by Koros and Nowak for demonstration of kinetically controlled hydrogenation rates at the given temperatures. Confidence intervals were calculated at a 95% confidence level.

Since the materials tested have uniform Ru dispersion, the Koros-Nowak analysis (Figure 5.3) provides an average site-time yield (STY) for this Ru/SiO<sub>2</sub> series. These are summarized for both acetone (Entry 1) and 2-pentanone (Entry 3) in Table 5.2. For comparison, the hydrogenation rate for 2-butanone was also determined at 322 K (Entry 2). Data in Table 5.2 show that ketone hydrogenation rates decrease with the length of the carbon chain such that the rate of acetone hydrogenation > 2-butanone hydrogenation > 2-pentanone hydrogenation.

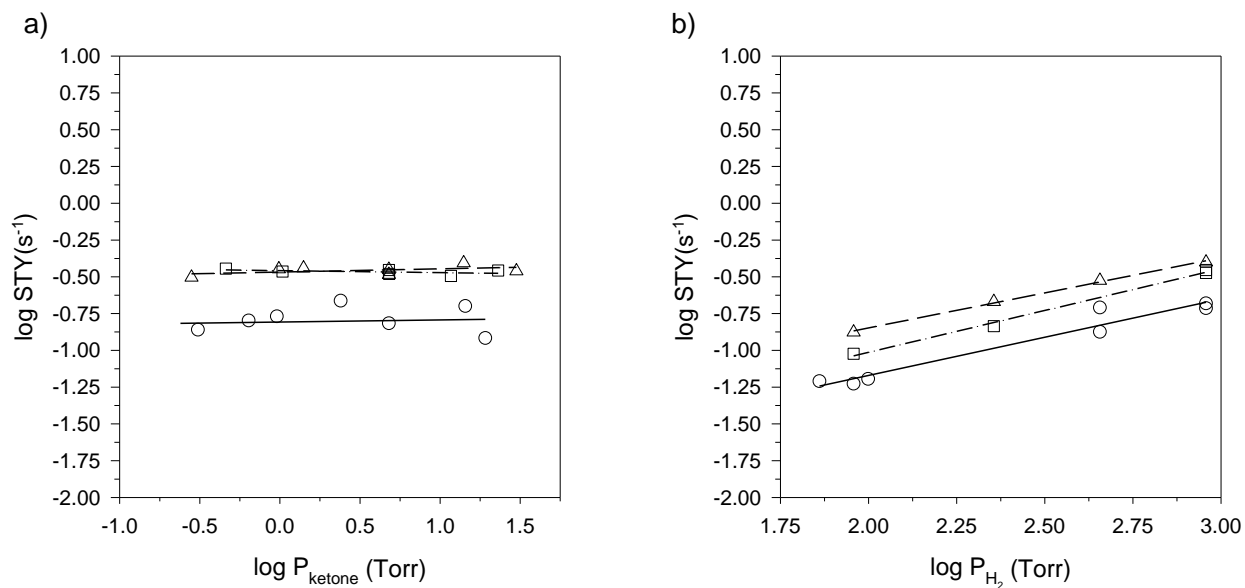
**Table 5.2** Initial STY of hydrogenation of various ketones measured at 322 K, 4.8 Torr of ketone and 910 Torr of H<sub>2</sub>. Confidence intervals are calculated at 95%.

Ketone	Average initial STY <sup>a</sup> (s <sup>-1</sup> )
Acetone	0.37 ± 0.04
2-butanone	0.33 ± 0.02
2-pentanone	0.14 ± 0.04

a- Site time yields represent the average over multiple Ru/SiO<sub>2</sub> catalysts with varied metal loading.

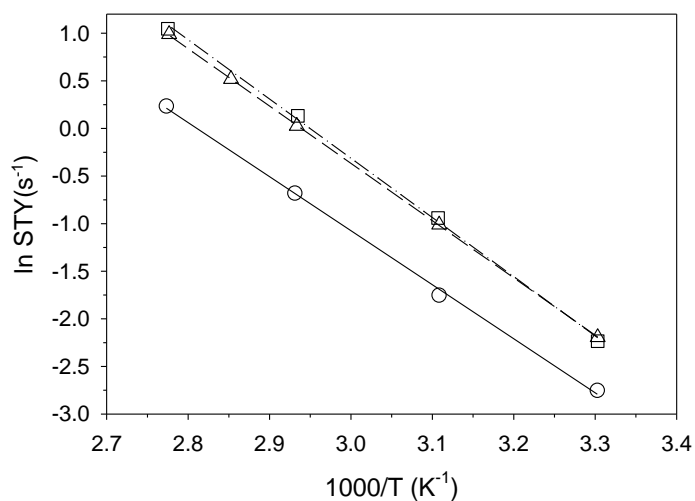
#### 5.3.4 Apparent Kinetics of ketone hydrogenation: low temperatures

Figure 5.4 illustrates the dependence of hydrogenation rates on ketone partial pressure (Figure 5.4a) and hydrogen partial pressure (Figure 5.4b) for acetone, 2-butanone, and 2-pentanone at 322K. Over the partial pressure ranges considered, rates of hydrogenation for each ketone exhibit an apparent zero order dependence on the ketone and an apparent half-order dependence on H<sub>2</sub>.



**Figure 5.4** Effect of (a) ketone and (b) hydrogen partial pressure on the site time yield of hydrogenation at 322 K for (○) 2-pentanone, (□) 2-butanone and (Δ) acetone. Ketone partial pressures varied from approximately 0.3 – 30 Torr. Hydrogen partial pressures varied from 90-910 Torr.

As illustrated in Figure 5.5, the apparent barrier for hydrogenation was approximately 50 kJ mol<sup>-1</sup> for all C<sub>3</sub>-C<sub>5</sub> ketones in the range of 303-359 K, which is consistent with previously reported apparent barriers for acetone hydrogenation over supported group VIII metals [19-21].



**Figure 5.5** Arrhenius plot for ketone hydrogenation from 303 - 359 K at a ketone and hydrogen partial pressure of 4.8 and 910 Torr respectively for (○) 2-pentanone, (□) 2-butanone and (Δ) acetone.

This suggests that differences in rates observed between acetone, 2-butanone, and 2-pentanone arise from differences in surface coverages and/or pre-exponential factors (activation entropies); however, further interpretation is difficult at this stage, and we defer in depth discussion to subsequent microkinetic analysis (Section 5.4.5). Apparent reaction orders and kinetic parameters for the individual ketones are summarized in Table 5.3.

**Table 5.3** Summary of apparent activation barriers and reaction orders based for the various ketones studied over supported Ru/SiO<sub>2</sub> catalysts. Activation barriers were determined at 4.8 and 910 Torr of ketone and H<sub>2</sub> respectively. Reaction orders were determined at 322 K. Confidence intervals calculated at 95%.

Ketone	Average STY (s <sup>-1</sup> ) <sup>a</sup>	A (Torr <sup>-0.5</sup> s <sup>-1</sup> ) <sup>b</sup>	E <sub>a</sub> (kJ mol <sup>-1</sup> )	Ketone reaction order	H <sub>2</sub> reaction order
2-pentanone	0.14 ± 0.04	2.1 x 10 <sup>7</sup>	49.5 ± 5.2	0.01 ± 0.18	0.52 ± 0.14
2-butanone	0.33 ± 0.02	9.5 x 10 <sup>7</sup>	51.8 ± 5.0	-0.01 ± 0.01	0.57 ± 0.12
Acetone	0.37 ± 0.04	4.8 x 10 <sup>7</sup>	50.1 ± 2.3	0.03 ± 0.22	0.48 ± 0.08

a- Reaction conditions of 322 K, 4.8 Torr ketone, 910 Torr H<sub>2</sub>. Average across multiple catalysts and Ru loadings

b- Calculated assuming an apparent power law expression  $r = Ae^{-E_a/RT}P_{H_2}^{0.5}$

### 5.3.5 Apparent Kinetics of ketone hydrogenation: high temperatures

A goal of this study is to provide an elementary rationale for differences in observed macroscopic rates of hydrogenation for C<sub>3</sub> – C<sub>5</sub> ketones. To reveal coverage effects that may underlie variations in site time yield, it is necessary to experimentally depart from the regime of (ketone) saturation kinetics described in the preceding section. To this end, an analogous set of high temperature kinetic data were collected. Rates of acetone hydrogenation were measured between 303 and 456 K at 4.8 Torr acetone and 910 Torr hydrogen. Reaction orders were probed by varying both ketone and hydrogen partial pressures at 442 K.

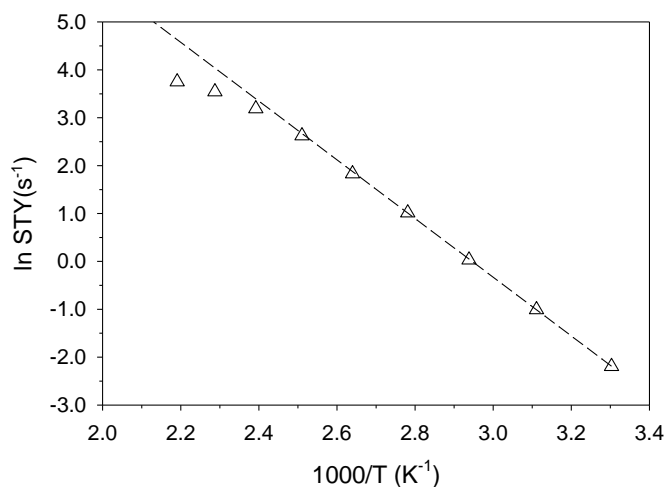


**Figure 5.6** Arrhenius plot for acetone hydrogenation from 303 - 456 K at ketone and hydrogen partial pressures of 4.8 and 910 Torr.

Figure 5.6 illustrates the trend in hydrogenation rates as a function of inverse temperature over this larger span. At lower temperatures, an apparent barrier of  $\approx 50 \text{ kJ mol}^{-1}$  is again observed. This barrier (evidenced by linearity) appears to extend to roughly 418 K ( $1000/T = 2.4 \text{ K}^{-1}$ ), at which point the apparent barrier begins to decrease, ultimately approaching zero as temperatures near 456 K ( $1000/T = 2.2 \text{ K}^{-1}$ ). Although plausible, we do not believe this observed decrease is attributed to the onset of mass transfer limitations. Again, rates in this experiment were measured over a deactivated catalyst, and volume-normalized rates were always well below initial rates that have been proven to be kinetically controlled (see Section 5.3.3).

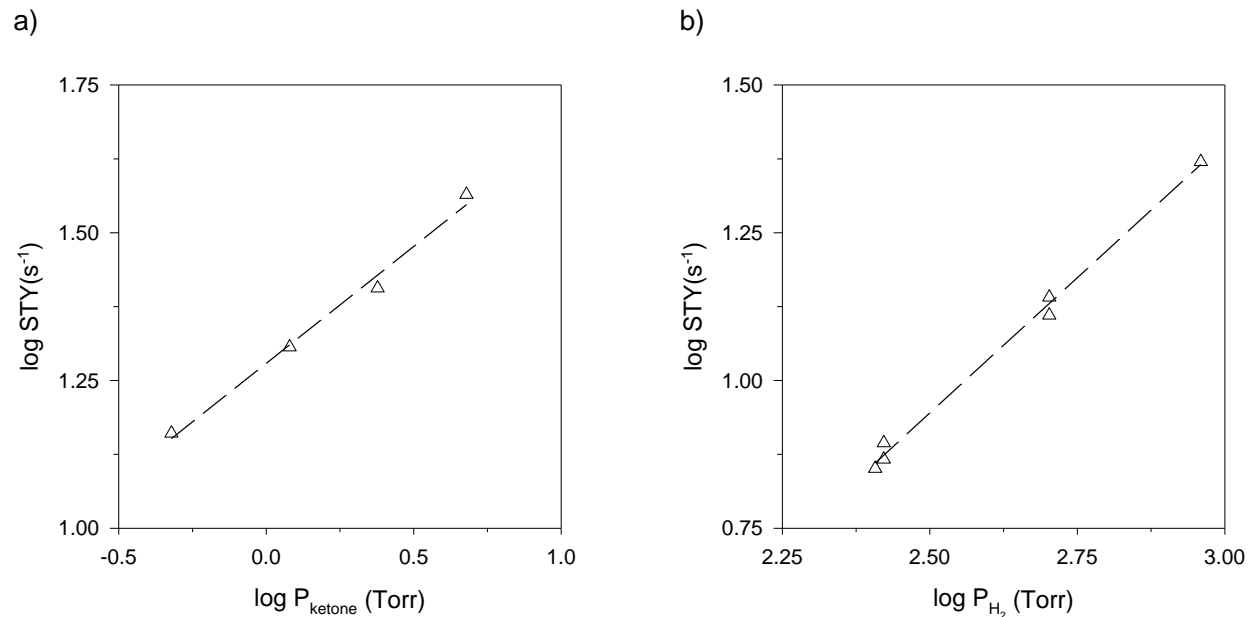


**Figure 5.7** Effect of (a) ketone and (b) hydrogen partial pressure on the site time yield of acetone hydrogenation at 442 K. Ketone partial pressures varied from 0.5 – 4.8 Torr. Hydrogen partial pressures varied from 250-910 Torr.

Figure 5.7 illustrates the response in hydrogenation rate to variations in ketone and hydrogen partial pressure at 442 K. Relative to trends at 322 K, the apparent reaction orders for acetone and hydrogen increase, respectively, to  $0.40 \pm 0.12$  and  $0.92 \pm 0.09$ . This observation is consistent with more sparsely covered Ru surfaces at higher temperatures, which may explain the decrease in apparent barrier at high temperatures: as the coverage of vacant sites increase, apparent barriers become increasingly influenced by exothermic heats of adsorption. Generally, this will manifest as a decrease in apparent barriers compared to those observed in regimes of saturation kinetics.

### 5.3.6 Apparent Kinetics of ketone hydrogenation: co-feeding conditions

To further probe the source of macroscopic differences in site-time yield between acetone, 2-butanone, and 2-pentanone, a series of experiments were performed wherein 2-pentanone hydrogenation rates were measured while co-feeding acetone and 2-butanone at 1:1 and 5:1 molar ratios. Perturbations to the hydrogenation rate from experiments with isolated ketone feeds provide

insight into competitive adsorption and coverage effects and thus aid in resolving differences in adsorption energetics of each ketone.

Table 5.4 summarizes rates of 2-pentanone hydrogenation at 322 K in the presence of acetone (Entries 1 and 2) and 2-butanone (Entries 3 and 4). Here, hydrogenation rates are normalized to those obtained for 2-pentanone in isolation (Section 5.3.3). In all cases, 2-pentanone hydrogenation rates decrease upon introducing a second ketone, which is consistent with competitive adsorption of ketones and/or their hydrogenated derivatives at metal surface sites. Interestingly, for equivalent partial pressures of the co-feed, 2-butanone leads to a larger reduction in 2-pentanone hydrogenation rates than acetone, implying a larger decrease in  $C_5$  surface coverages with the 2-butanone co-feed. Tentatively, this may be attributed either to a more favorable adsorption free energy of 2-butanone or to steric factors associated with the longer carbon chain ( $C_4$ ) relative to acetone ( $C_3$ ), which could plausibly lead to increased site blocking for 2-pentanone adsorption.

**Table 5.4** Summary of relative 2-pentanone hydrogenation rates at 322 K in the presence of different ketones over supported Ru/SiO<sub>2</sub> catalysts.

Ketone co-feed	$P_{2\text{-pentanone}}$ (Torr)	$P_{\text{co-feed}}$ (Torr)	$\frac{r_{2\text{-pentanone,co-feed}}}{r_{2\text{-pentanone}}}$
Acetone	4	4	0.81
Acetone	4	20	0.47
2-butanone	4	4	0.66
2-butanone	4	20	0.28

## 5.4 Discussion

### 5.4.1 Elementary surface steps

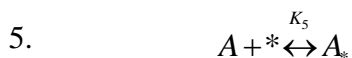
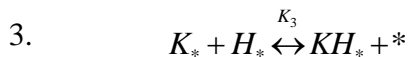
Because of the similarity in overall chemistry, apparent reaction orders, and apparent kinetic parameters, it is reasonable to assume that the hydrogenation of each C<sub>3</sub>-C<sub>5</sub> ketone can be described by a common set of elementary steps. The kinetics of carbonyl hydrogenation are generally interpreted in the context of the Horiuti-Polanyi mechanism, which is predicated on step-wise addition of hydrogen adatoms to an unsaturated, surface-bound hydrocarbon [19, 22-24]; however, there remains some uncertainty regarding the site requirements for this process on a given metal surface. In separate studies, hydrogenation kinetics have been reconciled with schemes in which the rate controlling step involves a reaction between a hydrogen atom and a hydrocarbon fragment that are both bound at a *single* type of active site [19] and schemes in which the rate controlling step involves a reaction between a hydrogen atom and a hydrocarbon fragment that are bound at *distinct* types of active sites [20, 21]. Because neither model can be excluded a priori, we consider both prior to framing a more fundamental analysis.

#### 5.4.2 Single site model

The conventional Horiuti-Polanyi scheme, applied to ketone hydrogenation, is presented as the series of elementary steps shown in Table 5.5. In this case, we consider that all adsorption and reaction steps involve a single class of active site, which is designated here as ‘\*’.

**Table 5.5** Proposed set of elementary steps to describe ketone hydrogenation over Ru surfaces. Proposed set of elementary steps to describe ketone hydrogenation over Ru surfaces.

Elementary step	Surface Reaction
1.	$K + * \xrightleftharpoons{K_1} K_*$
2.	$H_2 + 2* \xrightleftharpoons{K_2} 2H_*$



In this sequence, the ketone ( $K$ ) adsorbs molecularly at a metal site ( $*$ ), while hydrogen adsorbs dissociatively at the same type of site (Steps 1 and 2). In Steps 3 and 4, adsorbed hydrogen atoms add sequentially across the carbonyl group. The first hydrogen addition (Step 3) forms a half-hydrogenated intermediate ( $KH$ ). In Step 4, the addition of a second hydrogen atom to the half-hydrogenated intermediate forms the surface-bound alcohol ( $A$ ), which then desorbs from the surface (Step 5). Vannice has employed this model to explain observed trends in vapor-phase acetone hydrogenation over Pt [19], and it is worth considering whether this scheme can capture analogous trends observed here over Ru.

Through Langmuir-Hinshelwood analysis, one can develop overall rate laws from the scheme in Table 5.5. Based on the above elementary steps, we can derive coverage expressions for each of the relevant reactive species on the surface. In the case where hydrogen adsorption, step 2, is assumed to be rate determining, the coverage of all other species can be determined from equilibrium expressions (Eq. 5-7). From the site balance (Eq. 8), the expression for the coverage of vacant sites can be determined. Finally all the relevant coverage expressions can be substituted into Eq. (9), which defines the forward rate of hydrogen adsorption.

$$\theta_{K_*} = K_1 P_K \theta_* \quad (5)$$

$$\theta_{A_*} = K_5 P_A \theta_* \quad (6)$$

$$\theta_{KH_*} = \sqrt{\frac{K_3 \theta_{A_*} \theta_{K_*}}{K_4}} = \sqrt{\frac{K_1 K_3 K_5 P_K P_A}{K_4}} \theta_* \quad (7)$$

$$\theta_{K_*} + \theta_{KH_*} + \theta_{A_*} + \theta_* = 1 \quad (8)$$

$$r_{2+} = k_{2+} P_{H_2} \theta_*^2 = \frac{k_{2+} P_{H_2}}{(1 + K_1 P_K + \sqrt{K_1 K_3 K_4^{-1} K_5 P_K P_A} + K_5 P_A)^2} \quad (9)$$

With the rate of hydrogen adsorption limiting the reaction, Eq. (9), a 1<sup>st</sup> order dependence in hydrogen partial pressure is expected at all reaction conditions with zero order in ketone at most. H<sub>2</sub> adsorption can therefore be excluded as rate controlling since this scenario fails to capture apparent reaction orders over a broad range of experimental conditions.

To further aid in elucidating rate controlling phenomena, we performed an H<sub>2</sub>/D<sub>2</sub> switching experiment, which revealed a primary kinetic isotope effect (KIE) of approximately 3 during 2-pentanone hydrogenation. This result indicates that an H-X bond is involved in the rate determining step of ketone hydrogenation, which allows us to additionally exclude ketone adsorption (Step 1) and alcohol desorption (Step 5) as rate controlling. Surface reactions are therefore the only possible rate controlling steps in this scenario. By making the assumption that the first hydrogenation step (Step 3) controls the rate of reaction (and that, relative to this step, adsorption steps are equilibrated), one predicts observable ketone orders from -1 to 1 and hydrogen orders from -0.5 to 1.5, with precise orders depending on the most abundant surface intermediate (Eq. 10).

$$r_{3+} = k_{3+} \theta_{K_*} \theta_{H_*} = \frac{k_{3+} K_1 \sqrt{K_2 P_{H_2}} P_K}{(1 + K_1 P_K + \sqrt{K_2 P_{H_2}} + \frac{K_5 P_A}{K_4 \sqrt{K_2 P_{H_2}}} + K_5 P_A)^2} \quad (10)$$

Analogously, if one assumes that the second hydrogenation step (Step 4) is rate controlling, one predicts ketone orders between -1 and 1 and hydrogen orders between 0 and 1 (Eq. 11).

$$r_{4+} = k_{4+} \theta_{KH_*} \theta_{H_*} = \frac{k_{4+} K_1 K_2 K_3 P_K P_{H_2}}{(1 + K_1 P_K + \sqrt{K_2 P_{H_2}} + K_1 \sqrt{K_2 K_3 P_K} \sqrt{P_{H_2}} + K_5 P_A)^2} \quad (11)$$

Based on the range of possible reaction orders, one concludes that our observed trends loosely agree with a single-site model and that neither surface reaction can be excluded as potentially rate controlling. However, it is worth noting that Eq. (10) and Eq. (11) both predict maxima in the hydrogenation rate with respect to ketone partial pressure. This indicates that, for a single site model, saturation kinetics with respect to the ketone will only be observable over a narrow partial pressure range. Since we identify no rate maximum with respect to the ketone and that saturation kinetics exist over two orders of magnitude in ketone partial pressure (Figure 5.4), reconciliation with a competitive adsorption model is doubtful. Instead, we propose that the only way for ketone saturation kinetics to be observable alongside a half-order hydrogen dependence over such a large partial pressure range is for the rate controlling surface reaction to involve species adsorbed at two non-equivalent surface sites.

### 5.4.3 Two site model

Previous studies of acetone hydrogenation over Pt [20] and Ru [21] have invoked a two-site model to explain trends similar to those reported here. As illustrated in Table 5.6, this generally is

presented as a scenario in which hydrogen atoms and hydrocarbons adsorb at distinct surface sites, both of which are involved in surface hydrogenation steps.

**Table 5.6** Proposed set of elementary steps to describe ketone hydrogenation over Ru surfaces, with the non-competitive adsorption of hydrogen.

Elementary step	Surface Reaction
1.	$K + * \xrightleftharpoons{K_1} K_*$
2.	$H_2 + 2s \xrightleftharpoons{K_2} 2H_s$
3.	$K_* + H_s \xrightleftharpoons{K_3} KH_* + s$
4.	$KH_* + H_s \xrightleftharpoons{K_4} A_* + s$
5.	$A + * \xrightleftharpoons{K_5} A_*$

In this view, hydrogen binds preferentially at an ‘s’ site, whereas the ketone, half hydrogenated intermediate and alcohol all adsorb on ‘\*’ sites. Following a Langmuir-Hinshelwood analysis, we can similar to the previous section develop an overall rate expression for the case where H<sub>2</sub> adsorption is rate determining:

$$\theta_{K_*} = K_1 P_K \theta_* \quad (12)$$

$$\theta_{A_*} = K_5 P_A \theta_* \quad (13)$$

$$\theta_{KH_*} = \sqrt{\frac{K_3 \theta_{A_*} \theta_{K_*}}{K_4}} = \sqrt{\frac{K_1 K_3 K_5 P_K P_A}{K_4}} \theta_* \quad (14)$$

$$\theta_{K^*} + \theta_{KH^*} + \theta_{A^*} + \theta_* = 1 \quad (15)$$

$$\theta_{H_s} + \theta_s = 1 \quad (16)$$

$$r_{2+} = k_{2+} P_{H_2} \theta_s^2 = k_{2+} P_{H_2} \quad (17)$$

Based on Eq. (17) one would expect to observe zero order kinetics with respect to the ketone and first order kinetics with respect to hydrogen under all conditions. We can therefore again exclude H<sub>2</sub> adsorption (Step 2) as rate controlling since it does not match experimentally observed trends. Furthermore, as described in the preceding section, our observation of a primary KIE during H<sub>2</sub>/D<sub>2</sub> switching experiments indicates that ketone adsorption (Step 1) and alcohol desorption (Step 5) are not rate controlling. We therefore take adsorption steps to be quasi-equilibrated relative to the surface reactions, either of which may be rate determining. If the first hydrogen addition (Step 3) is controlling, Eq. (18) will describe the overall hydrogenation rate. From this model, one predicts that both ketone and hydrogen orders may range from 0 to 1.

$$r_{3+} = k_{3+} \theta_{K^*} \theta_{H_s} = \frac{k_{3+} K_1 \sqrt{K_2 P_{H_2}} P_K}{(1 + K_1 P_K + \frac{K_5 P_A}{K_4 \sqrt{K_2 P_{H_2}}} + K_5 P_A)(1 + \sqrt{K_2 P_{H_2}})} \quad (18)$$

By inspection of Eq. (18), a zero order ketone dependence and a half-order hydrogen dependence (observed reaction orders at 322K) could occur either under conditions where ‘\*’ sites are saturated with the ketone and ‘s’ sites are sparsely covered with hydrogen, or under conditions where ‘\*’ sites are dominated by the half-hydrogenated intermediate and ‘s’ sites are dominated by hydrogen atoms. A 0.9 order hydrogen dependence alongside a 0.4 order ketone dependence (observed reaction orders at 422K) can only result if the half-hydrogenated intermediate ( $K_5 P_A / K_4 \sqrt{K_2 P_{H_2}}$ )

) is the dominant species on ‘\*’ sites and hydrogen coverage approaches zero on ‘s’ sites. Specifically, this is the only scenario in which hydrogen orders can exceed 0.5. Applying these limiting assumptions and expressing the ketone and alcohol partial pressures in terms of fractional conversion, one generates Eq. (19):

$$r_{3+} = k_{3+} \frac{K_1 K_2 K_4}{K_5} \frac{P_{H_2} P_K}{P_A} = k_{3+} \frac{K_1 K_2 K_4}{K_5} P_{H_2} \frac{(1 - X_K)}{X_K} = k' \frac{(1 - X_K)}{X_K} \quad (19)$$

In this expression,  $X_K$  is the fractional conversion of the ketone. Since hydrogen was fed in large excess and ketone conversions were maintained at differential levels, hydrogen conversion is negligible and its partial pressure can be considered constant at the inlet value and lumped into the apparent rate constant,  $k'$ . From Eq. (19), one predicts that observed site time yields will be a strong function of conversion/contact time, increasing linearly from a zero y-intercept when plotted as a function of  $\frac{(1 - X_K)}{X_K}$ . By inspection of Figure 5.8, this trend is distinctly absent. Instead, we

observe that the hydrogenation STY is roughly invariant with conversion. Therefore, we exclude the first hydrogen addition as a likely rate determining step in the two-site model.

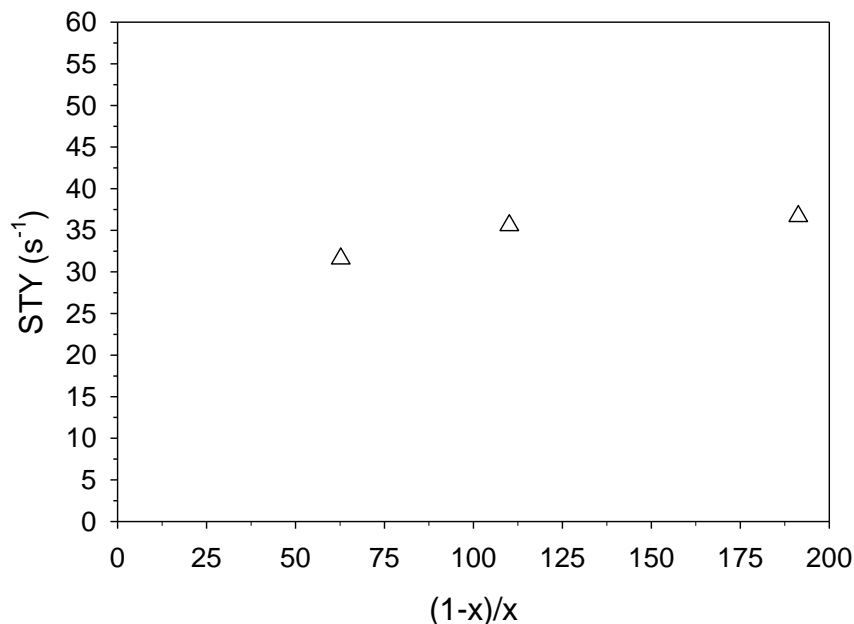


**Figure 5.8** Effect of ketone conversion on the rate of acetone hydrogenation at 442 K, 4.8 Torr acetone and 910 Torr H<sub>2</sub>.

Analogously, by assuming that the second hydrogen addition controls the reaction rate, one arrives at the overall rate expression given in Eq. (20), which again suggests that both ketone and hydrogen orders can range from 0 to 1.

$$r_{4+} = k_{4+} \theta_{KH_s} \theta_{H_s} = \frac{k_{4+} K_1 K_2 K_3 P_K P_{H_2}}{(1 + K_1 P_K + K_1 \sqrt{K_2 K_3 P_K \sqrt{P_{H_2} + K_5 P_A}})(1 + \sqrt{K_2 P_{H_2}})} \quad (20)$$

In this case, the zero (ketone) and half (hydrogen) reaction orders observed at low temperatures are anticipated in two scenarios—one in which ‘\*’ sites are dominated by the ketone and ‘s’ sites are dominated by hydrogen atoms and another in which ‘\*’ sites are dominated by the half-hydrogenated intermediate and ‘s’ sites are sparsely covered. At higher temperatures, either scenario can plausibly lead to a  $\approx 0.4$  order ketone dependence and  $\approx 0.9$  order hydrogen dependence so long as the vacant site coverage becomes comparable to that of adsorbed species.

Because physically realistic assumptions allow Eq. (20) to be qualitatively consistent with observed kinetic trends over a broad range of experimental conditions, we conclude that the second hydrogen addition is the most likely rate determining step in this scenario.

This analysis indicates that a model involving two distinct surface sites that preferentially coordinate either hydrogen or oxygenated hydrocarbons can capture experimental trends; however, it does not establish the nature of the two sites, nor does it consider whether preferential binding of individual species at unique sites is realistic on Ru surfaces. Before proceeding further with microkinetic analysis based on the two-site model, we first consider whether there exists a sound physical basis for doing so.

#### 5.4.4 Identifying potential adsorption sites on Ru surfaces

In this section, we consider the identity of possible adsorption sites and discuss whether it is realistic for adsorbates involved in ketone hydrogenation to populate two distinct categories. We limit discussion to the most thermodynamically stable Ru facet, Ru (0001) [25], which is illustrated as a 3 x 3 unit cell in Figure 5.9. On this surface, there exist four distinct sites on which adsorbates may bind: top, bridge, three-fold hollow (fcc) and three-fold hollow (hcp). Top sites are so-named because they are located directly atop a Ru atom, while bridge sites comprise the intersection of two neighboring Ru atoms. Three-fold hollow (hcp) sites are found at the intersection of three Ru atoms directly above a subsurface Ru atom, whereas three-fold hollow (fcc) sites represent the analogous intersection with no Ru atom directly below.

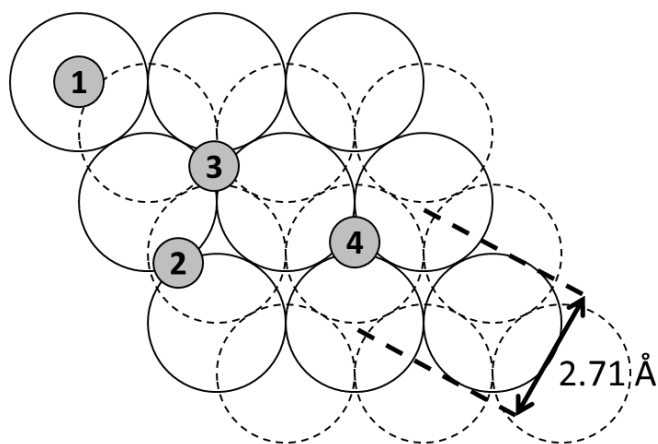


**Figure 5.9** Ru (0001) facet with a lattice constant of 2.71 Å with the distinct adsorption sites: 1) top, 2) bridge, 3) three-fold fcc and 4) three-fold hcp. Dashed lines indicate atoms in the second layer.

There is no reason to expect that a single adsorption site is universally preferred: a given species will bind preferentially at whichever site provides the greatest degree of energetic stabilization upon adsorption, and this will generally differ between adsorbates. For example, on Ru (0001), low-energy electron diffraction (LEED) experiments reveal that carbon monoxide adsorbs selectively at top sites [26], while oxygen atoms bind most favorably at three-fold hollow (hcp) sites [27]. Next, we extend this discussion to surface intermediates involved in ketone hydrogenation.

#### 5.4.4.1 Identifying potential adsorption sites on Ru surfaces: Hydrogen

The most straightforward case is that of hydrogen, for which surface science provides definitive resolution of adsorption phenomena. Scanning tunneling microscopy (STM) [28], high resolution electron energy loss spectroscopy (HREELS) [29] and LEED [30-33] indicate that molecular  $H_2$  dissociates on Ru surfaces, and that the resulting hydrogen atoms bind preferentially at three-fold hollow (fcc) sites. Stable H-adsorption at top, bridge, or three-fold hollow (hcp) sites is not generally observed. Importantly, this appears independent of hydrogen coverage, suggesting that

the insight can be extended to Ru surfaces under working H<sub>2</sub> pressures [31]. In support of experimental results, computational analyses consistently report large hydrogen binding energies at three-fold hollow (fcc) sites and conclude that these are the most likely sites for hydrogen adsorption [24, 25, 34, 35].

#### 5.4.4.2 Identifying potential adsorption sites on Ru surfaces: Ketone

Two ketone adsorption modes have been proposed on Group VIII metals [36, 37]; both are illustrated in Figure 5.10. First, carbonyl groups can adsorb end-on through interactions between surface metal atoms and an oxygen lone pair. This binding mode is designated as  $\eta_1(\text{O})$ . Second, the carbonyl can bind side-on through interactions between metal surface sites and both the carbon and oxygen of the carbonyl group. This binding mode is designated as  $\eta_2(\text{C,O})$ , and it will generally require two metal sites [36, 37]. Experimentally, both modes have been identified on Ru (0001) through electron energy loss spectroscopy (EELS) [37]. Density Functional Theory (DFT) calculations have also shown that  $\eta_1(\text{O})$  and  $\eta_2(\text{C,O})$  are the preferred modes of acetone adsorption on Ru, while 2-butanone preferentially binds in the  $\eta_1(\text{O})$  configuration [24]. To define precise site requirements, ketones bound as  $\eta_1(\text{O})$  species will be located at top sites, while those in the  $\eta_2(\text{C,O})$  configuration occupy a neighboring pair of top and bridge sites.

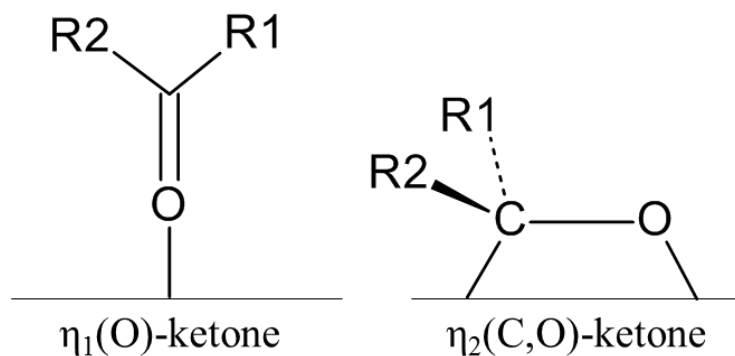


**Figure 5.10** Spectroscopically observed adsorption modes of acetone on a clean Ru (0001) surface [37]

#### 5.4.4.3 Identifying potential adsorption sites on Ru surfaces: Half-hydrogenated intermediate

In order to discuss the adsorption mode of the half-hydrogenated intermediate (KH), it is necessary to first establish its chemical identity. Depending on the sequence of hydrogen addition to the surface-bound ketone in the Horiuti-Polanyi scheme, the half-hydrogenated intermediate (product of Step 3, Table 5.5) will be either an alkoxide or a hydroxyalkyl. The former will be observed if the first hydrogen atom adds to the carbonyl carbon, while the latter will be observed if the first hydrogen atom adds to the carbonyl oxygen. As illustrated in Figure 5.11, each species will adopt a distinct surface configuration and thus have unique site requirements. Specifically, an alkoxide will bind at a single adsorption site through its oxygen atom [36], while a hydroxyalkyl will form a di-sigma bond, requiring two neighboring sites [24].

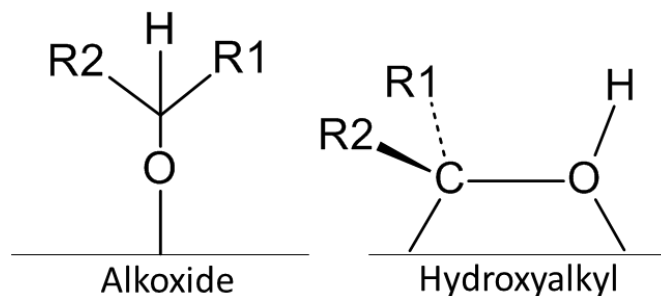


**Figure 5.11** Expected adsorption modes of alkoxide and hydroxyalkyl intermediates on the surface

The precise nature of the half-hydrogenated intermediate comprises a long-standing debate, which has been examined using both experimental and computational methods; here, we summarize the general consensus of the literature. Experimental studies of alcohol dehydrogenation overwhelmingly support alkoxide formation [36, 38-43]. To date, there is no spectroscopic evidence of hydroxyalkyl species existing as intermediates between the ketone and the alcohol in the hydrogenation/dehydrogenation landscape on metal surfaces. Similarly, DFT studies of ketone hydrogenation on Ru [5, 24] surfaces consistently report that—relative to the hydroxyalkyl species—alkoxide binding energies are large and the kinetic barrier to their formation (from the ketone) is small. In general, they conclude that the half-hydrogenated intermediate (KH) is most likely an alkoxide. Given the strong experimental and theoretical evidence, we extend this conclusion to the remainder of our analysis and disregard the hydroxyalkyl species as an abundant surface intermediate in this system.

On Ru (0001) surfaces, alkoxide binding has been considered primarily through computational and spectroscopic analysis of methoxy species formed during methanol adsorption. Specifically, perturbations in the vibrational spectra of adsorbed methoxides are taken to reflect the geometric orientation of the methoxide on the surface. From this, one can obtain insight into the binding

mode and the likely adsorption site. Computational analysis suggests that alkoxide species adsorbed in either type of three-fold hollow site will have an upright geometry, i.e., their C-O bond is orthogonal to the Ru surface. In contrast, if alkoxides bind at top and bridge sites, their C-O bond is tilted relative to the Ru surface [44]. DFT results, which are generally reported at low coverage, consistently reveal that methoxide species bind most favorably at three-fold hollow (hcp) sites [44-46] and possibly both three-fold hollow (hcp) and (fcc) sites [44]. Experimentally, methoxides formed at low coverages bind normal to the metal surface, which is indicative of adsorption at either type of three-fold hollow site [44, 47] and thus consistent with DFT predictions. At higher coverages, methoxides adopt tilted geometries, indicating a shift from three-fold hollow sites to top or bridging sites [47, 48]. Therefore, it appears that alkoxide species bind at multiple adsorption sites, and that their preferred mode is coverage dependent. In particular, evidence suggests that alkoxides—at the high coverages expected under working conditions—may be bound at top and bridge sites.

#### 5.4.4.4 Identifying potential adsorption sites on Ru surfaces: Alcohol

Finally, considering the alcohol product, experimental studies have not identified its preferred adsorption mode on Ru surfaces. Computational studies, however, consistently find top sites to be the most favorable location for alcohol adsorption on Ru (0001) [5, 24, 45].

From the above discussion, it is reasonable to conclude that hydrogen atoms bind most favorably at three-fold hollow (fcc) sites. Oxygenate binding, particularly in the case of the alkoxide, is less certain; however, it appears that there may be a slight preference toward adsorption at top or bridge sites under working conditions. It therefore stands to reason that ketone hydrogenation on Ru can

be cast in terms of elementary processes occurring at two distinct surface sites, particularly since this scenario reconciles with observed kinetic trends.

#### 5.4.5 Microkinetic analysis

The set of elementary steps given in Table 5.6 have a sound physical basis and reconcile with experimentally observed hydrogenation rates. Full kinetic parameterization of these elementary reactions is powerful in that it allows one to develop a predictive model of surface coverage and ketone hydrogenation rates under a wide range of experimental conditions. Unfortunately, free energies of activation are generally not known *a priori*, nor are they easily estimated. Furthermore, because we have measured here only macroscopic production rates of hydrogenation products, we lack the ability to (meaningfully) resolve and/or regress the complete set of kinetic parameters from our experimental data. To reduce the size of the necessary parameter set, we invoke a limiting assumption: that the second surface hydrogen addition (Step 4, Table 5.6) always controls the rate of ketone hydrogenation and that, relative to this step, all other processes are equilibrated. This results in the overall rate expression given in Eq. (20), which we have already demonstrated is qualitatively consistent with experimental data. In doing so, we reduce the burden of estimating activation free energies to a single quantity ( $k_{4+}$ ). Instead, the majority of parameters in the overall rate expression comprise reaction free energies ( $K_i$ ), many of which can be independently estimated from experimental data and published correlations.

We assume that both activation and reaction free energies may vary with the nature of the ketone being hydrogenated, formally requiring that the model be parameterized in triplicate to fully capture trends in acetone, 2-butanone, and 2-pentanone hydrogenation. Where possible, we rely

on correlations to reduce the need for independent parameter estimation. Our approach to doing so is detailed in sections 5.4.5.1 to 5.4.5.4.

#### 5.4.5.1 Microkinetic analysis: gas phase thermochemistry

Enthalpies and entropies for all surface species are necessary for calculating elementary reaction free energies for each step in Table 5.6. Here, we reference each surface species to its gas phase analog; accordingly, we begin by introducing Table 5.7, which summarizes tabulated and estimated thermodynamic data for stable gas phase species ( $\text{H}_2$ , 2-ketones, 2-alcohols) and gas phase analogs of surface intermediates (hydrogen atoms, alkoxies/alkoxides). Standard values of gas phase molecules are corrected to reaction temperature using published heat capacities, which are linear in temperature over our range of experimental conditions and thus well-described by the truncated expression given in Eq. (21). Parameters  $a$  and  $b$  were obtained in house by regression of published heat capacity data.

$$C_p = a + bT \tag{21}$$

**Table 5.7** Summary of energetics of stable gas phase species.

	$\Delta H_f^0(g)$ (kJ mol <sup>-1</sup> )	$S^0(g)$ (J mol <sup>-1</sup> K <sup>-1</sup> )	a (J mol <sup>-1</sup> K <sup>-1</sup> )	b (J mol <sup>-1</sup> K <sup>-2</sup> )
Acetone	-217.4	295.4	26.3	0.16
2-butanone	-238.5	338.2	37.2	0.22
2-pentanone	-259.1	378.2	38.2	0.29
Isopropanol	-272.3	309.8	26.3	0.21
2-butanol	-293.1	355.4	40.0	0.25
2-pentanol	-314.7	397.1	59.5	0.28
H <sub>2</sub>	0	130.7	29.0	-
H	218.0	114.7	20.8	-
H <sup>+</sup>	1534.1	108.8	20.8	-
Isopropoxy/propoxide	-47.3 <sup>†</sup>	293.0 <sup>†</sup>	-	-
2-butoxy/butoxide	-68.1 <sup>†</sup>	338.6 <sup>†</sup>	-	-
2-pentoxo/pentoxide	-89.7 <sup>†</sup>	380.3 <sup>†</sup>	-	-

<sup>†</sup>Estimated quantity

Tabulated gas-phase data are not available for gas-phase analogs of surface alkoxides; however, their entropies and enthalpies can be estimated based on the energetics of alcohol dissociation. The entropy change of alcohol deprotonation to form an alkoxide anion and a proton in the gas phase has been measured at 92 J mol<sup>-1</sup> K<sup>-1</sup>, which is independent of the alcohol's identity and chain length [49]. From this quantity, one can calculate the entropy of the gas-phase alkoxide anion:

$$S_{alkoxide(g)} = S_{alcohol(g)} + \Delta S_{diss(g)} - S_{H^+(g)} \quad (22)$$

Here,  $S_{H^+(g)}$  is the entropy of a proton in the gas phase, which is estimated to be 108.8 J mol<sup>-1</sup> K<sup>-1</sup> at 298 K [50] and  $\Delta S_{diss(g)}$  is the entropy of alcohol deprotonation, which we assume to be

temperature invariant. In this manner, we estimate the entropy of the alkoxide to be lower than that of the alcohol by  $\approx 17 \text{ J mol}^{-1} \text{ K}^{-1}$  at 298 K. Analogously (Eq. 23), one can calculate the enthalpy of the gas-phase alkoxy radical from the homolytic bond dissociation energy (BDE) of the RO-H group, which is also not expected to vary with chain length [19, 51, 52].

$$\Delta H_{f,alkoxy(g)} = \Delta H_{f,alcohol(g)} + BDE_{RO-H} - \Delta H_{f,H(g)} \quad (23)$$

Here, we have taken  $443 \text{ kJ mol}^{-1}$  as the BDE of any secondary alcohol. This value represents the average BDE of isopropanol measured using multiple experimental techniques [51], and we explicitly assume that it is temperature-invariant. Estimated gas-phase entropies (Eq. 22) and enthalpies (Eq. 23) for linear  $C_3 - C_5$  alkoxide species are summarized at 298 K alongside stable gas phase molecules in Table 5.7. Because alkoxide thermochemistry is always referenced to that of the gas-phase alcohol in our calculations, temperature corrections are included in the enthalpy and entropy of the alcohol; as such, we have not estimated heat capacities for the alkoxide species.

#### 5.4.5.2 Microkinetic analysis: adsorption energetics

Enthalpies and entropies for surface species are calculated by adjusting gas-phase quantities (Table 5.7) by their enthalpies and entropies of adsorption on Ru surfaces (Eq. 24 and 25), both of which must be estimated.

$$S_{j*} = S_{j(g)} + \Delta S_{j ads} \quad (24)$$

$$H_{j*} = \Delta H_{f,j(g)} + \Delta H_{j ads} \quad (25)$$

*Adsorption entropies*

Previously reported kinetic studies involving dissociative H<sub>2</sub> adsorption on Ru [53, 54], Pt [55, 56], Fe [57-59] and Cu [60] surfaces report that, on average, molecular H<sub>2</sub> loses approximately 90% of its gas phase entropy upon dissociative adsorption, which suggests a complete loss of translational entropy for molecular hydrogen. Accordingly, we estimate the entropy change for dissociative hydrogen adsorption ( $\Delta S_2$ ) to be  $-117.5 \text{ J mol}^{-1} \text{ K}^{-1}$  at 298 K. From this value and thermodynamic data in Table 5.7, one can calculate the entropy of a surface hydrogen atom ( $S_{H,s} = 6.6 \text{ J mol}^{-1} \text{ K}^{-1}$ ) and the adsorption entropy for a gas-phase hydrogen atom ( $\Delta S_{ads,H} = -108.1 \text{ J mol}^{-1} \text{ K}^{-1}$ ) at 298 K.

For all other species, which are taken to adsorb molecularly, adsorption entropies are calculated using the relationship proposed by Campbell for molecules with standard gas phase entropy below  $60R$  [61]:

$$\Delta S_{ads} = -(0.3S_{gas} + 0.7S_{trans,1D}) \quad (26)$$

In this correlation,  $S_{gas}$  is the total entropy of the molecule in the gas phase and  $S_{trans,1D}$  is the entropy contribution of 1 degree of translational freedom in the gas phase. The latter is calculated using the Sackur-Tetrode equation [61]:

$$S_{1D,trans} = \frac{1}{3} \left\{ 18.6R + R \ln \left[ \left( \frac{m}{m_{Ar}} \right)^{3/2} \left( \frac{T}{298} \right)^{5/2} \right] \right\} \quad (27)$$

Here,  $m$  and  $m_{Ar}$  are the molar masses of the species of interest and Argon respectively and  $R$  is the universal gas constant.

### *Adsorption enthalpies*

Based on experimental (TPD) and computational (DFT) analysis, one can estimate that the binding energy of a hydrogen atom on a clean Ru surface is roughly  $270 \text{ kJ mol}^{-1}$  [25, 62]. However, heats of dissociative hydrogen adsorption on Ru are a strong function of both coverage [63] and Ru particle size [64]; therefore, it is difficult to assign a specific hydrogen binding energy under the conditions of our study. Accordingly, we take  $270 \text{ kJ mol}^{-1}$  as an initial estimate and aim to regress a hydrogen binding energy ( $BE_H$ ) that permits reconciliation with experimental data. To fully specify the use of the hydrogen binding energy in our calculations, we take its value to be equal to the negative heat of adsorption of a gas-phase hydrogen atom onto a Ru surface.

$$\Delta H_H = -BE_H \quad (28)$$

With respect to ketone binding, Anton reported the desorption energy of acetone from a bare Ru (0001) surface to be  $54.4 \pm 10.5 \text{ kJ mol}^{-1}$  using temperature programmed desorption (TPD) [37]. Here, we take this value as equal to the negative of the enthalpy of acetone chemisorption assuming its adsorption to be non-activated. Analogous data for 2-butanone and 2-pentanone have not been reported; therefore, we employ a generalized correlation to estimate their heats of adsorption relative to that of acetone. In developing this model, we assume that the primary interaction between the ketone adsorbate and the Ru surface is through the carbonyl oxygen and that the strength of this interaction (i.e., the carbonyl binding energy on Ru) is identical for acetone, 2-butanone, and 2-pentanone. Differences in heats of adsorption are therefore entirely attributed to the effect of varying carbon chain length.

Typically, as the length of the carbon chain increases for a given class of functional molecules, adsorption becomes more exothermic. This is attributed to van der Waals interactions between the metal surface and methylene groups, which increase with chain length and stabilize adsorption

relative to the primary carbonyl-metal interaction [65, 66]. In general, heats of adsorption scale linearly with the length of the primary carbon chain. For example, desorption energies for n-alkanes over Ru [67], Pt [65, 66], Au [68] and Cu [65, 66, 69] surfaces gain 5 – 10 kJ mol<sup>-1</sup> for each additional carbon atom in the alkyl chain. Similarly, Sexton & Rendulic have reported that each additional carbon in the longest alkyl side chain of C<sub>1</sub>-C<sub>4</sub> alcohols and C<sub>1</sub>-C<sub>5</sub> ethers stabilizes their adsorption on Pt by 5.4 kJ mol<sup>-1</sup> [70]. It therefore stands to reason that enthalpies of ketone adsorption can be described here as a linear function of chain length. Because the enthalpy of acetone adsorption on Ru has been experimentally estimated, we reference all ketone heats of adsorption to that of acetone in this model. This provides a reasonable and convenient initial parameterization of ketone adsorption enthalpies in this system:

$$\Delta H_{ads,i} = \Delta H_{ads,Acetone} - \beta_K * (N_s - 2) \quad (29)$$

Here,  $\Delta H_{ads,Acetone}$  represents the enthalpy of acetone chemisorption,  $\beta_K$  represents the enthalpic stabilization conferred by one additional carbon atom in the main alkyl chain, and  $N_s$  is the number of carbon atoms in the longest alkyl side chain. Using Sexton's convention [70], the longest alkyl side chains in acetone, 2-butanone, and 2-pentanone have, respectively, two, three, and four carbon atoms.  $\Delta H_{ads,Acetone}$  is initially set at the experimentally reported value, -54.4 kJ mol<sup>-1</sup>, and  $\beta_K$  is taken to be 5.8 kJ mol<sup>-1</sup> Carbon<sup>-1</sup>, which has been previously reported to capture the trend in alkane chemisorption on Ru surfaces [65, 67]. At this stage, we view both quantities as potentially adjustable parameters.

To establish heats of alkoxide chemisorption on Ru, we employ an analogous correlation to that developed in Eq. (29). In doing so, it is helpful to define a quantifiable “anchor point” as we have done above using the heat of adsorption for acetone. Since the energetics of alkoxide binding have

not been experimentally measured on Ru, we estimate their values by extension of reported trends in hydroxide/alkoxide binding on both Ru and Pt surfaces. Specifically, Campbell has proposed that, on a variety of metal surfaces, there is a constant offset between hydroxide binding energies ( $BE_{OH}$ ) and alkoxide binding energies ( $BE_{Alkoxide}$ ) [71-73]. Accordingly, for Ru and Pt, one can develop Eq. (30):

$$\left( BE_{OH} - BE_{Alkoxide} \right)_{Ru} = \left( BE_{OH} - BE_{Alkoxide} \right)_{Pt} \quad (30)$$

On Pt (111), Campbell estimated that the methoxide binding energy is  $\approx 60 \text{ kJ mol}^{-1}$  smaller than the analogous hydroxide binding energy [71, 74]. Eq. (30) therefore suggests that, on Ru, the methoxide binding energy will also be smaller than the hydroxide binding energy by  $\approx 60 \text{ kJ mol}^{-1}$ . Using DFT methods, Heyden estimated a hydroxyl binding energy of  $336.8 \text{ kJ mol}^{-1}$  on Ru (0001) [45]. Accordingly, we estimate the methoxide binding energy on Ru (0001) to be  $276.8 \text{ kJ mol}^{-1}$ . As described above for ketone adsorption, we take this quantity as equal to the negative enthalpy of methoxide chemisorption such that  $\Delta H_{ads,methoxide} = -276.8 \text{ kJ mol}^{-1}$ . With this established, heats of alkoxide chemisorption are estimated relative to that of methoxide as a function of the length of the longest alkyl side chain in the adsorbate ( $N_s$ ), where methoxide has an alkyl chain length of one:

$$\Delta H_{ads,i} = \Delta H_{ads,methoxide} - \beta_{KH} * (N_s - 1) \quad (31)$$

As in the case of ketone chemisorption,  $\beta_{KH}$  is the parameter describing the amount of enthalpic stabilization per additional carbon atom in the longest alkyl side chain. Since stabilization is again expected to come from increasing van der Waals interactions with each methylene group in the

longest alkyl side chain, its value is taken as equal to that estimated for chain length stabilization in adsorbed ketones,  $5.8 \text{ kJ mol}^{-1} \text{ Carbon}^{-1}$ .

Alcohol heats of adsorption have not been reported on Ru; therefore, we relate their values to ketone adsorption enthalpies (Eq. 29) based on observed trends in experimental literature. Specifically, on Cu[66] and Pt[66, 75-77], isopropanol adsorption is roughly 10% more exothermic than acetone adsorption. We thus assume the same trend holds for alcohol adsorption on Ru and calculate their adsorption enthalpies using Eq. (32):

$$\Delta H_{ads,OH,i} = 1.10 \cdot \Delta H_{ads,K,i} \quad (32)$$

With respect to thermochemistry, we have at this point defined all necessary surface enthalpies and entropies using tabulated data and reasonable correlations. Accordingly, reaction enthalpies, reaction entropies, reaction free energies, and equilibrium constants can be computed for each elementary step of the scheme in Table 5.6 using Eq. (33) – (36).

$$\Delta H_i = \sum_j \nu_{i,j} \cdot H_j \quad (33)$$

$$\Delta S_i = \sum_j \nu_{i,j} \cdot S_j \quad (34)$$

$$\Delta G_i = \Delta H_i - T \cdot \Delta S_i \quad (35)$$

$$K_i = \exp\left(\frac{-\Delta G_i}{R \cdot T}\right) \quad (36)$$

Built into these reaction thermochemistries and equilibrium constants are five potentially adjustable parameters for which we have made reasonable initial guesses: The hydrogen binding

energy on Ru ( $BE_H$ ), the heat of acetone chemisorption on Ru ( $\Delta H_{ads,acetone}$ ), the heat of methoxide chemisorption on Ru ( $\Delta H_{ads,methoxide}$ ), and the variation in adsorption enthalpy with the length of the alkyl side chain in the ketone ( $\beta_K$ ) or the alkoxide ( $\beta_{KH}$ ).

#### 5.4.5.3 Microkinetic analysis: kinetics of the rate controlling step

The remaining undefined parameters are forward pre-exponential factors and energy barriers for the rate determining step, which we take to be the addition of a hydrogen atom to a surface alkoxide (Step 4, Table 5.6). Per Arrhenius, one may define the forward rate constant in terms of a pre-exponential factor ( $A_{4+}$ ) and an activation barrier ( $E_{a,4+}$ ).

$$k_{4+} = A_{4+} e^{-E_{a,4+}/RT} \quad (37)$$

Since this model considers hydrogenation of three separate ketones, it is ostensibly necessary to estimate six activation parameters: three barriers and three pre-exponential factors. Fortunately, the size of this parameter set can be reduced using Brønsted–Evans–Polanyi (BEP) linear scaling relations, which link the activation barrier for a given step to its reaction enthalpy. Of particular relevance, Sautet has parameterized a BEP relation governing the barrier of O–H dissociation in surface-bound alcohols to form their respective alkoxide [78]. Importantly, this is the reverse of the apparent rate controlling step during ketone hydrogenation—addition of a hydrogen atom to the oxygen atom of a surface bound alkoxide. Accordingly, we recast his correlation in the associative direction (Eq. 38), where the heat of reaction ( $\Delta H_4$ ) is defined, per Step 4 of our *hydrogenation* reaction sequence, as proceeding from the surface bound alkoxide to the surface bound alcohol.

$$E_{a,4+} = (1-\alpha)\Delta H_4 + \beta \quad (38)$$

Here, the value of  $\alpha$  reflects the earliness of the transition state and  $\beta$  is a reference activation barrier. From DFT analysis of alcohol dissociation on multiple metal surfaces, Sautet has estimated  $\alpha$  and  $\beta$  to be 0.11 and 0.83 eV respectively, and we fix their values here for the remainder of our analysis [78]. This correlation allows us to compute ketone-specific barriers from elementary reaction enthalpies, which have been defined in the preceding section; therefore, its use eliminates the need for independent estimation of activation barriers in this analysis.

At present, we have no reliable correlation permitting analogous estimation of elementary pre-exponential factors for each ketone. As such, separate pre-factors are specified for the hydrogenation of each ketone, and we aim to regress their values during model reconciliation with experimental data. As shown in Eq. (39), pre-exponential factors can be related to the entropy of activation ( $\Delta S_{4+}^\ddagger$ ) for a given elementary step [79]. We use this parameterization and work with activation entropies for the remainder of our analysis.

$$A_{4+} = e \frac{k_b T}{h} e^{\Delta S_{4+}^\ddagger / R} \quad (39)$$

To provide an order-of-magnitude initial estimate for each pre-factor, we assume activation entropies for step 4 ( $\Delta S_{4+}^\ddagger$ ) are near zero regardless of the ketone undergoing hydrogenation, which gives a pre-exponential factor of roughly  $10^{13} \text{ s}^{-1}$  for the rate controlling step in acetone, 2-butanone, and 2-pentanone hydrogenation.

Kinetic parameterization of the rate controlling step for each ketone thus adds three potentially variable activation entropies to the set of five uncertain quantities described in thermodynamic

parameterization of the model. In total, the microkinetic model developed here includes eight potentially adjustable parameters. They are identified along with their initial estimates in Table 5.8.

**Table 5.8** Summary of potentially adjustable parameters and their initial estimates.

Adjustable Parameter	Initial estimate	Units
$BE_H$	270	$\text{kJ mol}^{-1}$
$\Delta H_{\text{ads,acetone}}$	-54.4	$\text{kJ mol}^{-1}$
$\Delta H_{\text{ads,methoxide}}$	-276.8	$\text{kJ mol}^{-1}$
$\beta_K$	5.8	$\text{kJ mol}^{-1} \text{Carbon}^{-1}$
$\beta_{KH}$	5.8	$\text{kJ mol}^{-1} \text{Carbon}^{-1}$
$\Delta S_{4^\ddagger,\text{acetone}}$	0	$\text{J mol}^{-1} \text{K}^{-1}$
$\Delta S_{4^\ddagger,2\text{-butanone}}$	0	$\text{J mol}^{-1} \text{K}^{-1}$
$\Delta S_{4^\ddagger,2\text{-pentanone}}$	0	$\text{J mol}^{-1} \text{K}^{-1}$

#### 5.4.5.4 Microkinetic analysis: regression results

Prior to final optimization, the initial set of eight adjustable parameters was reduced to five through sensitivity analysis and preliminary regression. With our initial parameter set, the rate of ketone hydrogenation is insensitive to the value of  $\beta_K$ , which captures the effect of chain length on stabilizing ketone adsorption on Ru (Eq. 29). Accordingly, its value was fixed at the initial estimate of  $5.8 \text{ kJ mol}^{-1} \text{Carbon}^{-1}$ . Hydrogenation rates were moderately sensitive to the analogous quantity governing chain length stabilization of alkoxides,  $\beta_{KH}$  (Eq. 31); however, its regressed value ( $5.5 \pm 0.5 \text{ kJ mol}^{-1} \text{Carbon}^{-1}$ ) was statistically indistinguishable from the initial estimate. As in the case of ketone adsorption,  $\beta_{KH}$  was fixed at  $5.8 \text{ kJ mol}^{-1} \text{Carbon}^{-1}$ . Whether in describing ketone binding or alkoxide binding,  $\beta_i$  most likely reflects increasing van der Waals stabilization upon increasing the length of the carbon chain. In either case, interactions between methylene groups with the Ru surface should be similar, and it is not surprising that we are unable to resolve

a difference in the influence of chain length on their adsorption enthalpies from regression of kinetic data. Finally, the regressed adsorption enthalpy for the methoxide was found to vary less than 1% from the initial estimate. Its adsorption enthalpy was therefore fixed at the initial estimate of  $-276.8 \text{ kJ mol}^{-1}$ . The rate of hydrogenation was sensitive to the remaining five parameters, and their regressed values varied substantially from initial guesses. These estimates are presented with 95% confidence intervals in Table 5.9. Thermodynamic consistency of the model with the regressed parameter set was confirmed by ensuring that elementary reaction free energies weighted by their stoichiometric numbers sum to the overall gas phase free energy for ketone hydrogenation.

**Table 5.9** Summary of optimized parameters found from the regression of experimental data. Uncertainty in optimized values was estimated at a 95% confidence level.

Parameter	Optimized value	Units
$BE_H$	$233.2 \pm 2.8$	$\text{kJ mol}^{-1}$
$\Delta H_{\text{ads,acetone}}$	$-80.8 \pm 1.4$	$\text{kJ mol}^{-1}$
$\Delta H_{\text{ads,methoxide}}$	$-276.8^\dagger$	$\text{kJ mol}^{-1}$
$\beta_K$	$5.8^\dagger$	$\text{kJ mol}^{-1} \text{ Carbon}^{-1}$
$\beta_{KH}$	$5.8^\dagger$	$\text{kJ mol}^{-1} \text{ Carbon}^{-1}$
$\Delta S_{4+,acetone}$	$-44.1 \pm 3.5$	$\text{J mol}^{-1} \text{ K}^{-1}$
$\Delta S_{4+,2-butanone}$	$-45.9 \pm 3.9$	$\text{J mol}^{-1} \text{ K}^{-1}$
$\Delta S_{4+,2-pentanone}$	$-53.4 \pm 3.8$	$\text{J mol}^{-1} \text{ K}^{-1}$

<sup>†</sup>Parameter not varied during optimization.

With the parameter set summarized in Table 9, the kinetic model captures observed trends in the hydrogenation of  $C_3 - C_5$  ketones over a broad range of temperatures and partial pressures. This is illustrated at a high level by the parity plot in Figure 5.12, which includes the entire experimental data set collected in this study. Next, we discuss whether optimal model parameters are physically realistic and connect them with experimental observations.

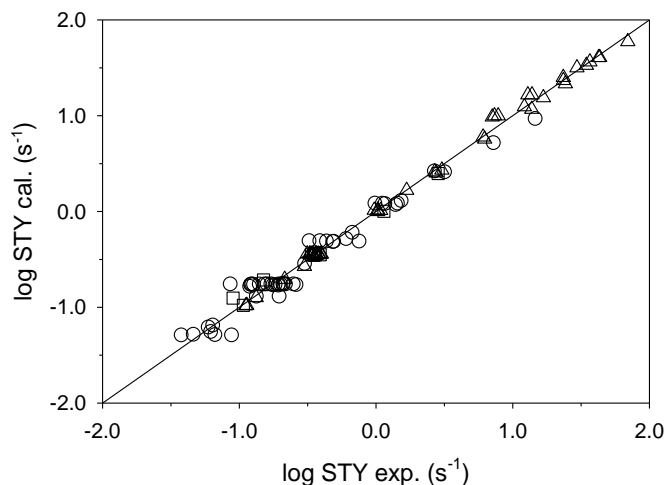


**Figure 5.12** Comparison of predicted to experimentally measured STY of ketone hydrogenation for (○) 2-pentanone, (□) 2-butanone and (Δ) acetone. Reaction conditions were varied across temperatures of 303-456 K, 0.3 - 30 Torr of ketone and 75 - 910 Torr of H<sub>2</sub>.

The binding energy of a hydrogen atom is estimated to be  $233.2 \pm 2.8 \text{ kJ mol}^{-1}$ , which is substantially lower than our initial value of  $270 \text{ kJ mol}^{-1}$ . Based on the regressed binding energy, we calculate the enthalpy of dissociative H<sub>2</sub> adsorption on Ru ( $\Delta H_2$ , 298K) to be  $-30.4 \text{ kJ mol}^{-1}$  under reaction conditions. In contrast, our initially estimated hydrogen binding energy suggests an adsorption enthalpy of  $-100 \text{ kJ mol}^{-1}$ , which is generally consistent with microcalorimetry data reported at low hydrogen coverages [62]. As hydrogen pressures and coverages increase, H<sub>2</sub> chemisorption becomes less exothermic, reportedly decreasing to anywhere from  $-50 \text{ kJ mol}^{-1}$  to  $-35 \text{ kJ mol}^{-1}$  on Ru (0001) depending on the hydrogen coverage [63, 80]. On supported catalysts, King has reported that the enthalpy of H<sub>2</sub> chemisorption on a 4% Ru/SiO<sub>2</sub> catalyst decreases to  $-43 \text{ kJ mol}^{-1}$  at a fractional hydrogen coverage of 0.4 [81] and further to  $-20$  to  $-30 \text{ kJ mol}^{-1}$  as the surface approaches hydrogen saturation [82]. In addition, the presence of co-adsorbates will generally decrease hydrogen binding energies. For example, the enthalpy of H<sub>2</sub> adsorption on Ru (0001) decreases to below  $-38 \text{ kJ mol}^{-1}$  on an oxygen pre-covered surface [37]. We therefore view the relatively small H-binding energy and heat of chemisorption in the optimal parameter set as a

reasonable consequence of repulsive lateral interactions due to elevated coverages of H<sub>2</sub> and other adsorbates under working conditions.

The regressed enthalpy of acetone adsorption ( $-80.8 \pm 1.4 \text{ kJ mol}^{-1}$ ) stands to reason given the relative oxophilicity and substantial oxygen binding energy of Ru. That stated, this heat of adsorption is significantly larger than our initial estimate, which was inferred from TPD experiments ( $-54.4 \pm 10.5 \text{ kJ mol}^{-1}$ ) on a bare Ru (0001) surface. A possible source of the discrepancy is the analysis of TPD data, which used a first-order Redhead equation and assumed a desorption pre-exponential factor of  $10^{13} \text{ s}^{-1}$ . Desorption always occurs with a substantial gain in entropy, and its activation entropies are often substantially greater than zero. This suggests that a desorption pre-factors of  $10^{13} \text{ s}^{-1}$  may be a considerable underestimate, leading one to infer an artificially low desorption energy through conventional TPD analysis [61, 74, 83].

With respect to the methoxide binding enthalpy, we observe that kinetic data are well described using the initial estimate of  $-276.8 \text{ kJ mol}^{-1}$ , and it was not necessary to further refine this value. The value agrees well with multiple DFT estimates for the binding energy of methoxide on Ru (0001). Specifically, Heyden has reported a methoxide adsorption enthalpy of  $-268 \text{ kJ mol}^{-1}$  [45] and Neurock has reported a value of  $-259 \text{ kJ mol}^{-1}$  [24], both of which are within 10% of our estimate.

Elementary activation barriers for the rate controlling step ( $E_{A4+}$ ) were computed from reaction enthalpies using the BEP relation given in Eq. (38). They are found to be statistically indistinguishable at 65.8, 65.3 and 65.8  $\text{kJ mol}^{-1}$  for acetone, 2-butanone, and 2-pentanone, respectively. The lack of variation in regressed elementary barriers is not surprising: surface species in this system were referenced to gas phase analogs; gas phase alkoxide enthalpies were

computed using a single alcohol bond dissociation energy ( $BDE_{OH} = 443 \text{ kJ mol}^{-1}$ ); and both ketone and alkoxide binding energies were parameterized to vary identically with chain length ( $\beta_K = \beta_{KH} = 5.8 \text{ kJ mol}^{-1} \text{ Carbon}^{-1}$ ). Accordingly, the elementary reaction enthalpy for the addition of a hydrogen atom to a surface-bound alkoxide (Step 4) is nearly identical for every ketone ( $\Delta H_4 \approx -16.1 \text{ kJ mol}^{-1}$ ), with minor variations attributed to differences in gas-phase heat capacities. Because we have coupled reaction and activation energies through a BEP relation, this leads to nearly identical elementary barriers for the rate controlling step in each ketone hydrogenation. This agrees with the observation that computationally-derived barriers for hydrogenation of surface alkoxides are invariant with chain length during the reduction of  $C_1$ - $C_4$  aldehydes and ketones over Ru (0001) [24].

Regressed activation entropies were estimated for each ketone (Table 5.9), all of which are substantially negative, indicating a relatively tight transition state. Values cluster around  $-48 \text{ J mol}^{-1} \text{ K}^{-1}$ , which translates to a pre-exponential factor of  $\sim 10^{11} \text{ s}^{-1}$  for each ketone and is reasonable for a bimolecular surface reaction. Although there is statistical overlap among our three regressed activation entropies, we do notice a slight trend in the magnitude of the pre-factor with the chain length of the ketone. Specifically, the activation entropy becomes more negative with the length of the main alkyl chain in the ketone, resulting in a decrease in pre-exponential factors as one goes from acetone ( $1.3 \times 10^{11} \text{ s}^{-1}$ ) to 2-butanone ( $1.2 \times 10^{11} \text{ s}^{-1}$ ) to 2-pentanone ( $4.3 \times 10^{10} \text{ s}^{-1}$ ). The relative magnitude of the pre-factors mirrors the trend in observed STYs for the three ketones (Table 5.2), indicating that our model has primarily attributed the decrease in STY with chain length to increasingly unfavorable activation entropies in the elementary hydrogenation of isopropoxide, butoxide, and pentoxide surface species. While this is a possible explanation, it is not immediately apparent why the activation entropy for a class of analogous chemical reactions

should necessarily scale with chain length. An alternate possibility is that our model fails to capture differences in the number of sites required for adsorption of C<sub>3</sub>, C<sub>4</sub>, and C<sub>5</sub> hydrocarbons. Considering that the atomic and molecular diameter of Ru and acetone are almost identical (~2.7 Å), one might assume that a single acetone monolayer realistically corresponds to one adsorbed acetone molecule per surface Ru atom. However, 2-pentanone is substantially larger (5.1 Å), and its adsorption should lead to an inherently more crowded surface and a lower monolayer coverage than that of acetone. Practically speaking, larger molecules may impose additional “site blocking” interactions that lead to fewer effective sites for 2-pentanone hydrogenation than there are for acetone hydrogenation. Both our experimental STYs and our model assume site accessibility is independent of chain length. If accessible sites do vary with the length of the ketone, then they are likely over-counted by CO chemisorption, which would lead to lower apparent STYs for the larger ketones.

#### 5.4.5.5 Microkinetic analysis: simulation results and comparison to experimental data

In addition to the elementary parameter estimates described in the preceding section, a rigorous interpretation of our apparent kinetic trends requires quantification of surface coverages under reaction conditions. Accordingly, Figure 5.13 presents anticipated surface coverages obtained with the optimized parameter set by assuming that steps 1, 2, 3, and 5 (Table 5.6) are equilibrated at a given set of reaction conditions. Data are presented for acetone (Figure 5.13a), 2-butanone (Figure 5.13b), and 2-pentanone (Figure 5.13c).

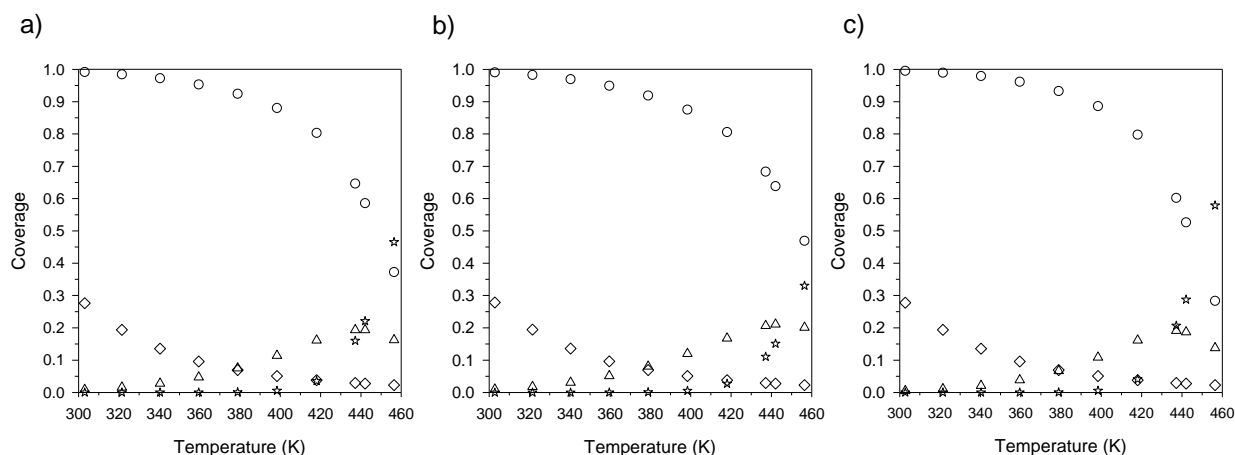


**Figure 5.13** Predicted coverages of ketone ( $\Delta$ ), alkoxide ( $\circ$ ), hydrogen ( $\diamond$ ) and vacant '\*' sites (\*) from 303–456 K at fixed partial pressures of 4.8 Torr ketone and 910 Torr  $H_2$  for a) acetone, b) 2-butanone, and c) 2-pentanone hydrogenation. Note that hydrocarbon species are assumed to bind at '\*' sites and hydrogen atoms bind at 's' sites.

From simulated coverages, several trends are apparent. First, independent of the ketone and throughout our temperature range, there are generally few vacancies in the '\*' site balance; rather, these sites are dominated by the alkoxide intermediate. In the range of 300 – 380 K,  $\theta_{KH}$  ranges from 0.9 – 1.0, indicating an alkoxide saturated surface. As temperatures increase beyond 380 K, the alkoxide coverage decreases from roughly 90% to roughly 40% as coverages of both the ketone and vacant sites increase, relative to the alkoxide, with reaction temperature. Similarly, kinetic Monte-Carlo simulations of carbonyl reduction on Ru (0001) have found the alkoxide coverage to be dominant, with a decreasing trend as temperature increases [24]. In contrast, hydrogen atoms appear to sparsely cover 's' sites. At low temperatures (300 – 360 K), hydrogen coverages vary from 10% to 30%, whereas at high temperatures, 's' sites appear to be predominately vacant. With these coverage trends established, interpretation of apparent reaction orders and kinetic barriers is straightforward. Table 5.10 summarizes experimentally observed and model-predicted values.

**Table 5.10** Comparison of experimentally measured and predicted apparent reaction kinetics for all ketones

Ketone	STY (s <sup>-1</sup> ) <sup>a</sup>		E <sub>a,apparent</sub> (kJ mol <sup>-1</sup> ) <sup>a</sup>		Ketone reaction order		H <sub>2</sub> reaction order	
	Measured	Predicted	Measured	Predicted	Measured	Predicted	Measured	Predicted
322 K								
2-pentanone	0.14	0.16	49.5	51.1	0.01	0	0.52	0.44
2-butanone	0.33	0.34	51.8	50.8	-0.01	0	0.57	0.46
Acetone	0.37	0.36	50.1	50.6	0.03	0	0.48	0.46
442 K								
Acetone	36.7	36.6	17.7	15.2	0.4	0.38	0.92	0.99

a – reaction conditions 4.8 Torr ketone, 910 Torr H<sub>2</sub>

By inspection of the overall rate expression (Eq. 20), one observes that low temperature reaction orders ( $n_{H_2} \approx 0.5$ ,  $n_K \approx 0$  at 322K) reconcile with the low temperature coverage regime, where alkoxides dominate ‘\*’ sites and ‘s’ sites are sparsely covered by hydrogen. At high temperatures, the alkoxide coverage decreases substantially, causing the observed increase in apparent reaction orders ( $n_{H_2} \approx 0.9$ ,  $n_K \approx 0.4$  at 422K).

In order to interpret trends in apparent activation energies, we derive Eq. (40), which specifies the complex functional dependence of the experimentally observable barrier on elementary activation energies, elementary reaction enthalpies, and surface coverages on both ‘\*’ and ‘s’ sites (Eq. 40).

$$E_{a,app} = (E_{a,4+} + \Delta H_2 + \Delta H_3) + \theta_* \Delta H_1 - (\theta_{H,s} + \theta_{KH,*}) \frac{\Delta H_2}{2} - \theta_{KH,*} \Delta H_3 \quad (40)$$

In low temperature coverage regimes where ‘\*’ sites are alkoxide-dominated ( $\theta_{KH,*} \approx 1.0$ ,  $\theta_* \approx 0.0$ ) and ‘s’ sites are mostly vacant ( $\theta_{H,s} \approx 0$ ,  $\theta_s \approx 1$ ), the apparent barrier reduces to  $\approx E_{A,4+} + 0.5\Delta H_2$ , where  $E_{A,4}$  is the elementary barrier of step 4 ( $\approx 66$  kJ mol<sup>-1</sup>) and  $\Delta H_2$  is the enthalpy of dissociative hydrogen chemisorption ( $\approx -30$  kJ mol<sup>-1</sup>). Thus, the difference between elementary and apparent

barriers on alkoxide dominated/hydrogen sparse surfaces (predicted at low temperatures) is primarily given by the enthalpy of dissociative hydrogen chemisorption, which is independent of the chain length of the ketone. Accordingly, apparent barriers are identical for C<sub>3</sub> – C<sub>5</sub> ketones at low reaction temperatures ( $\approx 50 \text{ kJ mol}^{-1}$ ) despite each species having unique adsorption ( $\Delta H_1$ ) and reaction enthalpies ( $\Delta H_3$ ).

At elevated temperatures, alkoxide and hydrogen coverages decrease and vacant sites become increasingly significant in ‘\*’ and ‘s’ site balances. In these coverage regimes,  $\Delta H_1$  ( $\approx -80 \text{ kJ mol}^{-1}$ ),  $\Delta H_2$  ( $\approx -30 \text{ kJ mol}^{-1}$ ), and  $\Delta H_3$  ( $\approx -17.5 \text{ kJ mol}^{-1}$ ) all influence the apparent barrier. Since each step is exothermic, this necessarily leads to a decrease in the apparent barrier relative to the elementary barrier of the rate controlling step. Furthermore, the effects of reaction enthalpies become increasingly pronounced as  $\theta_*$  and  $\theta_s$  both approach 1. In this limit, the apparent barrier is reduced by the full magnitude of ketone and hydrogen adsorption enthalpies. This most likely explains our observation of a significantly diminished apparent barrier ( $\approx 18 \text{ kJ mol}^{-1}$ ) at 442 K.

## 5.5 Conclusion

We have considered the hydrogenation of C<sub>3</sub>-C<sub>5</sub> ketones over Ru/SiO<sub>2</sub>, probing reaction kinetics over a range of ketone partial pressures (0.3 – 30 Torr), H<sub>2</sub> partial pressures (90 – 900 Torr), and reaction temperatures (303 and 456 K). Independent of the ketone, hydrogenations exhibit identical trends in apparent kinetics. Specifically, hydrogenation of acetone, 2-butanone, and 2-pentanone occur with an apparent barrier of approximately  $50 \text{ kJ mol}^{-1}$  between 303 and 363 K. In this temperature range, we additionally observe zero and half order dependencies on the ketone and molecular hydrogen. Apparent kinetics are sensitive to the reaction temperature, with reaction orders increasing for both the ketone and hydrogen. This is attributed to reduced coverages of

hydrogen and adsorbed hydrocarbons at elevated temperatures, a second consequence of which is that the apparent barrier also decreases with reaction temperature: as surfaces become dominated by vacant sites, exothermic heats of adsorption increasingly influence the observed kinetic barrier, decreasing it to below  $20 \text{ kJ mol}^{-1}$  at temperatures above roughly 420 K. Measured site time yields and apparent kinetic parameters were reconciled with elementary phenomena by developing a microkinetic model based on a Horiuti-Polanyi scheme in which hydrogen adatoms sequentially saturate surface-adsorbed ketones to form the alcohol. To explain our observation that saturation kinetics persist over several orders of magnitude in ketone partial pressure, we invoke the assumption that hydrogen atoms and hydrocarbons adsorb at distinct surface sites, which is justifiable based on spectroscopic analysis of adsorbates on Ru(0001) surfaces. Kinetic data are well-described by assuming that the addition of a hydrogen atom to the surface bound alkoxide controls the overall rate of hydrogenation. Parameter estimation suggests that the kinetics of the rate controlling step are, at an elementary level, roughly independent of chain length, proceeding with a kinetic barrier of  $66 \text{ kJ mol}^{-1}$  and a pre-exponential factor of  $\approx 10^{11} \text{ s}^{-1}$ . Experimentally, we do observe that measured STYs decrease with ketone chain length. In our model, this is captured by activation entropies becoming increasingly unfavorable with chain length, which is a possible explanation for the observed trend. Alternatively, the observed trend may reflect a failure to properly account for differences in the number of adsorption sites required for acetone, 2-butanone, and 2-pentanone binding. It stands to reason that ketone monolayer coverages will decrease with chain length. This would likely manifest as a decrease in observed site time yields, for which site counts were estimated by CO uptake, with the size of the ketone.

## 5.6 References

- [1] W.R.H. Wright, R. Palkovits, Development of Heterogeneous Catalysts for the Conversion of Levulinic Acid to  $\gamma$ -Valerolactone, *ChemSusChem*, 5 (2012) 1657-1667.
- [2] L.E. Manzer, Catalytic synthesis of  $\alpha$ -methylene- $\gamma$ -valerolactone: a biomass-derived acrylic monomer, *Appl. Catal., A*, 272 (2004) 249-256.
- [3] Z.-p. Yan, L. Lin, S. Liu, Synthesis of  $\gamma$ -Valerolactone by Hydrogenation of Biomass-derived Levulinic Acid over Ru/C Catalyst, *Energy Fuels*, 23 (2009) 3853-3858.
- [4] P.P. Upare, J.-M. Lee, D.W. Hwang, S.B. Halligudi, Y.K. Hwang, J.-S. Chang, Selective hydrogenation of levulinic acid to  $\gamma$ -valerolactone over carbon-supported noble metal catalysts, *Ind. Eng. Chem.*, 17 (2011) 287-292.
- [5] C. Michel, J. Zaffran, A.M. Ruppert, J. Matras-Michalska, M. Jedrzejczyk, J. Grams, P. Sautet, Role of water in metal catalyst performance for ketone hydrogenation: a joint experimental and theoretical study on levulinic acid conversion into gamma-valerolactone, *Chem. Commun.*, 50 (2014) 12450-12453.
- [6] M. Sudhakar, V.V. Kumar, G. Naresh, M.L. Kantam, S.K. Bhargava, A. Venugopal, Vapor phase hydrogenation of aqueous levulinic acid over hydroxyapatite supported metal (M = Pd, Pt, Ru, Cu, Ni) catalysts, *Appl. Catal., B*, 180 (2016) 113-120.
- [7] O.A. Abdelrahman, A. Heyden, J.Q. Bond, Analysis of Kinetics and Reaction Pathways in the Aqueous-Phase Hydrogenation of Levulinic Acid To Form  $\gamma$ -Valerolactone over Ru/C, *ACS Catal.*, 4 (2014) 1171-1181.
- [8] O.A. Abdelrahman, H.Y. Luo, A. Heyden, Y. Román-Leshkov, J.Q. Bond, Toward rational design of stable, supported metal catalysts for aqueous-phase processing: Insights from the hydrogenation of levulinic acid, *J. Catal.*, 329 (2015) 10-21.
- [9] M. Besson, P. Gallezot, Deactivation of metal catalysts in liquid phase organic reactions, *Catal. Today*, 81 (2003) 547-559.
- [10] W. Luo, U. Deka, A.M. Beale, E.R.H. van Eck, P.C.A. Bruijninx, B.M. Weckhuysen, Ruthenium-catalyzed hydrogenation of levulinic acid: Influence of the support and solvent on catalyst selectivity and stability, *J. Catal.*, 301 (2013) 175-186.
- [11] E.P. Maris, W.C. Ketchie, V. Oleshko, R.J. Davis, Metal Particle Growth during Glucose Hydrogenation over Ru/SiO<sub>2</sub> Evaluated by X-ray Absorption Spectroscopy and Electron Microscopy, *J. Phys. Chem. B*, 110 (2006) 7869-7876.
- [12] H.G. Manyar, D. Weber, H. Daly, J.M. Thompson, D.W. Rooney, L.F. Gladden, E. Hugh Stitt, J. Jose Delgado, S. Bernal, C. Hardacre, Deactivation and regeneration of ruthenium on silica in the liquid-phase hydrogenation of butan-2-one, *J. Catal.*, 265 (2009) 80-88.
- [13] A.S. Piskun, H.H. van de Bovenkamp, C.B. Rasrendra, J.G.M. Winkelman, H.J. Heeres, Kinetic modeling of levulinic acid hydrogenation to  $\gamma$ -valerolactone in water using a carbon supported Ru catalyst, *Appl. Catal., A*, 525 (2016) 158-167.
- [14] U.K. Singh, M.A. Vannice, Kinetics of liquid-phase hydrogenation reactions over supported metal catalysts — a review, *Appl. Catal., A*, 213 (2001) 1-24.
- [15] R.J. Madon, E. Iglesia, Catalytic reaction rates in thermodynamically non-ideal systems, *J. Mol. Catal. A: Chem.*, 163 (2000) 189-204.
- [16] T.J. Schwartz, T.S. Wesley, J.A. Dumesic, Modifying the Surface Properties of Heterogeneous Catalysts Using Polymer-Derived Microenvironments, *Top. Catal.*, 59 (2016) 19-28.

- [17] R.M. Koros, E.J. Nowak, A diagnostic test of the kinetic regime in a packed bed reactor, *Chem. Eng. Sci.*, 22 (1967) 470.
- [18] R.J. Madon, M. Boudart, Experimental criterion for the absence of artifacts in the measurement of rates of heterogeneous catalytic reactions, *Ind. Eng. Chem. Fundam.*, 21 (1982) 438-447.
- [19] B. Sen, M.A. Vannice, Metal-support effects on acetone hydrogenation over platinum catalysts, *J. Catal.*, 113 (1988) 52-71.
- [20] F. Rositani, S. Galvagno, Z. Poltarzewski, P. Staiti, P.L. Antonucci, Kinetics of acetone hydrogenation over Pt/Al<sub>2</sub>O<sub>3</sub> catalysts, *J. Chem. Technol. Biotechnol.*, 35 (1985) 234-240.
- [21] N.V. Pavlenko, A.I. Tripol'skii, G.I. Golodets, Vapor-phase hydrogenation of acetone on applied metals of the platinum group, *Theor Exp Chem*, 22 (1987) 667-675.
- [22] I. Horiuti, M. Polanyi, Exchange reactions of hydrogen on metallic catalysts, *Trans. Faraday Soc.*, 30 (1934) 1164-1172.
- [23] R. Alcalá, J. Greeley, M. Mavrikakis, J.A. Dumesic, Density-functional theory studies of acetone and propanal hydrogenation on Pt(111), *J. Chem. Phys.*, 116 (2002) 8973-8980.
- [24] N.K. Sinha, M. Neurock, A first principles analysis of the hydrogenation of C1-C4 aldehydes and ketones over Ru(0 0 1), *J. Catal.*, 295 (2012) 31-44.
- [25] J.A. Herron, S. Tonelli, M. Mavrikakis, Atomic and molecular adsorption on Ru(0001), *Surf. Sci.*, 614 (2013) 64-74.
- [26] G. Michalk, W. Moritz, H. Pfnür, D. Menzel, A LEED determination of the structures of Ru(001) and of CO/Ru(001)- $\sqrt{3} \times \sqrt{3}$  R30°, *Surf. Sci.*, 129 (1983) 92-106.
- [27] M. Lindroos, H. Pfnür, G. Held, D. Menzel, Adsorbate induced reconstruction by strong chemisorption: Ru(001)p(2×2)-O, *Surf. Sci.*, 222 (1989) 451-463.
- [28] M. Tatarkhanov, F. Rose, E. Fomin, D.F. Ogletree, M. Salmeron, Hydrogen adsorption on Ru(0 0 1) studied by scanning tunneling microscopy, *Surf. Sci.*, 602 (2008) 487-492.
- [29] M.A. Barteau, J.Q. Broughton, D. Menzel, Determination of hydrogen atom binding sites on Ru(001) by HREELS, *Surf. Sci.*, 133 (1983) 443-452.
- [30] M. Sokolowski, T. Koch, H. Pfnür, Ordered structures and phase diagram of atomic hydrogen chemisorbed on ruthenium (001), *Surf. Sci.*, 243 (1991) 261-272.
- [31] M. Lindroos, H. Pfnür, D. Menzel, Investigation of a disordered adsorption system by electron reflection: H/Ru(001) at intermediate coverages, *Surf. Sci.*, 192 (1987) 421-437.
- [32] K.L. Kostov, W. Widdra, D. Menzel, Hydrogen on Ru(0 0 1) revisited: vibrational structure, adsorption states, and lateral coupling, *Surf. Sci.*, 560 (2004) 130-144.
- [33] G. Held, H. Pfnür, D. Menzel, A LEED—IV investigation of the Ru(001)-p(2 × 1)-H structure, *Surf. Sci.*, 271 (1992) 21-31.
- [34] M.Y. Chou, J.R. Chelikowsky, First-principles study of hydrogen adsorption on Ru(0001): Possible occupation of subsurface sites, *Phys. Rev. Lett.*, 59 (1987) 1737-1740.
- [35] L. Xu, H.Y. Xiao, X.T. Zu, Hydrogen adsorption on Ru(0 0 1) surface from density-functional periodic calculations, *Chem. Phys.*, 315 (2005) 155-160.
- [36] M. Mavrikakis, M.A. Barteau, Oxygenate reaction pathways on transition metal surfaces, *J. Mol. Catal. A: Chem.*, 131 (1998) 135-147.
- [37] A.B. Anton, N.R. Avery, B.H. Toby, W.H. Weinberg, Adsorption of acetone both on the clean ruthenium(001) surface and on the ruthenium(001) surface modified chemically by the presence of an ordered oxygen adatom overlayer, *J. Am. Chem. Soc.*, 108 (1986) 684-694.
- [38] J. Hrbek, R.A. DePaola, F.M. Hoffmann, The interaction of methanol with Ru(001), *J. Chem. Phys.*, 81 (1984) 2818-2827.

- [39] R.B. Barros, A.R. Garcia, L.M. Ilharco, Effect of Oxygen Precoverage on the Reactivity of Methanol on Ru(001) Surfaces, *J. Phys. Chem. B*, 108 (2004) 4831-4839.
- [40] J.L. Davis, M.A. Barteau, Decarbonylation and decomposition pathways of alcohol's on Pd(111), *Surf. Sci.*, 187 (1987) 387-406.
- [41] M. Bowker, R.J. Madix, XPS, UPS and thermal desorption studies of alcohol adsorption on Cu(110), *Surf. Sci.*, 116 (1982) 549-572.
- [42] B.A. Sexton, K.D. Rendulic, A.E. Huges, Decomposition pathways of C1-C4 alcohols adsorbed on platinum (111), *Surf. Sci.*, 121 (1982) 181-198.
- [43] J.M. Sturm, C.J. Lee, F. Bijkerk, Reactions of ethanol on Ru(0001), *Surf. Sci.*, 612 (2013) 42-47.
- [44] M.N.D.S. Cordeiro, A.S.S. Pinto, J.A.N.F. Gomes, A DFT study of the chemisorption of methoxy on clean and low oxygen precovered Ru(0 0 0 1) surfaces, *Surf. Sci.*, 601 (2007) 2473-2485.
- [45] J. Lu, A. Heyden, Theoretical investigation of the reaction mechanism of the hydrodeoxygenation of guaiacol over a Ru(0 0 0 1) model surface, *J. Catal.*, 321 (2015) 39-50.
- [46] A.S.S. Pinto, R. Brito de Barros, M.N.D.S. Cordeiro, J.A.N.F. Gomes, A.R. Garcia, L.M. Ilharco, Fermi resonance coupling in the C–H stretching region of methoxide adsorbed on clean Ru(0 0 1): a combined RAIRS and theoretical study, *Surf. Sci.*, 566–568, Part 2 (2004) 965-970.
- [47] R.B. Barros, A.R. Garcia, L.M. Ilharco, Experimental evidence for methoxide geometry on clean Ru(0 0 1), *Surf. Sci.*, 572 (2004) 277-282.
- [48] R.B. Barros, A.R. Garcia, L.M. Ilharco, Adsorption of [D2]Methanol on Ru(001)□O Surfaces: The Influence of Preadsorbed Oxygen on the Methoxide Geometry, *ChemPhysChem*, 6 (2005) 1299-1306.
- [49] J.E. Bartmess, J.A. Scott, R.T. McIver, Scale of acidities in the gas phase from methanol to phenol, *J. Am. Chem. Soc.*, 101 (1979) 6046-6056.
- [50] M.W. Chase, J.L. Curnutt, J.R. Downey, R.A. McDonald, A.N. Syverud, E.A. Valenzuela, JANAF Thermochemical Tables, 1982 Supplement, *J. Phys. Chem. Ref. Data*, 11 (1982) 695-940.
- [51] Y.R. Luo, *Handbook of Bond Dissociation Energies in Organic Compounds*, CRC Press, 2002.
- [52] T.M. Ramond, G.E. Davico, R.L. Schwartz, W.C. Lineberger, Vibronic structure of alkoxy radicals via photoelectron spectroscopy, *J. Chem. Phys.*, 112 (2000) 1158-1169.
- [53] A.M. Karim, V. Prasad, G. Mpourmpakis, W.W. Lonergan, A.I. Frenkel, J.G. Chen, D.G. Vlachos, Correlating Particle Size and Shape of Supported Ru/ $\gamma$ -Al<sub>2</sub>O<sub>3</sub> Catalysts with NH<sub>3</sub> Decomposition Activity, *J. Am. Chem. Soc.*, 131 (2009) 12230-12239.
- [54] O. Hinrichsen, F. Rosowski, M. Muhler, G. Ertl, The microkinetics of ammonia synthesis catalyzed by cesium-promoted supported ruthenium, *Chem. Eng. Sci.*, 51 (1996) 1683-1690.
- [55] R.M. Rioux, M.A. Vannice, Dehydrogenation of isopropyl alcohol on carbon-supported Pt and Cu–Pt catalysts, *J. Catal.*, 233 (2005) 147-165.
- [56] M. Salciccioli, Y. Chen, D.G. Vlachos, Microkinetic Modeling and Reduced Rate Expressions of Ethylene Hydrogenation and Ethane Hydrogenolysis on Platinum, *Ind. Eng. Chem. Res.*, 50 (2011) 28-40.
- [57] W. Rachmady, M.A. Vannice, Acetic Acid Reduction by H<sub>2</sub> over Supported Pt Catalysts: A DRIFTS and TPD/TPR Study, *J. Catal.*, 207 (2002) 317-330.
- [58] W. Rachmady, M.A. Vannice, Acetic acid hydrogenation over supported platinum catalysts, *J. Catal.*, 192 (2000) 322-334.

- [59] W. Rachmady, M.A. Vannice, Acetic Acid Reduction to Acetaldehyde over Iron Catalysts: I. Kinetic Behavior, *J. Catal.*, 208 (2002) 158-169.
- [60] R.M. Rioux, M.A. Vannice, Hydrogenation/dehydrogenation reactions: isopropanol dehydrogenation over copper catalysts, *J. Catal.*, 216 (2003) 362-376.
- [61] C.T. Campbell, J.R.V. Sellers, The Entropies of Adsorbed Molecules, *J. Am. Chem. Soc.*, 134 (2012) 18109-18115.
- [62] P. Feulner, D. Menzel, The adsorption of hydrogen on ruthenium (001): Adsorption states, dipole moments and kinetics of adsorption and desorption, *Surf. Sci.*, 154 (1985) 465-488.
- [63] J.A. Schwarz, Adsorption-desorption kinetics of H<sub>2</sub> from clean and sulfur covered Ru(001), *Surf. Sci.*, 87 (1979) 525-538.
- [64] E.M. Fiordaliso, S. Murphy, R.M. Nielsen, S. Dahl, I. Chorkendorff, H<sub>2</sub> splitting on Pt, Ru and Rh nanoparticles supported on sputtered HOPG, *Surf. Sci.*, 606 (2012) 263-272.
- [65] R.Z. Lei, A.J. Gellman, B.E. Koel, Desorption energies of linear and cyclic alkanes on surfaces: anomalous scaling with length, *Surf. Sci.*, 554 (2004) 125-140.
- [66] B.A. Sexton, A.E. Hughes, A comparison of weak molecular adsorption of organic molecules on clean copper and platinum surfaces, *Surf. Sci.*, 140 (1984) 227-248.
- [67] J.L. Brand, M.V. Arena, A.A. Deckert, S.M. George, Surface diffusion of n-alkanes on Ru(001), *J. Chem. Phys.*, 92 (1990) 5136-5143.
- [68] S.M. Wetterer, D.J. Lavrich, T. Cummings, S.L. Bernasek, G. Scoles, Energetics and Kinetics of the Physisorption of Hydrocarbons on Au(111), *J. Phys. Chem. B*, 102 (1998) 9266-9275.
- [69] A.V. Teplyakov, A.B. Gurevich, M.X. Yang, B.E. Bent, J.G. Chen, NEXAFS and TPD studies of molecular adsorption of hydrocarbons on Cu(100): segmental correlations with the heats of adsorption, *Surf. Sci.*, 396 (1998) 340-348.
- [70] K.D. Rendulic, B.A. Sexton, Adsorption and dehydrogenation of alcohols and ethers on platinum (111), *J. Catal.*, 78 (1982) 126-135.
- [71] E.M. Karp, T.L. Silbaugh, C.T. Campbell, Bond Energies of Molecular Fragments to Metal Surfaces Track Their Bond Energies to H Atoms, *J. Am. Chem. Soc.*, 136 (2014) 4137-4140.
- [72] C.T. Campbell, J.C. Sharp, Y.X. Yao, E.M. Karp, T.L. Silbaugh, Insights into catalysis by gold nanoparticles and their support effects through surface science studies of model catalysts, *Farad. Discuss.*, 152 (2011) 227-239.
- [73] H.E. Bryndza, L.K. Fong, R.A. Paciello, W. Tam, J.E. Bercaw, Relative metal-hydrogen, -oxygen, -nitrogen, and -carbon bond strengths for organoruthenium and organoplatinum compounds; equilibrium studies of Cp\*(PMe<sub>3</sub>)<sub>2</sub>RuX and (DPPE)MePtX systems, *J. Am. Chem. Soc.*, 109 (1987) 1444-1456.
- [74] E.M. Karp, T.L. Silbaugh, M.C. Crowe, C.T. Campbell, Energetics of Adsorbed Methanol and Methoxy on Pt(111) by Microcalorimetry, *J. Am. Chem. Soc.*, 134 (2012) 20388-20395.
- [75] N.R. Avery, EELS identification of the adsorbed species from acetone adsorption on Pt(111), *Surf. Sci.*, 125 (1983) 771-786.
- [76] M.A. Vannice, W. Erley, H. Ibach, A RAIRS and HREELS study of acetone on Pt(111), *Surf. Sci.*, 254 (1991) 1-11.
- [77] M.A. Vannice, W. Erley, H. Ibach, A RAIRS and HREELS study of isopropyl alcohol on Pt(111), *Surf. Sci.*, 254 (1991) 12-20.
- [78] J. Zaffran, C. Michel, F. Delbecq, P. Sautet, Trade-Off between Accuracy and Universality in Linear Energy Relations for Alcohol Dehydrogenation on Transition Metals, *J. Phys. Chem. C*, 119 (2015) 12988-12998.

- [79] I. Chorkendorff, J.W. Niemantsverdriet, Concepts of modern catalysis and kinetics, John Wiley & Sons, 2006.
- [80] H. Shimizu, K. Christmann, G. Ertl, Model studies on bimetallic Cu/Ru catalysts, *J. Catal.*, 61 (1980) 412-429.
- [81] N. Savargaonkar, D. Uner, M. Pruski, T.S. King, Kinetics of Hydrogen Adsorption and Desorption on Silica-Supported Pt, Rh, and Ru Catalysts Studied by Solid State  $^1\text{H}$  NMR, *Langmuir*, 18 (2002) 4005-4009.
- [82] R.L. Narayan, T.S. King, Hydrogen adsorption states on silica-supported Ru–Ag and Ru–Cu bimetallic catalysts investigated via microcalorimetry, *Thermochim. Acta*, 312 (1998) 105-114.
- [83] H. Pfnür, P. Feulner, H.A. Engelhardt, D. Menzel, An example of “fast” desorption: Anomalously high pre-exponentials for CO desorption from Ru (001), *Chem. Phys. Lett.*, 59 (1978) 481-486.

## Chapter 6 Future work

With a kinetic understanding of ketone hydrogenation in the vapor phase developed in the previous chapter, it is of interest to use this kinetic framework as a reference point from which various complexities such as the effect of solvent environments can be investigated. This is especially relevant to the target reaction of this work, LA hydrogenation, as it is most likely to be carried out in the aqueous phase if it is to be commercialized. Therefore understanding the effect of the aqueous phase on reactivity of the proposed Ru catalysts, which are frequently reported to display solvent effects for the target reaction, is of significant practical importance. To accomplish this, the rate of ketone hydrogenation can be perturbed by introducing controlled concentrations of various solvent molecules in the vapor phase. With the desired reaction in mind, LA to GVL, the mono-functional ketone analog of LA (2-pentanone) is chosen to probe the effect of solvent. This will be accomplished by measuring the rate of ketone hydrogenation in the presence of various solvent molecules to the rate in their absence.

To measure the rate of 2-pentanone hydrogenation in the presence of the various solvent molecules a bracketing technique was employed. The rate of hydrogenation at a reference condition of known STY was allowed to stabilize until no appreciable deactivation was observed, at which point a solvent molecule was introduced into the reactor. Once the solvent molecule had been co-fed for ~ 45 mins it was removed from the feed to the reactor, restoring the system to the original reference condition. By comparing the STY of hydrogenation before and after the solvent molecule was introduced, the extent of deactivation/regeneration as a result of the solvent molecule could be accounted for. Once corrected a relative rate of hydrogenation can be calculated:

$$RR_i = \frac{STY_{w/solvent}}{STY_{no\ solvent}} \quad (1)$$

Where RR represent the relative rate in the presence of a given solvent molecule at a set of operating conditions. This procedure was repeated for a given solvent molecule at multiple temperatures and partial pressures.

**Table 6.1** Measured relative rate of 2-pentanone hydrogenation in the presence of various solvents. 2-pentanone and hydrogen partial pressure were maintained at 4 and 910 Torr respectively.

Solvent	Psolvent (Torr)	T (K)	RR
Water	4	303	1.06
Water	10	303	1.35
Water	39	322	1.84
Water	4	322	1.06
Water	10	322	1.21
Water	20	322	1.37
Water	38	322	1.85
Water	89	322	3.09
Water	89	322	3.25
Water	39	342	1.65
Water	4	342	1.04
Deuterium oxide	4	303	1.24
Deuterium oxide	10	303	2.13
Deuterium oxide	39	322	3.1
Deuterium oxide	20	322	1.97
Deuterium oxide	10	322	1.5
Deuterium oxide	4	322	1.26
Deuterium oxide	4	342	1.18
Deuterium oxide	39	342	1.81
Deuterium oxide	10	342	1.3

Deuterium oxide	20	342	1.58
Deuterium oxide	4	342	1.2
Methanol	38	303	1.33
Methanol	38	322	1.11
Methanol	4	322	0.92
Methanol	38	342	1.21
Methanol	4	342	0.99
Methanol	10	342	1.09
Methanol	38	342	1.14
Methanol	10	322	0.97
Methanol	38	322	1.14
Methanol	4	322	0.91
Methanol	1	322	0.92
Methanol	4	322	0.94
Methanol	38	322	1.23
Methanol	4	322	0.95
Methanol	38	322	1.14
Methanol	39	342	1.18
1,4 dioxane	4	303	0.54
1,4 dioxane	10	303	0.42
1,4 dioxane	4	322	0.55
1,4 dioxane	10	322	0.41
1,4 dioxane	38	322	0.22
1,4 dioxane	10	342	0.48
1,4 dioxane	4	342	0.60
1,4 dioxane	38	342	0.21

1,4 dioxane	1	322	0.83
1,4 dioxane	19	322	0.37
1,4 dioxane	4	322	0.34
1,4 dioxane	1	322	0.55
n-heptane	10	303	0.84
n-heptane	4	303	0.9
n-heptane	10	322	0.95
n-heptane	4	322	1
n-heptane	38	322	0.73
n-heptane	38	342	0.87
n-heptane	4	342	1.02
n-heptane	10	342	0.94

---

As can be seen from the trends in relative rates measured across various temperatures and partial pressures presented in Table 6.1, water promotes the apparent rate of hydrogenation to the greatest extent. Methanol appears to show a relatively marginal promotional effect, while the presence of n-heptane and THF appear to only decrease the rate of hydrogenation. The observed trends are in line with previous studies where the rate of 2-butanone hydrogenation is consistently found to be the fastest in a water environment, followed by alcohols as a solvent [1, 2].

It is therefore clear that a promotional effect exists in the presence of compounds such as water and methanol commonly used as solvents for ketone hydrogenation. However the nature of the promotional effect is unclear at this point. One possible explanation is that the solvent molecules may act as a more facile hydrogen source, relative to molecular hydrogen, whereby the ketone is

hydrogenated through transfer hydrogenation. To evaluate this hypothesis, the hydrogen atoms in the solvent molecules can be replaced with deuterium. Should the solvent molecules act as hydrogen donors, one would expect to observe deuterium atoms inserted across the carbonyl group in the resulting alcohol product to some extent. The same co-feeding experiments performed for water ( $\text{H}_2\text{O}$ ) and methanol ( $\text{CH}_3\text{OH}$ ) were therefore repeated with their perdeuterated analogs ( $\text{D}_2\text{O}$  and  $\text{CD}_3\text{OD}$ ).

Two different methods were employed to detect any deuterium atoms that had been incorporated into the 2-pentanol product. Gas effluent samples from the reactor were analyzed using GC-MS, comparing the fragmentation pattern of 2-pentanol produced under co-feeding conditions with that of a standard. Effluent streams from the reactor in the presence of a deuterated solvent, were also passed through traps which condensed greater than 98% by mass of all non-permanent gases (2-pentanone, 2-pentanol and solvent molecule). The collected samples were then analyzed using  $\text{H}^1$ -NMR which can determine whether any of the protons in the 2-pentanol produced had become deuterated. Briefly, in  $\text{H}^1$ -NMR only protons would show up in the spectra and their intensity decreases as they become deuterated or disappear upon complete deuteration. Shown in Figure 6.1 is the  $\text{H}^1$ -NMR of the liquid samples collected with  $\text{D}_2\text{O}$  and  $\text{CD}_3\text{OD}$  fed to the reactor at 40 Torr at 322 K. Of particular interest is the sextet peak at a chemical shift of 3.75 ppm which belongs to proton in the C-H bond of the carbonyl group in 2-pentanol (reference). In both co-feeding experiments ( $\text{D}_2\text{O}$  and  $\text{CD}_3\text{OD}$ ) the integral value of the carbonyl proton is equal to 1 within error, which indicates the no deuterium is incorporated. Furthermore, no deuterium was found to be incorporated into any of the 2-pentanol protons. Additional samples were also collected at conversions varying from less than 1% to 99% and the integral of the C-H carbonyl peak never changed from a value of 1.

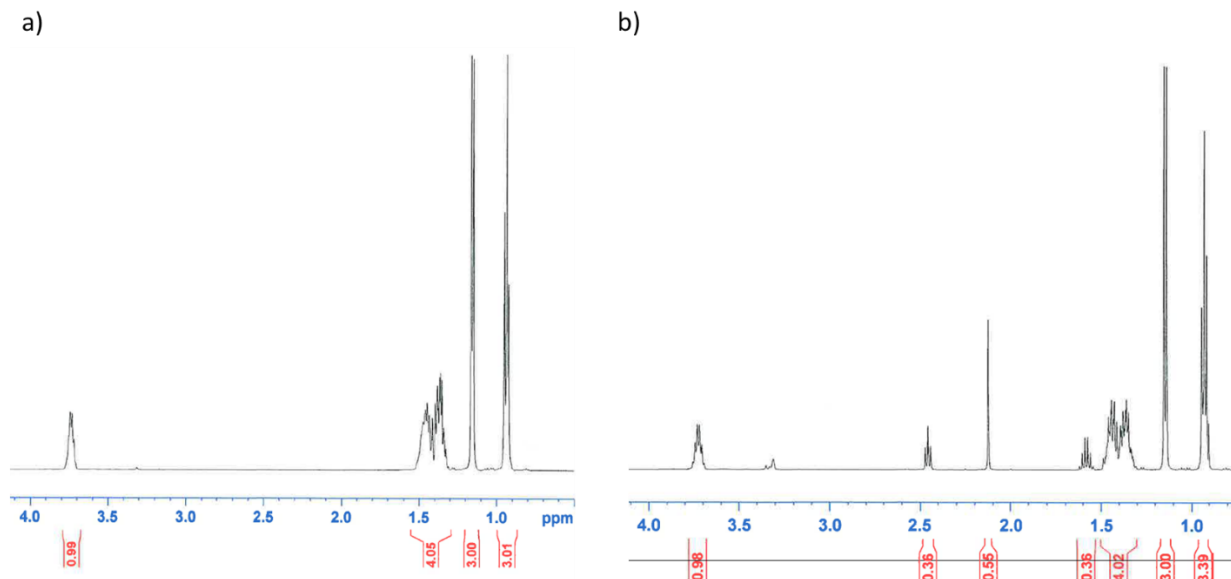


**Figure 6.1**  $^1\text{H}$ -NMR spectra of condensed reactor effluents under co-feeding conditions of 40 Torr of a)  $\text{D}_2\text{O}$  and b)  $\text{CD}_3\text{OD}$  at 322 K.

Turning to the results of the GC-MS analysis, shown in Figure 6.2 is the fragmentation pattern of a 2-pentanol standard alongside that of the reactor effluent gas sample in the presence of  $\text{D}_2\text{O}$  collected under identical conditions described for the NMR samples. The fragmentation pattern of 2-pentanol obtained under co-feeding conditions with  $\text{D}_2\text{O}$  is identical to that of a 2-pentanol standard (Figure 6.2), in agreement with the analysis of the  $^1\text{H}$ -NMR spectrum that no deuterium had been incorporated. We therefore conclude that the promotional effect is not reactive in nature; the solvent molecules do not act as hydrogen donors in any significant capacity.

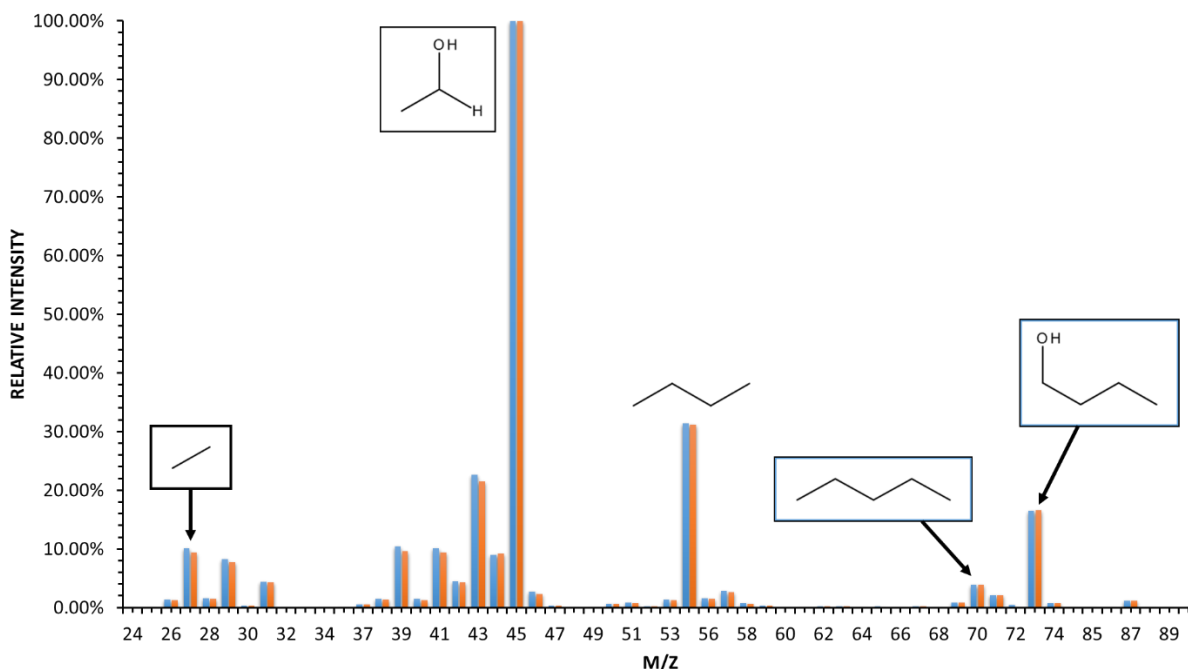


**Figure 6.2** Mass spectrum fragmentations of a 2-pentanol standard (blue) and reactor effluent (orange) at 322 K with 40 Torr of D<sub>2</sub>O co-fed with 4 Torr of 2-pentanone and 910 Torr H<sub>2</sub>.

Interestingly D<sub>2</sub>O appears to provide a larger promotional effect as compared to water at equivalent partial pressures of each compound, which is contradictory to the observed primary kinetic isotope effect (KIE) observed in H<sub>2</sub>/D<sub>2</sub> switching experiments (Chapter 5). This result is in agreement with the GC-MS and H<sup>1</sup>-NMR analysis; since the solvent molecules do not act as hydrogen donors there is no reason to expect the same KIE as when hydrogen was replaced for deuterium.

Another possible explanation for the observed promotional effect, is a manifestation of the traditional explanation provided for solvent effects in homogeneous chemistry. If a solvent environment affects the stability of a kinetically relevant transition state complex of a given reaction, the rate of reaction is expected to be a function of the solvent environment employed. Similarly one can postulate that if the transition state of the rate determining step, identified in

Chapter 5, can be stabilized by the presence of solvent molecules on the catalysts surface one would expect a promotional effect in the rate. So as to probe the plausibility of this hypothesis one can take a quantitative approach. We start by first defining the barrier of the rate determining step ( $E_{a,4}$ ) identified in Chapter 5 as the addition of hydrogen to a surface alkoxide:

$$E_{a,4} = E_{TS} - E_{alkoxide^*} - E_{H_s} \quad (2)$$

Where  $E_{TS}$  is the energy of the transition state on the surface,  $E_{alkoxide^*}$  and  $E_{H_s}$  are the energies of the surface alkoxide and hydrogen adatom involved in the rate determining step. In Chapter 5 the value of  $E_{a,4}$  was determined to be  $65.8 \text{ kJ mol}^{-1}$ , which we take as the reference barrier in the absence of any solvent molecules on the surface. According to the expression in Eq. (2), if the energy of the transition state ( $E_{TS}$ ) is stabilized relative to that of the reactants ( $E_{alkoxide^*}$  and  $E_{H_s}$ ) the barrier of the rate determining step would decrease. A lower barrier would result in a larger rate of hydrogenation, leading to an observed promotional effect if a solvent was to favorably stabilize the transition state. It stands to reason that if a solvent molecule could interact with the transition state, it could possibly interact with the surface alkoxide and hydrogen. It is therefore necessary to establish a method by which these interactions can be quantified. Following the concept of lateral surface interactions as formalized by Norskov [3], one can define the energy of the various species in the presence of a solvent molecule as:

$$E_i = E_{i,0} + 2\varepsilon_i(\theta_{solvent} - \theta_C) \quad (3)$$

Where  $E_{i,0}$  is the energy of a given adsorbate on the surface in the absence of any solvent molecules, which have been determined earlier in Chapter 5. A lateral interaction parameter  $\varepsilon_i$  is defined quantifying the extent of interaction between the adsorbate and solvent molecule on the

surface, a negative value indicates a stabilizing interaction between adsorbate and solvent molecule on the surface.  $\theta_{\text{solvent}}$  is the fractional coverage of the adsorbed solvent molecule on the surface while  $\theta_C$  is the critical fractional coverage below which no lateral interaction is expected ( $E_i = E_{i,0}$  for  $\theta_{\text{solvent}} < \theta_C$ ). Applying the lateral interaction definition of Eq. (3) into the formal definition of a surface reaction barrier Eq. (2), we can define the barrier in terms of possible solvent interactions with surface species.

$$E_{a,4i} = E_{a,4} + 2 * (\epsilon_{TS} - \epsilon_{\text{alkoxide}_s} - \epsilon_{H_s}) * (\theta_{\text{solvent}} - \theta_C) \quad (4)$$

The barrier of rate determining step in the presence of a solvent  $E_{a,4i}$  is now a function of the barrier in the absence of a solvent, fractional coverage of the solvent and the resultant lateral interactions of the species involved. DFT simulations on the possible effect of solvents on ketone hydrogenation on Ru (0001) surfaces indicate that the only change observed in surface energies, as a result of the solvent molecule's presence, occur in the transition state. We therefore set the lateral interaction of parameters of the alkoxide and hydrogen on the surface to zero, simplifying Eq. (4) to

$$E_{a,4i} = E_{a,4} + 2 * \epsilon_{TS,i} * (\theta_{\text{solvent}} - \theta_C) \quad (5)$$

In the above expression the barrier in the presence of a solvent then relies on two unknown parameters, the lateral interaction between the transition state and solvent ( $\epsilon_{TS,i}$ ) and the critical solvent coverage  $\theta_C$ . Unfortunately such values are not available in the existent literature, and are therefore estimated through regression of the data presented in Table 6.1.

To accomplish this we can return to the formal definition of the relative rates collected as per Eq. (1), expressing the relative rate in terms of the rate determining expression developed in chapter 5 for ketone hydrogenation.

$$RR_i = \frac{A_{4,i} e^{-E_{a,4i}} (\theta_{alkoxide} \theta_{H_s})_{solvent}}{A_4 e^{-E_{a,4}} \theta_{alkoxide} \theta_{H_s}} \quad (6)$$

While it is certainly plausible that the pre-exponential be influenced by the presence of a solvent molecule, initial regression indicates that the pre-exponential is relatively unperturbed (<1 % change). The value of the pre-exponential factor is therefore fixed equal to the value determined in Chapter 5 both in the presence and absence of a solvent molecule on the surface. Shown in Table 6.2 are the results of the preliminary regression of Eq. (6) to the relative rates presented in Table 6.1. Alongside the regression values, hydrogen bond donor ( $\alpha$ ) and acceptor ( $\beta$ ) values for each of the solvent molecules are presented since computational studies indicate that hydrogen bonding is a likely source of the stabilization effect [1].

**Table 6.2** Regression results of Eq. (6) and hydrogen bond donor and acceptor capability. Hydrogen bonding properties of water and deuterium oxide are taken to be the same.

Solvent molecule	$\Delta H_{\text{ads}}$ (kJ mol <sup>-1</sup> )	$\epsilon_{\text{TS}}$ (kJ mol <sup>-1</sup> )	$\theta_{\text{C}}$	HBD ( $\alpha$ )	HBA ( $\beta$ )
D <sub>2</sub> O	-81.2	-6.3	0	1.17	0.18
Water	-78.4	-6.1	0	1.17	0.18
Methanol	-81.4	-2.7	0.05	0.98	0.62
1,4 dioxane	-94.9	-3.8	0.56	0	0.37
n-heptane	-98.3	0	0	0	0

From the regression results it appears that water provides the greatest stabilization effect, in line with previous observations that hydrogenation is promoted the most in an aqueous environment [1, 2, 4]. Interestingly, n-heptane is the only solvent molecule which does not exhibit any stabilization through lateral interactions. N-heptane is also the only solvent molecule with no capacity for either accepting or donating hydrogen bonds. Further corroborating the hypotheses that hydrogen bonds are responsible for the stabilization effect observed, is that water which exhibits the greatest degree of hydrogen bonding also provides the largest stabilization effect. It is therefore reasonable to assign the stabilization effect to hydrogen bonding between the solvent molecules and the kinetically relevant transition state on the Ru surface.

## 6.1 References

- [1] B.S. Akpa, C. D'Agostino, L.F. Gladden, K. Hindle, H. Manyar, J. McGregor, R. Li, M. Neurock, N. Sinha, E.H. Stitt, D. Weber, J.A. Zeitler, D.W. Rooney, Solvent effects in the hydrogenation of 2-butanone, *Journal of Catalysis*, 289 (2012) 30-41.
- [2] H. Wan, A. Vitter, R.V. Chaudhari, B. Subramaniam, Kinetic investigations of unusual solvent effects during Ru/C catalyzed hydrogenation of model oxygenates, *J. Catal.*, 309 (2014) 174-184.
- [3] L.C. Grabow, B. Hvolbæk, J.K. Nørskov, Understanding Trends in Catalytic Activity: The Effect of Adsorbate–Adsorbate Interactions for CO Oxidation Over Transition Metals, *Top. Catal.*, 53 (2010) 298-310.
- [4] H.G. Manyar, D. Weber, H. Daly, J.M. Thompson, D.W. Rooney, L.F. Gladden, E. Hugh Stitt, J. Jose Delgado, S. Bernal, C. Hardacre, Deactivation and regeneration of ruthenium on silica in the liquid-phase hydrogenation of butan-2-one, *J. Catal.*, 265 (2009) 80-88.

**VITA**

## NAME OF AUTHOR:

Omar Abdelrahman Ali Abdelrahman

## PLACE OF BIRTH:

Ajman, United Arab Emirates (UAE)

## UNDERGRADUATE SCHOOLS ATTENDED:

American University of Sharjah, Sharjah, United Arab Emirates (UAE)

## DEGREES AWARDED:

Bachelors of Science in Chemical Engineering, 2011, American University of Sharjah